University of Glasgow | School of Engineering

High Repetition Rate Quantum Dot Mode-locked Lasers Operating at ~1.55 µm

Shahid Mahmood

August 2013

A thesis submitted for the degree of

Doctor of Philosophy (Ph.D.)

in the

College of Science & Engineering

School of Engineering

Declaration of Authorship

I, **Shahid Mahmood**, declare that this thesis titled **"High Repetition Rate Quantum Dot Mode-locked Lasers Operating at ~1.55 μm"** and the contributions presented in it are my own. I confirm that:

- This work was done wholly or mainly while in candidature for a research degree at this University.
- Where any part of this thesis has previously been submitted for a degree or any other qualification at this University or any other institution, this has been clearly stated.
- Where I have consulted the published work of others, this is always clearly attributed.
- Where I have quoted from the work of others, the source is always given. With the exception of such quotations, this thesis is entirely my own work.
- I have acknowledged all main sources of help.
- Where the thesis is based on work done by myself jointly with others, I have made clear exactly what was done by others and what I have contributed myself.

Signed: Shahid Mahmood

Date: August , 2013

In the name of Allah,

the most Beneficent and the most Merciful

Abstract

This thesis is concerned with the design, fabrication and investigation of InAs/InP quantum dot mode-locked lasers operating at ~1.55 μm with multi-gigahertz repetition rates. Devices with dual contact configuration operating at ~35 GHz were fabricated and mode-locking characteristics were investigated as a function of the saturable absorber length. The deposition of HR and AR coatings on the two cleaved facets provided an increase in the quantum efficiency and shifted the optimum mode-locking region to a higher injection current. This simple technological step increased the peak power of the emitted pulses by nearly a factor of 2. Furthermore, the appearance of two distinct lobes in the optical spectrum, which is a typical feature of quantum dot material systems, was also investigated. The sonogram technique confirmed the presence of two pulse trains under moderate values of current injection and stable locking of only one lobe at high injection currents. Finally, techniques for high repetition rate mode locking such as colliding pulse, asymmetric colliding pulse and double interval mode-locking were evaluated. Harmonic mode-locking at repetitions rates of ~71 GHz, ~107 GHz and ~238 GHz was demonstrated by placing the absorbers on cavity locations corresponding to the 2^{nd}, 3^{rd} and 7^{th} harmonic, respectively. A monolithically integrated coupled cavity device was also explored, in which an FIB-milled intra-cavity reflector provided mode-locking at a repetition rate of ~107 GHz.

Acknowledgements

First of all, I would like to express my utmost gratitude to my supervisors, Dr. Marc Sorel and Dr. Catrina Bryce, for giving me the opportunity to work on this project. I am especially very grateful to Dr. Marc Sorel for his valuable help, constant encouragement and useful discussions that lead to the conclusion of this thesis. Despite of his busy schedule, he was always able to provide me useful guidance throughout my PhD studies. Marc, you did a lot for me. Thanks very much.

I am very thankful to my colleagues, particularly Dr. Jehan Akbar, Dr. Azhar Naeem, Dr. Kamran Abid, Dr. Usman Younas, Dr. Wout Jansen, Dr. Gabor Mezosi, Dr. Steven Mcmaster, Dr. Giuseppe Tandoi, Dr. Mohsin Haji, Dr. Affar Shahid, Muhammad Mirza, Devnath Dhirhe, Saima, Olesya Ignatova and Maria Carla Camasta for their constant encouragement and making my research experience in Glasgow an enjoyable and memorable one.

Special thanks to Dr. Michael J. Strain, for his constructive suggestions and help during time of difficulty throughout the course of this project. I am grateful to him for allowing me to use his code in this work. Also, special thanks to Dr. Piotr Michal Stolarz and Vincenzo Pusino for their valuable help in the measurements process and spending long hours with me in the labs. Many thanks to Dr. Barry Holmes and Dr. Lianping Hou for support and sharing their knowledge. I am also grateful for the help I received from the technical staff of Rankine building and JWNC, especially Bill Ward, Thomas O Really, Dougi Lang, Mark, Ronnie, Eve, Linda, Mary, Dr. Hiaping and Hellen.

I would also like to express my gratitude to the Higher Education Commission (HEC) of Pakistan for their generous financial assistance through Hazara University Mansehra Pakistan, to undertake this research work.

I am particularly thankful to my family, principally to my parents who always prayed for my success. I am grateful for their support and encouragement,

which I received throughout my life. Allah blesses them. Thanks to my brothers Abdul Wahid, Zahid Ahmed, Rashid Mehmood and sister Salma Adil for their exceptional support and encouragement during my studies. It would be unjustified, not to thanks my wife Sumera Shahid for her patience, support and encouragement throughout the course of my PhD studies, even though we are miles apart.

Publications and Presentations

1. Jehan Akbar, Muhammad Hanif, Suneela Arif, Kamran Abid, Muhammad Azhar, A. Kelly and **Shahid Mahmood** "*Semiconductor Modelocked Lasers with monolithically integrated Semiconductor Optical amplifiers*" *in 2nd Annual International Conference on Optoelectronics ,* (*Submitted for Photonics and Applied Physics (OPAP 2014), 3rd-4th February 2014,* Singapore)

2. A. Catrina Coleman, **Shahid Mahmood**, Michael J. Strain, and Marc Sorel, "*Mode-Locked Quantum Dot Lasers", in PQE-2013 Conference, 6-10 January 2013,* Snowbird, Utah, USA. (Invited talk)

3. **Shahid Mahmood**, M. Haji, Philip. J. Poole, A.Catrina Bryce, Michael J. Strain and M. Sorel, *"High frequency optical pulse generation using quantum dot lasers" in 2nd SU2P Solid state lasers and non linear optics theme workshop, 25th June 2012, School of Engineering, University of Glasgow.* Glasgow, UK. (Poster presentation)

4. Michael J. Strain, **Shahid Mahmood**, Moss Haji Philip.J.Poole, P.Stolarz, A.C Bryce and Marc Sorel, "*Mode-Locking behavior in an InAs/InP Quantum Dot Laser with Dual Spectral Lobe", in SPIE Photonics Europe Conference, 16-19 April 2012,* Brussels, Belgium.

5. **Shahid Mahmood**, M. Haji, Philip. J. Poole, A.Catrina Bryce, M. Sorel and Michael J. Strain, *"High Harmonic Mode-locked InP Quantum Dot Lasers" in European Semiconductor Laser Workshop, 23-24 September 2011,* Lausanne, Switzerland. (Poster presentation)

6. **Shahid Mahmood**, A.Catrina Bryce and M. Sorel, *"Quantum dot mode-locked lasers" Engineering post graduate conference, University of Glasgow, 23-24 June 2009,* Glasgow, UK.

7. **Shahid Mahmood**, A.Catrina Bryce and M. Sorel, *"Quantum dot mode-locked lasers" Engineering post graduate conference, University of*

Glasgow, 28 April 2008, Heriot-Watt University, Edinburgh, UK. (Poster presentation)

To my Parents and Sumera:

Table of Contents

Declaration of Authorship ii

Abstract iv

Acknowledgements v

Publications and Presentations vii

Table of Contents x

List of Figures xvii

Abbreviations xxviii

Chapter 1 - Introduction 1

1.1. Introduction 1

1.2. State of the art in QD mode-locked lasers 2

1.3. Motivation 5

1.4. Thesis outline 5

1.5. References 7

Chapter 2 – Background Theory and Device Design 13

2.1 Introduction 13

2.2 Semiconductor lasers: Historical background 13

2.3 Optical waveguide 15

2.4 Energy diagram in direct bandgap semiconductor materials 16

2.5 Quantum confinement effects 17

2.6 Size of Quantum dot 19

2.7 Quantum dot semiconductor lasers 21

2.7.1 Optical confinement factor of QD structures 22

2.7.2 Threshold current density of QD structures 23

2.8 Mode-locking in lasers 24

2.8.1 Mode-locking principle 24

2.8.2 Mode-locking techniques 28

2.8.3 Conditions for passive mode-locking 29

2.9 Mode-locking in QD active media 31

2.10 Passive mode-locked laser configurations for high repetition frequencies 34

2.11 Conclusions 37

2.12 References 38

Chapter 3 – Fabrication of Mode-locked Lasers 44

3.1 Introduction 44

3.2 Fabrication of ridge waveguide lasers 44

3.3 Lithography 47

- *Photolithography:* 47
- *Electron beam lithography:* 48

3.4 Resist 50

- *Poly methyl methacrylate (PMMA):* 51
- *Hydrogen Silsesquioxane (HSQ):* 53

3.5 Silica(SiO_2) deposition 54

3.6 Planarisation.....55

3.7 Dry Etching.....56

3.8 Etching of InAs/InP QD material.....59

3.9 Wet etching of SiO_2 mask.....59

3.10 Dry etching of dielectric layer 60

3.11 PMMA Plasma ashing.....62

3.12 Device metal contacts.....62

3.13 Conclusions.....64

3.14 References.....65

Chapter 4 – Characterisation of Mode-locked Quantum Dot Lasers.....68

4.1 Introduction.....68

4.2 InAs/InP QD material structure 68

4.3 Ridge waveguide lasers 71

4.3.1 *L-I* curves 72

4.3.2 Characteristic temperature 74

4.4 Characterisation of mode-locked lasers 76

- *Light-current characteristics:* 76
- *Optical spectra measurements:* 77
- *RF spectra measurements:* 78
- *Autocorrelation measurements:* 79
- *Comparison of mode-locking with 5.2 and 7.2 % SA lengths:* 82

4.5 Thin film coatings 84

4.5.1 HR coating 84

4.5.2 AR coating 87

4.6 Mode-locked lasers results after thin film coating 89

4.7 Dual wavelength mode-locked lasers 98

4.7.1 Device design and results 98

4.7.2 Sonogram measurements 104

4.8 Conclusions 107

4.9 References 108

Chapter 5 – Harmonically Mode-locked Semiconductor Lasers 114

5.1 Introduction 114

5.2 Colliding pulse mode-locked (CPM) laser design 114

5.2.1 Characterization of CPM lasers 116

- *Light-current characteristics:* 117
- *Optical spectra and Autocorrelation measurements:* 118

5.3 Asymmetric CPM (ACPM) laser design 124

5.3.1 Characterization of ACPM lasers.....125

- *Light-current characteristics:* 125
- *Optical spectra and Autocorrelation measurements:* 126

5.4 Double interval mode-locking laser design 131

5.4.1 Characterization of DIM lasers 132

- *Light- current characteristics:* 132
- *Optical spectra and Autocorrelation measurements:* 133

5.5 Conclusions.....138

5.6 References.....140

Chapter 6 – Monolithic Coupled Cavity Mode-locked Lasers.....143

6.1 Introduction.....143

6.2 Monolithic coupled cavity laser 143

6.3 Coupled cavity laser design 145

6.4 Design of sub-cavity ratios 146

6.5 ICR design and simulations 148

6.6 The RIE lag effect 150

6.6.1 Deep etched waveguide design 152

- *Deep etched waveguide:* 152

6.6.2 Split waveguide design 155

6.6.3 Self aligned bi-level etching design 158

6.7 Focus ion beam milling 161

6.7.1 Deep slot solutions 163

I. Removal of upper cladding: 163

II. Wide single slot: 163

6.7.2 FIB milling of wide slots 166

6.7.3 Mode-locking results at low temperature 169

- *Mode-locking in FP mode:* 170
- *Mode-locking in SA floating mode:* 172
- *Mode-locking in SA reverse bias mode:* 173
- *Discussion on mode-locking results at low temperature:* 175

6.8 Conclusions 176

6.9 References 178

Chapter 7 - Conclusions 182

7.1 Conclusions 182

7.2 Future work 184

Appendix ‘A’ 186

Appendix ‘B’ 190

Appendix ‘C’.....192

List of Figures

Figure 2.1: Double heterostructure laser diode: schematic of (a) material the structure and (b) refractive index profile [7].....15

Figure 2.2 : Schematic representation of (a) shallow etched and (b) deep etched ridge waveguide design. 16

Figure 2.3 : Schematic of a band model of a III-V semiconductor material with a direct bandgap [2].....17

Figure 2.4: Active region structure and density of states versus energy level for Bulk, Quantum well, Quantum wire and Quantum dot [10]. 19

Figure 2.5: Schematic representation of the QD energy level and conduction band offset 19

Figure 2.6: Schematic representation of the first (E_1^{QD}) and second (E_2^{QD}) energy levels in a QD.....21

Figure 2.7: Schematic of the conduction band of a semiconductor QD material with 5 layers of QDs in the active region (Figure not to scale). 21

Figure 2.8 : Schematic geometry of a single QD (pyramid).....22

Figure 2.9: (a) Schematic of the gain spectrum profile of the laser ; (b) Longitudinal modes inside the cavity; (c) Laser output spectrum [9].....26

Figure 2.10: Illustration of mode-locked laser output in the time domain [9, 22].27

Figure 2.11: Gain and loss dynamics during passive mode-locking operation in a semiconductor QD laser [16]. 29

Figure 2.12: Schematic representation of the gain and absorption versus carrier density [2, 22]. 30

Figure 2.13: Schematics of different cavity configurations for semiconductor passive mode-locking: (a) two section (b) colliding pulse (c) multiple colliding

pulse (d) asymmetric colliding pulse (e) double interval and (f) coupled cavity mode-locked lasers [24].....36

Figure 3.1: The schematic drawings showing the cross-sectional view (leftt) and three dimensional view (right) of the main steps steps involved in the fabrication of ridge waveguide lasers 45

Figure 3.2: A schematic drawing of a two section mode-locked laser illustarting gain and SA section. Top view (left) and three dimensional view (right).....46

Figure 3.3: Contact Photolithographic process [2].....48

Figure 3.4: Schematic illustration of the E-beam writing procedure and parameters [2, 4].....49

Figure 3.5: Schematic showing (a) Positive and (b) Negative resist exposure.....50

Figure 3.6: Schematic of the lift off steps (a) Etched contact window after device passivation (200nm SiO_2, 300nm hard baked HSQ and 100nm SiO_2) (b) spinning of bi-layers of PMMA (PMMA 2010 15% and PMMA 2041 4%, with a thickness of 1200 nm and 120 nm, respectively)(c) Exposure and development of PMMA resists (d) Metal deposition for *p*-contact (e) Metal lift off in hot acetone. 52

Figure 3.7: Deep etched ridge waveguide using HSQ as a hard mask.....54

Figure 3.8: Planarised and metal coated waveguide. 56

Figure 3.9: Schematic showing the steps involved in the RIE etching process [15]. 57

Figure 3.10: Modelled interferometric trace vs. etching depth obtained with Etch Director.....60

Figure 3.11: Interferometer trace recorded during the etching of a QD test sample with ET340.....60

Figure 3.12: (a) Energy Band diagram of metal semiconductor showing formation of potential barrier at equilibrium and (b) with high doping tunnelling through narrow barriers [25].....63

Figure 4.1: Schematic diagram of a shallow etched ridge waveguide structure. ...71

Figure 4.2: Simulation results for 1.535 μm deep ridge waveguide design: (a) Modal effective index versus waveguide width for fundamental, 1st and 2nd order mode and (b) Fundamental transverse mode for a 2.5 μm wide waveguide. 72

Figure 4.3 : *L-I* curve of 1200 μm long RWL device. 73

Figure 4.4 : *L-I* curves of RWL devices, for different lengths of the SA. 74

Figure 4.5 : Measured *L-I* curves for a 1200 μm long RWL, for varying TEC temperature values. 75

Figure 4.6 : Plot of the natural logarithm of I_{th} versus T for a 1200 μm long RWL. 75

Figure 4.7: (a) *L-I* curves for different reverse voltages and (b) Output power map as a function of the gain current and reverse voltage. 77

Figure 4.8 : Schematic of experimental setup for optical spectrum measurements of the mode-locked lasers. 77

Figure 4.9: Optical spectra for a device biased at 90 mA gain current and -3.2 V reverse biased voltage (a) optical spectrum and (b) corresponding mode-spacing. 78

Figure 4.10: Schematic of the experimental setup for RF spectrum measurements of the mode-locked lasers. 79

Figure 4.11: Measured RF spectrum at 90 mA gain current and -3.2 V reverse biased voltage. 79

Figure 4.12: Schematic of the experimental setup for the autocorrelation measurements of mode-locked lasers. 80

Figure 4.13 : (a) A typical pulse train of a mode-locked laser and (b) the deconvolved $sech^2$ fit pulse at 90 mA gain current and -3.2 V SA reverse voltage. 81

Figure 4.14 : (a) Pulse width (b) and TBP as a function of gain current for different values of absorber reverse voltages.....82

Figure 4.15: Mode-locking maps for devices with a SA length corresponding to (a) 5.2 % and (b) 7.2 % of the total laser cavity.....83

Figure 4.16 : Schematic illustration of a FP laser with HR coated facet.....85

Figure 4.17: Maximum and minimum intensities of amplified spontaneous emission (ASE) spectrum. 86

Figure 4.18: *L-I* curve of uncoated (AC/AC) and HR coated (HR/AC) FP lasers. (AC/AC : as cleaved/as cleaved, HR/AC: HR coated/as cleaved).....86

Figure 4.19: Schematic illustration of FP laser with AR and HR coated facets....88

Figure 4.20: Reflectivity as a function of SiO_2 layer thickness for emission wavelength of 1550 nm. 88

Figure 4.21: *L-I* curves of HR coated (HR/AC) and AR coated (HR/AC) FP lasers. (HR/AC : HR coated/as cleaved, HR/AR: HR coated/AR coated).....89

Figure 4.22: Schematic illustration of mode-locked laser with (a) HR coated and cleaved facet (b) HR and AR coated facets. 90

Figure 4.23: The *L-I* curves of (a) the uncoated and (b) HR coated lasers for different reverse biased voltages. The SA length is 9.3% of the total cavity length. 91

Figure 4.24: Measured (a) optical and (b) RF spectra of a HR coated laser with 9.3% SA length. 91

Figure 4.25: (a) A pulse train of a HR coated mode-locked laser and (b) the deconvolved $sech^2$ fit pulse at 66 mA gain current and -2 V SA reverse voltage. 92

Figure 4.26: The *L-I* curves of (a) uncoated and (b) HR coated laser. The SA of the device is 5.2 % of the total cavity length. 93

Figure 4.27: Measured optical and RF spectra of (a, c) uncoated and (b, d) HR coated laser.....93

Figure 4.28: (a) The pulse train and (b) a single $sech^2$ fit pulse at 60 mA gain current and -2.2 V SA reverse voltage. 94

Figure 4.29: (a) The pulse train and (b) the Lorentzian and $sech^2$ fit of a single pulse at 90 mA gain current and -4 V SA reverse voltage. 95

Figure 4.30: The *L-I* curves of a HR/AR coated device taken from the AR coated facet, for different reverse biased voltages (the SA length is 5.2 % of the total cavity length).....95

Figure 4.31: (a) The pulse train and (b) the single Lorentzian and $sech^2$ fit pulse for a HR/AR coated device at 88 mA gain current and -2.4 V SA reverse voltage. 96

Figure 4.32: Mode-locking map for an (a) uncoated and (b) HR/AR coated device. 96

Figure 4.33: Comparison of peak powers of uncoated and HR/AR coated devices at SA reverse voltage of -2.4 V. 97

Figure 4.34: Peak wavelength map measured as a function of the gain current for SA reverse bias voltages of (a) -2.8 V and (b) -3.1 V. 99

Figure 4.35: Peak wavelength as a function of the gain current for SA reverse bias voltages of (a) -2.8 V and (b) -3.1 V. 100

Figure 4.36**:** Peak frequency map measured as a function of the gain current for SA reverse bias voltages of (a) -2.8 V and (b) -3.1 V. 101

Figure 4.37: Spectral distance between the lobes versus the square root of the optical power (The red curve shows the measured data, while the green line is the square root dependence). 102

Figure 4.38: Measured optical and RF spectra: (a) optical and (b) RF spectrum for low level injection current (region A). (c) optical and (d) RF spectrum for mid level injection current (region B). (e) optical and (f) RF spectrum for high level injection current (region C).....104

Figure 4.39: Schematic diagram of the sonogram system in which time delayed pulses are cross-correlated with a spectrally filtered pulse in a non -linear detector. 105

Figure 4.40: Sonogram traces of the pulses emitted at (a) 60 mA (b) 82.5 mA and (c) 90 mA, respectively.....105

Figure 4.41: Sonogram traces of the pulse group delay corresponding to (a) single lobe emission for 60 mA of injection current (b) dual lobe emission for 82.5 mA of injection current and (c) dual lobe emission with 90 mA injection current. ..106

Figure 5.1: Schematic of a CPM laser with two gain and one SA section. The SA section is positioned at *x=L/2* of the cavity length *L*. 115

Figure 5.2: (a) *L-I* curves for different reverse voltages (b) Output power map as a function of gain current and reverse voltage. Bold black lines correspond to mode-locked pulses having extinction ratio of at least 50 %. 117

Figure 5.3: (a) Optical spectrum and (b) corresponding mode spacing at V_{SA} = -1.8 V and I_g = 64mA.....118

Figure 5.4 : Peak wavelength map as a function of gain current at SA reverse voltages fixed at (a) -1.0V (b) -1.8V (c) -2.0 V. Gain current range between the black dotted lines corresponds to mode-locked pulses having extinction ratio of at least 50 %.....119

Figure 5.5: Optical spectrum for fixed V_{SA} = -1.8 V (a) in the process of splitting (b) after splitting.....120

Figure 5.6 : For fixed V_{SA} = -1.8 V (I) optical spectra and (II) autocorrelation traces at I_g fixed at (a) 64 mA (b) 80 mA (c) 104 mA (d) 114 mA.....122

Figure 5.7: Schematic illustrating ACPM with two gain and one SA section. The SA is positioned at *x=L/3* of the cavity length *L*. 125

Figure 5.8: (a) *L-I* curves at different SA reverse voltages (b) Output power map as a function of gain current and reverse voltages. Bold black lines correspond to mode-locked pulses having extinction ratio of at least 50 %. 126

Figure 5.9 : (a) Optical spectrum and (b) corresponding mode spacing at V_{SA} = -1.9 V and I_g = 62 mA. 127

Figure 5.10: Peak wavelength map as a function of gain current at SA reverse voltages of (a) -0.6 V (b) -1.0V (c) -1.9V. Gain current range between the black dotted lines corresponds to mode-locked pulses having extinction ratio of at least 50 %.....128

Figure 5.11 : Optical spectra for fixed V_{SA} = -1.0 V (a) in the process of splitting and (b) after splitting. 129

Figure 5.12: For fixed V_{SA} = -1.9 V (I) optical spectra and (II) autocorrelation traces for I_g fixed at (a) 56 mA (b) 62 mA (c) 76 mA (d) 90 mA. 130

Figure 5.13: Schematic illustrating the DIM technique with three gain an two SA sections positioned at *x=L/3.2* and *y=L/2.3* of the cavity length *L*. 132

Figure 5.14: (a) *L-I* curves at different SA reverse voltages (b) Output power map as a function of gain current and reverse voltages. Bold black lines correspond to mode-locked pulses having extinction ratio of at least 50 %. 133

Figure 5.15: (a) Optical spectrum and (b) corresponding mode spacing at V_{SA} = -2.0 V and I_g = 98 mA. 133

Figure 5.16: Peak wavelength map as a function of gain current at SA reverse voltage of (a) -0.6 V (b) -1.0 V (b) -2.0 V. Gain current range between the black dotted lines correspond to mode-locked pulses having extinction ratio of at least 50 %.....135

Figure 5.17: Optical spectra for fixed V_{SA} = -0.6 V (a) in the process of splitting and (b) after splitting. 136

Figure 5.18: For fixed V_{SA} = -2.0 V (I) optical spectra and (II) autocorrelation traces at I_g of (a) 84 mA (b) 92 mA (c) 98 mA (d) 114 mA. 137

Figure 6.1: Schematic of a monolithic coupled cavity device with the intra-cavity reflector. 144

Figure 6.2: Schematic representing mode spacing corresponding to (a) the fundamental mode-locking (FP mode-locked laser) (b) CCM laser with *M=5*...145

Figure 6.3: Planar view of two parallel devices with 1 and 2 slots ICR. 146

Figure 6.4: Schematics of coupled cavity devices where I(a-d) represent cavity ratios 1:2, 1:3, 1:4 and 1:11, respectively, with both facets cleaved. II(a-d) represent cavity ratios 1:2, 1:3, 1:4 and 1:11, respectively, with one cleaved facet on the long gain section and one back reflector *R* formed by four etched slots on the short gain section. 147

Figure 6.5: Schematic of a deep etched ICR, with two etched slots. 149

Figure 6.6: Simulated reflectivities for a 2.5 μm deep ICR, consisting of one, two and four slots. 150

Figure 6.7 : SEM image of the waveguides incorporating slots. The figures show the RIE lag effect for (a) a 40 min etch and (b) a 60 min etch in a $CH_4/H_2/O_2$ chemistry. 150

Figure 6.8: Etching depth vs etching time for trench (or waveguide) and 362 nm-wide slots. 151

Figure 6.9: (a) Schematic of the deep etched waveguide design (b) Cross-sectional view of the ICR (slots) , which shows the RIE lag effect where $h_2 > h_1$. 152

Figure 6.10: (a) Top view of an ICR consisting of two slots in a deeply etched waveguide (b) Deep etched back reflector of the waveguide. 153

Figure 6.11 : (a) and (b) Missing *p*-contact metal on the top of waveguide (c) Incomplete lift-off between two gain sections as well as between SA and gain section shown by a magnified view on the lower left corner (d) Broken facet of the deep etched waveguide during cleaving. 154

Figure 6.12: (a) Schematic of a split waveguide design with deep etched ICR and (b) magnified view of the deep etched ICR in the gap region. 155

Figure 6.13 : (a) Schematic of the split waveguide geometry after the shallow etch step; (b) second lithographic step with HSQ to define the pattern for the slots;

(c) patterning of PMMA resist to protect the waveguide during the deep etching step (d) shallow etched WG with deep etched slots and trench. 156

Figure 6.14 : (a) Residual HSQ in the slot area (Top view) and (b) layer of residual HSQ resist in a single slot (cross-sectional view). 157

Figure 6.15: Slots are not etched in the gap region, where thick layer of residual resist persisted. 157

Figure 6.16 : Schematic of shallow etched waveguide design with deep etched ICR(slots) and a trench 158

Figure 6.17: (a) Schematic of the HSQ mask for waveguide (WG) and slots; (b) shallow etching of the WG and slots; (c) patterning of PMMA resist to protect the waveguide (the inset on the lower right corner shows a magnified view of the layer of PMMA and HSQ on the top of WG); (d) shallow etched WG with deep etched slots and trench. 159

Figure 6.18: (a) Shallow etched waveguide, with four deep etched slots and a deep trench (b) Cross-sectional view of ~3.1 μm deep four slots. 160

Figure 6.19: (a) White and black dotted lines illustrate the part of the slots which is not etched and etched, respectively. (b) Optical microscope image of the waveguide and slots after resist stripping. 161

Figure 6.20 : Schematic of devices on which FIB milling was carried out. 162

Figure 6.21 : SEM images of 0.206 μm wide and 1.39 μm deep slots: (a) top view and (b) cross-sectional view. SEM images of 0.383 μm wide and 1.88 μm deep slots: (c) top view and (d) cross-sectional view. 162

Figure 6.22: SEM image of (a) FIB milled rectangular pattern prior to mill the deep slots; (b) a 0.871 μm wide slot opening with 3.32 μm deep slots; (c) a single slot along the waveguide to define the ICR and (d) at the end of the waveguide to define the back mirror. 164

Figure 6.23: Measurement results of a two-section FP laser with a single-slot FIB milled mirror: (a) the *L-I* curve and (b) the optical spectrum (at 100 mA) where both sections are forward biased. 165

Figure 6.24: Measurements of (a) the *L-I* curve and (b) the optical spectrum (at 130 mA) of a coupled cavity lasers when all the sections are forward biased. ..166

Figure 6.25: Reflectivity from a slot with a width of 3.5 (black curve) and 4.2 µm (red curve) as a function of the wavelength. 167

Figure 6.26: SEM images of wider slots: (a) top and (b) side view. 167

Figure 6.27: Measurements results of a two section laser with one deep single slot when both sections are forward biased: (a) the *L-I* curve and (b) the optical spectrum (at 78 mA). 168

Figure 6.28: Measurements results of a coupled cavity lasers with single-slots when all the sections are forward biased: (a) the *L-I* curve and (b) the optical spectrum (at 100 mA). 169

Figure 6.29: Optical spectra of the coupled cavity device measured at a heat sink temperature of -20°C , where all sections are forward biased at (a) 70 mA (b) 140 mA, respectively. 171

Figure 6.30: The autocorrelation trace of the coupled cavity device measured at heat sink temperature of -20°C , where all the sections are forward biased at (a) 70 mA and (b) 140 mA. 171

Figure 6.31: Optical spectra of the coupled cavity device measured at a heat sink temperature of -20°C , where SA is floating and the two gain sections are forward biased at (a) 70 mA and (b) 120 mA. 172

Figure 6.32: Autocorrelation trace of the coupled cavity device measured at a heat sink temperature of -20°C , where SA is floating and the two gain sections are forward biased at (a) 70 mA and (b) 120 mA. 173

Figure 6.33: Optical spectra of the coupled cavity device measured at a heat sink temperature of -20°C , where SA is reverse biased and two gain sections are

forward biased at (a) V_{SA}= -0.2 V, I_g= 80 mA and (b) V_{SA}= -2.4 V, I_g= 120 mA. 174

Figure 6.34: Autocorrelation trace of the coupled cavity device when the SA is reverse biased and the two gain sections are forward biased at (a) V_{SA}= -0.2 V, I_g= 80 mA and (b) V_{SA}= -2.4 V, I_g= 120 mA.....174

Abbreviations

Symbol	*Description*	*Symbol*	*Description*
ACPM	Asymmetric colliding pulse mode-locking	AC	As cleaved
AR	Anti reflection	ASE	Amplified spontaneous emission
BPM	Beam propagation method	BSS	Beam step size
CAMFR	Cavity modelling framework	CBE	Chemical beam epitaxy
CCM	Coupled cavity mode-locking/locked	COD	Catastrophic optical damage
CPM	Colliding pulse mode-locking	CW	Continuous wave
DBR	Distributed Bragg reflector	DFB	Distributed feed back
DH	Double heterostructure	DIM	Double interval mode-locking
DOS	Density of states	*e*-beam	Electron beam
E-beam	Electron beam	EDFA	Erbium doped fibre amplifier
ES	Excited state	EPSRC	Engineering and Physical Sciences Research Council
FBG	Fibre Bragg grating	FIB	Focused ion beam
FP	Fabry-Perot	FSR	Free spectral range

Symbol	*Description*	*Symbol*	*Description*
FWHM	Full width half maximum	FWM	Four wave mixing
GHz	Gigahertz	GS	Ground state
GSS	Ground state splitting	HF	Hydrofluoric acid
HR	Highly reflection	HSQ	Hydrogen silsesquioxane
ICP	Inductively coupled plasma	ICR	Intra cavity reflector
IPA	Isopropanol	JWNC	James Watt Nano fabrication centre
LD	Laser driver	*L-I*	Light-current
LN	Liquid Nitrogen	MBE	Molecular beam epitaxy
MCPM	Multi colliding pulse mode-locking	MIBK	Methyl isobutyl ketone
ML	Mode-locking / Locked	MLLs	Mode-locked lasers
MOCVD	Metal organic chemical vapour deposition	OSA	Optical spectrum analyser
PECVD	Plasma enhanced chemical vapour deposition	PMMA	Poly methyl methacrylate
QCSE	Quantum confined stark effect	QD	Quantum dot
Qdash	Quantum dash	QW	Quantum well
RBW	Resolution bandwidth	RF	Radio frequency
RIE	Reactive ion etching	RO	Reverse osmosis
RTA	Rapid thermal annealer	RWLs	Ridge waveguide lasers

Symbol	*Description*	*Symbol*	*Description*
SA	Saturable absorber	SEM	Scanning electron
SHB	Spectral hole burning	SHG	Second harmonic
SMLLs	Semiconductor mode-	SPM	Self-phase modulation
TBP	Time bandwidth product	TE	Transverse electric
TEC	Thermoelectric controller	THz	Tera hertz
TMAH	Tetra Methyl Ammonium Hydroxide	UV	Ultra violet
VBW	Video bandwidth	VRU	Variable resolution unit
WG	Waveguide	XPM	Cross phase modulation

Chapter 1

Introduction

1.1. Introduction

Semiconductor lasers have been one of the most successful technological developments of the last century. Since their first demonstration in 1962 [1], semiconductor lasers have experienced tremendous improvements in terms of performance and reliability which made them a well-established and indispensable technology for a large variety of applications. Some of these applications such as optical communication systems [2, 3], optical sampling [4], optical source in fibre radio [5], non-linear optoelectronics and spectroscopy [6] require sources capable of generating short optical pulses and/or repetition rates ranging up to hundreds of GHz [3, 7]. Monolithic semiconductor lasers operating in Q-switching, gain switching and mode-locking are excellent candidates to perform such a task [8]. Among these techniques, mode-locking is the preferred approach since it can achieve very short pulse durations down to few hundred femtoseconds [9-11] and higher repetition rates of several hundreds of GHz [12-15]. Compared to their fibre and solid state counterparts, semiconductor mode locked lasers (SMLLs) offer many advantages, such as compactness, robustness, low cost and ease of integration [2, 3]. Despite their several advantages, both the maximum average power and minimum pulse width of SMMLs are limited in comparison to solid state lasers, which are capable of generating pulses with femtosecond durations

[16] owing to their broad gain bandwidth, and average output powers of several tens of Watts [17].

The work presented in this thesis was part of the project "High power, High Frequency Mode-locked Semiconductor Lasers", supported by the Engineering and Physical Sciences Research Council (EPSRC). The main aim of the project was to increase both the average power and the repetition rate of monolithically integrated SMLLs emitting at wavelengths of 780-850 nm and 1550 nm. This ambitious aim required the convergence of several skills and technologies that included the design of an optimised epilayer structure, the theoretical understanding of the complex interplay between non-linearities, gain and losses, the engineering of the cavity dispersion and material bandgap, the development of coupled-cavity geometries. One of the tasks of the research was dedicated to the investigation of material structures such as quantum dots that provide a wider gain bandwidth and are therefore of interest for both narrow pulse generation and high repetition rates. The work presented in this thesis is concerned with the design, fabrication and investigation of InAs/InP quantum dot mode-locked lasers operating at 1550 nm with repetition rates of several hundreds of GHz.

1.2. State of the art in QD mode-locked lasers

This section presents a brief review of the research that has been carried out in the field of quantum dot mode-locked lasers.

A QD laser was first proposed by Dingle and Henry in 1976 [18]. Their approach was based on the application of size quantization concept to the semiconductor gain medium and had previously led to the successful development of QW lasers [19]. In 1982, Arkawa *et al.* published the first theoretical treatment of three-dimensional confined QD lasers and, thanks to the discrete nature of the density of states, they predicted a lower temperature sensitivity of the threshold current [20]. The first injection laser based on self-assembled QD was realised in 1994 [21]. Since then, rapid progress has been made and the successful fabrication of QD lasers has been reported on different

epilayer structures and for different emission wavelengths. In 2001, Haung *et al.* reported the first two section semiconductor QD mode-locked laser operating at 1.3 μm [22]. They demonstrated mode-locking with ~17 ps pulses at a repetition rate of 7.4 GHz. In 2004, Thompson *et al*. demonstrated for the first time Fourier transform limited 10 ps pulses at 18 GHz repetition rate, using passive mode-locking in QD laser emitting at ~1.3 μm [23]. Increased repetition rates up to 35 GHz with Fourier transform limited pulses of 7 ps duration were achieved on a 1130 μm long cavity [24]. Around the same period, Tan, W.K *et al.* also demonstrated 35 GHz passive mode-locked two section laser [25]. Later, Laemmlin, M. *at al.* were able to further improve the repetition frequency up to 80 GHz, using a 500 μm long cavity [26]. In 2005, E. U. Rafailov *et al.* for the first time achieved sub-picosecond pulse generation from a two section QD laser and demonstrated pulses as short as 390 fs [10]. Later, many other groups also reported the generation of sub-picoseconds pulse [11, 26, 27]. Thompson *et al*. demonstrated subpicosecond pulse generation with increased output power, using a tapered waveguide configuration [11, 27] and achieved 360 fs Fourier transform limited pulses with a peak power of 2.25 W [11]. Higher repetition rates in mode-locked lasers might be achieved by decreasing the length of cavity or by using harmonic mode-locking techniques. The major drawbacks of short cavities are the reduction of the gain that can prevent lasing [2] and the problems associated to the cleaving and handling of cavities shorter than 200-300 μm. Therefore, harmonic mode-locking is the preferred technique to achieve repetition rates higher than ~100 GHz. In 2005, Thompson *et al*. reported colliding pulse mode locking (CPM) for the first time in QD lasers [28], where the CPM operation was demonstrated on a 3.9 mm long laser device operating at a repetition rate of 20 GHz. In the following year, Tan, W.K *et al.* also reported on CPM operation at repetition rates up to 37 GHz, using a 2.1 mm cavity length [29]. Using multi-contact asymmetric cavity geometry, mode-locking has been demonstrated at 1^{st}, 2^{nd}, 3^{rd} and 6^{th} harmonics corresponding to repetition rates of 39, 78, 117 and 238 GHz, respectively [15]. Li Yan et *al.* demonstrated harmonic mode-locking using double interval model-locking (DIM) technique and they were able to

achieve repetition rates up to 60 GHz , which corresponded to the 10^{th} harmonic of the fundamental frequency [30].In the DIM technique, two separate saturable absorbers (SAs) are used and mode-locking occurs at a repetition rate that correspond to least common multiple between the sub-cavities formed by the SAs [30].

Early works were carried out on QD mode-locked lasers based on GaAs material system emitting in the wavelength range of 1.1-1.3 μm [22, 31, 32]. Improvements in the growth techniques and understanding in the dot formation enabled the development of epilayer structures on InP based materials, which can emit longer wavelengths [33]. In particular, InP based QD laser emitting in the wavelength range of 1.3-1.5 μm are of great interest as they can be employed in optical fibre communication systems [34]. The first QD laser based on InP material system was demonstrated in 1998 by Ustinov, V.M *et al.* [35], followed by several other groups [34, 36-38]. In 2005, passive mode-locking at 1550 nm was demonstrated in a single section QD laser for the first time [39]. Mode-locking in a single section laser is of great interest as high repetition rates can be generated without incorporating any SA section in the cavity [40-44]. Because the InAs/InP QD material is highly non-linear [45], passive mode-locking in single section FP devices is attributed to non linear optical effects within the QD gain cavity such as self-phase modulation (SPM), cross-phase modulation (XPM) and four-wave mixing (FWM) [42]. Pulse generation at 1.55 μm with repetition rates of 346 and 245 GHz has been achieved using a single section 120 and 170 μm long quantum-dash (elongated QDs) based laser cavities, respectively [41]. Changing the length of the cavity enabled Lu Z.G *et al.* to achieve repetition rates from 10 to 100 GHz in the C and L-band wavelength range [9]. They also reported a C- band mode-locked laser operating at 50 GHz repetition rate with record short pulses of 295 fs [9, 46]. The same group also demonstrated repetition rates up to 437 GHz by coupling a single section QD laser with an external fibre cavity formed by a fibre Bragg grating (FBG) [9]. Later they were able to further increase the repetition rates up to 1.01 THz by using the external coupled cavity effect [47]. Generally, passive mode-locking in two section lasers based on InP

QD material system is more challenging due to increased waveguide internal losses [48]. Heck *et al.* were able to demonstrate in 2007, the first ever two section QD mode-locked laser operating at 1.55 μm with a repetition rate of 4.6 GHz [49]. The same group later reported the first QD mode-locked ring laser (using a CPM mechanism) with repetition rates of 5 GHz [50]. In 2011, Rosales *et al.* realized a 450 μm long two section quantum dash laser and demonstrated repetition rates up to 95 GHz with pulse duration of 1.4 ps [51]. Finally, the unique spectral behaviour of the QD lasers has been object of interest for many groups due to their unusual splitting in to two separate lobes resulting in the emission of two wavelength peaks [11, 43, 44, 52, 53]. Dual wavelength behaviour is believed to occur due to ground state splitting (GSS) [43, 52, 54], which has been attributed either to spectral hole burning (SHB) [52] or Rabi oscillation phenomenon [44].

1.3. Motivation

The research work presented in this thesis focuses on the development of InAs/InP quantum dot mode-locked lasers emitting at a wavelength of 1.55 μm and operating at high repetition rates. The delta-like density of states (DOS) typical of quantum dot gain media brings several advantages, lower absorption saturation, higher gain saturation energy, lower threshold current, lower temperature sensitivity and lower internal losses [55]. Also, the inhomogeneous broadening of the quantum dot size substantially increases the width of the gain bandwidth [2]. These properties make QD gain media an attractive choice for the development of mode-locked lasers that operate at high repetition rates. The main aim of this work is to investigate harmonic mode locking for high repetition rates by placing the absorber at spatial harmonics of the cavity, as well as by developing monolithic coupled cavity mode-locked (CCM) laser geometries.

1.4. Thesis outline

Chapter 1 introduces and motivates the research work, and provides a historical perspective on the development of QD mode-locked semiconductor lasers.

Chapter 2 describes the operating principles of QD semiconductor lasers along with the basic concept of mode-locking. Finally, the main semiconductor mode-locked laser configurations, which can be used for high repetition frequencies are introduced.

Chapter 3 provides an overview of the fabrication work carried out in this research. This includes a general description of the fabrication flow for making mode-locked semiconductor devices together with a more detailed explanation of those technological steps that were developed or optimised in this research.

Chapter 4 presents the design of the InAs/InP QD epitaxial material and discusses the main results obtained from the dual-section QD mode-locked lasers as a function of the biasing conditions and for different lengths of the SA section. The improvement in the mode-locking performance with the deposition of AR and HR coatings on the cleaved facets is also presented. Finally, the splitting of the optical spectrum into two sets of modes is discussed along with the main features of dual wavelength mode-locked operation.

Chapter 5 presents the results obtained from the higher order harmonically mode-locked lasers. The design of colliding pulse, asymmetric colliding pulse and double interval mode-locking geometries is presented and results on the 2^{nd}, 3^{rd} and 7^{th} harmonic mode-locking are discussed.

Chapter 6 describes the monolithic coupled cavity laser device design that incorporates intra-cavity reflectors (ICR) along with the main fabrication steps. A detailed description of the ICR design, patterning and dry etching of the slots are presented as these tasks proved particularly challenging in the development of the devices. The focused ion beam (FIB) milling of devices with different slot openings is also described as a possible alternative to dry etching. Finally, the results of the FIB milled coupled cavity devices are analysed.

Chapter 7 provides the conclusions and suggestions for future work.

1.5. References

1. *Hall, R.N., et al., Coherent light emission from GaAs junctions. Physical Review Letters, 1962. 9(9): p. 366-368.*

2. *Rafailov, E.U., M.A. Cataluna, and W. Sibbett, Mode-locked quantum-dot lasers. Nature photonics, 2007. 1(7): p. 395-401.*

3. *Avrutin, E.A., J.H. Marsh, and E.L. Portnoi, Monolithic and multi-gigahertz mode-locked semiconductor lasers: constructions, experiments, models and applications. Optoelectronics, IEE Proceedings -, 2000. 147(4): p. 251-278.*

4. *Derickson, D.J., et al., Short pulse generation using multisegment mode-locked semiconductor lasers. Quantum Electronics, IEEE Journal of, 1992. 28(10): p. 2186-2202.*

5. *Novak, D., C. Lim, and A.F. Liu. Optimization of millimeter-wave signal generation using multi-electrode semiconductor lasers with subharmonic electrical injection. in Microwave Photonics, 1996. MWP '96. Technical Digest., 1996 Internatonal Topical Meeting on. 1996.*

6. *Bradley, D.J. and M.H. Holbrook, Mode-locked semiconductor lasers and their spectroscopic applications. Philosophical Transactions of the Royal Society of London. Series A, Mathematical and Physical Sciences, 1982. 307(1500): p. 521-530.*

7. *Williams, K.A., M.G. Thompson, and I.H. White, Long-wavelength monolithic mode-locked diode lasers. New Journal of Physics, 2004. 6(1): p. 179.*

8. *Vasil'Ev, P.P., Ultrashort pulse generation in diode lasers. Optical and quantum electronics, 1992. 24(8): p. 801-824.*

9. *Lu, Z.G., et al., Ultra-high repetition rate InAs/InP quantum dot mode-locked lasers. Optics Communications, 2011. 284(9): p. 2323-2326.*

10. Rafailov, E.U., et al., High-power picosecond and femtosecond pulse generation from a two-section mode-locked quantum-dot laser. Applied Physics Letters, 2005. 87(8): p. 081107-3.

11. Thompson, M.G., R.V. Penty, and I.H. White. Regimes of mode-locking in tapered quantum dot laser diodes. in Semiconductor Laser Conference, 2008. ISLC 2008. IEEE 21st International. 2008: IEEE.

12. Yanson, D.A., et al., Ultrafast harmonic mode-locking of monolithic compound-cavity laser diodes incorporating photonic-bandgap reflectors. Quantum Electronics, IEEE Journal of, 2002. 38(1): p. 1-11.

13. Arahira, S., Y. Matsui, and Y. Ogawa, Mode-locking at very high repetition rates more than terahertz in passively mode-locked distributed-Bragg-reflector laser diodes. Quantum Electronics, IEEE Journal of, 1996. 32(7): p. 1211-1224.

14. Shimizu, T., I. Ogura, and H. Yokoyama, 860 GHz rate asymmetric colliding pulse modelocked diode lasers. Electronics Letters, 1997. 33(22): p. 1868-1869.

15. Rae, A.R., et al. Harmonic mode-locking of a quantum-dot laser diode. in Lasers and Electro-Optics Society, 2006. LEOS 2006. 19th Annual Meeting of the IEEE. 2006: IEEE.

16. Ell, R., et al., Generation of 5-fs pulses and octave-spanning spectra directly from a Ti: sapphire laser. Optics letters, 2001. 26(6): p. 373-375.

17. Innerhofer, E., et al., 60-W average power in 810-fs pulses from a thin-disk Yb:YAG laser. Opt. Lett., 2003. 28(5): p. 367-369.

18. R. Dingle and C.H. Henry, "Quantum effects in heterostructure lasers," U.S. Patent No. 3982207. 1976.

19. Ledentsov, N.N., et al. QD lasers: physics and applications. in Asia-Pacific Optical Communications. 2005: International Society for Optics and Photonics.

20. *Arakawa, Y. and H. Sakaki, Multidimensional quantum well laser and temperature dependence of its threshold current. Applied Physics Letters, 1982. 40(11): p. 939-941.*

21. *Kirstaedter, N., et al., Low threshold, large T_o injection laser emission from (InGa)As quantum dots. Electronics Letters, 1994. 30(17): p. 1416-1417.*

22. *Huang, X., et al., Passive mode-locking in 1.3 μm two-section InAs quantum dot lasers. Applied Physics Letters, 2001. 78(19): p. 2825-2827.*

23. *Thompson, M.G., et al., Transform-limited optical pulses from 18 GHz monolithic modelocked quantum dot lasers operating at ~1.3 μm. Electronics Letters, 2004. 40(5): p. 346-347.*

24. *Kuntz, M., et al., 35 GHz mode-locking of 1.3 mu m quantum dot lasers. Applied Physics Letters, 2004. 85(5): p. 843-845.*

25. *Tan, W.K., et al. 35 GHz pure passively mode locked quantum dot lasers operating close to 1.3 μm. in Lasers and Electro-Optics Society, 2004. LEOS 2004. The 17th Annual Meeting of the IEEE. 2004.*

26. *Laemmlin, M., et al., Distortion-free optical amplification of 20-80 GHz modelocked laser pulses at 1.3 μm using quantum dots. Electronics Letters, 2006. 42(12): p. 697-699.*

27. *Thompson, M.G., et al., Subpicosecond high-power mode locking using flared waveguide monolithic quantum-dot lasers. Applied Physics Letters, 2006. 88(13): p. 133119-3.*

28. *Thompson, M.G., et al., Colliding-pulse modelocked quantum dot lasers. Electronics Letters, 2005. 41(5): p. 248-250.*

29. *Tan, W.K., et al. 37 GHz colliding pulse mode locking operation of quantum dot asers operating close to 1.3 μm. in Lasers and Electro-Optics, 2006 and 2006 Quantum Electronics and Laser Science Conference. CLEO/QELS 2006. Conference on. 2006.*

30. *Li, Y., et al., Harmonic mode-locking using the double interval technique in quantum dot lasers. Opt. Express, 2010. 18(14): p. 14637-14643.*

31. *Thompson, M.G., et al., 10 GHz hybrid modelocking of monolithic InGaAs quantum dot lasers. Electronics Letters, 2003. 39(15): p. 1121-1122.*

32. *Thompson, M.G., et al. Mode-locked quantum dot lasers for picosecond pulse generation. in Integrated Optoelectronic Devices 2004. 2004: International Society for Optics and Photonics.*

33. *Anantathanasarn, S., et al., Lasing of wavelength-tunable (1.55 μm region) InAs/InGaAsP/InP (100) quantum dots grown by metal organic vapor-phase epitaxy. Applied Physics Letters, 2006. 89(7): p. 073115-3.*

34. *Nishi, K., et al., Long-wavelength lasing from InAs self-assembled quantum dots on (311) B InP. Applied Physics Letters, 1998. 73(4): p. 526-528.*

35. *Ustinov, V.M., et al., Low-threshold quantum-dot injection heterolaser emitting at 1.84 μm. Technical Physics Letters, 1998. 24(1): p. 22-23.*

36. *Fafard, S., et al. Toward quantum dot laser diodes emitting at 1.5 μm in 1998 International Conference on Applications of Photonic Technology. 1998: International Society for Optics and Photonics.*

37. *Wang, R.H., et al., Room-temperature operation of InAs quantum-dash lasers on InP [001]. Photonics Technology Letters, IEEE, 2001. 13(8): p. 767-769.*

38. *Allen, C.N., et al., InAs self-assembled quantum-dot lasers grown on (100) InP. Applied Physics Letters, 2002. 80(19): p. 3629-3631.*

39. *Renaudier, J., et al., 45 GHz self-pulsation with narrow linewidth in quantum dot Fabry-Perot semiconductor lasers at 1.5 μm. Electronics Letters, 2005. 41(18): p. 1007-1008.*

40. Jiaren, L., et al. Passively mode-locked quantum dot diode lasers. in Lasers & Electro Optics & The Pacific Rim Conference on Lasers and Electro-Optics, 2009. CLEO/PACIFIC RIM '09. Conference on. 2009.

41. Merghem, K., et al., Pulse generation at 346 GHz using a passively mode locked quantum-dash-based laser at 1.55 μm. Applied Physics Letters, 2009. 94(2): p. 021107-021107-3.

42. Lu, Z.G., et al., 312-fs pulse generation from a passive C-band InAs/InP quantum dot mode-locked laser. Opt. Express, 2008. 16(14): p. 10835-10840.

43. Tahvili, M.S., et al., Dual-wavelength passive and hybrid mode-locking of 3, 4.5 and 10 GHz InAs/InP(100) quantum dot lasers. Opt. Express, 2012. 20(7): p. 8117-8135.

44. Liu, J., et al., Dual-wavelength 92.5 GHz self-mode-locked InP-based quantum dot laser. Optics letters, 2008. 33(15): p. 1702-1704.

45. Lu, Z.G., et al., Highly efficient non-degenerate four-wave mixing process in InAs/InGaAsP quantum dots. Electronics Letters, 2006. 42(19): p. 1112-1114.

46. Lu, Z.G., et al. A passive mode-locked InAs/InP quantum dot laser with pulse duration of less than 300 fs. in SPIE OPTO: Integrated Optoelectronic Devices. 2009: International Society for Optics and Photonics.

47. Liu, J., et al., THz optical pulses from a coupled-cavity quantum-dot laser. Optics Communications, 2012. 285(6): p. 1323-1325.

48. Lin, C.Y., et al., Cavity design and characteristics of monolithic long-wavelength InAs/InP quantum dash passively mode-locked lasers. Opt. Express, 2009. 17(22): p. 19739-19748.

49. Heck, M.J.R., et al., Observation of Q-switching and mode-locking in two-section InAs/InP (100) quantum dot lasers around 1.55 μm. Optics Express, 2007. 15(25): p. 16292-16301.

50. Heck, M.J.R., et al., 5-GHz passively mode-locked quantum dot ring laser diode at 1.5 μm 2008.

51. Rosales, R., et al. High repetition rate two-section InAs/InP quantum-dash passively mode locked lasers. in Compound Semiconductor Week (CSW/IPRM), 2011 and 23rd International Conference on Indium Phosphide and Related Materials. 2011.

52. Mesaritakis, C., et al., Pulse width narrowing due to dual ground state emission in quantum dot passively mode locked lasers. Applied Physics Letters, 2010. 96(21): p. 211110-3.

53. Li, S.G., et al., Two-color quantum dot laser with tunable wavelength gap. Applied Physics Letters, 2009. 95(25): p. 251111-3.

54. Charis, M., et al., Dual ground-state pulse generation from a passively mode-locked InAs/InGaAs quantum dot laser. Applied Physics Letters, 2011. 99(14): p. 141109.

55. Thompson, M.G., et al., InGaAs quantum-dot mode-locked laser diodes. Selected Topics in Quantum Electronics, IEEE Journal of, 2009. 15(3): p. 661-672.

Chapter 2

Background Theory and Device Design

2.1 Introduction

This chapter provides a brief description of the semiconductor diode lasers and some fundamental properties of quantum dot material. The basic concept of mode-locking, types of mode-locking and the necessary conditions to obtain mode-locking are also discussed. Finally, the various device structures used to achieve high repetition rates in this research along with their basic working mechanism are discussed. The details of fabrication steps, device characterisation and discussions of the devices performance are given in the subsequent chapters.

2.2 Semiconductor lasers: Historical background

The basic operating principles of semiconductors lasers are briefly described in this section. A more comprehensive discussion on the subject can be found in the references [1-3]. Semiconductor lasers have brought a tremendous change in the field of telecommunication, medicine, sensing, manufacturing, entertainment industry, military equipment and consumer electronics due to their small size, low cost, high efficiency and easy integration in complex systems.

Semiconductor lasers are also attractive due to emission of light in a wide spectral range, i.e. from ultraviolet to far infrared depending on the material system used. This wavelength range covered by semiconductor materials includes 0.85, 1.31 and 1.55 μm , which are important for optical fibre communications [1, 2]. The most commonly used material system include GaAs/AlGaAs, emitting between 0.7-0.9 μm and InGaAsP/InP emitting in the range of 1.0-1.6 μm [1] .

To achieve optical gain in any laser system, population inversion is required. In semiconductor lasers, the population inversion can be achieved by injecting electrons and holes into the active region of the device. Since their first demonstration in 1962, semiconductor lasers have been extensively studied and improved [4]. A major breakthrough was the demonstration of a direct bandgap GaAs *p*-*n* junction [5], which, however suffered from poor carrier and optical confinement, required very high injection current and could only operate under pulsed operation at low temperatures. Most of these limitations were addressed and removed by the developments of the double heterostructure (DH) laser in 1969 [6]. In DH lasers, a thin undoped or lightly doped, lower bandgap and high refractive index active layer (e.g GaAs) is sandwiched between *p* and *n*-type cladding layers, with wider bandgap and lower refractive index (e.g AlGaAs) [7]. A schematic of the DH material structure and the refractive index discontinuity between the active layer and surrounding layers are shown in Figure 2.1 (a) and (b), respectively [7]. The DH layer structure improves both carriers and optical confinement as compared to the homojunction lasers. Shortly after its first demonstration, the DH geometry provided laser devices continuous wave operation at room temperature [8]. The rapid improvements in wafer growing technology enabled to control the epitaxial layer thicknesses in sub-nanometres ranges and led to the development of nanostructures such as quantum wells (QW) and quantum dots (QD) that further reduced the threshold currents and improved the device performance. The QD semiconductor laser structure will be discussed later in this chapter.

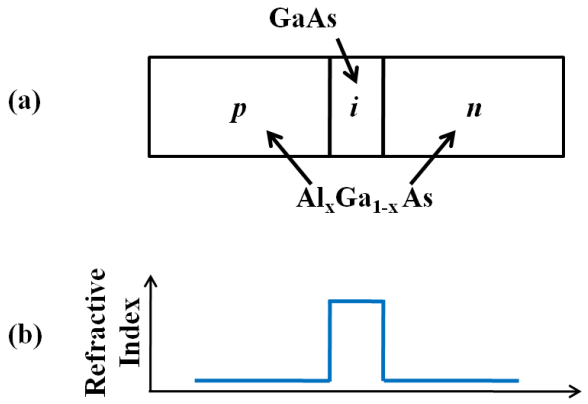

Figure 2.1: Double heterostructure laser diode: schematic of (a) material the structure and (b) refractive index profile [7].

2.3 Optical waveguide

The optical confinement in the vertical direction is provided by the refractive index difference between the core and the surrounding cladding layers, as discussed before. Because of their ease of fabrication, etched ridge waveguide geometries are the preferred solutions for defining the lateral optical confinement. In ridge waveguides the confinement is provided by the effective refractive index step that is formed between the etched and non-etched areas of the semiconductor material. A careful choice of the ridge width and height is of great importance in order to obtain stable single mode operation of the laser and low current threshold.

Depending on the device design and requirements, either shallow or deep etched waveguides designs can be employed [1], as schematically shown in Figure 2.2 (a) and (b), respectively. In shallow etched waveguides, the waveguide does not penetrate through the active core layer, which leads to a small refractive index step and therefore to a relatively weak optical confinement. The main advantage is that non-radiative recombination due to the carriers interaction with the etched surfaces is negligible. A further benefit arises from the reduced interaction between the optical mode and the ridge side-walls leading to lower scattering losses.

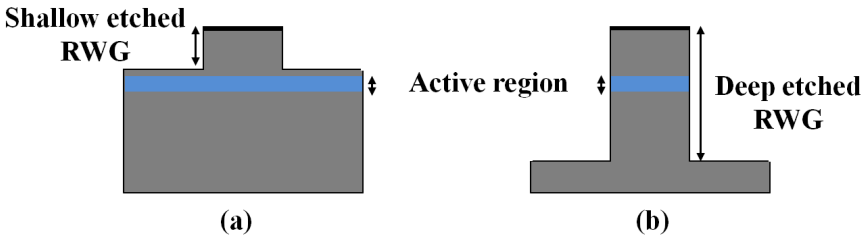

Figure 2.2 : Schematic representation of (a) shallow etched and (b) deep etched ridge waveguide design.

In deep etched waveguide geometry, the horizontal confinement of the optical mode is much stronger because of the very high lateral refractive index step. The main disadvantage is an increased non-radiative recombination on the etched sidewalls and higher optical scattering losses. Also, the oxidation of the exposed active core layer may lead to a reduction in the device lifetime. Therefore, shallow etching is usually preferred in the fabrication of simple Fabry-Perot (FP) cavity lasers as these devices do not require a high lateral confinement.

In this research work, both shallow and deep etched ridge waveguides were fabricated. The results discussed in chapters 4, 5 and 6 were obtained from shallow etched ridge waveguide devices. A detailed discussion on the fabrication of the shallow etched ridge waveguide devices is given in chapter 3, while the deep etched design is discussed in chapter 6.

2.4 Energy diagram in direct bandgap semiconductor materials

The understanding of the basic semiconductor material properties helps in interpreting the behaviour of the mode-locked laser diodes and designing the optimum devices. The direct bandgap III-V compound semiconductor materials were extensively studied for the development of efficient semiconductor lasers. The GaAs and InP direct band gap materials are usually preferred as a substrate thanks to their better lattice matching to both ternary (e.g $Ga_{1-x}Al_xAs$) and quaternary (e.g $Ga_xIn_xAs_{1-y}P_y$) compounds [9].

For a direct bandgap bulk semiconductor material, a typical energy versus wave vector *(E-k)* diagram is illustrated in Figure 2.3, which consists of a conduction band and three valence bands referred to as; heavy hole, light hole and the split-off band [2]. If the bottom of the conduction band and top of the valence band occur at the same value of the wave vector k , then the energy of the electron E_e and hole E_h are represented by the following parabolic functions [10].

$$E_e = E_c + \frac{\hbar^2 k^2}{2m_e^*} \qquad E_h = E_v - \frac{\hbar^2 k^2}{2m_h^*}$$

Equation 2.1

Where $E_{c,v}$ are the conduction and valence band energies, $m_{e,h}^*$ are the effective masses of electrons and holes respectively, and k is the wave vector .

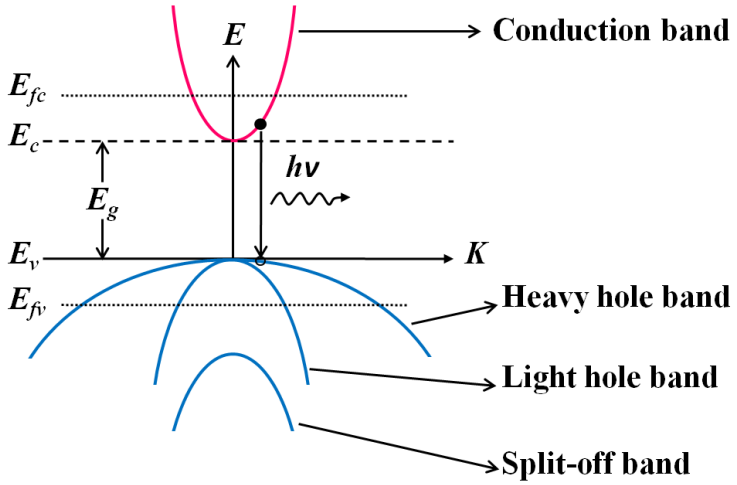

Figure 2.3 : Schematic of a band model of a III-V semiconductor material with a direct bandgap [2].

2.5 Quantum confinement effects

If the thickness of the active layer of the double heterostructure laser is reduced to dimensions comparable to the De-Broglie wavelength *(λ=h/p),* quantum mechanical effects arises in the energy levels [2, 11, 12]. The quantization effect leads to a modified energy band structure and distribution of the density of states in a narrower region, which results in a spectral confinement

of the carriers in the quantized energy states at the bottom of the conduction and top of the valence bands [11, 13].

In 1982, Arakawa and Sakaki theoretically proposed the use of heterostructures with carrier confinement in one (quantum well), two (quantum wire) and three (quantum dot) directions for improving the temperature performance of the lasers [14]. The density of states $\rho(E)$ for the bulk, quantum well, quantum wire and quantum dot semiconductor materials are shown in Figure 2.4.

If the carriers are confined in one, two and three dimensions in quantum wells, wires and dots, respectively, then the energy of the confined carriers with respect to the band edge in infinitely deep rectangular shape potential wells is described as [10]:

1D confinement, $$\boldsymbol{E_l = \frac{\hbar^2 \pi^2 l^2}{2m^* L_x^2} + \frac{\hbar^2 \left(k_y^2 + k_z^2\right)}{2m^*}}$$

Equation 2.2

2D confinement, $$\boldsymbol{E_{l,m} = \frac{\hbar^2 \pi^2}{2m^*}\left(\frac{l^2}{L_x^2} + \frac{m^2}{L_y^2}\right) + \frac{\hbar^2 k_z^2}{2m^*}}$$

Equation 2.3

3D confinement, $$\boldsymbol{E_{l,m,n} = \frac{\hbar^2 \pi^2}{2m^*}\left(\frac{l^2}{L_x^2} + \frac{m^2}{L_y^2} + \frac{n^2}{L_z^2}\right)}$$

Equation 2.4

Three dimensional confinement in QD materials leads to the formation of discrete states as a function of energy, so the density of states is represented by a delta function at the allowed energies [11, 12, 14], which generates high optical and differential gain (rate of increase of gain with carrier density) [11, 15]. The QD mimics the properties of an atom, hence it is sometimes termed as artificial atom [16].

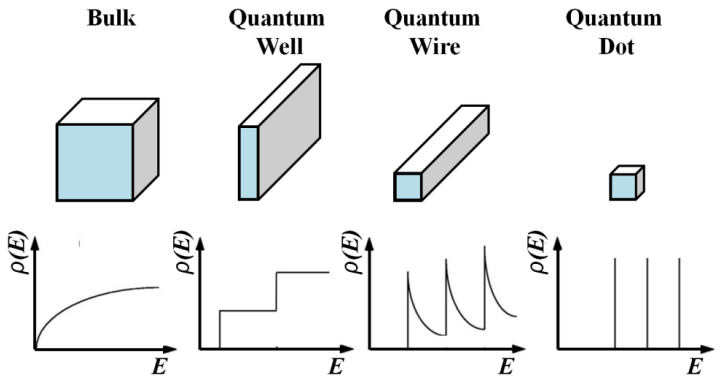

Figure 2.4: Active region structure and density of states versus energy level for Bulk, Quantum well, Quantum wire and Quantum dot [10].

2.6 Size of Quantum dot

The splitting of the conduction and valence band into discrete energy levels due to the three dimensional confinement is strongly dependent on the size of the quantum dots. There is a minimum and maximum limit for the quantum dot size below which there is no bound state and above which the energy levels can no longer be treated as discrete.

Minimum size: Any change in the QD size can substantially modifies the bandgap between the energy levels. The decrease in the QD size will always refers to a wider bandgap, resulting in a blue shifted radiation emission (i.e shorter wavelength) [17]. The decrease in QD size raises the position of lowest energy level in the conduction band and induces a large conduction band offset *(ΔE_c)* as shown in the Figure 2.5. An increase in bandgap energy signifies the presence of fewer electron levels in QDs, this sets a minimum limit on the QD size.

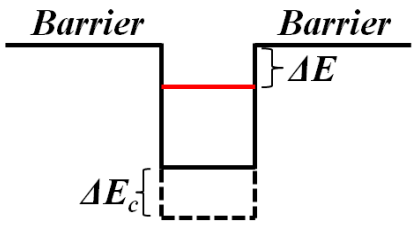

Figure 2.5: Schematic representation of the QD energy level and conduction band offset.

The existence of at least one electron level is imperative for working of a QD laser, therefore, this argument sets the lower limit on the QD size [18, 19]. The critical size *(D_{min})* required for one electronic level to exists is strongly dependent on the conduction band offset *(ΔE_c)* of the semiconductor heterojunction in use. One electronic level exists in spherical QD if the conduction band offset *(ΔE_c)* in a corresponding heterojunction exceeds the value [18, 19]:

$$\boldsymbol{\Delta E_c = \frac{\hbar^2}{2m_e^*}\left(\frac{\pi}{D_{min}}\right)^2}$$

Equation 2.5

where $\hbar$ is Plank's constant divided by 2 π, m_e^* is the electron effective mass and D_{min} is the critical size of the QD. Using above relation (Equation 2.5), the lowest limit of QD size can be estimated. For direct bandgap GaAs/$Al_{0.4}Ga_{0.6}As$ heterostructure system, assuming conduction band offset of ~0.3eV, the QD size should not be smaller than 4 nm [18].

If the size of a QD is closer to the critical limit, the energy difference *(ΔE)* between occupied energy level and barrier material becomes very small as shown in Figure 2.5. Small lattice thermal vibrations lead to a complete discharge of carriers from the QD due to small energy difference. Therefore, such small sized QDs are not ideal for laser devices [19]. Therefore, the size of the QD should be much larger than the critical size *(D_{min})* for real device realisation.

Maximum size: The limit for maximum size of the QD is defined using the concept of thermal energy *kT*. If the separation between energy levels of the QD is comparable to the thermal energy *kT*, then the thermal impact (due to small lattice thermal vibrations) between the energy levels is inevitable [18]. In order to prevent the depletion of the QD as a result of small lattice thermal vibrations of the carriers, the energy levels gap $\left(E_2^{QD} - E_1^{QD}\right)$ inside the QD must be greater than thermal energy *kT* [18, 19]. This argument sets the maximum limit for the size of a QD. The condition that limits the population of the higher energy levels due to thermal excitation in QD can be written as [18, 19]:

$$kT \leq \frac{1}{3}\left(E_2^{QD} - E_1^{QD}\right)$$

Equation 2.6

In Equation 2.6, E_1^{QD}, and E_2^{QD}, are energies of the first and second levels in the QD, respectively, as shown in Figure 2.6. This reveals that separation between energy levels of the QD should be three times of the thermal energy (*kT)* to avoid thermal excitation. The maximum size of the QD is given as a function of temperature, from the given relation (Equation 2.6) an upper limit of QD size can be estimated as 12 nm for GaAs/AlGaAs heterostructure system [18].

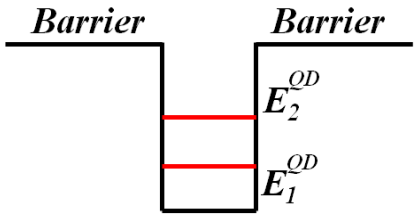

Figure 2.6: Schematic representation of the first (E_1^{QD}) and second (E_2^{QD}) energy levels in a QD.

2.7 Quantum dot semiconductor lasers

A schematic view of a typical QD material consisting of 5 sheets of QDs stacked upon each other is shown in Figure 2.7. The active region is embedded

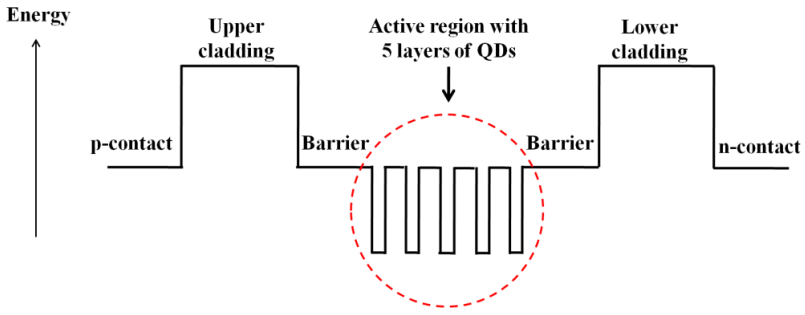

Figure 2.7: Schematic of the conduction band of a semiconductor QD material with 5 layers of QDs in the active region (Figure not to scale).

within a double heterostructure consisting of cladding layers with higher bandgap and lower refractive index that improve the confinement of the injected charge carriers and emitted photons [20].

2.7.1 Optical confinement factor of QD structures

The optical confinement factor *(Γ)* represents the fraction of the optical mode that overlaps with the active region [3]. In QD active regions, the optical confinement factor is approximately given by the ratio between the total dot volume to the total waveguide volume. The optical confinement factor in QD arrays can be separated into the in-plane Γ_{xy} and vertical confinement factors Γ_z, respectively [19]:

$$\boldsymbol{\Gamma = \Gamma_{xy}\Gamma_z}$$

Equation 2.7

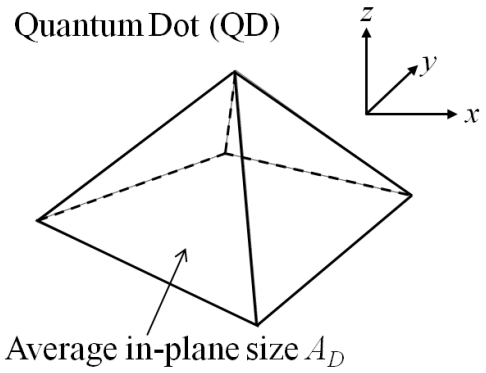

Figure 2.8 : Schematic geometry of a single QD (pyramid).

In the case of a QD with pyramidal shape (Figure 2.8), the in-plane confinement factor *(Γ_{xy})* for a QD layer is given by [19]:

$$\boldsymbol{\Gamma_{xy} = \frac{N_D A_D}{A} = \zeta}$$

Equation 2.8

where *A* is the total area of the *xy* plane and the product $N_D A_D$ represents the area covered by the N_D number of QDs, each having an average in- plane size A_D. The factor ξ in the equation stands for the area covered by QDs [19].

The vertical component of the confinement factor is the ratio of the light intensity within the region where population inversion occurs to the total light intensity in the whole heterostructure [19]:

$$\boldsymbol{\Gamma_z = \frac{1}{A}\left[\frac{\int_{QD} |E(z)^2| dz}{\int_{whole} |E(z)^2| dz}\right]}$$

Equation 2.9

The numerator term in Equation 2.9, gives the light intensity in the active layer, averaged over an area *A*, whereas the denominator term gives the light intensity in the whole laser structure.

Equation 2.8 and Equation 2.9 show that the in-plane and vertical optical confinement factors can be increased either by increasing the ξ (area covered) i.e the number of QDs or the number of QDs layers in the active region [19].

2.7.2 Threshold current density of QD structures

The minimum value of the current density at which optical gain overcomes the cavity losses is called threshold current density *(J_{th})*. The value of the current density at which the semiconductor material becomes transparent is called transparency current density *(J_{tr})* and the corresponding current is called transparency current *(I_{tr})*. The transparency current density is always lower than the threshold current density because of the losses of the cavity (mirrors). For QD materials, transparency current and transparency current density can be expressed by the following equations [19, 21]:

$$\boldsymbol{I_{tr} = \frac{1}{2}\left[\frac{eN_D}{\tau_D}\right]} \qquad \boldsymbol{J_{tr} = \frac{I_{tr}}{A} = \frac{1}{2}\left[\frac{e\zeta}{A_D\tau_D}\right]\left[\frac{N_{tr}}{N_D}\right]^2}$$

Equation 2.10

where τ_D is the recombination time constant in QD and the other constants are the same as those described in Section 2.7.1. The minimum value of the threshold carrier density N_{th} required to overcome the total losses α_{tot} is given by [19, 21] :

$$N_{th} = N_D \left[1 + \frac{\zeta_{min}}{\zeta}\right]$$

Equation 2.11

In the above equation ξ_{min} represents the minimum area dot coverage. The threshold current density J_{th} can then be approximated by the following relation [19, 21] :

$$J_{th} \approx \frac{1}{2}\left[\frac{e\zeta}{A_D \tau_D}\right]\left[1 + \frac{\zeta_{min}}{\zeta}\right]^2$$

Equation 2.12

2.8 Mode-locking in lasers

Mode-locking is a well established technique used to generate coherent, high repetition rate and ultra short pulses by virtue of phase locking of the longitudinal modes inside a laser cavity [22]. The mode-locked lasers (MLLs) are extremely desirable in applications such as high speed optical interconnects, optical time division multiplexed transmissions, generation and recovery of clock signals, ultrafast signal processing [23, 24]. Additional applications include optoelectronic measurement applications such as analogue to digital conversion, electro-optic sampling and impulse response testing of optical components, THz generations [16, 23-26].

2.8.1 Mode-locking principle

A schematic of the gain spectrum profile, the longitudinal modes and the lasing output of the laser are shown in Figure 2.9. The longitudinal modes λ_m of the resonator are equally spaced in the frequency domain (Equation 2.13 and Equation 2.14).

$$\lambda_m = \frac{2n_g L}{m}$$

Equation 2.13

$$\Delta \boldsymbol{f} = \frac{\boldsymbol{c}}{\boldsymbol{2 n_g L}}$$

Equation 2.14

The aggregate electric field (composed of the frequency components corresponding to the oscillating modes) of the laser output as a function of time can be written as [9, 22]:

$$\boldsymbol{E(t)} = \sum_{\boldsymbol{n=0}}^{\boldsymbol{N-1}} \boldsymbol{(A_o)_n}\ \boldsymbol{e^{[i(\omega_n t+\delta_n)]}}$$

Equation 2.15

where $(A_o)_n$, ω_n and δ_n represent the amplitude, angular frequency and phase of the n_{th} mode, respectively. If the laser modes are forced to maintain a fixed relative phase (δ) to each other, such that the phase of the n_{th} mode becomes $\delta_n = \delta$, then the laser modes are said to be phase or mode-locked and lead to the emission of pulses, which are periodic in time, as shown in Figure 2.10 [9]. In MLLs the sum of the individual electric fields constitutes the total irradiance, hence Equation 2.15 can be written as:

$$\boldsymbol{E(t)} = \boldsymbol{A_o e^{i\delta}} \sum_{\boldsymbol{n=0}}^{\boldsymbol{N-1}} \boldsymbol{e^{(i\omega_n t)}}$$

Equation 2.16

The angular frequency ω_n can be replaced by $(\omega - n\delta\omega)$, where ω and $\delta\omega$ are the angular frequency of the highest frequency mode and the angular frequency separation between the modes, respectively. Hence Equation 2.16 can be written as:

$$\boldsymbol{E(t)} = \boldsymbol{A_o}\ \boldsymbol{e^{i\delta}}\ \sum_{\boldsymbol{n=0}}^{\boldsymbol{N-1}} \boldsymbol{e^{[i(\omega - n\delta\omega)t]}}\ = \boldsymbol{A_o}\ \boldsymbol{e^{[i(\omega t+\delta)]}}\ \sum_{\boldsymbol{n=1}}^{\boldsymbol{N-1}} \boldsymbol{e^{-in\delta\omega t}}$$

Equation 2.17

The electric field of the phase locked modes can also be written in the following form:

$$E(t) = A_o\, e^{[i(\omega t+\delta)]} \frac{sin(\frac{N\delta\omega t}{2})}{sin(\frac{\delta\omega t}{2})}$$

Equation 2.18

The total irradiance *I(t)* is given by:

$$I(t) = E(t).E^{*}(t) = A_o^2 \frac{sin^2(\frac{N\delta\omega t}{2})}{sin^2(\frac{\delta\omega t}{2})}$$

Equation 2.19

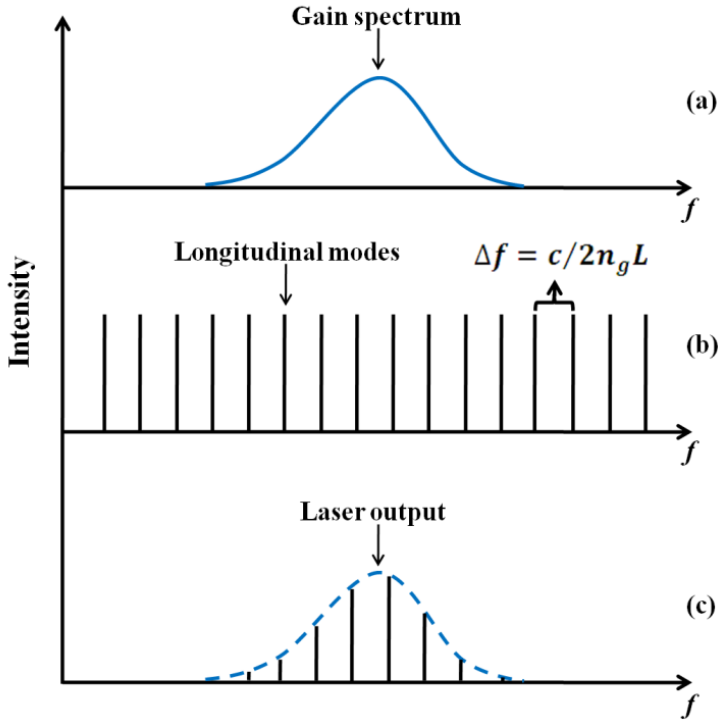

Figure 2.9: (a) Schematic of the gain spectrum profile of the laser ; (b) Longitudinal modes inside the cavity; (c) Laser output spectrum [9].

The total irradiance *I(t)* takes the form of equally spaced pulses with a periodicity equal to the cavity round trip time $T= 2n_gL/c$. For $N=3$ modes, the

locked pulses are illustrated in Figure 2.10. The width *(Δτ)* of the emitted pulses is inversely related to spectral bandwidth of the phase locked modes [22]. The repetition rate of the periodic pulses is inversely related to the cavity length *L* as given below [23, 24]:

$$f = M\frac{c}{2n_g L}$$

Equation 2.20

where *c* is the speed of light, n_g is the group refractive index and *M* is the number of pulses coexisting in the laser cavity. For common configurations of the laser cavity that operate on the fundamental frequency only one pulse exists in the cavity at any one time and *M=1* [23, 24]. Alternative configurations can be used to generate mode-locking at higher order harmonics of the fundamental frequency i.e *M >1*. These regimes of mode-locking in which several pulses coexist in the laser cavity are called harmonic mode-locking and are commonly achieved by colliding pulse, asymmetric colliding pulse or coupled cavity laser configurations, as will be discussed in chapters 5 and 6 [24].

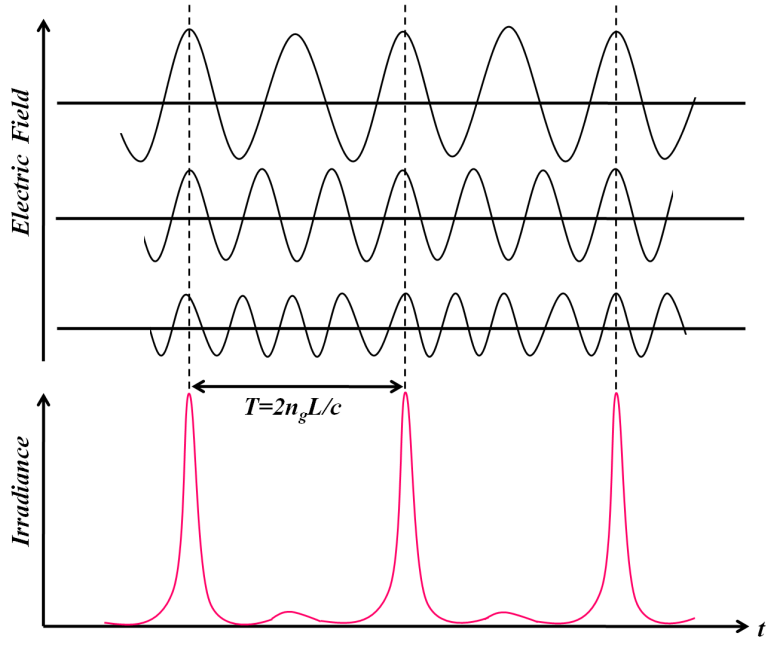

Figure 2.10: Illustration of mode-locked laser output in the time domain [9, 22].

2.8.2 Mode-locking techniques

Three techniques namely active, passive and hybrid mode-locking are commonly employed to achieve phase locking of the semiconductor laser modes.

Active mode-locking is achieved by modulating the gain or losses of the semiconductor laser by an external electrical signal at a frequency corresponding to the cavity round trip (Δf) [9]. High repetition rates cannot be easily achieved using the active mode-locking technique due to lack of high frequency electrical signal generators [22].

Passive mode-locking is achieved by incorporating a saturable absorber (SA) in the laser cavity and does not require any external modulated source [16, 24, 26]. Generally, the mode locking in semiconductor lasers is achieved by reverse biasing a short section of the laser so that its effective bandgap decreases due to the quantum confined stark effect (QCSE). Over an appropriate range of reverse voltage biasing and section lengths, the SA acts as an intensity dependent loss element, where loss is reduced for high optical intensities resulting in a self initiating mode-locking process. The saturation mechanism in the SA occurs due to band filling effect, where the majority of states near the conduction band are occupied and are unable to accommodate any further electrons from the valence band [27]. The pulses in the passive mode-locked laser are continuously reshaped due to interplay between the SA absorption and gain saturation. The saturation mechanism induced in the SA section generates shorter optical pulses as compared to that obtained from the active mode-locking.

Hybrid mode-locking is a combination of both active and passive mode-locking, where an electrical signal applied to the gain or SA section stabilize the pulse train and reduce the phase noise [16, 27]. This technique exploits the advantages of both, active and passive mode-locking. It therefore enables to reduce the timing jitter due to synchronization with the stable external source and generate very short pulses thanks to saturable absorption mechanism.

2.8.3 Conditions for passive mode-locking

This research mainly focuses on the passive mode-locking; therefore the following section briefly reviews its background theory and operating principles. The laser emission starts with modes oscillating in the laser cavity in noisy intensity bursts due to their relative random phases [16, 27]. The noisy bursts with high intensity peaks experience lower loss in the SA due to absorption of the saturation, whereas the low intensity wings experience higher attenuation. These noisy bursts are continuously reshaped after each round trip in the cavity and become shorter and more intense due to lower losses in the SA and amplification in the gain section. The steady state is reached when the laser emits a train of mode-locked pulses with a round trip frequency corresponding to the cavity round trip time. As a whole the short pulse generation results from the interplay between saturable absorption, gain saturation, and carrier life times in both the SA and gain sections [27]. The SA and gain exhibit ultrafast carrier dynamics in passively mode-locked semiconductor QD lasers compared to their QW counterpart.

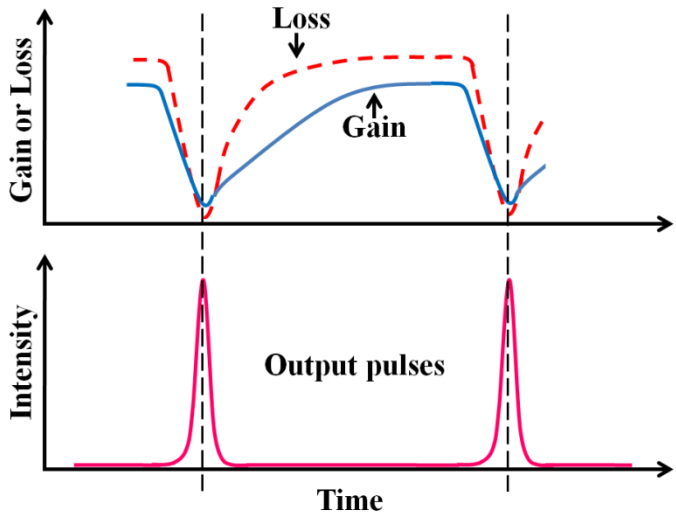

Figure 2.11: Gain and loss dynamics during passive mode-locking operation in a semiconductor QD laser [16].

Figure 2.11 shows the pulse shortening mechanism caused by the time dependent gain and loss profiles in a passively mode-locked QD laser system. In the steady state condition, before the arrival of the pulse, the unsaturated losses

are higher than the gain [16, 22]. The leading edge of the optical pulse experiences loss during the passage through the SA. The increase in the intensity of the pulse saturates the loss before the gain, resulting in a net gain window where amplification of the central part of the optical pulse occurs. Because of the fast recovery of the SA from saturated state to the initial high loss state, the trailing edge of the pulse also suffers a net loss.

In general it can be shown that the following conditions must be satisfied in order to achieve mode-locking in semiconductor lasers:

- Faster saturation of the loss is required compared to the saturation of the gain, i.e the saturation energy E_a^{sat} of the SA must be less than the saturation energy E_g^{sat} of the gain. The SA and gain saturation energies are given by [23, 26]:

$$E_a^{sat} = \frac{h\nu A}{d\alpha/dn} \qquad E_g^{sat} = \frac{h\nu A}{dg/dn}$$

where h is the Plank's constant, ν is optical frequency, A is the optical mode cross-sectional area, $d\alpha/dn$ and dg/dn are the differential loss and gain, respectively.

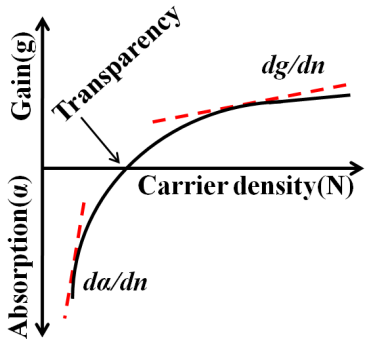

Figure 2.12: Schematic representation of the gain and absorption versus carrier density [2, 22].

The dependence of the differential loss and gain on carrier density in a semiconductor laser is illustrated in Figure 2.12. From the tangent lines drawn on the absorption and gain curves it can be

inferred that $d\alpha/dn > dg/dn$ resulting in $E_a^{sat} < E_g^{sat}$, which is an essential requirement for passive mode-locking [26].

- When the gain saturates below the unsaturated loss, no spontaneous emission occurs. This effect occurs at each round trip pass of the pulse through the SA, therefore the SA is required to recover faster than the gain section [26], i.e. $\tau_a < \tau_g$, where τ_a and τ_g are the carrier recovery times of the absorber and gain sections, respectively.

These two conditions translate into SA losses that are greater than the gain all the time, except near the peak of the optical pulse [22].

2.9 Mode-locking in QD active media

The first quantum dot mode-locked lasers emitting around 1.3 μm was demonstrated by Huang et al, in 2001 [28]. Thereon, improvements in the growth techniques have enabled the development of quantum dot gain media in several different material systems and pushed the operating wavelength into the C-band telecommunication window (1.55 μm) [29-31]. Quantum dot materials due to their three dimensional confinement nature possess several advantages, which might lead to improvements in the mode-locking performance as compared to the conventional bulk and QW materials. The broader gain bandwidth, ultra fast carrier dynamics, lower absorption saturation, higher gain saturation energy, lower threshold current, lower temperature sensitivity and lower internal losses are the main advantages that make QDs an attractive choice for development of mode-locked lasers [32].

Gain spectra : In self assembled QDs, the inhomogeneous broadened gain spectrum is originated from the variations of dot sizes and leads to broader lasing spectra [23]. Due to the wider optical spectrum, sub picoseconds pulses corresponding to an optical spectrum bandwidth of 14 nm have been achieved in InAs/GaAs based QD material [33]. Similarly, 295 fs pulses have been reported on InAs/InP QD material with an optical spectrum width of 17.9 nm [31]. If the

dispersion is reduced and the entire gain bandwidth is locked, then the broader gain bandwidth of the QDs has the potential to generate sub-100 fs optical pulses [16].

Recovery time : In semiconductor QD structures, ultrafast recovery time has been observed under both absorption and gain operations [16]. The result contradicts preliminary studies that predicted slower carrier dynamics arising from the phonon bottle-neck [16, 34]. In two section QD mode-locked lasers the SA exhibits ultrafast carrier recovery and it has been shown that the absorber recovery time can be decreased by two orders of magnitudes (62 ps to 700 fs) when the applied reverse voltage is increased from 0 to -10 V [16, 35]. In QD mode-locked lasers the exponential decrease in pulse width with increasing the reverse bias voltage is attributed to the strong dependence of the absorber recovery time on the applied reverse bias [16, 36]. In passive mode-locked lasers the absorber recovery time sets an upper limit on the maximum repetition rate. Thanks to faster recovery time of the QD gain material, ML repetition rates beyond 1THz can be obtained [16]. The QD gain medium also exhibits weaker quantum confined stark effect (QCSE) compared to the QW material [37]. Hence, the reverse biased applied to the QD absorbers reduces the recovery time without increasing the absorber loss, which turns out to be ideal for mode-locking operation.

Saturation energy: The relatively higher differential gain in the QD material as compared to the QW material translates into a lower E^{sat}, which can enhance the pulse shortening mechanism [23, 37]. In QD mode-locked lasers, the carrier density in the gain section is higher than in the SA section due to QD delta function-like density of states that results in a lower differential gain for high carrier density. Hence, the high differential gain in the QD SA section saturates the absorber at lower saturation energy as compared to the gain section. The saturation energy of the QD absorber is 2-5 times smaller than in QW absorber [23].

Reduced carrier diffusion: The diffusion of carriers is strongly reduced in QDs compared to QWs [16, 38]. In fact, the three dimensional

confinement nature of QDs provides strong carrier localisation leading to reduced side wall recombination effects [38]. This enables the fabrication of deep etched wave- guide structures without degrading the lasing performance due to presence of dangling bonds in the waveguide sidewalls [39], as well as enabling the integration of photonic crystal, chirped mirrors for dispersion compensation and DFBs [16]. The deeply etched ridge waveguide structures provide strong index guiding of the optical mode and suppression of the current spreading [40, 41]. The strong index step also results in a symmetric far field which improves the coupling efficiency to an optical fibre [40]. The QD lasers also show higher threshold to catastrophic optical damage (COD), due to the reduced carriers diffusion [42], which enables laser operation under higher injection current without degrading the facet mirrors [16]. The reduced carrier diffusion in QD lasers on the cleaved facets also reduces the occurrence of beam filamentation as demonstrated in [36], where high power operation of tapered QD mode-locked laser was demonstrated without degrading the beam.

Low threshold current: The main advantage in using the QDs as an active material in lasers is the significant decrease in the threshold current. This is due to the reduced dimensionality of the active region, which reduces the number of carriers needed to reach the transparency [10-12, 15]. The electrons are spread over a small energy range with high density at the gain peak, hence the population inversion is expected to be achieved with lower injection current. In QD lasers, mode-locking typically initiates at current values very close to the threshold [28, 43], which is advantageous since the carriers that contribute to non-stimulated emission are reduced [44], resulting in a lower amplified spontaneous emission (ASE) inside the cavity [45]. The ASE is the main source of variations in the gain, index of refraction and photon density, and therefore leads to the fluctuations in the cavity round trip time and contributes to jitter [26]. The QD material is even more attractive when longer laser cavities (which produce more ASE) are required for low repetition rate of mode-locking.

Less temperature dependence: The reduction of the temperature dependence of the threshold current is an added benefit of quantum dot lasers [14, 15]. This is attributed to the reduced size of quantum dots, which creates a large separation between ground and excited states hence thermal excitation of the carriers becomes less likely to occur [46]. Temperature insensitive and stable mode-locked operation up to 80°C in QD mode-locked laser has been reported in [47]. The lower temperature sensitivity of QD mode-locked lasers is of great interest for the development of uncooled devices.

2.10 Passive mode-locked laser configurations for high repetition frequencies

Monolithic semiconductor mode-locked lasers due to their short cavity length are ideal for generating repetition rates of several ten of gigahertz, as expressed by Equation 2.20. A schematic of a typical mode-locked laser configuration is illustrated in Figure 2.13 (a). Sub-picosecond pulse widths at 240 GHz have been achieved using this geometry on a bulk GaAs active layer diode laser where a short cavity length of 160 μm was fabricated, incorporating a 10 μm long oxygen implanted SA [24, 48]. The same geometry has been used to generate, 0.65 ps pulses at 110 GHz using bulk InGaAsP/InP diode laser emitting at 1.535 μm [24, 49]. Repetition rates of 245 GHz and 346 GHz have been achieved on using 170 μm and 120 μm long single section InAs/InP quantum dash (QDash) cavities without incorporating a SA [50]. Although higher repetition rates could in theory be achieved by defining even shorter cavities (i.e. micro-rings or FP with deeply etched mirrors), the total gain within the cavity would not be sufficient for lasing operation. To overcome this limitation, harmonic mode-locking can be used in which the pulse repetition rate multiplication is performed with in a long laser cavity. Harmonic mode-locking is achieved when $M>1$ pulses circulate in the laser cavity simultaneously such that mode-locking at higher harmonics of the fundamental frequency occurs [24]. M corresponds to the number of pulses circulating in the cavity (harmonic number) as given by Equation 2.20. The most common techniques for harmonic mode-locking are

colliding pulse mode-locking (CPM), asymmetric CPM (ACPM), double interval mode-locking (DIM) and coupled cavity mode-locking (CCM).

In semiconductor laser diodes, colliding pulse mode-locking (CPM) is achieved by placing a SA precisely in the middle point of the cavity rather than at one of the facets of the cavity. The cavity geometry of a CPM device is illustrated in Figure 2.13 (b), where L_1 and L_2 represent the lengths of the two gain sections, respectively, and $L_1 = L_2$. In the steady state, two pulses circulating in the cavity collide simultaneously in the SA section, resulting in a repetition frequency twice to that of mode-locked lasers having the SA at the facet of the cavity. Nearly transform limited pulses have been achieved by CPM at a repetition rate of 350 GHz using InGaAsP QW material [51]. In QDs, the first CPM was demonstrated at a repetition rate of 20 GHz using InGaAs/GaAs semiconductor material emitting at around 1.1 μm [52]. Higher harmonics can also be obtained by the multiple colliding pulse mode-locking (MCPM) configuration illustrated in Figure 2.13 (c) [53]. In MCPM more than two pulses circulate in the cavity and higher repetition frequency can be achieved compared to the CPM device with a single SA.

A similar geometry is the asymmetric colliding pulse mode-locking (ACPM) where a single SA is used but shifted from the middle point of the cavity [54]. ACPM is illustrated in Figure 2.13 (d), where SA is placed at an integer fractional position of the cavity length L/n ,where L is total cavity length and n is an integer [55]. The position of the SA divides the cavity in two gain sections of length L_1 and L_2. Using this technique Shimizu *et al.* demonstrated ACPM at a maximum repetition frequency of 380 GHz, which corresponds to 7^{th} harmonic of the fundamental frequency [54]. However, for further higher order harmonics SA is required to be placed closer to the facet and will cover most of the cavity segment required to generate the higher order harmonic. To overcome this limitation, Shimizu *et al* also verified that a single SA can be positioned at mL/n, where L is length of the cavity and m and n are relatively prime such that ($m<n$) [54]. This geometry can also generate high frequency optical pulses at nf (where f is fundamental frequency) and can relax the limitation imposed by the SA position

overlap. They were able to demonstrate repetition frequency up to 580 GHz and 860 GHz corresponding to the eight and twelfth harmonic of the fundamental frequency, using 600 μm long cavity [54]. The first ACPM geometry in a QD laser was demonstrated by Rae A.R. *et al*, achieving a 117 GHz repetition rate at the third harmonic of the fundamental frequency using InGaAs/GaAs QD material emitting at 1.2 μm [56].

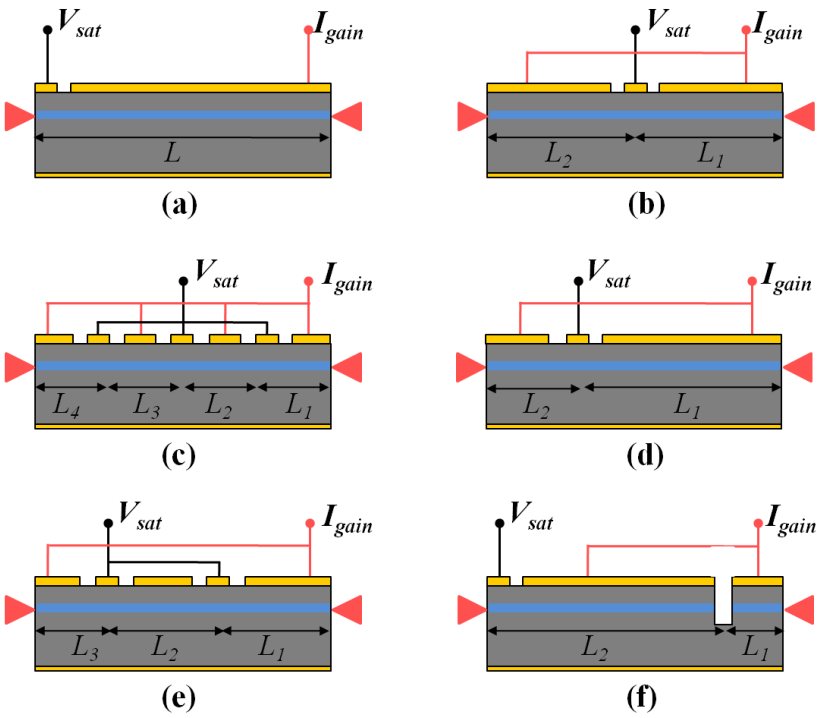

Figure 2.13: Schematics of different cavity configurations for semiconductor passive mode-locking: (a) two section (b) colliding pulse (c) multiple colliding pulse (d) asymmetric colliding pulse (e) double interval and (f) coupled cavity mode-locked lasers [24].

Higher order passive mode-locking can also be achieved by using the double interval mode-locking (DIM) technique, in which two separate SAs positioned at specific locations within the cavity trigger the higher order harmonic mode-locking, as illustrated in Figure 2.13 (e). In this configuration, two disconnected SAs divide the cavity length into three gain sections of length L_1, L_2 and L_3, respectively. Using the DIM technique, 10^{th} harmonic mode-locking was demonstrated with two SAs located at a position corresponding to 2^{nd} and 5^{th}

harmonic, respectively, in a 6.75 mm long cavity, fabricated on a InAs/InGaAs QD active medium [57].

The highest repetition frequency and harmonic number in a semiconductor laser has been demonstrated on a monolithic coupled cavity mode-locked (CCM) laser. This configuration has generated a repetition frequency as high as 2.1 THz, which is the highest mode-locking frequency obtained from any semiconductor laser [58, 59]. A monolithically integrated CCM laser comprises an air gap that divides the cavity into two sub cavities of length L_1 and L_2, as illustrated in Figure 2.13 (f). This air gap positioned at $1/M^{th}$ of the cavity acts as a reflector and mode-locking at the M^{th} (where $M>2$) harmonic of the fundamental frequency is achieved if the ratio between the lengths of two coupled sub cavities is given by $L_1:L_2=1:(M-1)$ [60]. This coupled cavity construction allows only common FP modes to propagate within the laser cavity.

2.11 Conclusions

This chapter presented the basic operating principles of the semiconductor laser along with some fundamental properties of QD active media. The quantum confinement effects exploited in QD lasers was introduced and the concept of mode-locking along with some conventional mode-locking techniques used in semiconductor lasers was discussed. Since the passive mode-locking technique was used in this research, the conditions for passive mode-locking were described in detail together with a discussion on the advantages of QD gain medium for mode-locking operation. Finally, the main semiconductor mode-locked laser configurations, which can be used for high repetition frequencies were introduced. The CPM, ACML, DIM and CCM geometries were all designed and fabricated in the current research and will be discussed in detail in the following chapters.

2.12 References

1. *Coldren, L.A. and S. Corzine, Diode Lasers and Photonic Integrated Circuits. 1995: John Wiley & Sons.*
2. *Agrawal, G.P. and N.K. Dutta, Long-wavelength semiconductor lasers. 1986: Van Nostrand Reinhold.*
3. *Weisbuch, C., The Development of Concepts in Light-Emitting Devices. Brazilian Journal of Physics, 1996. vol. 26(Issue 1): p. p.21-42.*
4. *Holonyak, N., Jr., The semiconductor laser: a thirty-five-year perspective. Proceedings of the IEEE, 1997. 85(11): p. 1678-1693.*
5. *Hall, R.N., et al., Coherent Light Emission From GaAs Junctions. Physical Review Letters, 1962. 9(9): p. 366-368.*
6. *Kroemer, H., A proposed class of hetero-junction injection lasers. Proceedings of the IEEE, 1963. 51(12): p. 1782-1783.*
7. *Sze, S.M., Semiconductor devices, physics and technology. 1985: Wiley.*
8. *Alferov, Z., The history and future of semiconductor heterostructures. Semiconductors, 1998. 32(1): p. 1-14.*
9. *Wilson, J. and J.F.B. Hawkes, Optoelectronics, an introduction. 1989: Prentice-Hall.*
10. *Zory, P.S., Quantum well lasers. 1993: Academic Press.*
11. *Kapon, E., Semiconductor Lasers: Fundamentals I. 1998: Academic Press.*
12. *Bimberg, D. and C. Ribbat, Quantum dots: lasers and amplifiers. Microelectronics Journal, 2003. 34(5-8): p. 323-328.*
13. *Ledentsov, N.N., et al., Quantum-dot heterostructure lasers. Selected Topics in Quantum Electronics, IEEE Journal of, 2000. 6(3): p. 439-451.*
14. *Arakawa, Y. and H. Sakaki, Multidimensional quantum well laser and temperature dependence of its threshold current. Applied Physics Letters, 1982. 40(11): p. 939-941.*

15. *Arakawa, Y. and A. Yariv, Quantum well lasers--Gain, spectra, dynamics. Quantum Electronics, IEEE Journal of, 1986. 22(9): p. 1887-1899.*

16. *Rafailov, E.U., M.A. Cataluna, and W. Sibbett, Mode-locked quantum-dot lasers. Nat Photon, 2007. 1(7): p. 395-401.*

17. *Krupanidhi, S.B., III–VCompoundSemiconductor QuantumDots for Nanoeletronics (Review). Journal of the Indian Institute of Science, 2007. 87:1: p. 1-14.*

18. *Ledentsov, N., et al., Quantum dot heterostructures: Fabrication, properties, lasers (Review). Semiconductors, 1998. 32(4): p. 343-365.*

19. *Bimberg, D., M. Grundmann, and N.N. Ledentsov, Quantum dot heterostructures. 1999: John Wiley.*

20. *Bimberg, D., et al., Quantum dot lasers: breakthrough in optoelectronics. Thin Solid Films, 2000. 367(1-2): p. 235-249.*

21. *Grundmann Marius and Bimberg Dieter, Gain and Threshold of Quantum Dot Lasers: Theory and Comparison to Experiments. Japanese Journal of Applied Physics, 1997. 36(Part 1, No. 6B): p. 4181-4187.*

22. *Vasil'ev, P.P., Ultrashort pulse generation in diode lasers. Optical and Quantum Electronics, 1992. 24(8): p. 801-824.*

23. *L W Shi, et al., Status and trends of short pulse generation using mode-locked lasers based on advanced quantum-dot active media Journal of Physics D: Applied Physics, 2007. vol. 40(Issue 18): p. 307-318.*

24. *Avrutin, E.A., J.H. Marsh, and E.L. Portnoi, Monolithic and multi-gigahertz mode-locked semiconductor lasers: constructions, experiments, models and applications. Optoelectronics, IEE Proceedings -, 2000. 147(4): p. 251-278.*

25. *Wada, O., Femtosecond all-optical devices for ultrafast communication and signal processing. New Journal of Physics 2004. vol. 6(Issue 1): p. 1-35.*

26. *Derickson, D.J., et al., Short pulse generation using multisegment mode-locked semiconductor lasers. Quantum Electronics, IEEE Journal of, 1992. 28(10): p. 2186-2202.*

27. *Tandoi, G., Monolithic high power mode locked GaAs/AlGaAs quantum well lasers, in Department of Electronics and Electrical Engineering. 2011, University of Glasgow.*

28. *Huang, X., et al., Passive mode-locking in 1.3 μm two-section InAs quantum dot lasers. Applied Physics Letters, 2001. 78(19): p. 2825-2827.*

29. *Heck, M.J.R., et al., Observation of Q-switching and mode-locking in two-section InAs/InP (100) quantum dot lasers around 1.55 μm. Opt. Express, 2007. 15(25): p. 16292-16301.*

30. *Renaudier, J., et al., 45 GHz self-pulsation with narrow linewidth in quantum dot Fabry-Perot semiconductor lasers at 1.5 μm. Electronics Letters, 2005. 41(18): p. 1007-1008.*

31. *Lu, Z.G., et al. A passive mode-locked InAs/InP quantum dot laser with pulse duration of less than 300 fs. in Quantum Dots, Particles, and Nanoclusters VI. 2009. San Jose, CA, USA: SPIE.*

32. *Thompson, M.G., et al., InGaAs Quantum-Dot Mode-Locked Laser Diodes. Selected Topics in Quantum Electronics, IEEE Journal of, 2009. 15(3): p. 661-672.*

33. *Rafailov, E.U., et al., High-power picosecond and femtosecond pulse generation from a two-section mode-locked quantum-dot laser. Applied Physics Letters, 2005. 87(8): p. 081107-3.*

34. *Mukai, K., et al., Phonon bottleneck in self-formed In_{x}Ga_{1-x}As/GaAs quantum dots by electroluminescence and time-resolved photoluminescence. Physical Review B, 1996. 54(8): p. R5243-R5246.*

35. *Malins, D.B., et al., Ultrafast electroabsorption dynamics in an InAs quantum dot saturable absorber at 1.3 μm. Applied Physics Letters, 2006. 89(17): p. 171111.*

36. *Thompson, M.G., et al., Subpicosecond high-power mode locking using flared waveguide monolithic quantum-dot lasers. Applied Physics Letters, 2006. 88(13): p. 133119-3.*

37. *Thompson, M.G., et al. Properties of InGaAs quantum dot saturable absorbers in monolithic mode-locked lasers. in Semiconductor Laser Conference, 2004. Conference Digest. 2004 IEEE 19th International. 2004.*

38. *Moore, S.A., et al., Reduced surface sidewall recombination and diffusion in quantum-dot lasers. Photonics Technology Letters, IEEE, 2006. 18(17): p. 1861-1863.*

39. *Notzel, R., et al. Recent advances in long wavelength quantum dot lasers and amplifiers. in Optical Fiber Communication - includes post deadline papers, 2009. OFC 2009. Conference on. 2009.*

40. *M Kuntz, et al., Direct modulation and mode locking of 1.3 μm quantum dot lasers New Journal of Physics, 2004. 6: p. 181.*

41. *Kuntz, M., et al., 35 GHz mode-locking of 1.3 μm quantum dot lasers. Applied Physics Letters, 2004. 85(5): p. 843-845.*

42. *Grundmann, et al., Progress in Quantum Dot Lasers: 1100 nm, 1300 nm, and High Power Applications. Japanese Journal of Applied Physics., 2000. 39(4B): p. 2341.*

43. *Lu, Z.G., et al., An L-band monolithic InAs/InP quantum dot mode-locked laser with femtosecond pulses. Opt. Express, 2009. 17(16): p. 13609-13614.*

44. *Zhang, L., et al. Low timing jitter, 5 GHz optical pulses from monolithic two-section passively mode-locked 1250/1310 nm quantum dot lasers for high-speed optical interconnects. in Optical Fiber Communication Conference, 2005. Technical Digest. OFC/NFOEC. 2005.*

45. *Berg, T.W. and J. Mork, Quantum dot amplifiers with high output power and low noise. Applied Physics Letters, 2003. 82(18): p. 3083-3085.*

46. Shchekin, O.B., et al., Discrete energy level separation and the threshold temperature dependence of quantum dot lasers. Applied Physics Letters, 2000. 77(4): p. 466-468.

47. Cataluna, M.A., et al., Stable mode-locked operation up to 80^{o}C from an InGaAs quantum-dot laser. Photonics Technology Letters, IEEE, 2006. 18(14): p. 1500-1502.

48. Portnoi, E.L. and A.V. Chelnokov. Passive mode locking in a short-cavity diode laser. in Semiconductor Laser Conference, 1990. Conference Digest. 12th IEEE International. 1990.

49. Deryagin, A.G., et al., Generation of 110 GHz train of subpicosecond pulses in 1.535 μm spectral region by passively modelocked InGaAsP/InP laser diodes. Electronics Letters, 1994. 30(4): p. 309-311.

50. Merghem, K., et al., Pulse generation at 346 GHz using a passively mode locked quantum-dash-based laser at 1.55 mu m. Applied Physics Letters, 2009. 94(2): p. 021107-3.

51. Young-Kai, Chen, and M.C. Wu, Monolithic colliding-pulse mode-locked quantum-well lasers. Quantum Electronics, IEEE Journal of, 1992. 28(10): p. 2176-2185.

52. Thompson, M.G., et al. 20 GHz colliding pulse mode-locking of InGaAs quantum dot lasers. in Lasers and Electro-Optics, 2005. (CLEO). Conference on. 2005.

53. Martins-Filho, J.F., et al., Monolithic multiple colliding pulse mode-locked quantum-well lasers, experiment and theory. Selected Topics in Quantum Electronics, IEEE Journal of, 1995. 1(2): p. 539-551.

54. Shimizu, T., I. Ogura, and H. Yokoyama, 860 GHz rate asymmetric colliding pulse modelocked diode lasers. Electronics Letters, 1997. 33(22): p. 1868-1869.

55. Shimizu, T., X. Wang, and H. Yokoyama, Asymmetric Colliding-Pulse Mode-Locking in InGaAsP Semiconductor Lasers. Optical Review, 1995. 2(6): p. 401-403.

56. Rae, A.R., et al. Harmonic Mode-Locking of a Quantum-Dot Laser Diode. in Lasers and Electro-Optics Society, 2006. LEOS 2006. 19th Annual Meeting of the IEEE. 2006.

57. Li, Y., et al., Harmonic mode-locking using the double interval technique in quantum dot lasers. Opt. Express, 2010. 18(14): p. 14637-14643.

58. Yanson, D.A., et al., Ultrafast harmonic mode-locking of monolithic compound-cavity laser diodes incorporating photonic-bandgap reflectors. Quantum Electronics, IEEE Journal of, 2002. 38(1): p. 1-11.

59. Yanson, D.A., et al., Terahertz repetition frequencies from harmonic mode-locked monolithic compound-cavity laser diodes. Applied Physics Letters, 2001. 78(23): p. 3571-3573.

60. Yanson, D.A., et al. Terahertz-frequency mode-locking of monolithic compound-cavity laser diodes. in Lasers and Electro-Optics Society, 2002. LEOS 2002. The 15th Annual Meeting of the IEEE. 2002.

Chapter 3

Fabrication of Mode-locked Lasers

3.1 Introduction

This chapter describes the fabrication technology and steps involved in the fabrication of the semiconductor InAs/InP quantum dot (QD) mode-locked lasers. The fabrication stages are summarised in the order in which they were carried out. All the fabrication procedures were performed at the James Watt Nanofabrication Centre (JWNC) at the University of Glasgow.

3.2 Fabrication of ridge waveguide lasers

A major part of this research work involved the fabrication of ridge waveguide structures, for realizing mode-locked lasers based on quantum dot material. The cross-sectional and three-dimensional view of the main fabrication steps of the shallow etched ridge waveguides are illustrated in Figure 3.1. The fabrication of the ridge waveguides involves four lithography steps. In the first step, alignment markers are defined, that are used for the positioning of the resist exposures in the successive lithography stages. The second lithography step is the realisation of the ridge waveguides followed by the opening of the contact

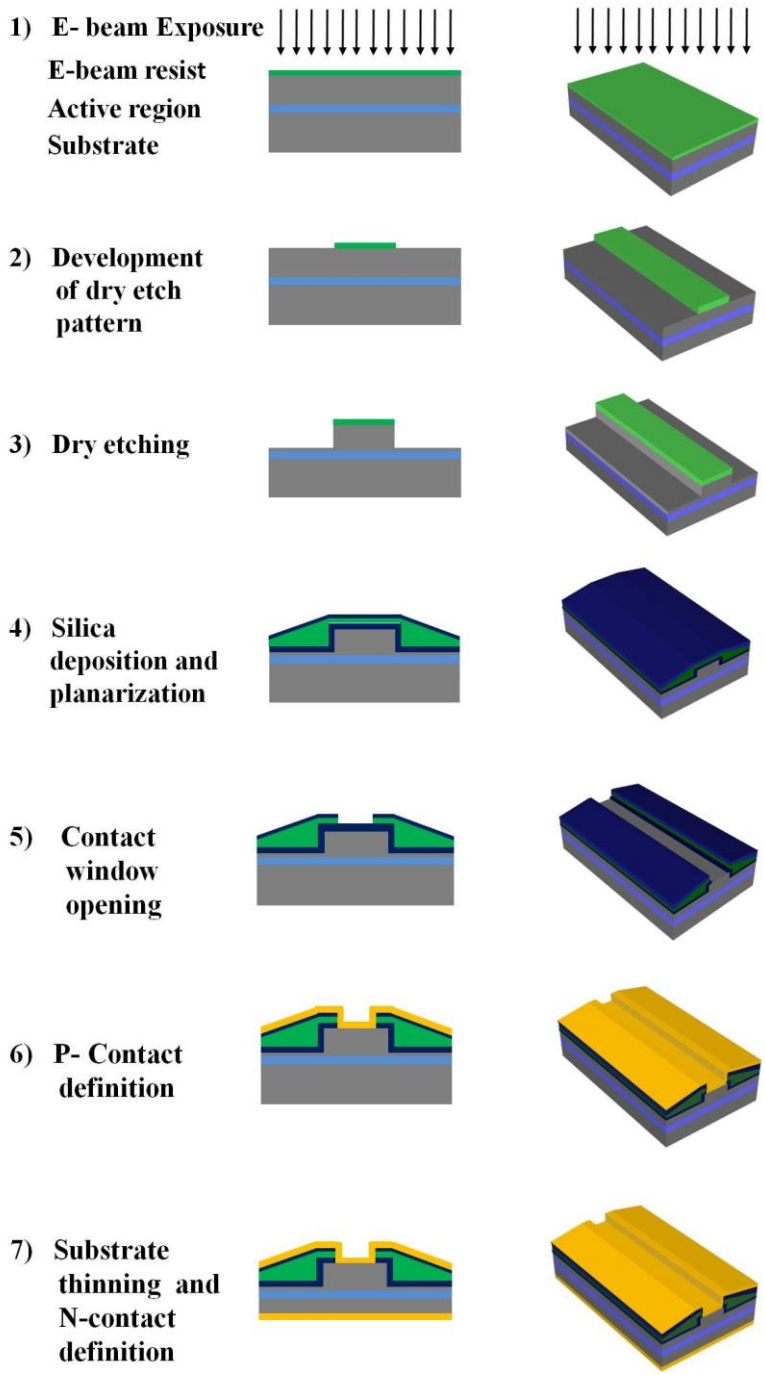

Figure 3.1: The schematic drawings showing the cross-sectional view (left) and three-dimensional view (right) of the main steps involved in the fabrication of ridge waveguide lasers.

window in the dielectric layer on top of the ridge waveguides. The final step is the definition of *p*-type contact layer for electrical biasing. After completion of the lithography stages, mechanical thinning of the backside of the sample is performed to reduce the sample thickness to 150-200 µm for better thermal performance and device cleaving. The fabrication process is terminated by evaporating the *n*-type contact metallisation at the backside of the sample followed by rapid thermal annealing. Finally, the sample is cleaved in individual laser bars which are mounted on brass pads using conductive epoxy for testing. The steps illustrated in Figure 3.1 are valid for all devices realised in this project, except for design options investigated for the fabrication of coupled cavity devices. These will be discussed in the chapter 6.

The QD modelocked lasers were fabricated with two or more *p*-type contact sections because the multi contact geometry gives more flexibility when biasing the different sections, such as the saturable absorber (SA) and gain sections. In this research work the gain and SA sections were separated by a 15 µm gap in the *p*-contact metal pad for electrical isolation. The measured resistance between the two sections was around 10 kΩ. Figure 3.2 gives a schematic drawing of planar and three dimensional view of a two section ML laser.

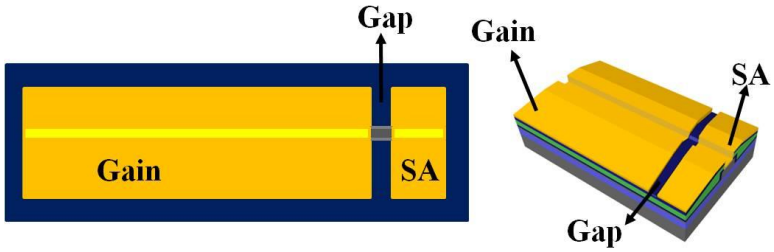

Figure 3.2: A schematic drawing of a two section mode-locked laser illustrating gain and SA section. Top view (left) and three dimensional view (right).

3.3 Lithography

For the fabrication of the semiconductor devices the desired pattern is transferred onto the semiconductor substrate by lithography. A radiation sensitive polymer called resist is deposited on the semiconductor sample surface and exposed to the radiation to transfer the desired pattern.

Different types of lithography processes can be used for exposing the resists, such as photolithography, E-beam lithography, X-ray lithography and ion beam lithography. The exposure wavelength of the particular lithographic process defines the minimum achievable feature size. Photolithography and E-beam lithography are used in the JWNC for exposure of the resists. Photolithography, which has a typical resolution of a few hundreds of nm, is commonly used in the fabrication process, where pattern resolution is not so crucial. In this work, E-beam lithography was used for the fabrication of the ridge waveguide devices.

- ***Photolithography:***

Photolithography is a fast and cost effective process for the fabrication of feature sizes as small as a few microns. Photolithography is ideal for mass production as an entire wafer can be exposed in a few seconds and the same mask is used repetitively. In the photolithographic process, a UV-radiation sensitive resist film is spun on the substrate and the desired pattern is transferred onto the substrate by interposing the mask between the UV source and the resist [1]. Contact photolithography is normally used in which the mask is placed in direct contact with the photoresist to limit the diffraction of the incident light. Following resist activation by the UV radiation, the exposed sample is developed with a developing solution. The contact photolithographic process is shown in the Figure 3.3 [2].

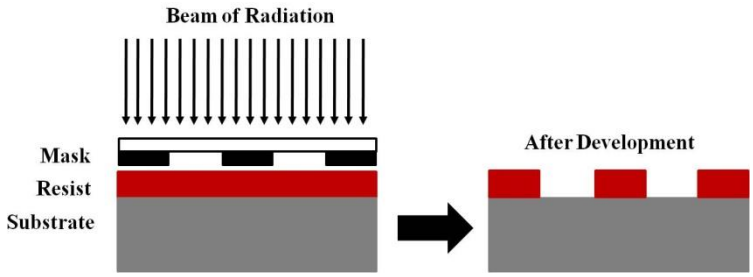

Figure 3.3: Contact Photolithographic process [2]

- ***Electron beam lithography:***

Due to small dimension of the devices fabricated in this project, the high resolution (in the order of a few nm) electron beam lithography was mostly used. Besides its high resolution, its flexibility in modifying the pattern designs and better layer to layer alignment makes it more suitable for nano-fabrication. In contrast to the photolithography, high energetic and collimated beam of electrons directly writes the pattern into the resist [2]. Nano-lithography is carried out using a Vistec VB6- UHR-EWF E-beam tool, commonly known as VB6. This E-beam tool uses 100 kV electron beams and able to produce a minimum beam diameter of 4 nm with resolution of 0.5 nm [2]. In this work resolution of 1.25 nm is used to define all patterns.

The pattern is defined using layout generator software such as L-EDIT, and converted in a GDSII-type file format. This pattern is then fractured into square lattice grid where the minimum distance between the lattice grid that defines the resolution of the process [2, 3]. The selection of the optimum beam spot size and beam step size (BSS) is a critical step for writing features where resolution or pattern edge roughness are very critical. The beam spot size has a width which is depends on the diameter of the aperture in the E-beam column and beam current. The beam scans the grid row by row horizontally, exposing dots separated by the fixed distance called BSS [2, 4]. The BSS is therefore integer multiple of the resolution and the multiplier is known as the variable resolution

unit (VRU). The VRU is typically set so that the BSS is 1/5 of the minimum feature size in the pattern. In the present work, a beam spot size of 9 nm and a VRU of 7 gave the best compromise in terms of writing speed and pattern resolution.

In case of large patterns such as metal contact pads a beam spot size of 33 nm and a VRU of 20 were used. The schematic illustration of the e-beam writing procedure is shown in Figure 3.4 and the value of E-beam dose, beam spot size and VRU for the different steps of lithography are summarised in the Table 3.1.

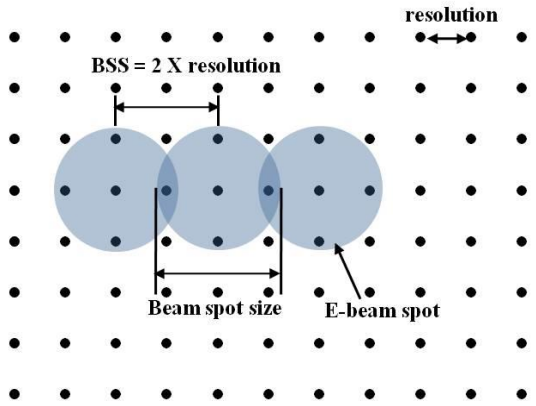

Figure 3.4: Schematic illustration of the E-beam writing procedure and parameters [2, 4].

E-beam Step	**Resist**	**Dose**	**VRU**	**Beam spot size**
Marker	PMMA	360	25	33
Ridge	HSQ	380	7	9
Window	PMMA	450	8	12
p-contact	PMMA	370	20	33

Table 3.1: Resists and E-beam parameters used for writing the different patterns..

3.4 Resist

Good adhesion, uniform thickness, etch resistance , thermally stable, light/electron sensitive and long shelf life are the properties which needs to be considered for a homogenous and repeatable pattern definition [1]. Moreover, the tone of the resist may be either positive or negative. In the positive resist the region exposed to the radiation is soluble in the developing solution, while the unexposed region remains insoluble; in the negative resist the region exposed to the radiation is insoluble in the developing solution, and the unexposed region is soluble. This is illustrated in the Figure 3.5 (a) and (b) respectively. The use of the positive or negative resist depends on the type of fabrication process. As an example, if the total area of the pattern to be written is small compared to the total area of the sample then a negative resist is preferred for minimising the electron beam writing time.

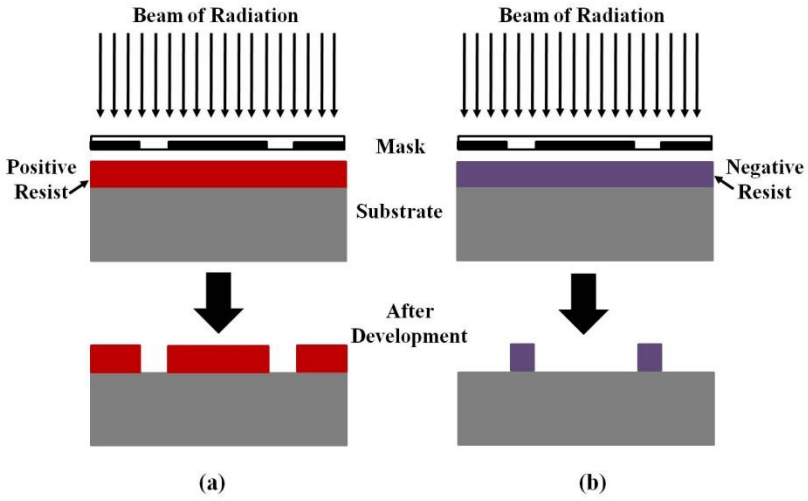

Figure 3.5: Schematic showing (a) Positive and (b) Negative resist exposure.

In order to get a uniform thickness of the resist film on the substrate, a resist spinner is used. The final thickness *z* of the resist film depends on the spin speed, as defined by the following equation [1]:

$$z = kP/\sqrt{\omega}$$

where P is the percentage of solid content of the resist, ω is the spin speed and k is a constant that depends on the resist type.

In this work, Poly methyl methacrylate (PMMA) and Hydrogen silsesquioxane (HSQ) were used as E-beam resists for defining the various patterns at different stages of the fabrication. The E-beam parameters as well as the resist development need to be thoroughly optimized for each type of resist as described in the following sections.

- ***Poly methyl methacrylate (PMMA):***

PMMA is a positive tone resist with high resolution, low contrast and poor dry etch resistance. The nominal E-beam dose for PMMA resist ranges from 100 to 500 μC/cm^2.Two types of PMMA resists were used for the definition of the markers, contact windows and metal contact pads: The PMMA 2010 15% (lower molecular weight) and the PMMA 2041 4% (higher molecular weight) resists, which give a layer thickness of around 1200 nm and 120 nm, respectively. A uniform resist layer is obtained by spinning the PMMA resist at 5000 rpm for 60 seconds. Mono layer, bi-layer or tri-layer resist can be used depending on the fabrication step requirements.

In this work bi-layer of PMMA resists with different molecular weight were used for the definition of the markers and metal contact pads, where lift-off of the metal layer was required. The sensitive PMMA 2010 (15%) was spun as a first layer followed by a 30 minute hard baking at 180°C. Hard baking improves the adhesion of the resist on the sample surface and removes any residual solvent molecules from the resist layer. A less sensitive layer of PMMA 2041 (4%) is subsequently spun with the same spin speed and a hard baking at 180°C for 90 minutes. After the exposure, MIBK and IPA (1:1 ratio) mixture kept at 23^{o}C was

used for 30 seconds to develop the bi layers of PMMA. The sample was then rinsed in RO water for 60 seconds and finally it was soaked in IPA for 30 seconds. The PMMA 2041 4% resist, being less sensitive, produces an undercut that facilitates the metal lift off process as schematically shown in the Figure 3.6.

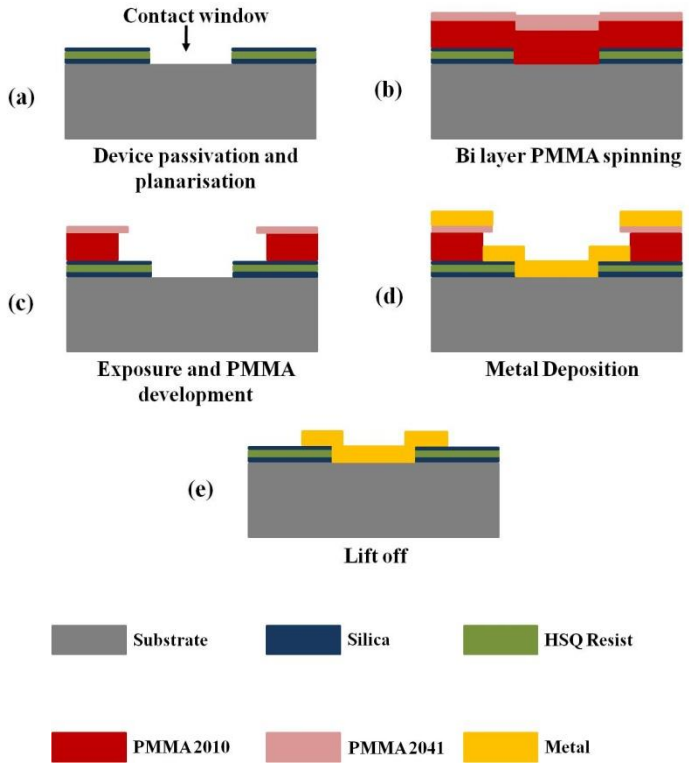

Figure 3.6: Schematic of the lift off steps (a) Etched contact window after device passivation (200nm SiO_2, 300nm hard baked HSQ and 100nm SiO_2) (b) spinning of bi-layers of PMMA (PMMA 2010 15% and PMMA 2041 4%, with a thickness of 1200 nm and 120 nm, respectively)(c) Exposure and development of PMMA resists (d) Metal deposition for *p*-contact (e) Metal lift off in hot acetone.

The tri-layer PMMA resist process was used for defining the contact window. A more sensitive bi-layer of PMMA 2010 (15%) was first spun on the sample. The sample was hard baked for 30 minutes at 180°C after each layer deposition to improve adhesion and reduce resist contamination. A PMMA 2041 (4%) layer was spun to form the third layer of the resist and hard baked at 180°C

for 90 minutes. The tri-layer PMMA was developed using the same developer mixture described before, but with a slightly longer exposure time of 35 seconds. The use of a thick tri-layer resists is required to protect the sample during the etching process because the usual PMMA versus SiO_2 etch selectivity in a fluorine based chemistry is around 1:2 [5].

- ***Hydrogen Silsesquioxane (HSQ):***

HSQ is a negative E-beam tone resist with high resolution and high contrast, and it is ideal for defining the ridge waveguides mask due to its minimal sidewall roughness [6] and high etch resistance [7]. More conventional E-beam resists such as PMMA would require the transfer of the pattern into a hard mask such as SiO_2 or SiN_3 because of their limited resistance to dry etching. This additional etching step increases the complexity of the process and amplifies both the edge roughness and pattern imperfections. In this work, HSQ resist was used for the definition of the ridge waveguides.

The silica-like structures of the HSQ after the E-beam exposure make it an ideal hard mask for dry etching. The selectivity of the HSQ for etching III-V semiconductor materials ranges from 6 to 12, thus enabling the etching of waveguides as deep as 5.4 µm with a 600 nm thick HSQ film [5]. Also, because HSQ is a negative tone resist the writing time is considerably reduced when writing optical waveguides which typically cover a very small fraction of the sample surface. Figure 3.7 shows a scanning electron microscope (SEM) image of a ~5.2 µm deep ridge waveguide with an HSQ hard mask.

The optimum process comprises the spinning of a non-diluted HSQ (100%) at 2000 rpm for 60 seconds which gives a film thickness of around 600 nm. The sample is pre-baked (before spinning resist) at 90ºC for 2 minutes in order to remove any vapours on the surface and post baked at 90ºC for 15 minutes. The sample is exposed with E-beam dose of 380 µC/cm^2 and developed

with 100% Tetra Methyl Ammonium Hydroxide (TMAH) at 23ºC, followed by a 60 seconds rinse in RO water and a 15 second rinse in IPA.

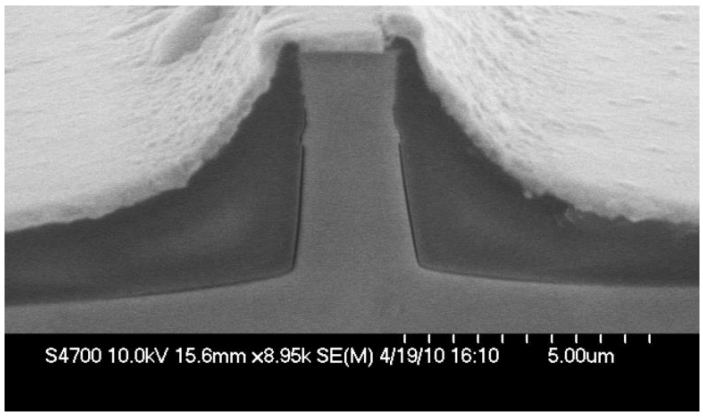

Figure 3.7: Deep etched ridge waveguide using HSQ as a hard mask

3.5 Silica(SiO_2) deposition

After etching of the ridge waveguide structures deposition of a dielectric layer is required to cover the exposed areas of the guiding structures [8]. The dielectric layer (or passivation layer) protects the etched guiding structures from degradation (leakage and long term stability problems) due to mechanical abrasion or foreign materials [9] and provides electrical isolation.

In this work, silane (SiH_4) and N_2O have been used in a low temperature (300ºC) Plasmalab 80Plus PECVD (Plasma Enhanced Chemical Vapour Deposition) tool to deposit a 200 nm silica (SiO_2) film [10]. In the PECVD reaction, gases are delivered in the vacuum chamber, where an RF source is used to initiate the plasma [11]. The substrate is placed on a heated electrode and the reactants are dissociated by the energy of the RF source. The RF generated plasma decomposes SiH_4 and N_2O to form the dielectric SiO_2, as given by the following chemical reaction:

$$SiH_4 + 2N_2O \rightarrow SiO_2 + 2H_2 + 2N_2$$

The properties (thickness, uniformity and deposition rate) of the deposited layer are influenced by the PECVD parameters such as RF power, pressure and temperature. The optimised recipe is given in the Table 3.2.

Parameter	**Value**		
Gas	SiH_4	N_2O	N_2
Flow (sccm)	9	710	171
Power (W)	10		
Pressure (mT)	1010		
Temperature ($^{\circ}$C)	300		

Table 3.2: Plasmalab 80Plus parameters for SiO_2 film deposition [3, 4].

3.6 Planarisation

In a non planar surface such as ridge waveguide structures a conformal coverage is essential to improve the uniformity of subsequent lithographic steps or layer depositions [10]. Planarization also provides uniform *p*-type contact metallisation and an extra protection in the probe measurements during laser characterization.

The planarisation process involves spinning the HSQ on the sample following the silica layer deposition by PECVD. Neat (100%) HSQ was spun at 4000 rpm and subsequently baked at 180ºC for an hour. The use of HSQ for the planarisation simplifies the process as compared with the conventional BCB (benzocyclobutene polymer) or polyimide-based planarisation which require several processing steps and higher curing temperatures [12]. The thickness of the HSQ film on the top of the ridge waveguide is lower than on the etched areas besides the ridge waveguide and dependent on the spin speed. The resultant thickness on the top of the waveguide is around 200- 250 nm while the thickness

on the etched surfaces is 400 nm. The HSQ layer is finally covered by a 100 nm-thick PECVD SiO_2 in order to cover any pinholes present on the HSQ passivation layer and for good adhesion with metals. The SEM image of a shallow etched ridge waveguide after the planarisation process is shown in Figure 3.8.

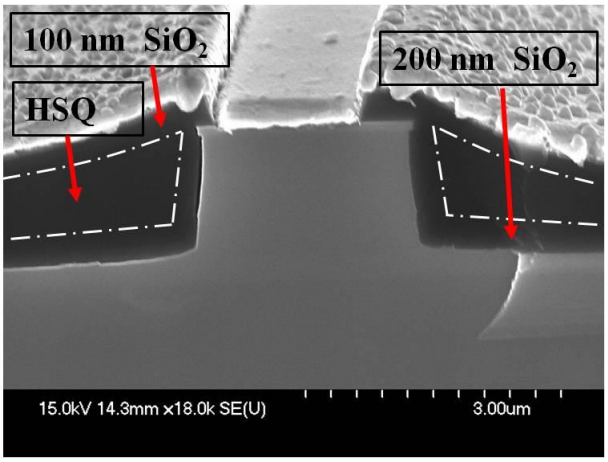

Figure 3.8: Planarised and metal coated waveguide.

3.7 Dry Etching

Dry etching is used to remove the unmasked area of the semiconductor material by high energetic ion beams or plasma driven chemical reactions. This can be performed by either as a physical or chemical technique. The physical dry etching process (ion beam milling and sputtering) is carried out by transferring the momentum of high energy moving ions to the atoms of the target material to physically knock them out. The chemical etching employs gaseous chemical reactants to form plasma composed of ions, electrons and free radicals, where free radicals react chemically with the target [13]. The physical etching is highly damaging to the substrate and chemical etching is very isotropic. Therefore optimal etching processes make use of a combination of physical and chemical etching [13].

In this work, a Plasmafab ET340 machine was used for the RIE (Reactive Ion Etching) of the ridge waveguides. In the RIE process, chemically reactive

gases are used to produce neutral and ionized energetic particles that can etch the substrate [13]. The RIE machine consists of two parallel electrodes placed in a vacuum chamber in which plasma generation and ion acceleration is controlled by the RF power applied to the electrodes. The free radicals (active neutrals) in the plasma chemically react with the material to be etched and as a result volatile products are produced. The chemical reaction of the radicals combined with the physical bombardment of the ions results in a faster chemical etching process with anisotropy, better selectivity and low damage to the substrate [14].

The schematic in Figure 3.9, illustrates the basic steps involved in the RIE etching, which are also summarized below [15]:

1. Generation of etchant species in the plasma.
2. Transportation of the reactant to the substrate surface via diffusion process.
3. Adsorption of reactant on the substrate surface.
4. Chemical reaction of radicals with substrate to form volatile compounds along with ion bombardment.
5. Desorption of the volatile compounds from the surface and pumping away from the vacuum system.

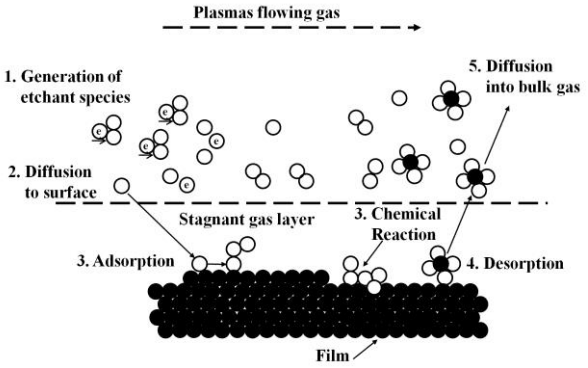

Figure 3.9: Schematic showing the steps involved in the RIE etching process [15].

The etching of InP has been widely studied with either Chlorine (Cl_2) or methane and hydrogen mixture (CH_4/H_2) based chemistries [16]. Chlorine based

chemistries provide smooth surfaces, vertical sidewalls and increased volatility of the by-product ($InCl_x$) when operated at elevated temperature (more than 130ºC) [16, 17]. The desired etching features such as anisotropy and smooth surfaces with chlorine based chemistry are highly temperature dependent, which limits the use of such chemistry in comparison to methane based chemistries. Also, the non corrosive and less toxic nature of the CH_4/H_2 plasma is an added advantage as opposed to Cl_2 based chemistries [18]. The drawback of CH_4/H_2 chemistries comes from the formation of the hydrocarbons based polymer which contaminates the chamber and consequently reduces the etch rate and enhances the surface roughness. The introduction of O_2 in the etching chemistry results in the reduction of the polymer formation and provides a better control over the lateral etch rate which consequently improves the verticality of the etched sidewalls [19].

In the CH_4/H_2 RIE etching chemistry, the chemical reaction of the plasma constitution with InP results in the formation of volatile phosphine (PH_3) along with indium containing compound $In(CH_3)_3$ [18, 20]. The main chemical reaction in the chamber forming the by-products is [20]:

$$CH_4 \xrightarrow{e} CH_3 + H$$

$$H_2 \xrightarrow{e} 2H$$

$$3CH_3 + 3H + InP \xrightarrow{e} In(CH_3)_3 + PH_3$$

The parameters (chamber pressure, RF power, gas flow) effecting the etch rate have been discussed in [18]. The results indicate an increase in the etch rate and polymer deposition rate as the total pressure of chamber and RF power are increased. Similarly, an increase in the gas flow rate causes increase in the polymers deposition rate and etch rate. For an ideal etching process, the etch rate should be maximised while the polymer deposition rate minimised. Therefore, in order to get the desired etch result, an optimised etch recipe was developed.

3.8 Etching of InAs/InP QD material

The etch recipe was optimised on a number of test samples. The optimal etch recipe is given in the Table 3.3 below:

Flow $CH_4/H_2/O$ (sccm)	**Time (Minutes)**	**Pressure (mTorr)**	**RF-Power (W)**
6/54/8	31.5	Open Valve (25-30)	50

Table 3.3: Optimised etch recipe for InAs/InP QD material.

In order to stop the etching process at the desired depth, an end point detection method was used. In this method a laser beam is focused on the area to be etched and interferometer traces are recorded. Before etching the samples the wafer structure was modelled using a Matlab programme called Etch Director which plots the interferometric trace as a function of etch depth. The modelled trace is shown in Figure 3.10. Besides the fringes typical of interferometric signals, a change in the signal amplitude is clearly visible between the upper cladding and the core layer due to different refractive indexes of the materials. The recorded trace for a QD test sample as a function of time is illustrated in Figure 3.11.

3.9 Wet etching of SiO_2 mask

The wet chemical etching of the SiO_2 hard mask is required after the RIE etching of the waveguide. Buffered HF (hydro fluoric acid) in a 1:5 ratio was used for one minute, followed by a RO water rinse for 5 minutes.

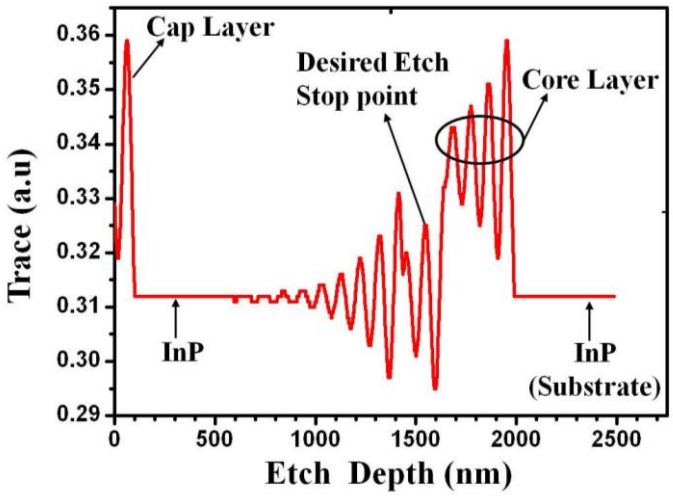

Figure 3.10: Modelled interferometric trace vs. etching depth obtained with Etch Director.

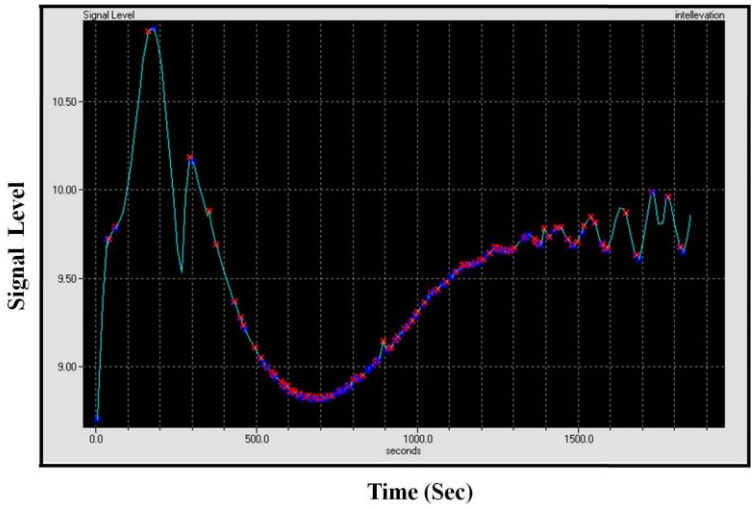

Figure 3.11: Interferometer trace recorded during the etching of a QD test sample with ET340.

3.10 Dry etching of dielectric layer

To inject the current in the semiconductor waveguide, it is required to open a window in the dielectric (SiO_2 + HSQ+ SiO_2) layer covering the top

surface of the waveguide. A 1.5 µm wide window pattern was transferred with E-beam lithography using tri-layer of PMMA and developed as discussed in section 3.4.

A Plasmalab80plus by Oxford Instruments is used to etch the dielectric layer with a plasma formed by CHF_3 and Argon gases [21]. The presence of the heavy noble gas Ar keeps the plasma stabilised and controls the undesirable increase in the temperature [22]. In addition it significantly changes the population of reactive species in the plasma resulting in a faster etch rate and anisotropic process [23]. The main chemical reactions occurring in the chamber are given as [24]:

$$e^- + CHF_3 \rightarrow 3F + CH + e^-$$

$$4F + SiO_2 \rightarrow SiF_4 + O_2$$

The CHF_3/Ar plasma does not chemically react with the semiconductor (cap layer), therefore the etching of the cap layer is only due to sputtering of high energy ions and it is very slow (3-5 nm/min).

Prior to the etching, the sample was given a short O_2 clean in the same machine, in order to remove any residual PMMA particles. The details of the recipes for the O_2 cleaning and SiO_2/HSQ dielectric etching are given in Table 3.4 and Figure 3.5, respectively.

Flow O_2 (sccm)	**Time (Minutes)**	**Pressure (mTorr)**	**RF-Power (W)**
10	2	50	10

Table 3.4 : Parameters for O_2 clean in Plasma lab80plus.

Flow CHF_3 /Ar (sccm)	**Time (Minutes)**	**Pressure (mTorr)**	**RF-Power (W)**
25/18	26	30	200

Table 3.5: Process parameters for the etching of the dielectric layer composed of SiO_2 and HSQ in Plasma lab80plus.

3.11 PMMA Plasma ashing

The removal of the resist after the dry etching can be done by wet chemical etching with chemical solutions such as H_2SO_4/H_2O_2, tricholoroethylene, or cholorobenzene [13]. However, the mechanical handling of the sample in the solutions can cause damage to the surface of the sample. An alternative approach is plasma ashing, in which an energetic plasma causes oxidation or burning of the resist film. The process parameters used are shown in Table 3.6.

Flow O_2 (sccm)	**Time (Minutes)**	**Pressure (mTorr)**	**RF-Power (W)**
50	15	50	100

Table 3.6 : Parameters for O_2 ashing in Plasma lab80plus.

3.12 Device metal contacts

The definition of the metal contacts for electrical biasing of the devices is the final step of the fabrication process. The contact resistance at the interface between the metal contact and the semiconductor material is a critical parameter. because a high contact resistance results in excessive heating and may lead to

electrical breakdown of the device. Ideally, the contact must be ohmic. Ohmic contacts are metal-semiconductor contacts having negligible contact resistance and a quasi-linear current-voltage relationship [15]. When a metal is deposited on a semiconductor the formation of a potential barrier at the metal-semiconductor interface occurs, as shown in Figure 3.12 (a).The doped interface layer of the semiconductor plays a vital role in the current transport mechanism across the potential barrier. In lightly doped semiconductors, thermionic emission dominates current transport across a wider depletion region, while in highly doped semiconductors the quantum mechanical tunnelling through a narrower barrier becomes dominant. This is shown in Figure 3.12 (b) [25]. High doping of the semiconductor cap layer is therefore important to favour quantum mechanical tunnelling. The semiconductor material used in this work has a 100 nm thick highly doped Be (1×10^{19} cm^{-3}) cap layer for the *p*-type contact and Si doped (1×10^{18} cm^{-3}) layer for *n*- type contact.

Before depositing the *p*-type metal contact plasma ashing was done in order to remove any micro masking of resist from the pattern area. The sample was then de-oxidized in HCl and RO water solution mixed in the ratio of 1:5 for 30 seconds. A layer stack of Ti/Pt/Au with thicknesses of 33/33/240 nm was used for the *p*-type contact metalization.

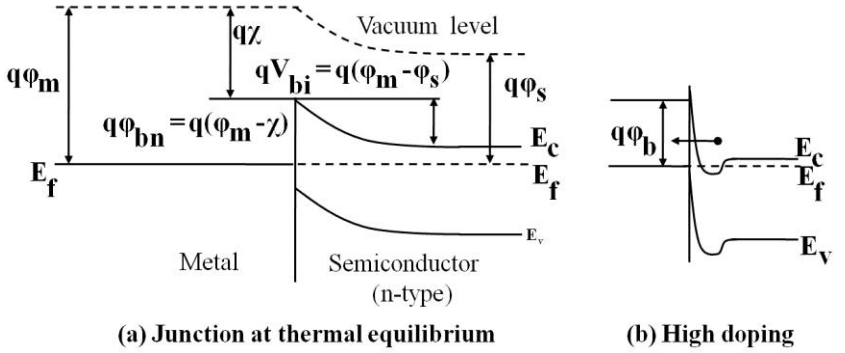

Figure 3.12: (a) Energy Band diagram of metal semiconductor showing formation of potential barrier at equilibrium and (b) with high doping tunnelling through narrow barriers [25].

The Ti metal layer is used to provide better adhesion with the SiO_2 dielectric layer. The Pt metal layer acts as a diffusion barrier and prevents the penetration of Au in the semiconductor material, while the Au enhances the conductivity and facilitates probing of the device [4]. Prior to *n*-contact metallisation, mechanical thinning of the sample is carried out in order to reduce the series resistance and thus improving thermal management of the device. The *n*-type contact recipe Au/Ge/Au/Ni/Au is evaporated on the backside of the chip and the thickness of the each layer is 14/14/14/11/240 nm, respectively [4]. The contacts are then annealed using an RTA (Rapid Thermal Annealer) for 60 seconds at 380ºC.

3.13 Conclusions

In this chapter a detailed description of the fabrication technology and processes used in the realization of the InAs/InGaAsP/InP QD mode-locked lasers was given. Particular emphasis was placed on the lithography and dry etching steps, for which process development was required to ensure accurate fabrication of the sub-micron features and smooth and vertical optical waveguide sidewalls. The detail of the fabrication steps in the order they were carried out is given in the Appendices.

3.14 References

1. *Razeghi, M., Technology of Quantum Devices. 2010: Springer US.*
2. *Thoms, S., E-beam lithography course notes and documentation, [Available online]: http://www.jwnc.gla.ac.uk/: 2011.*
3. *Samarelli., A., Micro ring resonators in Silicon-on-Insulator, in Department of Electronics and Electrical Engineering,. 2011, University of Glasgow,UK: Glasgow.*
4. *Tandoi, G., Monolithic high power mode locked GaAs/AlGaAs quantum well lasers. , in Department of Electronics and Electrical Engineering. 2011, University of Glasgow: Glasgow.*
5. *Gabor , M., Semiconductor ring lasers for all-optical signal processing . PhD dissertation, Department of Electronics and Electrical Engineering University of Glasgow, 2010.*
6. *Namatsu, H., et al., Nano-patterning of a hydrogen silsesquioxane resist with reduced linewidth fluctuations. Microelectronic Engineering, 1998. 41-42(0): p. 331-334.*
7. *O Faolain, L., Fabrication of photonic crystals using a spin-coated hydrogen silsesquioxane hard mask. J. Vac. Sci. Technol. B, 2006. 24(1): p. 336.*
8. *Demir, H.V., et al., Self-aligning planarization and passivation for integration applications in III-V semiconductor devices. Semiconductor Manufacturing, IEEE Transactions on, 2005. 18(1): p. 182-189.*
9. *Mai, C.C. and T.S. Whitehouse, Low-Temperature Passivation of Semiconductor Devices and Their Reliability. Reliability, IEEE Transactions on, 1970. R-19(2): p. 71-74.*
10. *Ghandhi, S.K., VLSI fabrication principles : silicon and gallium arsenide / Sorab K. Ghandhi. 1983, New York :: Wiley.*

11. *Oxford instruments, surface technology systems, .[Available Online]: http://www.oxinst.com/products/etching-deposition-growth/processes-techniques/plasma-deposition/pecvd/Pages/pecvd.aspx : 2011.*

12. *Lianping, H., et al., 10-GHz Mode-Locked Extended Cavity Laser Integrated With Surface-Etched DBR Fabricated by Quantum-Well Intermixing. Photonics Technology Letters, IEEE, 2011. 23(2): p. 82-84.*

13. *Ghandhi, S.K., VLSI fabrication principles: silicon and gallium arsenide. 1994: J. Wiley.*

14. *Larsson, D., Fabrication and characterisation of low-noise monolithic mode-locked lasers. Ph.D Thesis. Technical University of Denmark. 2006.*

15. *Sze, S.M., Semiconductor devices, physics and technology. 1985: Wiley.*

16. *Lee, J.S.Y.a.Y.T., Parametric reactive ion etching of InP using Cl_2 and CH4 gases: effects of H_2 and Ar addition. Semicond. Sci. Technol, 2002 17(3): p. 230–236.*

17. *McNevin, S., Chemical etching of GaAs and InP by chlorine: The thermodynamically predicted dependence on Cl_2 pressure and temperature. J. Vac. Sci. Technol. B, 1986. 4(5): p. 1216.*

18. *Hayes, T., Reactive ion etching of InP using CH_4/H_2 mixtures: Mechanisms of etching and anisotropy. J. Vac. Sci. Technol. B, 1989. 7(5): p. 1130.*

19. *Schramm, J., Fabrication of high-aspect-ratio InP-based vertical-cavity laser mirrors using $CH_4/H_2/O_2/Ar$ reactive ion etching. J. Vac. Sci. Technol. B, 1997. 15(6): p. 2031.*

20. *Feurprier, Y., Proposal for an etching mechanism of InP in CH_4-H_2 mixtures based on plasma diagnostics and surface analysis. J. Vac. Sci. Technol. A, 1998. 16(3): p. 1552.*

21. Paul, A.K., Short Communication, Plasma etching process for realization of micromechanical structures for MEMS. J. Indian Inst. Sci. , 2001. 81: p. 669.

22. Jansen, H., A survey on the reactive ion etching of silicon in microtechnology J. Micromech. Microeng, 1996. 6: p. 14.

23. Metwalli, E. and C.G. Pantano, Reactive ion etching of glasses: Composition dependence. Nuclear Instruments and Methods in Physics Research Section B: Beam Interactions with Materials and Atoms, 2003. 207(1): p. 21-27.

24. Plummer, J.D., Silicon VLSI Technology. 2000: Prentice Hall

25. V.L, R., A review of the theory and technology for ohmic contacts to group III-V compound semiconductors. Solid-State Electronics, 1975. 18(6): p. 541-550.

Chapter 4

Characterisation of Mode-locked Quantum Dot Lasers

4.1 Introduction

This chapter gives a detail overview of the characterisation of mode-locked lasers fabricated on quantum dot material. The design of the InAs/InP quantum dot (QD) epitaxial structure used for the device fabrication will be presented first, followed by the discussion on the initial testing of the material using ridge waveguide lasers. The experimental results of ~35 GHz mode-locked laser with optimised saturable absorber (SA) length are then presented, together with the investigations on the HR/AR coatings for improving mode-locking performance. Finally, the results describing the dual wavelength mode-locking operation are discussed in section 4.7.

4.2 InAs/InP QD material structure

The growth of InAs QDs on InP substrate can provide an active layer for generating wavelengths at around 1.55 μm [1-3]. The InAs QDs on InP substrate have been grown by a number of groups [4-9], using either metal organic chemical vapour deposition (MOCVD), chemical beam epitaxy (CBE) or

molecular beam epitaxy (MBE). In all these deposition techniques self organized growth of QDs is done by adopting the Stransky-Krastanov method that induces strain between the lattice mismatched substrate (of lower lattice constant) and the deposited layer (of slightly higher lattice constant) [10]. The deposited layer first forms a two dimensional wetting layer on the substrate that subsequently turns into three dimensional islands (quantum dot) after the critical thickness is deposited. The size and density of the QDs depends on the growth parameters such as capping technique, substrate temperature and growth rate [1, 11].

The active layer used in this project is an InAs/InP QD array grown using a CBE technique by P.J Poole [1] at the Institute for Microstructural Sciences, National Research Council, Ottawa,ON, Canada. In the undoped active region of the material is stacked with five layers of QDs.

From the n-type InP substrate up, the layers are arranged in the following order.

- A 330 nm thick InP lower *n*-type cladding layer, Si doped at 1×10^{18} cm^{-3}.
- A 165 nm thick InP layer, Si doped at 5×10^{17} cm^{-3}; this layer has a lower doping in order to reduce the diffusion of impurities into the active region.
- A 350 nm thick undoped waveguide core layer.
- A 200 nm thick InP *p*-type upper cladding layer, Be doped at $\sim5\times10^{17}$ cm^{-3}.
- A 15 nm thick InGaAsP etch stop layer, Be doped at $\sim5\times10^{17}$ cm^{-3}.
- A 135 nm thick InP *p*-type upper cladding layer, Be doped at ~ 0.5 to 1×10^{18} cm^{-3}.
- A 1185 nm thick InP *p*-type upper cladding layer, Be doped at 1×10^{18} cm^{-3}.

- A 100 nm InGaAs contact layer at the top, Be doped at 1×10^{19} cm^{-3}.

Epitaxial Surface of the Wafer							
Material		**Thickness**	**Doping**		**Ga%**	**As%**	**Strain%**
InGaAs		100 nm	1×10^{19}	Be	47	100	0
InP		1100 nm	$\sim1\times10^{18}$	Be	0	0	0
InP		135 nm	$\sim0.5 - 1\times10^{19}$	Be	0	0	0
InGaAsP		15 nm	$\sim1\times10^{17}$	Be			
InP		200 nm	$\sim1\times10^{17}$	Be	0	0	0
InGaAsP		113.6 nm			19	40.5	0.04
InAs	5	5.6 ML			0	100	-3.1
GaP	5	1 ML			100	0	7.7
InGaAsP	5	29.9 nm			19	40.5	0.04
InGaAsP		82.9 nm			19	40.5	0.04
InP		165 nm	5×10^{17}	Si	0	0	0
InP		330 nm	1×10^{18}	Si	0	0	0
Substrate							

Table 4.1: Epitaxial layer structure of the wafer.

The undoped active region contains a 82.9 nm InGaAsP (1.15Q) barrier layer at the bottom and a 113.6 nm at the top; in between these two barrier layers

there is a stack of five layers of InAs QDs. Each QD layer is 5.6 ML thick and beneath each QD layer there is a 29.9 nm thick InGaAsP (1.15Q) layer and a 1 ML thick GaP layer. The GaP layer is used to reduce the As/P exchange, when the surface is exposed to As flux to form the InAs QDs [5]. The InGaAsP waveguide core, and the InAs and GaP layers are 0.04 %, -3.1 % and 7.7 % strained, respectively.

4.3 Ridge waveguide lasers

As discussed in detail in chapter 3, the ridge waveguide geometry was employed in the design of the lasers developed in this research work. The optimal ridge width and height were found with a mode solver. The average refractive index method was applied to calculate the refractive index of the very thin epilayers constituting the core, to simplify the simulations process. A schematic of shallow etched waveguides fabricated in this work is shown in Figure 4.1.

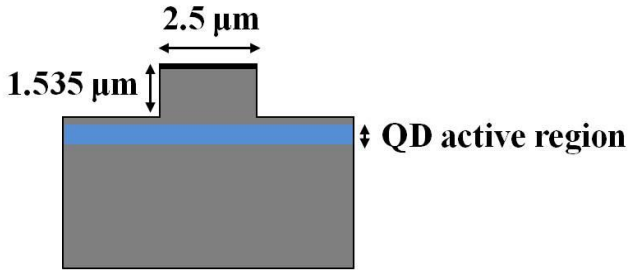

Figure 4.1: Schematic diagram of a shallow etched ridge waveguide structure.

For a shallow etched design, the effective modal index for the fundamental, 1st and 2nd order TE polarised modes as a function of the waveguide width for 1.535 µm high ridge was computed as shown in Figure 4.2 (a). The computed fundamental transverse *(TE)* mode of a 2.5 µm wide and 1.535 µm high ridge waveguide is shown in Figure 4.2 (b).

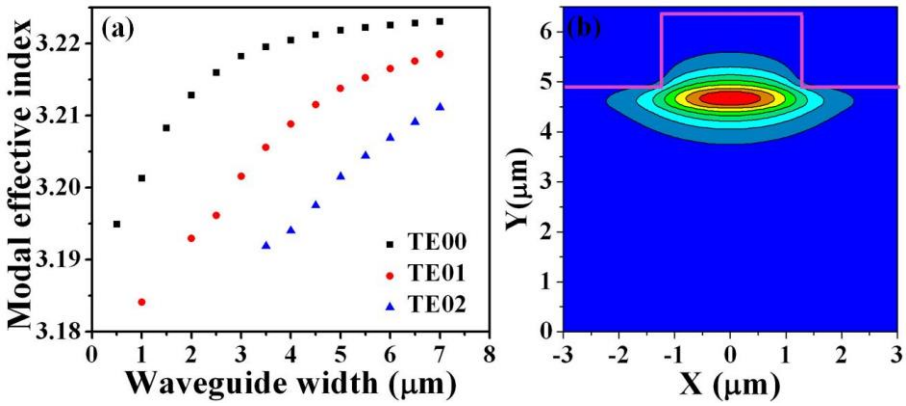

Figure 4.2: Simulation results for 1.535 μm deep ridge waveguide design: (a) Modal effective index versus waveguide width for fundamental, 1st and 2nd order mode and (b) Fundamental transverse mode for a 2.5 μm wide waveguide.

4.3.1 *L-I* curves

Ridge waveguide lasers (RWLs) due to a better confinement of carriers and photons exhibit lower threshold current and can operate on a single transversal mode. The characterisation required mounting the devices on brass sub-mounts that were placed on copper heat sink kept at a constant temperature of 20°C thanks to thermoelectric controller (TEC). A laser current driver (LD) and a germanium (Ge) photodetector controlled by a LabView program were used to automatically control the measurements and collect the data for subsequent analysis. The *L-I* curves were used to determine the threshold current (I_{th}) and the external quantum efficiency (η_{ext}) from the slope of *L-I* curve. A typical *L-I* curve for a 1200 μm long device is shown Figure 4.3.

The measured threshold current (I_{th}) and threshold current density (J_{th}) are 24 mA and 800 A/cm^2, corresponding to J_{th} of 160 A/cm^2 per layer of quantum dot. The slope efficiency is found to be 0.14 W/A per facet.

The external quantum efficiency η_{ext}, is defined as the rate of increase in the photon output as a function of injection current [12]:

$$\eta_{ext} = \frac{d(P_o/h\nu)}{d(\frac{A}{q}[J - J_{th}]}$$

Equation 4.1

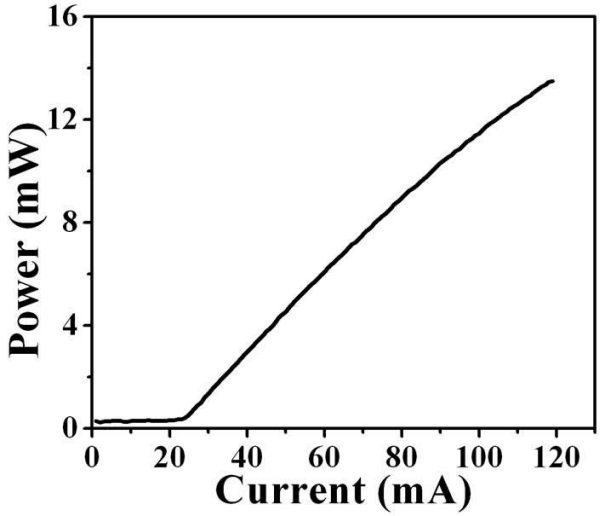

Figure 4.3 : *L-I* curve of 1200 μm long RWL device.

Using the above equation the external quantum efficiency calculated for RWL is 36.5 %. Approximately similar values for threshold current density per layer (170 A/cm^2), slope efficiency (0.17mW/mA) and external quantum efficiency (22 %) are reported in [3].

FP mode-locked lasers with varying SA lengths (3.2-19%) were also fabricated, in order to find the optimum length of the SA, which is strongly dependent on the epilayer design and waveguide geometry. A too short SA length is insufficient to initiate the mode-locking, whereas, too long lengths result in higher absorption losses that might reduce the efficiency of the pulse shaping mechanism. Figure 4.4 shows a family of *L-I* curves for different lengths of the SA obtained with a floating SA section. As expected, the higher absorption of long SAs leads to reduction in the slope efficiency and increase in the threshold current. The step like behaviour appears in the *L-I* curves at the lasing threshold due to an increase in the saturated losses [13].

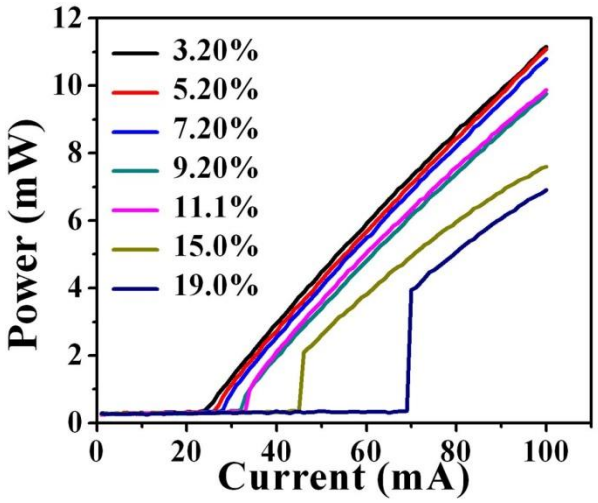

Figure 4.4 : *L-I* curves of RWL devices, for different lengths of the SA.

4.3.2 Characteristic temperature

In semiconductor lasers the threshold current, slope efficiency and output power strongly depends on the operating temperature [14-17]. Figure 4.5 shows the typical *L-I* curves of a RWL operated under CW operation, for various heat sink temperatures ranging from 10°C to 60°C. It is evident that I_{th} increased, while the slope efficiency and output power decrease. The temperature sensitivity of a semiconductor laser is well described by the characteristics temperature T_o that relates the threshold current and temperature through the following empirical equation [15, 17, 18].

$$I_{th} = I_o \exp\left(\frac{T}{T_o}\right)$$

Equation 4.2

where I_{th} is threshold current, I_o is intercept of the threshold current at 0K, known as the characteristic current, and T is the operating temperature in Kelvin. The greater the value of T_o, the less sensitive the threshold current is to the temperature. The value of T_o is calculated by plotting the natural logarithm of the threshold current versus the operating temperature, as shown in Figure 4.6.

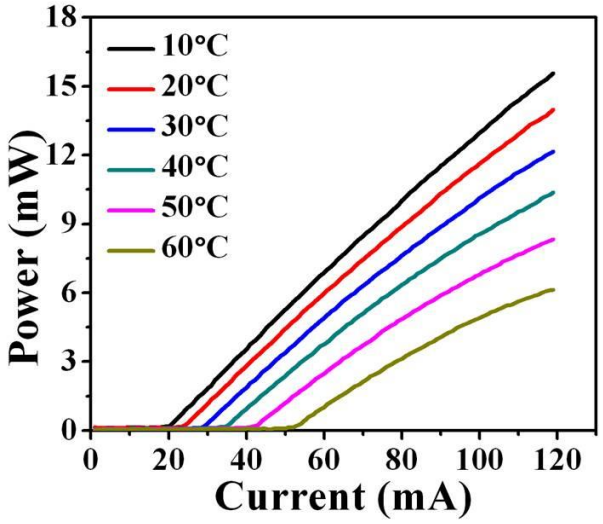

Figure 4.5 : Measured *L-I* curves for a 1200 μm long RWL, for varying TEC temperature values.

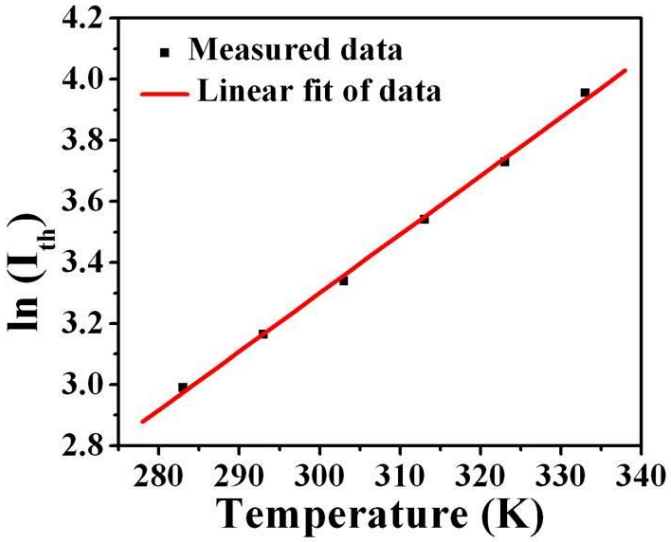

Figure 4.6 : Plot of the natural logarithm of I_{th} versus T for a 1200 μm long RWL.

Using the intercept of the linearly fitted data the calculated value of T_o for the material structure used in this project is 52 K. As a comparison, typical value of T_o for InGaAsP/InP double heterostructure and quantum well lasers tend to fall in the 50-70 K range [14]. This low value of T_o, for InGaAsP/InP material is attributed to the increase in Auger recombination along with possible leakage of carriers. Typical value of T_o for 5 and 6 layers of InAs/InP QDs material are found

to be in the range of 56-72 K [19-21]. The vertical stacking of the QD layers substantially improve the T_o value, as demonstrated by the record value of 113 K for a QD laser consisting of thirty vertically stacked QD layers and emitting around 1529 nm [22].

4.4 Characterisation of mode-locked lasers

The simplest design for passive mode-locking in semiconductor lasers consists of a Fabry-Perot cavity with two separate biasing sections, namely the saturable absorber and the gain. The characterisation of the two section mode-locked lasers was carried out by forward biasing the gain and reverse biasing the absorber section. The laser bar was fixed on a copper mount attached to a thermo electric cooler (TEC) and all the measurements discussed in this chapter were recorded at a temperature of the copper mount of 20°C. Because the lasers were fabricated on an *n*-type substrate, the electrical ground was connected to copper mount and electrical probes were used to contact the *p*-type sections. The output light from the device was coupled into a single mode lensed fibre and connected to the measurement instruments via an optical isolator. The full characterisation of the passively mode-locked lasers was carried out by measuring the light-current *(L-I)* characteristics, optical spectra, RF spectra and second harmonic generation (SHG) intensity autocorrelation. The experimental setups along with the results of the measurements are discussed in the next sections.

- ***Light-current characteristics:***

The threshold current of the devices increases by increasing the reverse voltage in the SA and exhibits the typical step-like behaviour already discussed in section 4.3.1. The typical *L-I* curves and output power maps of a 1220 μm long device with a 1117 μm gain and 88 μm (7.2 %) SA sections are illustrated in Figure 4.7 (a) and (b), respectively.

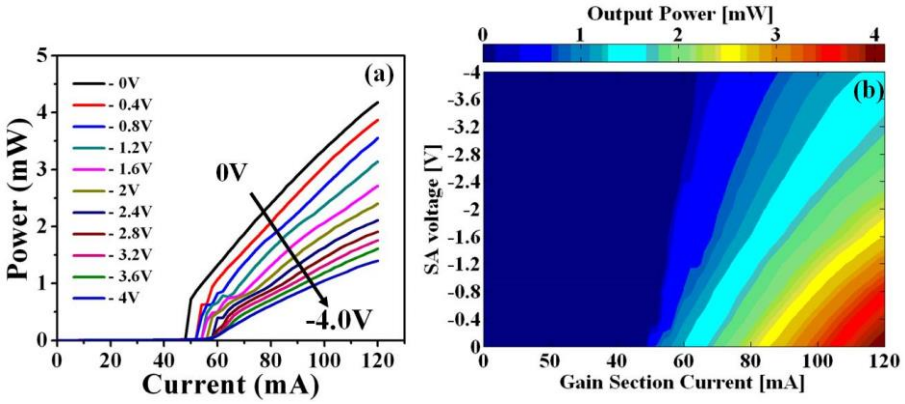

Figure 4.7: (a) *L-I* curves for different reverse voltages and (b) Output power map as a function of the gain current and reverse voltage.

- ***Optical spectra measurements:***

The optical spectra of the devices were recorded by coupling the output light into an optical spectrum analyser (OSA) through a single mode lensed fibre. Figure 4.8 shows the schematic of the experimental setup used for the measurement of the optical spectra.

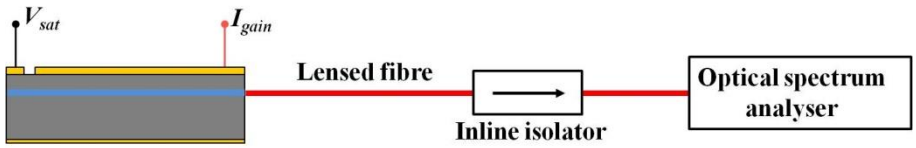

Figure 4.8 : Schematic of experimental setup for optical spectrum measurements of the mode-locked lasers.

In the mode-locking regime, the locking that occurs between the longitudinal modes substantially broadens the 3 dB bandwidth of the optical spectrum. The precise pulse repetition rate was estimated by determining the mode spacing of the cavity longitudinal modes with an OSA resolution bandwidth of 0.06 nm. Figure 4.9 shows the optical spectrum of a device with a 7.2% absorber under optimal mode-locking biasing conditions, which correspond to an injected current of 90 mA and a reverse biasing of -3.2V on the SA section. The

3 dB bandwidth of the optical spectrum was 7.73 nm, with a peak wavelength at 1562 nm. The zoom-in of the optical spectrum of Figure 4.9 (b) indicates a mode spacing of around 0.28 nm, which corresponds to a 35 GHz pulse repetition frequency. This repetition frequency was later confirmed by the RF measurements.

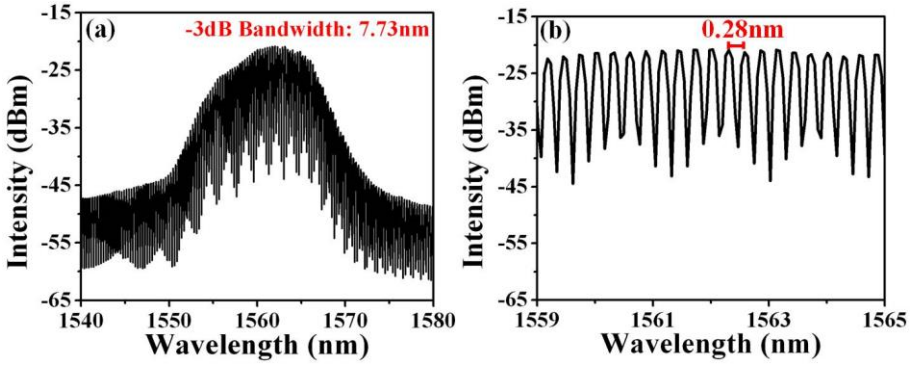

Figure 4.9: Optical spectra for a device biased at 90 mA gain current and -3.2 V reverse biased voltage (a) optical spectrum and (b) corresponding mode-spacing.

Within the mode-locked region of operation, for higher gain current the devices mode-lock with a spectrum exhibiting a dual lobe. This phenomenon has been reported in QD mode-locked lasers by a number of groups [23-27] and will be discussed in details in section 4.7.

- ***RF spectra measurements:***

The mode-locking repetition frequency of the device was confirmed by observing the radio frequency (RF) spectra of the output light with a 45 GHz bandwidth photo detector connected to a 40 GHz RF spectrum analyser. Figure 4.10 shows the schematic of the experimental setup used for the measurement of the RF spectra.

A typical example of an RF spectrum (VBW= 10KHz, RBW= 300KHz , span=1 GHz) recorded for a gain section current of 90 mA and SA section reverse biased voltage of -3. 2 V is shown in Figure 4.11.

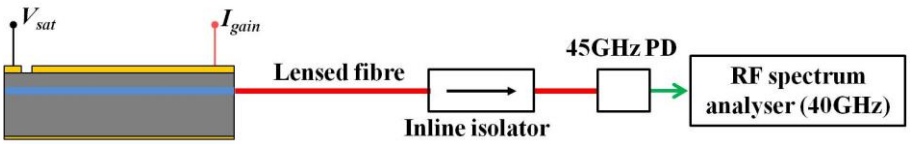

Figure 4.10: Schematic of the experimental setup for RF spectrum measurements of the mode-locked lasers.

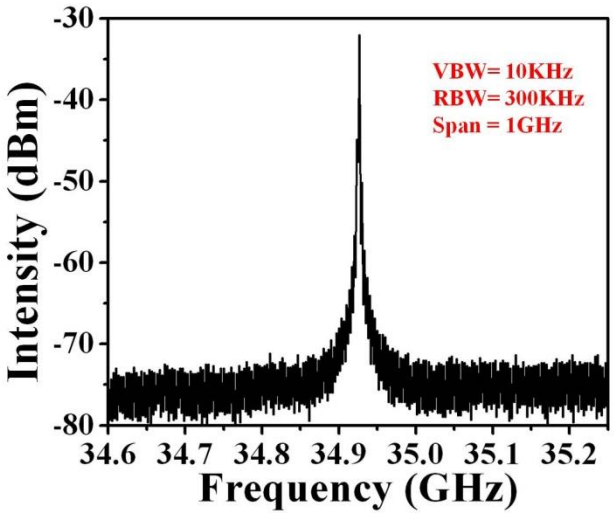

Figure 4.11: Measured RF spectrum at 90 mA gain current and -3.2 V reverse biased voltage.

The RF spectrum of the device is ~40 dB above the noise floor, suggesting a stable and complete mode-locking. The fundamental frequency of the mode-locking is 34.92 GHz in excellent agreement with the measured optical mode spacing. When dual lobes appeared in optical spectrum, dual peaks were also recorded in the RF spectrum suggesting the presence of two separate pulse trains travelling in the cavity. This feature will be discussed later in this chapter.

- ***Autocorrelation measurements:***

The measurement of short optical pulses (< 10 ps) is not accurate with conventional photodetectors due to their response time being greater than 10 ps. Therefore, the non-linear intensity autocorrelation technique is commonly employed to measure the pulses accurately in the sub 10 ps range. The most

common method for producing intensity autocorrelation is through second harmonic generation (SHG) on a non-linear crystal [28, 29].

Figure 4.12 shows the schematic of the experimental setup used for the characterisation of the optical pulses of the mode-locked lasers.

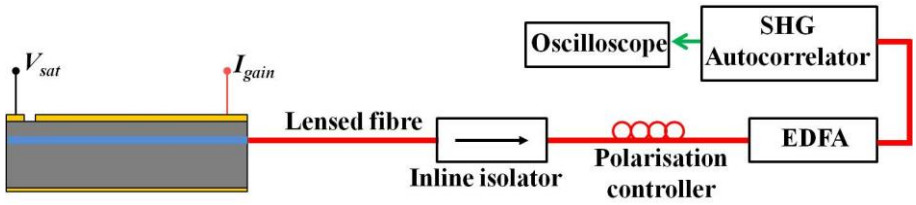

Figure 4.12: Schematic of the experimental setup for the autocorrelation measurements of mode-locked lasers.

The output light from the device was coupled through a lensed fibre into an inline isolator, a polarisation controller, a dispersion compensated erbium doped fibre amplifier (EDFA) and finally sent into a (SHG) intensity autocorrelator. The polarisation controller was used to adjust the polarisation before the intensity autocorrelator, while the dispersion compensated EDFA was used to minimise the additional dispersion in the pulses introduced by the EDFA [28]. In the SHG intensity autocorrelator the incident train of pulses is splitted into two orthogonal polarised beams, and sent to a Michelson interferometer with a variable delay in one arm. The beams from the output of the interferometer are focused by a lens onto a SHG crystal and the SHG signal is converted into an electrical signal by a photomultiplier tube and monitored on an oscilloscope.

The autocorrelation traces of the device operating under optimal mode-locking condition were observed for a gain section current of 90 mA and SA section reverse biased voltage of -3. 2 V (Figure 4.13 (a)). The pulse spacing in the pulse train was around 28.25 ps, which corresponds to a repetition rate of ~ 35 GHz. The actual pulse width can be determined by deconvolving the measured pulse width of the autocorrelation trace. To estimate the actual pulse width, the pulse shape can be assumed to be hyperbolic secant, Lorentzian or Gaussian [30]

depending on the type of gain medium, device geometry, dispersion and operating conditions. The pulses from semiconductor mode-locked devices are usually well approximated by a secant as shown by the good fit of a $sech^2$ curve with the autocorrelation pulse, (Figure 4.13 (b)). For a $sech^2$ pulse profile, the FWHM (Δt) of the pulse is evaluated from the autocorrelation trace FWHM $(\Delta\tau)$, using the expression, $\Delta t = 0.6482\ \Delta\tau$ [30]. The pulse width, assuming $sech^2$ pulse profile, was estimated to be 2.2 ps.

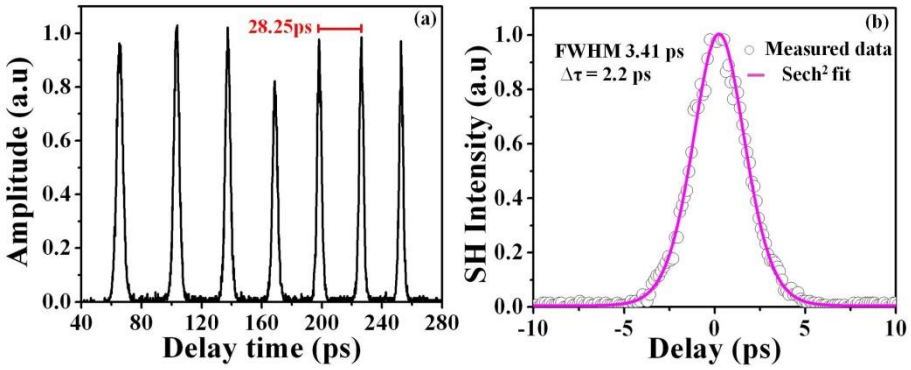

Figure 4.13 : (a) A typical pulse train of a mode-locked laser and (b) the deconvolved $sech^2$ fit pulse at 90 mA gain current and -3.2 V SA reverse voltage.

The pulse width as a function of the gain current for different reverse bias voltages applied to the SA is shown in Figure 4.14 (a). The pulse broadening occurs at higher gain current and is due to self phase modulation (SPM), whereas, the pulse shortening occurs at higher reverse bias voltages and is a consequence of a faster absorber recovery time. Both the pulse broadening and shortening effects are clearly visible in Figure 4.14 (a).

The time bandwidth product (TBP), calculated as the product of pulse width and the optical spectrum FWHM, is an accurate measure of the chirp present in the pulse train [29]. For a $sech^2$ pulse the theoretical TBP in the Fourier transform-limited case is $\Delta t.\Delta\nu = 0.3148$ [30]. Figure 4.14 (b) shows the TBP as a function of the gain current for different reverse bias voltages applied to the SA.

The measured values of TBP for different biasing conditions are much higher than the theoretical limit, indicating that the mode-locked pulses are highly chirped.

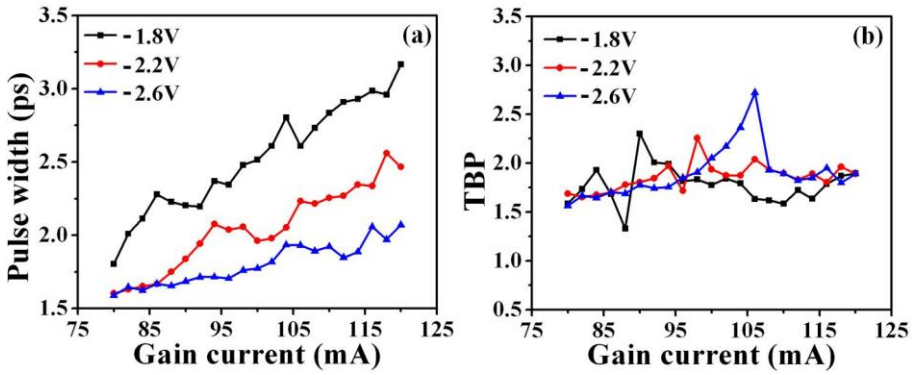

Figure 4.14 : (a) Pulse width (b) and TBP as a function of gain current for different values of absorber reverse voltages.

In semiconductor lasers, the gain and loss saturations induce changes in the carrier density leading to variations in the refractive index. This causes strong SPM, and thus substantial chirp to the pulses i.e. the time domain variation of the instantaneous frequency of the pulse causes spreading in time of the pulses [31]. As a consequence, the pulses may not remain Fourier transform-limited.

- ***Comparison of mode-locking with 5.2 and 7.2 % SA lengths:***

In order to find the optimum length of the SA, two-section mode-locked lasers with varying SA lengths (3.2-19%) were fabricated. The length of SA is a very important factor in determining the range of stable mode-locking. Too short SAs cannot trigger the mode-locking, while too long SAs increase the losses and make the mode-locking unstable. Stable mode-locking is achieved by appropriate spectral alignment of both SA and gain curves [32], therefore, the length of the SA plays an important role in detuning the energy gap between gain and absorber sections. As a whole, the interplay between saturable absorption, gain saturation along with carrier life time in the SA and gain section determines the stable mode-locking range [33]. The two-section devices exhibited optimum mode-locking for SA lengths corresponding to 5.2 and 7.2 % of the whole laser cavity. No mode-

locking was observed with 3.2 % and SA longer than 7.2 %. Compared to GaAs based material systems, these lengths are very short since stable mode-locking has been demonstrated by using absorber lengths up to 26 % of the total cavity in GaAs/AlGaAs devices [34]. This is due to the fact that compared to GaAs based material system, InP-based materials exhibit higher threshold current densities and waveguide internal losses, thus causing higher absorption [35].

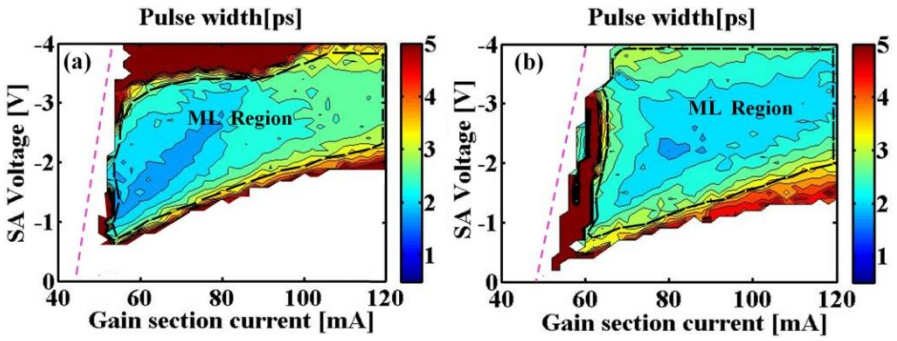

Figure 4.15: Mode-locking maps for devices with a SA length corresponding to (a) 5.2 % and (b) 7.2 % of the total laser cavity.

The mode-locking maps for two devices with 5.2 and 7.2 % SA lengths are shown in Figure 4.15 (a) and (b), respectively. The contour maps show the average values of the deconvolved pulse widths as a function of the gain section current and SA reverse voltage. The region enclosed by the black dotted line corresponds to the biasing conditions for which mode locking was observed. The pink dashed line approximately indicates the lasing threshold for increasing reverse voltages. The lasing threshold at 0 V reversed biasing on the SA was 44 mA and 48 mA for the 5.2 and 7.2 % SA, respectively. In both cases mode-locking initiates very close to threshold and the pulse widths are typically below 3.5 ps. The region of optimal mode-locking occurs at higher gain current for the longer SA for the same reversed voltage applied. This is expected because longer SAs are less easily saturated, and thus require higher gain current to generate mode locking. The mode-locking map for long SA is wider compared to the shorter one. This is most likely due the fact that for short SAs the band edges of the gain and SA sections become substantially detuned at higher reverse voltages.

Therefore, at lower gain currents for reverse voltages above -3 V no mode locking was observed on the device with the short SA. The measured values of TBP for different biasing conditions are much higher than the theoretical limit for both SA lengths, indicating that the mode-locked pulses are highly chirped. The TBP measurements for 5.2 % SA device will be discussed in section 4.7.

4.5 Thin film coatings

In a semiconductor laser, the cleaved facets provide the required optical feedback due to refractive index difference between the air and semiconductor material. For uncoated facets at normal incidence of the light, the reflectivity coefficient R is given by [36]:

$$\boldsymbol{R = \left(\frac{n_2 - n_1}{n_2 + n_1}\right)^2}$$

Equation 4.3

where n_2 is the refractive index of the semiconductor material and n_1 is the refractive index of the air. Typical values of semiconductor refractive indices yield $R \approx 0.25\text{-}0.35$. It is sometimes desirable to deposit high/anti reflection (HR/AR) thin film coatings at the facets of the lasers to decrease/increase the mirror losses and therefore improves the external quantum efficiency and/or decrease the lasing threshold [36].

4.5.1 HR coating

The standard high reflective coatings are composed of a stack of layers of low and high refractive index materials. Bi-layer combinations of dielectric-metal commonly employed for HR coating films are Al_2O_3/Si [37], SiO_2/Ti/Au [38] and Al_2O_3/TiO_2[39]. The two available methods in our department for the deposition of coating materials are sputter deposition and E-beam evaporation. In this work, both methods were used for depositing HR coating materials on the bare cleaved facet of the device. The deposited HR coating material was composed of SiO_2, Ti and Au layer with nominal thicknesses of 300 nm, 10 nm and 150 nm,

respectively, as shown by the schematic of Figure 4.16. First, 300 nm of SiO_2 was deposited by sputtering, followed by the deposition of 10 nm Ti and 150 nm Au by E-beam evaporation. The 10 nm Ti layer was used to improve the adhesion between the SiO_2 and Au layers [38].

Figure 4.16 : Schematic illustration of a FP laser with HR coated facet.

The simulated results in reference [38] showed that the reflectance of the deposited HR coating is about 93%. The reflectivity of the HR coatings was measured by using the net modal equation based on the well known Hakki-Paoli method [40]:

$$G_{net} = \frac{1}{L} ln\left(\frac{S-1}{S+1}\right) + \frac{1}{2L} ln\left(\frac{1}{R_1 R_2}\right)$$

Equation 4.4

where L is the cavity length, $R_1$and R_2 are the facet power reflectivities, $S = \sqrt{\frac{I_{max}}{I_{min}}}$ with I_{max} and I_{min} are the maximum and minimum intensities of the amplified spontaneous emission (ASE) spectrum as shown in Figure 4.17. The ASE spectrum of the HR-coated laser was measured at 12 mA (below the threshold current of 15.72 mA) and compared to the ASE spectrum of the same device before applying HR coating at 12 mA. Assuming a front cleaved facet reflectivity of ~30 %, the HR coating reflectivity is found to be ~ 93 %, which is in excellent agreement with the simulated reflectivity reported in [38].

Figure 4.18 shows the *L-I* curve of the uncoated (as cleaved/as cleaved facets) and HR coated (HR coated/as cleaved facets) FP lasers. The uncoated FP

laser exhibited a threshold current and output power of 25.92 mA and 9.02 mW (at 90 mA), respectively, with a slope efficiency of around 0.138 mW/mA. On the HR-coated FP laser the threshold current was reduced to 15.72 mA and the output power was increased to 11.77 mW (at 90 mA) with a slope efficiency that increased to around 0.154 mW/mA. The output was taken from the cleaved facet.

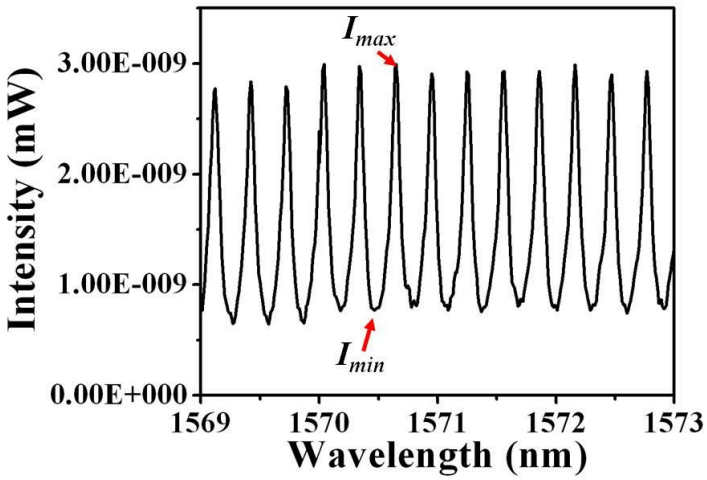

Figure 4.17: Maximum and minimum intensities of amplified spontaneous emission (ASE) spectrum.

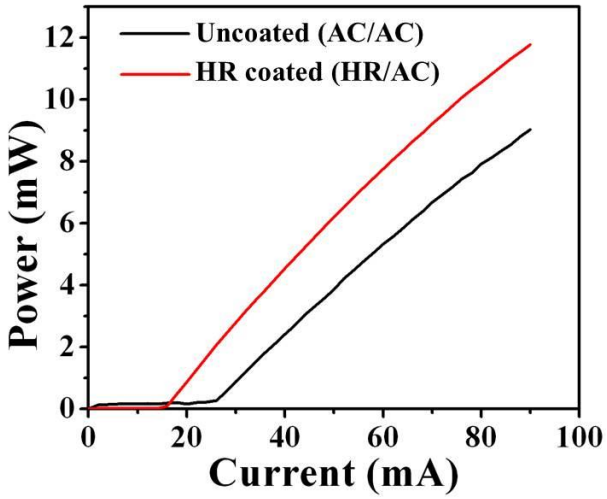

Figure 4.18: *L-I* curve of uncoated (AC/AC) and HR coated (HR/AC) FP lasers. (AC/AC : as cleaved/as cleaved, HR/AC: HR coated/as cleaved)

4.5.2 AR coating

The typical AR coatings deposited on the cleaved facets of semiconductor lasers are composed of either a single layer or a stack of alternating layers with different refractive indexes [39]. The standard single layer AR coating materials are either ZrO_2 or SiN Multilayer AR coating films are commonly composed of alternating layers of Al_2O_3/TiO_2 [39] and TiO_2/ SiO_2 [41] The semiconductor device can be effectively AR-coated with a single layer dielectric material if the refractive index (n_f) of the coating film is equal to the square root of the semiconductor index (n_s) at the desired wavelength i.e $n_f = \sqrt{n_s}$. In order to obtain a minimum in reflectance the desired thickness (d_f) of the deposited AR coating material should be [42]:

$$\boldsymbol{d_f = \frac{\lambda_o}{4n_f}}$$

Equation 4.5

where λ_o is the free space wavelength of the light at normal incidence.

Single layer AR coating materials such as TiO_2 or SiO_2, are not ideal for InP devices, as their indices do not match the required value imposed by Equation 4.5. Both SiN and ZrO_2 are better candidates as their refractive index is much closer to the required value for zero reflectivity. Better results, both in terms of bandwidth and absolute value of the reflectivity are obtained with multilayer AR coatings. In this research, reflectivity values of 5-10% were required, therefore a single layer film of SiO_2 was the best compromise between simplicity of the deposition process and desired reflectivity values. A single layer of SiO_2 is shown by a schematic in Figure 4.19.

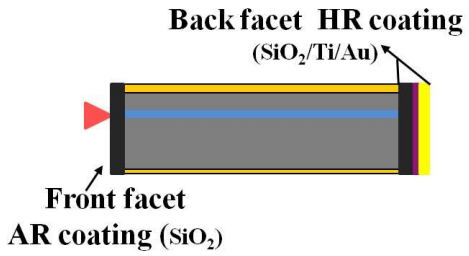

Figure 4.19: Schematic illustration of FP laser with AR and HR coated facets

A simple anti-reflection coating thickness calculator designed by Brigham Young university [43] was used to evaluate the percentage reflections for various thicknesses of the single SiO_2 layer for a wavelength of 1550 nm. The results of Figure 4.20 indicate that a 300 nm-thick layer of SiO_2 provides the reflectivity of ~5%.

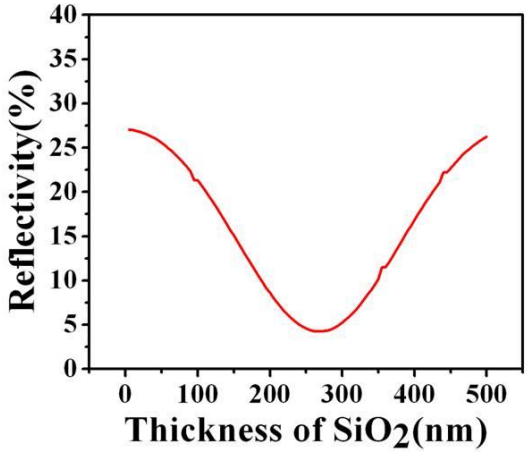

Figure 4.20: Reflectivity as a function of SiO_2 layer thickness for emission wavelength of 1550 nm.

Comparing the ASE spectra of AR and HR coated lasers and using the net gain equation (Equation 4.4), the reflectivity of the AR coated laser can be calculated. Similarly to what done for evaluating the HR coating, the ASE spectra of the device were recorded before and after applying the AR coating at 12 mA (when back facet was HR coated). Based on the previously calculated back facet

reflectivity of ~93 %, the AR coating reflectivity was found to be ~ 8 %, which is within the desired range.

Figure 4.21 shows the *L-I* curves of the HR (HR coated/as cleaved facets) and AR coated (HR coated/AR coated facets) FP lasers. For the AR coated laser the threshold current increased to 31.41 mA and output power reached 12.32 mW at 90 mA, with the slope efficiency increasing to around 0.211 mW/mA.

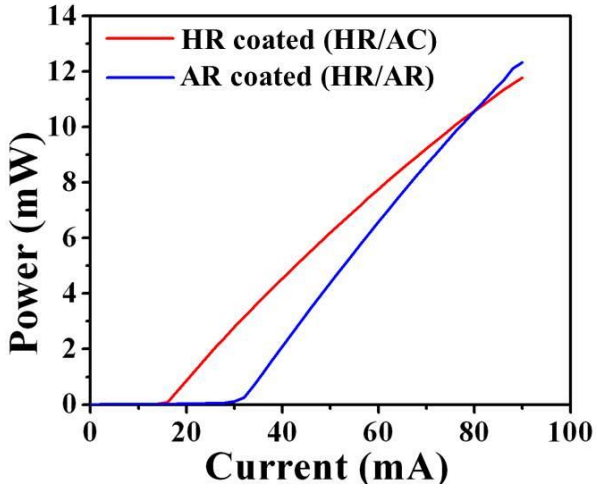

Figure 4.21: *L-I* curves of HR coated (HR/AC) and AR coated (HR/AC) FP lasers. (HR/AC : HR coated/as cleaved, HR/AR: HR coated/AR coated).

4.6 Mode-locked lasers results after thin film coating

Thin film coating applied can significantly modify the saturation behaviour of the absorber and as a result able to change the mode-locking performance of the device. Therefore, in this work SA lengths of 5.2% and 9.3% were chosen to study the mode-locking performance of the devices with coated facets. SMLLs were HR coated on gain side, while the SA side facet was uncoated as shown by schematic in Figure 4.22 (a). The same device was later AR coated from the SA side (see Figure 4.22 (b)).

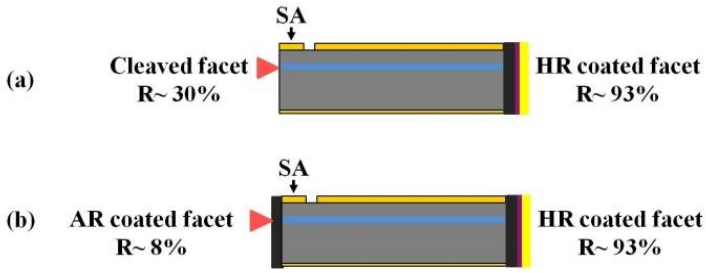

Figure 4.22: Schematic illustration of mode-locked laser with (a) HR coated and cleaved facet (b) HR and AR coated facets.

The *L-I* characteristics, optical spectra, RF spectra and autocorrelation traces for HR and AR coated laser devices were measured from the SA side. The mode-locking performance of the devices before coating (uncoated) and after HR and HR/AR coatings was compared.

The motivation for coating the facet of the devices is based on the theoretical investigations presented in [44], where improvement in passively mode-locked monolithic semiconductor lasers is predicted by placing the SA close to the AR coated facet. Using this approach the total mirror losses for the HR/AR coated device remain very similar to the uncoated device (since the product R_1R_2 is constant). This study reveals that HR/AR configuration leads to a substantial increase in the output power and increase in the mode-locking region with shortening of the pulses which in turns increase the peak power.

- ***Results for 9.3 % SA length:***

HR coating results: The *L-I* curves of the device before and after the HR coating are shown in Figure 4.23 (a) and (b), respectively. The output of the device after HR coating was taken from the cleaved facet. For uncoated device, the absorption losses were too high and threshold current increased up to 80 mA at 0 V, therefore, no mode-locking measurements were possible. After HR coating, the threshold current halved decreasing to 38 mA at 0 V.

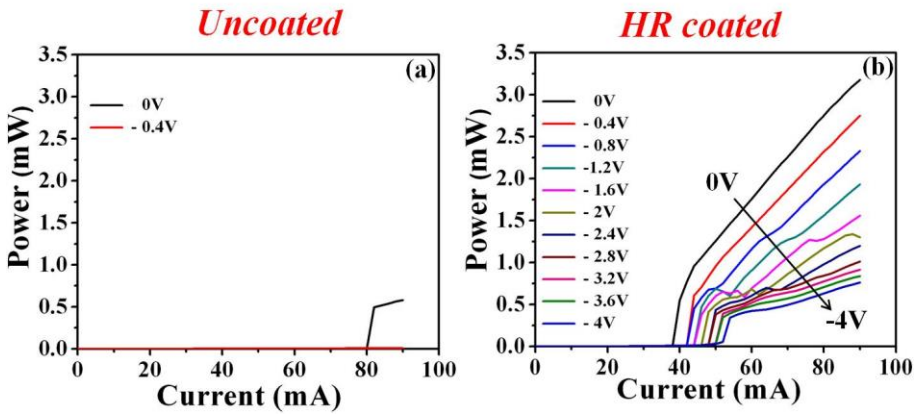

Figure 4.23: The *L-I* curves of (a) the uncoated and (b) HR coated lasers for different reverse biased voltages. The SA length is 9.3% of the total cavity length.

Figure 4.24 (a) and (b), show the optical and RF spectra of a device under optimal mode-locking biasing conditions, which correspond to an injected current of 66 mA and a reverse biasing of -2 V on the SA section. The 3 dB bandwidth of the optical spectrum was 5.93 nm, with a peak wavelength at 1574 nm. The RF frequency is ~ 36.8 GHz, in good agreement with the cavity length.

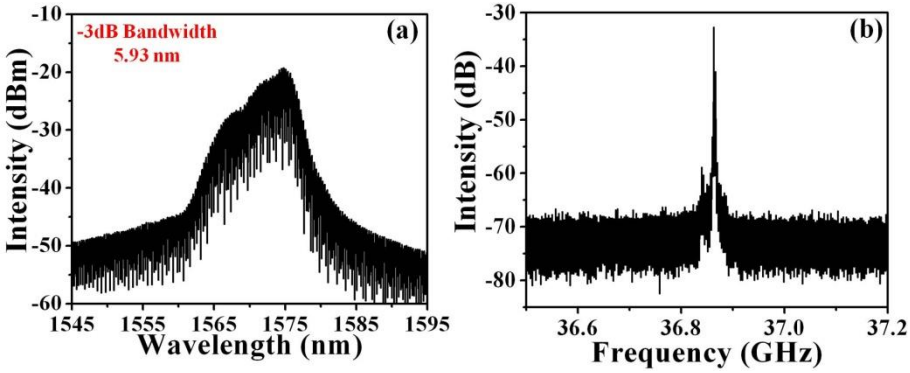

Figure 4.24: Measured (a) optical and (b) RF spectra of a HR coated laser with 9.3% SA length.

The autocorrelation traces of the device operating under optimal mode-locking condition are shown in Figure 4.25 (a). The pulse spacing in the pulse train was around 27.58 ps, which corresponds to a repetition rate of ~ 36 GHz. The pulse width, assuming a sech^2 pulse profile, was estimated to be 2.21 ps as shown by the fitting of Figure 4.25 (b).

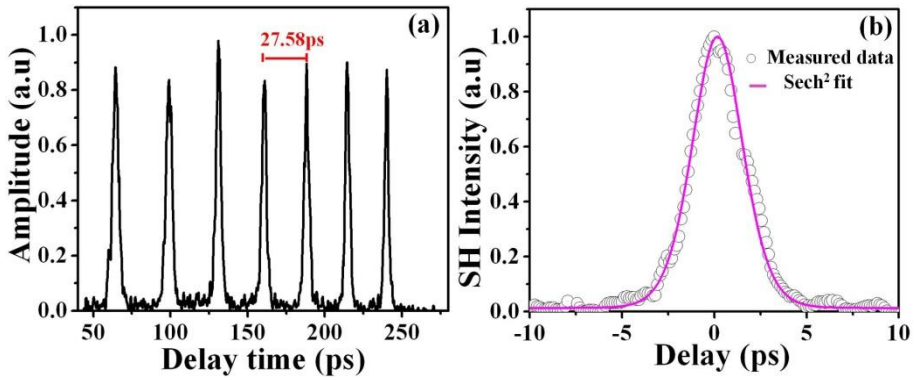

Figure 4.25: (a) A pulse train of a HR coated mode-locked laser and (b) the deconvolved $sech^2$ fit pulse at 66 mA gain current and -2 V SA reverse voltage.

HR/AR coating results: In order to assess the performance of the HR/AR coating technology, the cleaved facet of the device was AR coated. The *L-I* curve for the HR/AR coated laser shows a marginal increase of 6 mA compared to the uncoated device. This is largely expected as the total mirror losses for the uncoated device ($R_1 \approx 30\%$, $R_2 \approx 30\%$) is very similar to the HR/AR device ($R_1 \approx 8\%$, $R_2 \approx 93\%$). These results indicate that the HR/AR coating technology is robust and reliable, and confirms that the high losses introduced by a 9.3%-long SA can be partially compensated by increasing the cavity gain through the deposition of a HR coating.

- ***Results for 5.2 % SA length:***

HR coating results: The *L-I* curves before and after the deposition of the HR coating are shown in Figure 4.26 (a) and (b), respectively. For the HR coated device, there is significant decrease in threshold current, and an increase in output power and slope efficiency.

The optical spectra of the uncoated and HR coated device under the optimal biasing conditions are shown in Figure 4.27 (a) and (b), respectively. The optical spectrum of an uncoated laser was measured at 60 mA of gain current and with a reverse bias voltage of -2.2 V, while the HR coated device was measured at a gain current of 90 mA and a reverse bias voltage of -4 V.

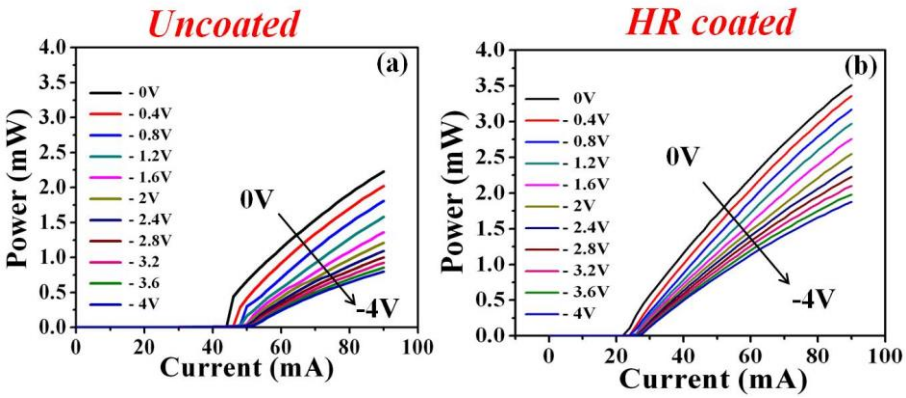

Figure 4.26: The *L-I* curves of (a) uncoated and (b) HR coated laser. The SA of the device is 5.2 % of the total cavity length.

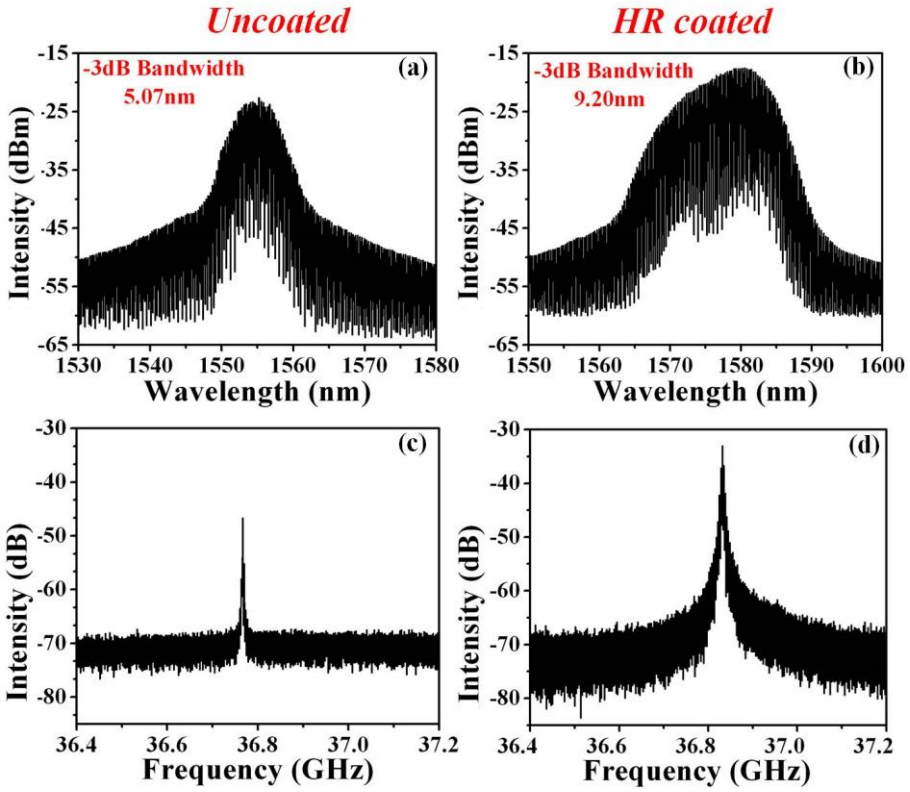

Figure 4.27: Measured optical and RF spectra of (a, c) uncoated and (b, d) HR coated laser.

The optical spectra of the HR coated laser are 4.13 nm wider compared to the uncoated laser, suggesting the emission of narrower pulses. Figure 4.27 (c) and (d)

show the RF spectra of uncoated and HR coated lasers measured under the same biasing conditions.

The autocorrelation traces for the uncoated device recorded under optimal mode-locking condition are shown in Figure 4.28 (a). The spacing between consecutive pulses corresponds to a repetition rate of ~ 36.5 GHz. A single pulse of a measured autocorrelation trace with a $sech^2$ curve fitting is shown in Figure 4.28 (b), which deconvolves to a width of 2.1 ps.

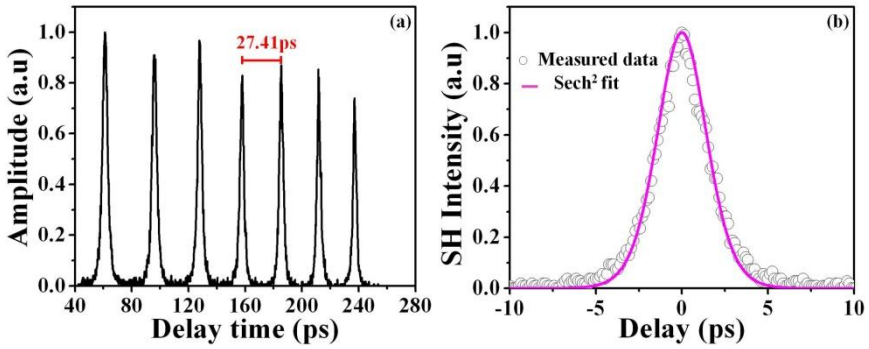

Figure 4.28: (a) The pulse train and (b) a single $sech^2$ fit pulse at 60 mA gain current and -2.2 V SA reverse voltage.

In the HR coated laser, pulses start to appear for gain section current of 60 mA and SA reverse biased voltage of -2 V, but pulses with maximum extinction ratio were seen when the gain section was forward biased at 80 mA and the SA reversed biased at -3 V and above. The pulse train emitted from the HR coated laser for a gain current of 90 mA and a SA reversed voltage of -4 V is shown in Figure 4.29 (a). The spacing between the two pulses corresponds to a repetition rate of ~37 GHz. An isolated pulse fitted with Lorentzian and $sech^2$ profile is shown in Figure 4.29 (b). The FWHM of the pulse is 6.50 ps, which deconvolves to 3.25 ps pulse duration assuming a Lorentzian function, which better fits the pulse profile. However, the noisy autocorrelation trace and the high TBP (~3.6) indicate unstable mode-locking and the presence of a very strong chirp in the pulse in the HR-coated device.

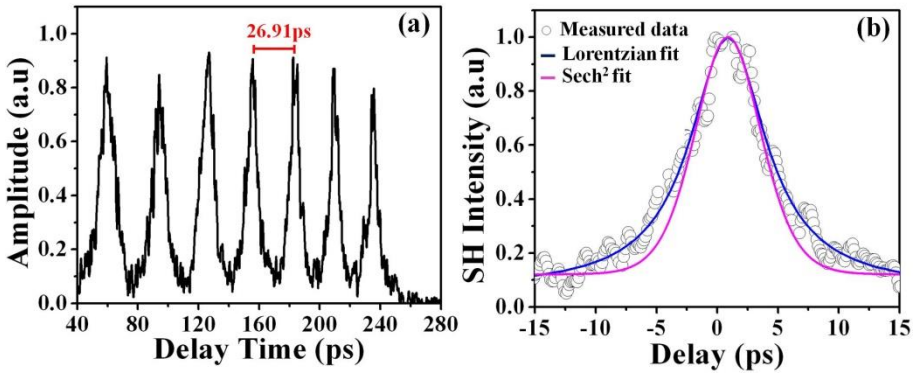

Figure 4.29: (a) The pulse train and (b) the Lorentzian and sech^2 fit of a single pulse at 90 mA gain current and -4 V SA reverse voltage.

HR/AR coating results: Figure 4.30 shows the *L-I* curve of the HR/AR coated device for different reverse biasing voltages. At 0 V, the threshold current is 54 mA, which is a marginal increase compared to the threshold of the uncoated device. The quantum efficiency of HR/AR coated device is increased by a factor of ~2, compared to uncoated device.

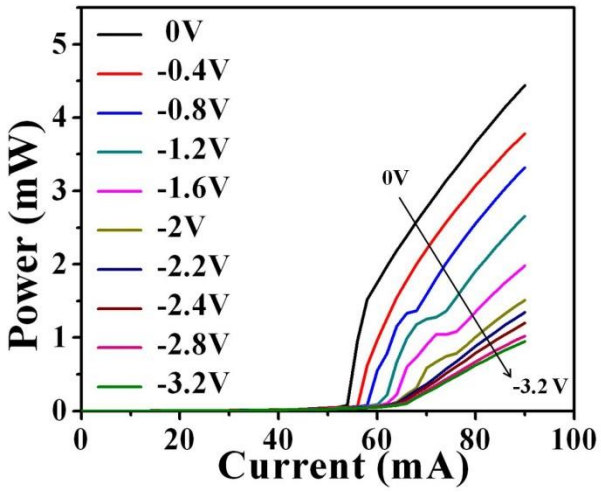

Figure 4.30: The *L-I* curves of a HR/AR coated device taken from the AR coated facet, for different reverse biased voltages (the SA length is 5.2 % of the total cavity length).

The autocorrelation trace for the HR/AR coated device in the region of maximum extinction ratio in the pulse autocorrelation is shown in Figure 4.31 (a).

The spacing between two consecutive pulses in the pulse train corresponds to a repetition rate of ~36.3 GHz. A single pulse fitted with a Lorentzian and sech^2 curve is shown in Figure 4.31 (b). The Lorentzian function exhibits a better fitting and deconvolves to a 1.28 ps pulse duration.

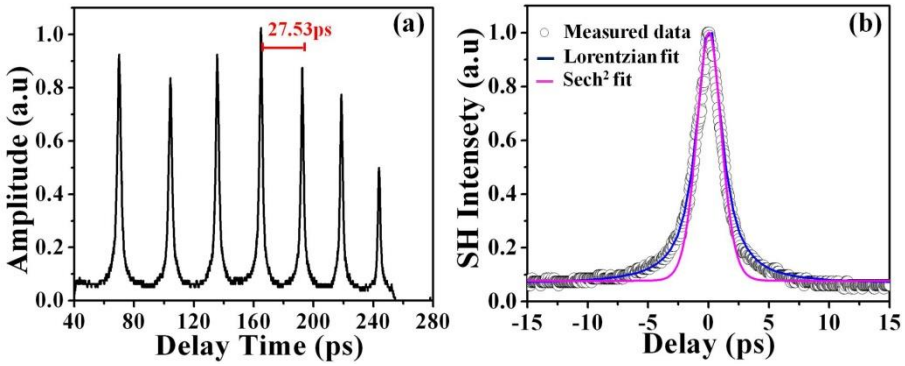

Figure 4.31: (a) The pulse train and (b) the single Lorentzian and sech^2 fit pulse for a HR/AR coated device at 88 mA gain current and -2.4 V SA reverse voltage.

Comparison of uncoated and HR/AR coated device: Figure 4.32 shows the mode-locking maps of a device before and after HR/AR coating. For comparison purposes, the average values of the deconvolved (sech^2) pulse widths are shown as a function of the gain section current and SA reverse voltage.

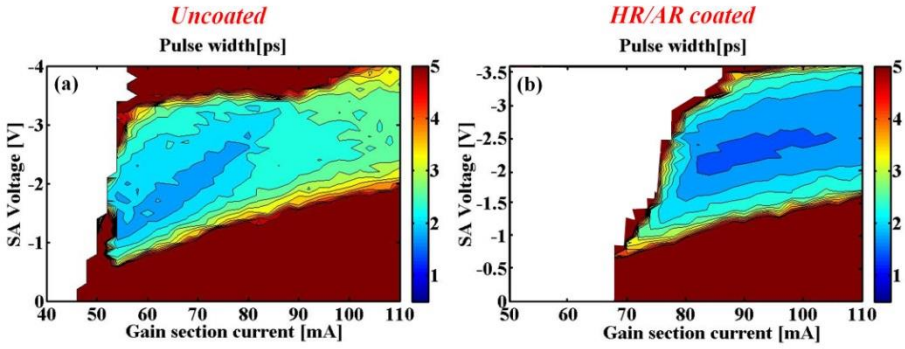

Figure 4.32: Mode-locking map for an (a) uncoated and (b) HR/AR coated device.

The region over which mode locking occurs is larger on the uncoated device, however, the mode-locking region for the HR/AR coated device shifts to

higher values of the gain current. The extension of the mode-locking region for the HR/AR device could not be completely identified as the high resistance of the *p*-type contacts prevented measurements for current values higher than 110 mA. The shift of the mode-locking region to higher currents should also be accompanied by a reduction of the phase noise as predicted by the theoretical work reported in [44]. However, an important advantage of moving to a HR/AR configuration is that the average power under optimum mode locking strongly increases due to the combination of a higher quantum efficiency (i.e. it nearly doubles from the AR-coated side) and mode locking occurring at higher currents. Because the pulse width does not change much the pulse peak power increases substantially.

Figure 4.33 shows the comparison of the pulse peak power for an uncoated and a HR/AR coated device. The HR/AR coated device has a maximum peak power of 61 mW for I_g = 108 mA, which corresponds to an increase of ~27 mW (i.e by a factor of 1.8) compared to the maximum peak power in an uncoated device.

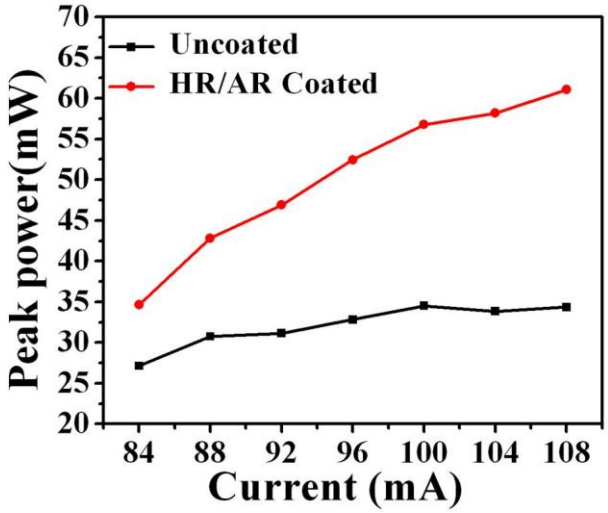

Figure 4.33: Comparison of peak powers of uncoated and HR/AR coated devices at SA reverse voltage of -2.4 V.

4.7 Dual wavelength mode-locked lasers

The unique gain and spectral behaviour of quantum dot lasers considerably differ from other semiconductor lasers such as bulk and quantum-well. The large bandwidth of the QD ensemble can produce pulses with temporal widths in the range of hundreds of femtoseconds (fs) [24, 45]. The optical spectrum of QD lasers has also been the focus of interest for a number of groups due to the unusual splitting into two lobes, which might lead to the emission of two distinct wavelengths [23-27] and to the generation of stable dual-wavelength mode-locking. The most common cause of this phenomenon is the simultaneous lasing from the ground state (GS) and excited state (ES) under CW operation [46]. Dual wavelength emission via the GS and ES is well understood and has been ascribed to the saturation of the GS with the increase in the injection current which in turns initiates transitions from the ES [47]. Besides, dual wavelength emission from GS and ES transitions, dual wavelength behaviour has also been reported due to splitting of single energy states i.e ground state splitting (GSS) [26, 27, 48]. The GSS under CW operation has been explained either as a consequence of the spectral hole burning (SHB) [26] or as a result of Rabi oscillations [23]. Although the exact physical reason of this splitting phenomenon is still being investigated, its impact on the mode-locking is of great interest because of the rich variety of dynamics and for the potential to generate dual wavelength mode-locking for THz generation [27].

4.7.1 Device design and results

The device used to evaluate the dual-wavelength performance is identical to that presented in section 4.4. The cavity is a two section device comprising of a gain section and a SA section with a length equivalent to ~5.2% of the total cavity length (~ 1165 μm). The device characterisation was carried out at a heat sink temperature of 20°C and under CW current injection mode with the same setup previously described. Mode-locking over a very wide range of biasing conditions

with the appearance of two spectral lobes was observed. The peak wavelength maps as a function of the gain section current are shown in Figure 4.34 (a) and (b), for reverse voltages of -2.8 and -3.1 V. At approximately twice the current threshold (at 0 V), the spectrum under mode-locking exhibits a transition from single lobe to a dual-lobe shape as the current biasing is increased. More precisely, the single spectral lobe at 1555 nm observed at low gain currents splits into one large lobe that shifts to the red (~1565 nm) and one narrower lobe that shifts to the blue (~1545 nm).

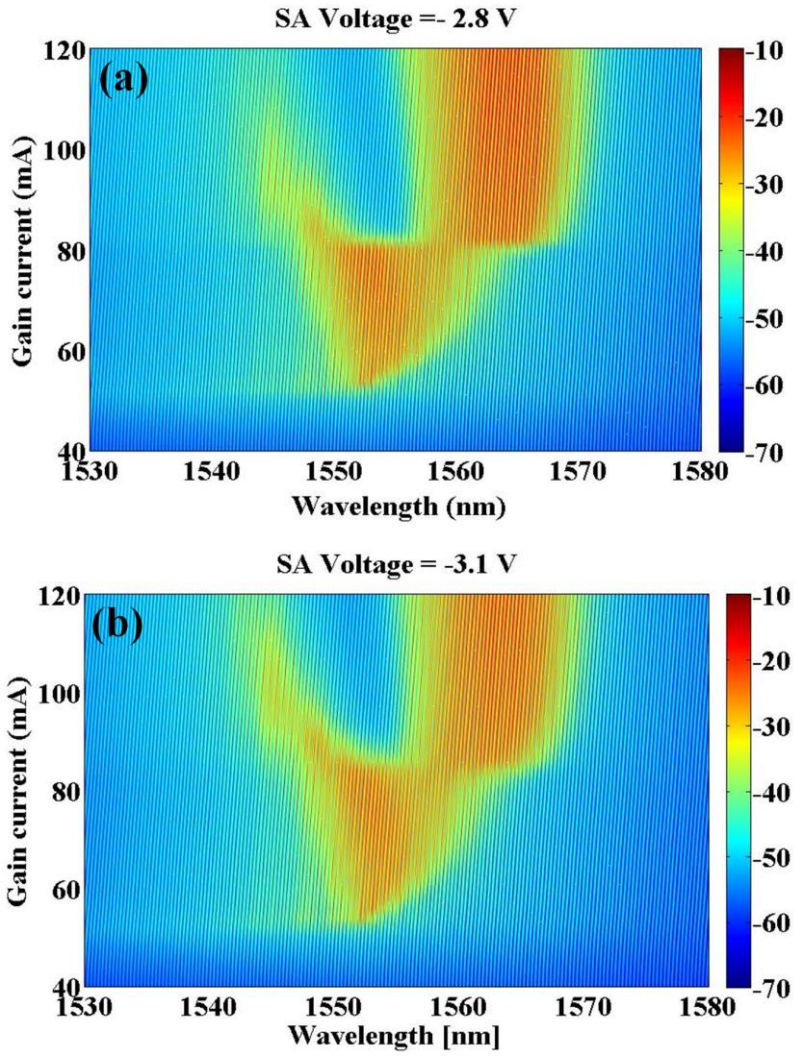

Figure 4.34: Peak wavelength map measured as a function of the gain current for SA reverse bias voltages of (a) -2.8 V and (b) -3.1 V.

The spectral splitting occurs at higher gain currents if the reverse voltage is increased. The shift in the peak wavelengths as a function of the gain current is shown in Figure 4.35 (a) and (b) for a reverse voltage of -2.8 and -3.1 V, respectively.

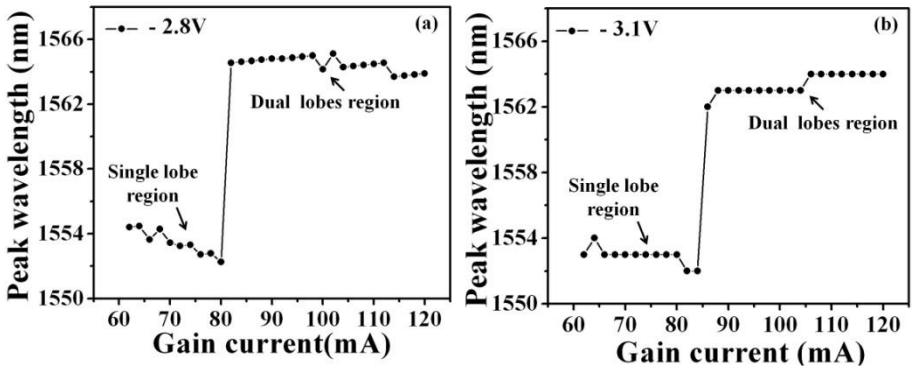

Figure 4.35: Peak wavelength as a function of the gain current for SA reverse bias voltages of (a) -2.8 V and (b) -3.1 V.

The peak frequency maps as a function of the gain section current are shown in Figure 4.36 (a) and (b), for reverse voltages of -2.8 and -3.1 V, respectively. These maps correspond to peak wavelength maps shown in Figure 4.34. At low gain current only single RF peak appears, while, for the short current range where the optical spectrum starts to exhibit a transition from single lobe to a dual-lobe shape, the corresponding RF spectrum exhibits two peaks. As the gain current is further increased, the separation of the two optical spectrum lobes increases and the RF shows a single RF peak.

The dual-wavelength behaviour observed is most probably originated by GSS. In fact, in the presence of GSS, the lobes separate gradually as the injection current is increased and their separation is in the range of 5-20 nm. In the case of GS and ES transitions, the splitting is not gradual as two separate spectral lobes suddenly appear at high injection current [27], with a separation that can be as high as 70 nm [49].

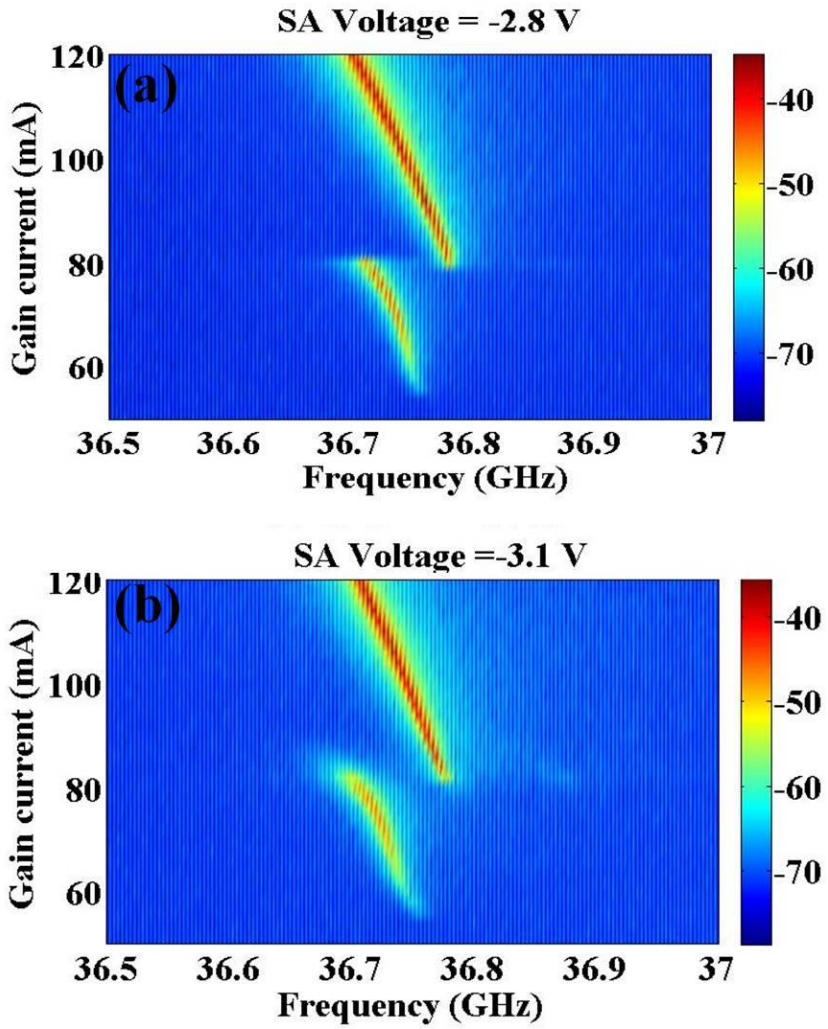

Figure 4.36**:** Peak frequency map measured as a function of the gain current for SA reverse bias voltages of (a) -2.8 V and (b) -3.1 V.

Therefore, the observation of the spectral behaviour as a function of the injected current leads to the conclusion that the two lobes are generated by transitions from the same state rather than by emission from GS and ES. An explanation for the optical spectrum peak splitting has been proposed on the basis of the Rabi oscillation model [23]. Rabi oscillation occurs due to interaction of electromagnetic field with two-level quantum mechanical systems, resulting in a periodic energy exchange between electromagnetic field and the quantum mechanical system [50]. If the coupling between the two-level quantum

mechanical system such as QDs and the electromagnetic field in the cavity is strong enough that it overcomes the cavity decay rate then this coupled system results in two eigenenergies i.e splitting of the states (known as vacuum Rabi splitting) [51]. Whilst the Rabi splitting of a single QD strongly coupled to optical cavities has been widely documented, fewer studies have been performed on ensemble of QDs where a non-negligible degree of complexity is added by the non-uniformity in the dot size. The experiment in [52] suggests that an ensemble of QDs may exhibit Rabi splitting. If the splitting is originated by the Rabi oscillation model, then the spectral separation of the two sub bands should be proportional to the square root of the power density of the electromagnetic field [53].

In order to investigate this prediction the spectral separation of the two lobes was plotted as a function of the square root of the emitted power as shown in Figure 4.37. The result shows that the spectral separation of the two lobes is approximately linear up to a spectral separation of ~15 nm, as expected by the Rabi model, but becomes sub-linear for high gain currents

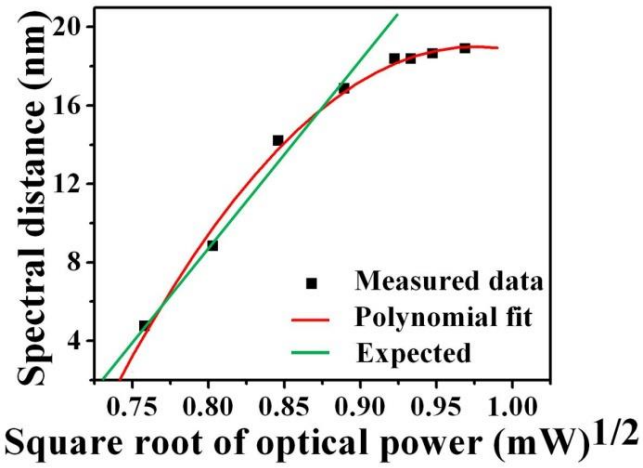

Figure 4.37: Spectral distance between the lobes versus the square root of the optical power (The red curve shows the measured data, while the green line is the square root dependence).

Similar experimental results have been demonstrated in [48, 54]. In these papers, however, the authors cast doubts on the Rabi oscillation being the cause of the optical spectrum splitting. They suggest state filling effects [54] or SHB [26] as a possible cause for the spectral splitting. Most likely, the cause for the spectral splitting is a combination of the effects described above, where saturation effects become dominant for high currents.

Because of the very unusual spectral evolution of these lasers, it is interesting to analyse in more detail the device behaviour under mode-locking operation. The analysis was focused on three spectral region of interest (A, B and C) with different and distinct lasing properties. Region 'A' corresponds to low level of injection current, where the optical spectrum has a single lobe and shows red shift with increasing injection current. This region exhibits a single and narrow RF peak denoting the presence of a stable pulse train travelling in the cavity. The optical and RF spectra corresponding to region 'A' for 66 mA of gain current are shown in Figure 4.38 (a) and (b), respectively. Region 'B' corresponds to a medium level of injection current where lobe splitting starts to occur and the optical spectrum shows two distinct lobes separated approximately by 5 nm. This dual spectral lobe is associated with dual peaks in the RF spectrum that indicate the presence of two separate pulse trains travelling in the cavity with repetition rates separated by ~100 MHz. The optical and RF spectra corresponding to region 'B' for 82 mA of gain current are shown in Figure 4.38 (c) and (d), respectively. Region 'C' corresponds to a high level of injection current, where the separation of the two optical spectrum lobes increases and the RF shows a single RF peak. The spectrum and RF spectra corresponding to region 'C' for 90 mA of gain current are shown in Figure 4.38 (e) and (f), respectively

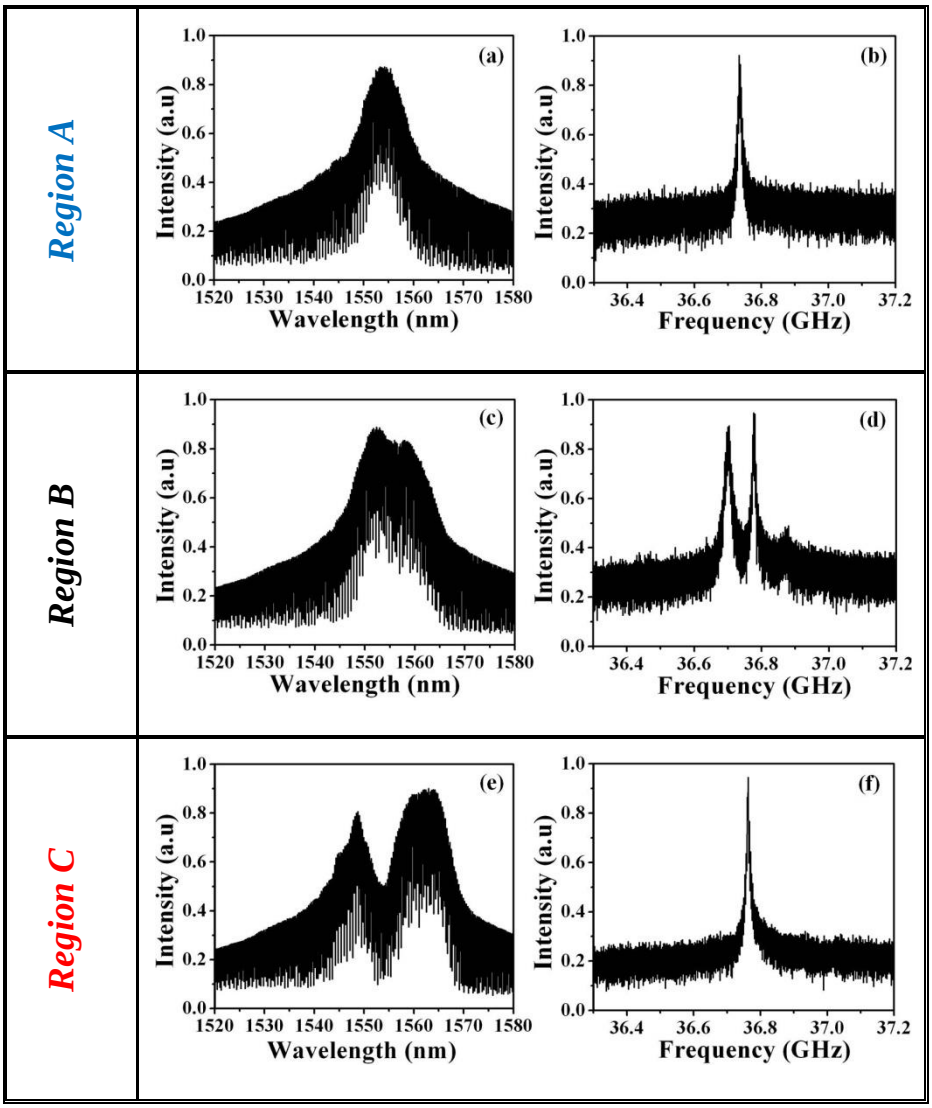

Figure 4.38: Measured optical and RF spectra: (a) optical and (b) RF spectrum for low level injection current (region A). (c) optical and (d) RF spectrum for mid level injection current (region B). (e) optical and (f) RF spectrum for high level injection current (region C).

4.7.2 Sonogram measurements

As expected, the autocorrelation measurements in region B, where two trains of pulses are simultaneously present, did not provide any meaningful outcomes Therefore it was decided to analyse the device behaviour with the sonogram technique, which is a more sophisticated autocorrelation technique that

provides a spectrally resolved pulse characterisation and allows to retrieve the phase profile of the pulses. The sonogram is a representation of a pulse in the frequency-time space and measures the group delay of each frequency component of the pulse (i.e. the time of arrival of a series of spectral slices) [55].

The sonogram setup for the optical pulse measurements was developed by the author's colleague Dr. Piotr Michal Stolarz [56]. This setup consists of a collinear Michelson interferometer, with an acousto-optic band pass filter in one arm for frequency slicing and a variable delay stage placed in the second arm (Figure 4.39).

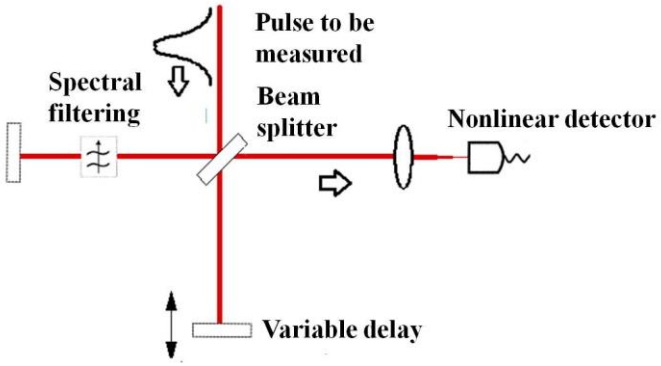

Figure 4.39: Schematic diagram of the sonogram system in which time delayed pulses are cross-correlated with a spectrally filtered pulse in a non -linear detector.

Figure 4.40 (a, b and c) show the sonogram traces obtained for the three mode-locking regions previously discussed i.e low (60 mA), mid (82.5 mA) and high (90 mA).

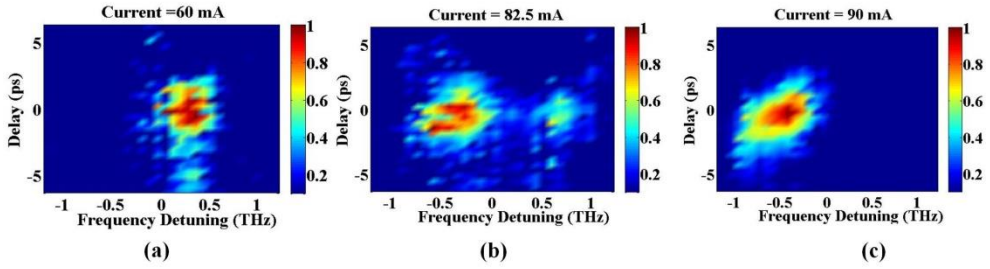

Figure 4.40: Sonogram traces of the pulses emitted at (a) 60 mA (b) 82.5 mA and (c) 90 mA, respectively.

Figure 4.41 shows the group delay of the pulses measured in all the three mode-locking regions. For low injection current, the group delay shows an increasing trend with wavelength, indicating a red chirp pulse, as shown in Figure 4.41 (a). Similarly, in the case where two pulses propagate in the cavity, the sonogram shows that both pulses are red chirped (Figure 4.41 (b)), although the chirp of the pulse generated by the short wavelength lobe is strongly reduced.

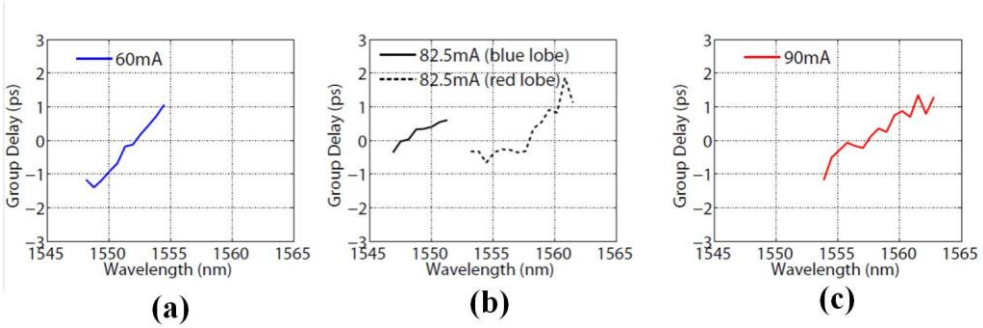

Figure 4.41: Sonogram traces of the pulse group delay corresponding to (a) single lobe emission for 60 mA of injection current (b) dual lobe emission for 82.5 mA of injection current and (c) dual lobe emission with 90 mA injection current.

Finally, the measurement corresponding to the high injection current region shows that the short wavelength lobe in the optical spectrum does not appear in the pulse sonogram, confirming that only the red lobe of the spectrum is contributing to the mode-locked pulse. The pulse shows a red chirp similar to that of the dual pulse operation (Figure 4.41 (c)). The sonogram measurements confirmed the presence of two pulse trains under some biasing conditions and that only the modes of the red-shifted lobe contribute to mode locking at high injection currents.

In reference [27] it was claimed that in QD lasers with dual wavelength spectrum both mode groups contribute to the mode-locking. Differently from this observation, the sonogram measurements indicate that only one lobe is locked at high injection currents. For some biasing conditions, both mode groups contribute to mode-locking but do not lock together, i.e. two distinct pulse trains are emitted.

4.8 Conclusions

This first part of this chapter presented the design of the InAs/InP QD epitaxial material used for the fabrication of the devices, together with the results on ridge waveguide lasers. These measurements confirmed the good performance of the epitaxial material that exhibited a threshold current density (per QD layer) on ridge waveguide FP lasers as low as 160 A/cm^2. This figure is comparable to the best reported values for QD lasers emitting at 1550 nm. The second part of the chapter discussed the mode locking performance of standard dual-section FP cavities. It was found that mode-locking can only be obtained for SA lengths ranging from 5.2%-7.2% of the total cavity length. The mode-locking performance were further improved by depositing a HR and AR coating on the two cleaved facets in order to shift the mode-locking operation to higher injection current and increase the quantum efficiency from the AR-coated facet. This simple technological step gave an increase of more than ~50 % on the peak power of the emitted pulses for higher gain current values. Finally, the presence of two distinct lobes in the optical spectrum of the device for high injection currents was investigated in terms of its mode locking performance. Under a particular range of biasing conditions, the sonogram measurements confirmed the presence of two pulse trains, each being generated by one of the two spectral lobes. At high injection currents, it was shown that the lower wavelength lobe does not contribute any longer to mode locking and only one pulse train is observed.

4.9 References

1. *Poole, P.J., et al., Growth of InAs/InP-based quantum dots for 1.55 um laser applications. Journal of Crystal Growth, 2009. 311(6): p. 1482-1486.*

2. *Poole, P.J., et al., Using As/P exchange processes to modify InAs/InP quantum dots. Journal of Crystal Growth, 2003. 257(1-2): p. 89-96.*

3. *Lu, Z.G., et al., An L-band monolithic InAs/InP quantum dot mode-locked laser with femtosecond pulses. Opt. Express, 2009. 17(16): p. 13609-13614.*

4. *Fafard, S., et al., InAs self-assembled quantum dots on InP by molecular beam epitaxy. Applied Physics Letters, 1996. 68(7): p. 991-993.*

5. *Poole, P.J., et al., Growth of InAs/InP-based quantum dots for 1.55um laser applications. Journal of Crystal Growth, 2009. 311(6): p. 1482-1486.*

6. *Richard NO¨ TZEL, et al., Self Assembled InAs/InP Quantum Dots for Telecom Applications in the 1.55um Wavelength Range: Wavelength Tuning, Stacking, Polarization Control, and Lasing. Japanese Journal of Applied Physics, 2006. 45(8B): p. 6544–6549.*

7. *Ustinov, V., et al., Arrays of strained InAs quantum dots in an (In Ga)As matrix, grown on InP substrates by molecular-beam epitaxy. Semiconductors, 1997. 31(10): p. 1080-1083.*

8. *Ustinov, V.M., et al., Effect of matrix on InAs self-organized quantum dots on InP substrate. Applied Physics Letters, 1998. 72(3): p. 362-364.*

9. *Taskinen, M., et al., Self-organized InAs islands on (100) InP by metalorganic vapor-phase epitaxy. Surface Science, 1997. 376(1-3): p. 60-68.*

10. *Krupanidhi, S.B., III–VCompoundSemiconductor QuantumDots for Nanoeletronics (Review). Journal of the Indian Institute of Science, 2007. 87:1: p. 1-14.*

11. *Ban, K.-Y., et al., Use of a GaAsSb buffer layer for the formation of small, uniform, and dense InAs quantum dots. Applied Physics Letters, 2010. 96(18): p. 183101-183101-3.*

12. *J. Wilson, J.F.B.H., Optoelectronics : An introduction. 1989, New York ; London : Prentice Hall, 1989.*

13. *Arahira, S., Y. Matsui, and Y. Ogawa, Mode-locking at very high repetition rates more than terahertz in passively mode-locked distributed-Bragg-reflector laser diodes. Quantum Electronics, IEEE Journal of, 1996. 32(7): p. 1211-1224.*

14. *Coldren, L.A., S.W. Corzine, and M.L. Mashanovitch, Diode Lasers and Photonic Integrated Circuits. 1995: John Wiley and Sons.*

15. *Han, J.-H. and S.-W. Park, Effect of temperature and injection current on characteristics of TO-CAN packaged Fabryâ€“Perot laser diode. Current Applied Physics, 2007. 7(1): p. 6-9.*

16. *Fan, H.-S., et al., Opposite temperature effects of quantum-dot laser under dual-wavelength operation. Applied Physics Letters, 2007. 90(18): p. 181113-3.*

17. *Svelto, O. and D.C. Hanna, Principles of Lasers. 1998: Plenum Press.*

18. *Bhattacharya, P., Semiconductor Optoelectronic Devices (2nd ed.). 1996: Prentice Hall.*

19. *Lelarge, F., et al., Room temperature continuous-wave operation of buried ridge stripe lasers using InAs-InP (100) quantum dots as active core. Photonics Technology Letters, IEEE, 2005. 17(7): p. 1369-1371.*

20. *Moreau, G., et al., Effect of layer stacking and p-type doping on the performance of InAs/InP quantum-dash-in-a-well lasers emitting at 1.55 Î¼m. Applied Physics Letters, 2006. 89: p. 241123.*

21. *Li, S.G., et al., Room temperature continuous-wave operation of InAs/ InP (100) quantum dot lasers grown by gas-source molecular-beam epitaxy. Applied Physics Letters, 2008. 93: p. 111109.*

22. *Akahane, K., N. Yamamoto, and T. Kawanishi, High Characteristic Temperature of Highly Stacked Quantum-Dot Laser for 1.55-um band. Photonics Technology Letters, IEEE, 2010. 22(2): p. 103-105.*

23. *Liu, J., et al., Dual-wavelength 92.5 GHz self-mode-locked InP-based quantum dot laser. Opt. Lett., 2008. 33(15): p. 1702-1704.*

24. *Thompson, M.G., R.V. Penty, and I.H. White. Regimes of mode-locking in tapered quantum dot laser diodes. in Semiconductor Laser Conference, 2008. ISLC 2008. IEEE 21st International. 2008.*

25. *Cataluna, M.A., et al., Dual-wavelength mode-locked quantum-dot laser, via ground and excited state transitions: experimental and theoretical investigation. Opt. Express, 2010. 18(12): p. 12832-12838.*

26. *Mesaritakis, C., et al., Pulse width narrowing due to dual ground state emission in quantum dot passively mode locked lasers. Applied Physics Letters, 2010. 96(21): p. 211110-3.*

27. *Tahvili, M.S., et al., Dual-wavelength passive and hybrid mode-locking of 3, 4.5 and 10 GHz InAs/InP(100) quantum dot lasers. Opt. Express, 2012. 20(7): p. 8117-8135.*

28. *Kresten Yvind, Ph.D. Thesis, "Semiconductor mode locked lasers for optical communication systems" Technical University of Denmark, 2003: Denmark.*

29. *Paez, F.C., Ph.D. Thesis, "Comaprative study of passive modelocking configurations in semiconductor lasers" University of Glasgow, 1997:Glasgow, Uk.*

30. *Sala, K., G. Kenney-Wallace, and G. Hall, CW autocorrelation measurements of picosecond laser pulses. Quantum Electronics, IEEE Journal of, 1980. 16(9): p. 990-996.*

31. *Tandoi, G., Monolithic high power mode locked GaAs/AlGaAs quantum well lasers, in in Department of Electronics and Electrical Engineering. 2011, University of Glasgow.*

32. *Javaloyes, J. and S. Balle, Mode-locking in semiconductor Fabry-Perot lasers. Quantum Electronics, IEEE Journal of. 46(7): p. 1023-1030.*

33. *K A Williams, M.G. Thompson, and a.I.H. White, Long-wavelength monolithic mode-locked diode lasers. New Journal of Physics 2004. 6(179): p. 1-30.*

34. *Thompson, M.G., et al. Absorber length optimisation for sub-picosecond pulse generation and ultra-low jitter performance in passively mode-locked 1.3 /spl mu/m quantum-dot laser diodes. in Optical Fiber Communication Conference, 2006 and the 2006 National Fiber Optic Engineers Conference. OFC 2006. 2006.*

35. *Lester, L.F., et al. Reconfigurable, multi-section quantum dot mode-locked lasers. in Lasers and Electro-Optics (CLEO) and Quantum Electronics and Laser Science Conference (QELS), 2010 Conference on. 2010: IEEE.*

36. *Weisbuch, C., The Development of Concepts in Light-Emitting Devices. Brazilian Journal of Physics, 1996. vol. 26(Issue 1): p. p.21-42.*

37. *Kheraj, V.A., et al., Optimization of facet coating for highly strained InGaAs quantum well lasers operating at 1200 nm. Optics & Laser Technology, 2007. 39(7): p. 1395-1399.*

38. *Jang, S.J., et al., Performance improvement by metal-dielectric HR coating in laterally coupled DFB laser with metal surface gratings. Applied Physics B, 2010. 100(3): p. 553-558.*

39. *Morton, D.E., I. Stevenson, and M. Garcia, Design and development of optical coatings on laser bar facets. 2004: p. 413-423.*

40. *Minch, J., et al., Theory and experiment of $In_{1-x}Ga_xAs_yP_{1-y}$ and $In_{1-x-y}Ga_xAl_yAs$ long-wavelength strained quantum-well lasers. Quantum Electronics, IEEE Journal of, 1999. 35(5): p. 771-782.*

41. *Lee, J., et al., Broadband Double-Layer Antireflection Coatings for Semiconductor Laser Amplifiers. Japanese Journal of Applied Physics, 1997. 36(Part 2, No. 1A/B): p. L52-L54*

42. *Connelly, M.J., Semiconductor Optical Amplifiers. 2002: Springer.*

43. *[Available online]: http://www.photonics.byu.edu/antireflection.phtml : 2012.*

44. *Javaloyes, J. and S. Balle, Anticolliding design for monolithic passively mode-locked semiconductor lasers. Optics letters, 2011. 36(22): p. 4407-4409.*

45. *Lu, Z.G., et al. A passive mode-locked InAs/InP quantum dot laser with pulse duration of less than 300 fs. . in Proc. SPIE 7224, Quantum Dots, Particles, and Nanoclusters VI, 722413, 2009*

46. *Naderi, N.A., et al., Two-color multi-section quantum dot distributed feedback laser. Opt. Express, 2010. 18(26): p. 27028-27035.*

47. *Markus, A., et al., Simultaneous two-state lasing in quantum-dot lasers. Applied Physics Letters, 2003. 82(12): p. 1818-1820.*

48. *Mesaritakis, C., et al., Dual ground-state pulse generation from a passively mode-locked InAs/InGaAs quantum dot laser. Applied Physics Letters, 2011. 99(14): p. 141109-3.*

49. *Cataluna, M.A., et al., Stable mode locking via ground- or excited-state transitions in a two-section quantum-dot laser. Applied Physics Letters, 2006. 89(8): p. 081124-3.*

50. *Paschotta, R., Encyclopedia of Laser Physics and Technology: Rabi oscillations. [Available online]:http://www.rp-photonics.com: 2013.*

51. Khitrova, G., et al., Vacuum Rabi splitting in semiconductors. Nat Phys, 2006. 2(2): p. 81-90.

52. Haroche, S., et al., Radiative Properties of Rydberg States in Resonant Cavities, in Advances in Atomic and Molecular Physics. 1985, Academic Press. p. 347-411.

53. Kamada, H., et al., Exciton Rabi Oscillation in a Single Quantum Dot. Physical Review Letters, 2001. 87(24): p. 246401.

54. Li, S.G., et al., Two-color quantum dot laser with tunable wavelength gap. Applied Physics Letters, 2009. 95(25): p. 251111-3.

55. Reid, D.T., Algorithm for complete and rapid retrieval of ultrashort pulse amplitude and phase from a sonogram. Quantum Electronics, IEEE Journal of, 1999. 35(11): p. 1584-1589.

56. Piotr Micha l Stolarz, Ph.D. Thesis, "Development of a Phase Sensitive Pulse Measurement Technique for Semiconductor Mode Locked Lasers" University of GLasgow,UK 2012:UK.

Chapter 5

Harmonically Mode-locked Semiconductor Lasers

5.1 Introduction

This chapter will present the results obtained from the harmonic mode-locked lasers designed and fabricated in this project. Harmonic mode-locking was implemented using colliding pulse mode-locking (CPM), asymmetric colliding pulse mode-locking (ACMP) and double interval mode-locking (DIM) techniques. The devices were characterised and compared by measuring their optical power, optical spectra and second harmonic generation (SHG) autocorrelation.

5.2 Colliding pulse mode-locked (CPM) laser design

The CPM operation was implemented in QD Fabry-Perot (FP) cavity, using the device design illustrated in Figure 5.1. The device consists of a 1200 μm long, 2.5 μm wide ridge waveguide, in which the *p*-contact of the device is divided into long and short sections that are electrically isolated by a 20 μm-wide gap. The long sections are used as gain while short sections can be used as either absorber or gain sections. This multi-section geometry provides a high degree of

flexibility as it allows to assess the device performance for different configurations of the SA position within the cavity and for different repetition rates. For CPM only a single SA section positioned in the middle of the cavity is used, hence dividing the cavity in two equal gain sections. The shorter SA section in the middle is reversed biased, whereas the rest of the sections are forward biased and connected in parallel in order to achieve the same current density through the various sections. A FP mode-locked laser with 1220 μm long cavity and a SA placed at one of the cavity facets exhibits a repetition frequency close to 35 GHz as shown by the RF traces presented in chapter 4, section 4.4. Therefore, the CPM laser devices are expected to operate at a repetition frequency of around 71 GHz.

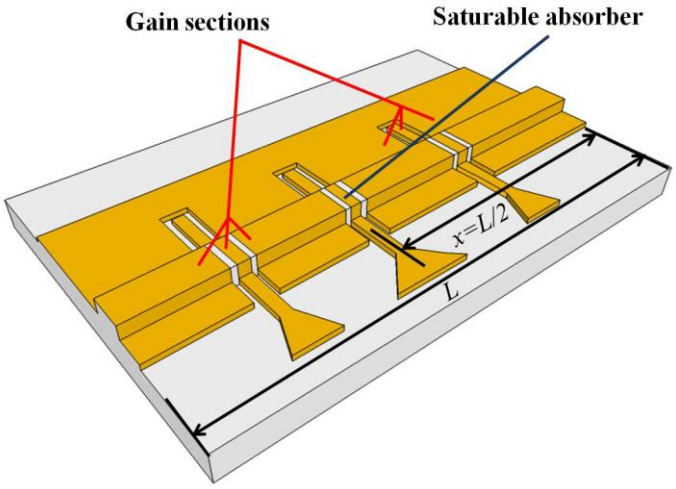

Figure 5.1: **S**chematic of a CPM laser with two gain and one SA section. The SA section is positioned at $x=L/2$ of the cavity length L.

Higher repetition rates can be achieved by placing an absorber at spatial harmonics of the cavity length, which leads to repetition rates corresponding to these harmonics [1]. To generate the M^{th} harmonic of the fundamental repetition frequency, the absorber should be positioned at:

$$\boldsymbol{x = \frac{L}{M}}$$

Equation 5.1

where L is the full cavity length, and x is the distance from one end facet to the centre of the absorber section. As discussed in chapter 2, the repetition frequency of the pulse train emitted by the mode-locked laser is given by [2, 3]:

$$f = \frac{Mc}{2n_g L}$$

Equation 5.2

Equation 5.2 can be also expressed as a function of the absorber position *'x'*:

$$f = \frac{c}{2n_g x}$$

Equation 5.3

In the CPM configuration, the mode-locking is achieved at the second harmonic of the fundamental repetition frequency i.e. $M=2$ [3]. Under optimal bias conditions, two counter propagating pulses inside the laser cavity are formed [4]; which simultaneously saturate the central SA. The coexistence of two counter-propagating pulses inside the cavity results in a two-fold increase of the fundamental repetition frequency.

5.2.1 Characterization of CPM lasers

The CPM lasers were characterised as a function of the reverse biasing on the central SA section and forward biasing on the sections forming the two gain cavities. The measurement setups and the thermal stabilization of the copper heat sink were the same as those discussed in chapter 4. The RF spectra of these devices could not be measured due to bandwidth limitation of the available RF spectrum analyser; however, the repetition frequency of these devices was evaluated through the modal spacing of the optical spectrum and temporal pulse train measured with the autocorrelator. The results obtained from these devices are given in the subsequent sections.

- ***Light-current characteristics:***

The output power of the colliding pulse mode-locked laser devices was measured for gain current up to 120 mA and SA reverse voltages up to -4.0 V. As expected, the *L-I* curves exhibit an increase in the threshold current and a reduction in the external quantum efficiency for increasing reverse biasing of the SA section as shown in Figure 5.2 (a).

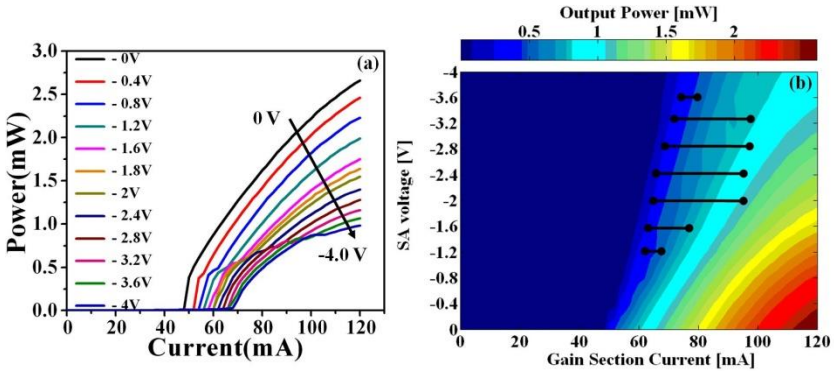

Figure 5.2: (a) *L-I* curves for different reverse voltages (b) Output power map as a function of gain current and reverse voltage. Bold black lines correspond to mode-locked pulses having extinction ratio of at least 50 %.

Similarly to the devices presented in chapter 4, a step like behaviour appears in the *L-I* curves at the lasing threshold due to an increase in the saturated losses [5]. As current is increased from threshold, the step like behaviour is followed by a kink in the *L-I* curves. This kink is found to have a strong correspondence to the optical spectrum splitting and shifting of the peak wavelength, an attribute of QD mode-locked lasers already discussed in chapter 4, section 4.7. The output power map is illustrated in Figure 5.2 (b) for different biasing conditions of the device. The regions indicated by bold black lines in the map designate the set of biasing conditions corresponding to mode-locked pulses having extinction ratio of at least 50 %.

- ***Optical spectra and Autocorrelation measurements:***

The optical spectra of the CPM lasers were measured by using the experimental setup discussed in chapter 4, section 4.4, with a resolution bandwidth of 0.06 nm. The optical spectrum shown in Figure 5.3 (a) is measured under optimum mode-locking conditions at V_{SA}= -1.8 V and I_{gain}= 64 mA, and confirms that longitudinal modes are lasing at every second mode with a mode spacing of 71 GHz corresponding to the second harmonic of the cavity.

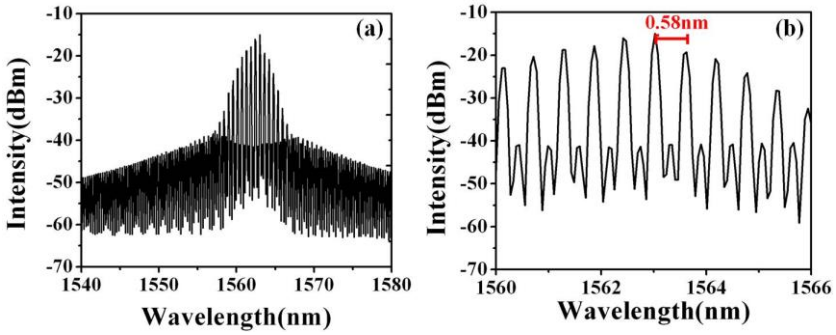

Figure 5.3: (a) Optical spectrum and (b) corresponding mode spacing at

V_{SA} = -1.8 V and I_g = 64mA.

The wavelength maps as a function of the gain current for various reverse bias voltages are illustrated in Figure 5.4. The map of Figure 5.4 (a) corresponds to a low reverse voltage for which poor mode-locking has been observed. Figure 5.4 (b) and (c) correspond to reverse voltages in the optimum mode-locking range, i.e -1.8 and -2 V, respectively. In these maps, the region between the black dotted lines corresponds to mode-locked pulses having extinction ratio of at least 50 % and for current values exceeding 100 mA, the suppression of every second mode is much weaker.

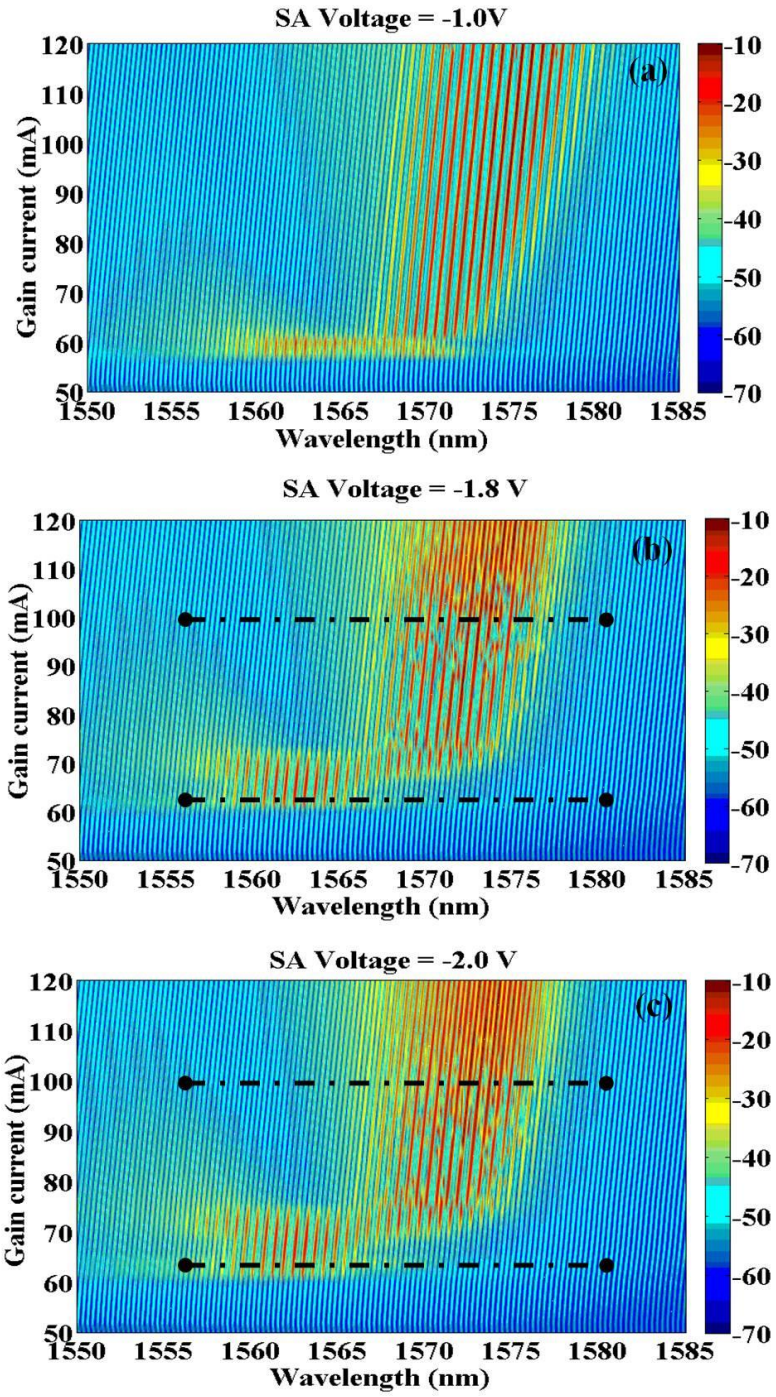

Figure 5.4 : Peak wavelength map as a function of gain current at SA reverse voltages fixed at (a) -1.0V (b) -1.8V (c) -2.0 V. Gain current range between the black dotted lines corresponds to mode-locked pulses having extinction ratio of at least 50 %.

It is also evident from the wavelength maps that an increase in the gain current, suddenly red-shifts the peak wavelength by approximately 10 nm. This red shift is preceded by a splitting of the optical spectrum splitting, which is similar to the phenomenon observed previously in QD mode-locked lasers and was already discussed in chapter 4, section 4.7 [6-8].

The evolution of the optical spectrum can be better appreciated on the optical spectra of Figure 5.5, in which the SA reverse voltage is kept fixed at -1.8 V. The optical spectrum splitting accompanied by broadening occurs in a narrow current injection range from 68 to 72 mA. The optical spectrum splitting starts at 68 mA, where a lobe starts to appear at longer wavelengths. At 70 mA both lower and higher wavelength lobes have almost equal intensity as shown in Figure 5.5 (a). For current injection values above 70 mA the intensity of the lower wavelength lobe decreases and it becomes almost completely suppressed at 76 mA while the higher wavelength lobe dominates, as shown in Figure 5.5 (b).

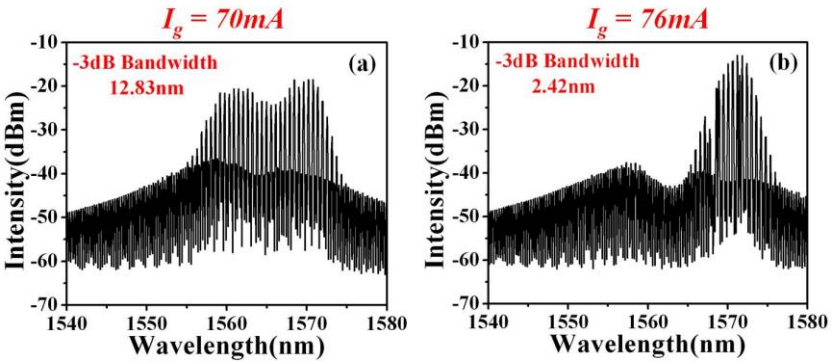

Figure 5.5: Optical spectrum for fixed V_{SA} = -1.8 V (a) in the process of splitting (b) after splitting.

The 3 dB bandwidth of the optical spectrum during the splitting process at 70 mA is nearly 5 times larger than the bandwidth of the longer wavelength lobe at 76 mA. The kink in the *L-I* curves and the significant suppression in the lower wavelength lobe along with the sudden shift in peak wavelength after splitting were not observed in the QD mode-locked lasers discussed in chapter 4. Therefore, in CPM devices the optical spectral evolution with injected current is

slightly different from what has been observed before. The optical spectrum splitting (accompanied with broadening and sudden shifting in peak wavelength) and the kink in the *L-I* curves occur over the same narrow current injection range. Both the presence of the kink in the *L-I* curves and sudden shift in peak wavelength, might be a consequence of spatial hole burning [9] owing to non uniform population inversion of QDs or inhomogeneous broadening (due to variation in QDs size and shape) and gain saturation [10]. The exact mechanisms at the origin of this phenomenon are, however, not completely clear and are most likely connected to those generating the dual wavelength behaviour observed by other groups [6-8] as well as in the lasers of chapter 4.

The autocorrelation traces were recorded using the same setup, as presented in chapter 4, section 4.4. The optical pulses with a slight pedestal were observed to appear just above the threshold current, at SA reverse voltages ranging from -0.8 V to -4 V. The maximum extinction ratio of the AC traces was observed close to threshold at SA reverse voltages ranging from -1.8 to -2.4 V. More than 60 % pulse modulation was observed for gain current values ranging from 62 mA to 72 mA when the SA reverse voltage was kept fixed at -1.8 V. The optical spectra and corresponding autocorrelation traces obtained from the device with a SA section reverse voltage of -1.8 V are shown in Figure 5.6. Close to threshold the optical spectrum is centred around 1563 nm and consists of a single lobe with every second mode very clearly suppressed as shown Figure 5.6 (I-a). The corresponding autocorrelation trace is shown in Figure 5.6 (II-a), where the extinction ratio of the pulses is more than 60 % (i.e 60 % pulse modulation). An increase in gain current splits and broadens the optical spectrum with a sudden shift in the peak wavelength, as discussed before. For a current value of 80 mA the peak wavelength is red shifted by as much as 9 nm. The spectral shift from the blue to red lobe is also accompanied by an increase in pulse pedestal, with a reduction of extinction ratio to around 50 %, as shown in Figure 5.6 (II-b).

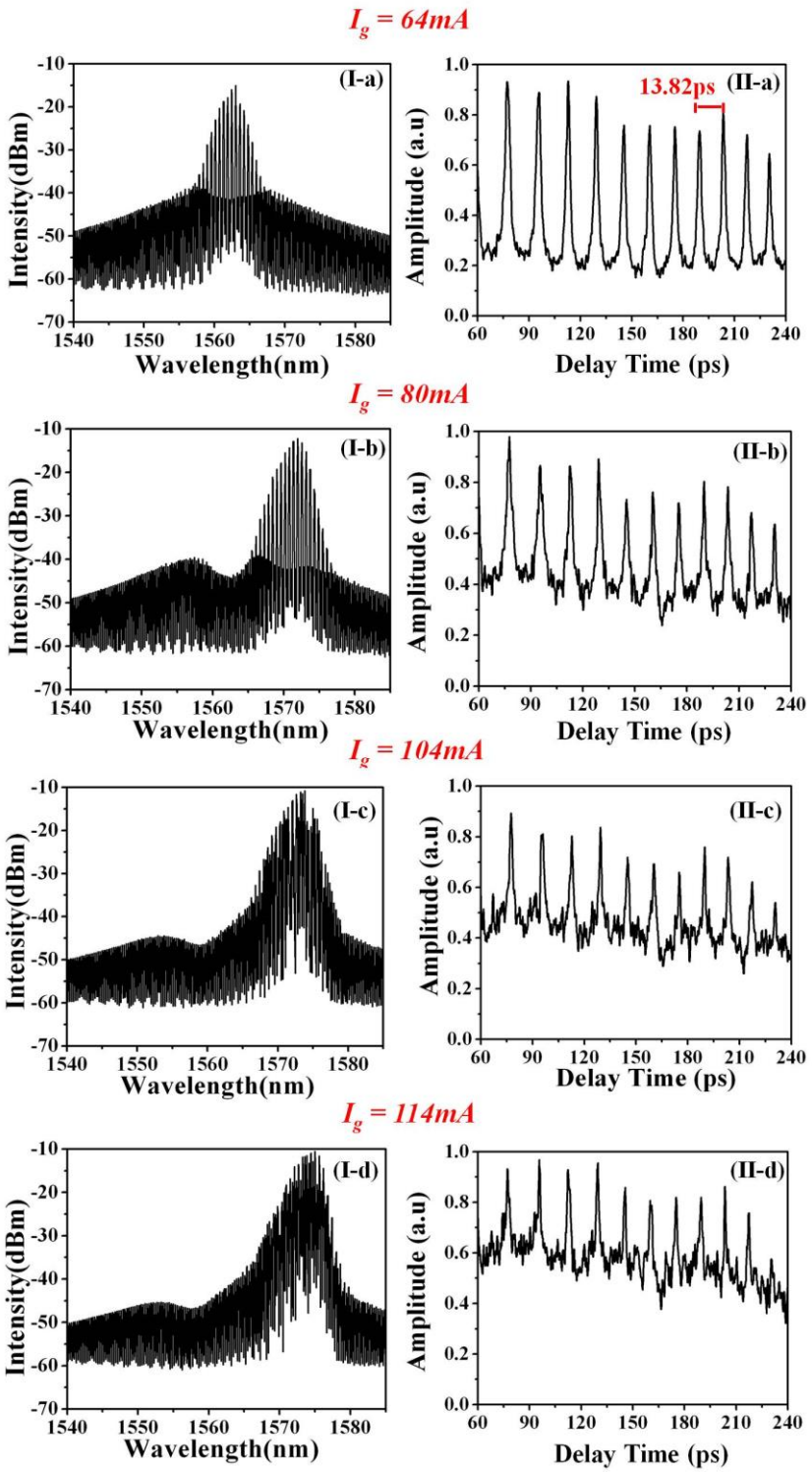

Figure 5.6 : For fixed V_{SA} = -1.8 V (I) optical spectra and (II) autocorrelation traces at I_g fixed at (a) 64 mA (b) 80 mA (c) 104 mA (d) 114 mA.

If the gain current is increased even further, the optical spectrum is further red shifted but at the same time the suppression of every second mode becomes much weaker as shown in Figure 5.6 (I-c and I-d). The pulse modulation of corresponding intensity autocorrelation traces reduces well below 50% (see Figure 5.6 (II-c and II-d).

The appearance of a pedestal in the pulse trains for high forward current biasing indicates that the pulse shaping mechanism is not fully accomplished thus leading to unstable mode-locking. Two main reasons for pulse pedestal in CPM laser were identified. Firstly, a non-optimal length for the various sections of the device, being originated by imperfect cleaving. The section lengths after device cleaving were carefully inspected under an optical microscope and deviations of 1 to 1.5 % from the designed dimensions were measured. Although these figures correspond to cleaving inaccuracies as small as 10 μm, they add a substantial phase mismatch to the pulses propagating inside the device sections. Secondly, a suitable balance is required for the detuning of the energy gaps between the gain and absorber section, as stable mode-locking is only achieved by the proper alignment of the gain peak and SA band edges [11]. The multi-contact mode-locked laser geometries presented here consist of a gain, gap (passive) and absorber section, where the total length of the gap section includes all the non-metallised portions of the cavity. In the multi-contact device used as a CPM laser 86.6 %, 10 % and 3.3 % of the total cavity length account for the gain (forward biased) , gap (unbiased) and absorber (reverse biased) sections. Optimal mode-locking was observed in the two section InAs/InP QD mode-locked laser devices discussed in chapter 4 for gain, gap and absorber section lengths in the range of 91.55-93.47 %, 1.22-1.28 % and 5.23- 7.21 %, respectively. A comparison between the two designs indicates that the passive section in the multi-section laser device is nearly 8 times larger than in the two section laser. This difference adds to the absorption which is likely to cause an imbalance between the gain and absorption required to sustain stable mode-locking operation. A similar reason might be at the origin of the substantial pedestal observed in multi contact QD

lasers for higher order harmonic mode-locking [12, 13]. Moreover, compared to the GaAs/AlGaAs based material system, InP-based materials exhibit higher threshold current densities and waveguide internal losses, thus causing higher absorption [13]. As a consequence, the absorber lengths in InP-based MLLs are usually very short (in the range of 3-6 %) [14-16] compared to GaAs based material system, where stable mode-locking has been demonstrated by using absorber lengths up to 26 % of the total cavity [17]. The very high internal losses in InP-based materials make the design of multi-section devices very critical as each un-biased gap can substantially add to the overall absorption losses of the cavity. In the multi contact cavity design the use of more than one SA simultaneously for multi colliding pulse (MCPM) operation, in order to achieve higher harmonics could not be demonstrated due to absorption losses being too high.

Optical pulses with a maximum in their modulation (around 60 % or above) are measured just above threshold for a very short gain current range. As the gain current is increased the gain peak is red- shifted compared to the SA band edge resulting in an increased pulse pedestal as shown in Figure 5.6 (II-c) and (II-d). The pulse FWHM of the autocorrelation trace for optimum mode locking (i.e V_{SA}= -1.8 V and I_g= 64 mA) is around 2.47 ps. The analysis of the experimental results showed that CPM was achieved at 71 GHz with a fairly large ±4% variation in the repetition frequency depending on the biasing conditions.

5.3 Asymmetric CPM (ACPM) laser design

The CPM geometry described above was extended to asymmetric CPM (ACPM) by placing the SA section at an integer fractional position of the cavity length, which generates high order mode-locking as defined by Equation 5.1 [1, 18]. The ridge waveguide structures and the split *p*-type metal contact was the same as that used in the CPM case. In the ACPM configuration a 60 μm-long SA section was positioned at one third of the cavity length, dividing the 1200 μm-long cavity in two gain sections with lengths of 400 μm and 800μm, respectively. A

schematic of an ACPM configuration is illustrated in Figure 5.7. The device was characterised by reverse biasing the shorter SA section and forward biasing the rest of the sections, hence forming the two asymmetrical gain sections. The position of the SA at *x=L/3* generates mode-locking at the third harmonic *(i.e M=3)* of the fundamental repetition frequency.

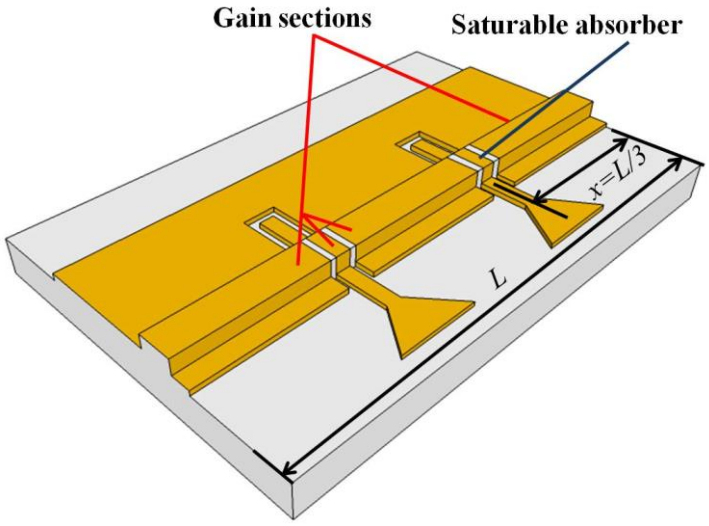

Figure 5.7: Schematic illustrating ACPM with two gain and one SA section. The SA is positioned at *x=L/3* of the cavity length *L*.

5.3.1 Characterization of ACPM lasers

The asymmetric colliding pulse mode-locked lasers are characterised using the same setup as previously discussed. Similar to colliding pulse mode-locked lasers, the single SA section was reverse biased while the rest of the sections contributing to the two gain sections were forward biased. Measurement results obtained from asymmetric colliding pulse mode-locked lasers are discussed in the subsequent sections.

- ***Light-current characteristics:***

Similar to CPM laser devices, the light current *(L-I)* characteristics for ACPM devices exhibit a step like behaviour (see Figure 5.8 (a)). The output

power map for a wide range of biasing condition is illustrated in Figure 5.8 (b), where the regions indicated by bold black lines in the map designate the output power corresponding to the mode-locked pulses having extinction ratio of more than 50 %. The *L-I* curves of this device were measured up to gain current of 100 mA and SA reverse voltage of -2.8 V to avoid the break down of the devices due to high resistance.

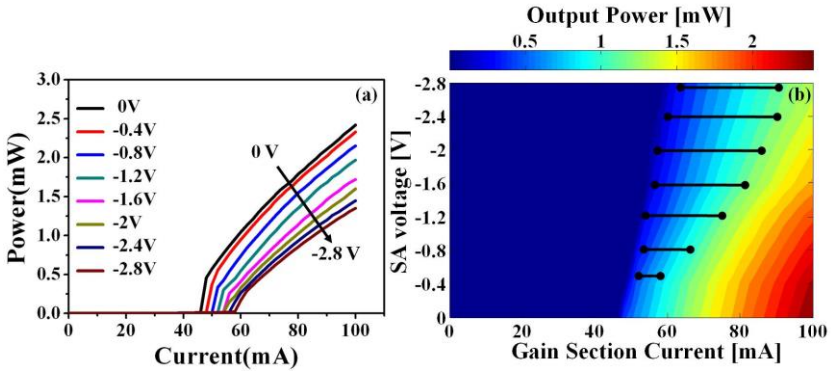

Figure 5.8: (a) *L-I* curves at different SA reverse voltages (b) Output power map as a function of gain current and reverse voltages. Bold black lines correspond to mode-locked pulses having extinction ratio of at least 50 %.

- ***Optical spectra and Autocorrelation measurements:***

The optical spectrum of ACPM devices show that longitudinal modes are lasing at every third mode of the cavity. The optimum mode-locking is observed at V_{SA} = -1.9 V for short current range. The corresponding optical spectrum over a wide wavelength range and a zoomed spectrum that shows a mode spacing of around 0.87 nm are shown in Figure 5.9 (a), and (b), respectively. This mode spacing is approximately three times the mode-spacing of the fundamental frequency (i.e. 0.28 nm), which is the third harmonic of the fundamental repetition frequency and thus the expected ACPM operation is confirmed. The optical spectra of the device were measured for gain current up to 90 mA and SA reverse voltages up to -2.8 V.

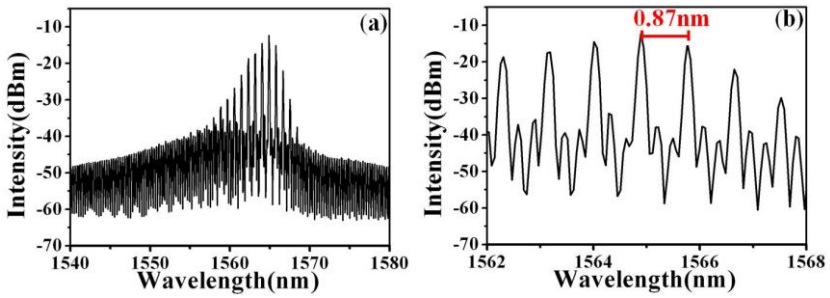

Figure 5.9 : (a) Optical spectrum and (b) corresponding mode spacing at V_{SA} = -1.9 V and I_g = 62 mA.

The wavelength map as a function of the gain current is illustrated Figure 5.10 (a), (b) and (c) where the absorber reverse voltage is kept at a fixed value of -0.6 V, -1.0 V and -1.9 V, respectively. The wavelength map shown in Figure 5.10 (c) corresponds to a reverse voltage value in the optimum mode-locking range, i.e -1.9 V. Similarly to what discussed in previous devices, a red shift in the peak wavelength accompanied by an optical spectrum splitting was observed with increasing gain current. It is apparent from the wavelength map that optical spectrum splitting occurs around 74 and 80 mA for fixed reverse voltages of -0.6 and -1.0 V, respectively. Since the maximum injected current in the device was limited to 90 mA, no splitting was observed for the higher reverse voltage value of -1.9 V and it is expected to occur around a gain current of 90-95 mA.

For a fixed reverse voltage of -1.0 V, the optical spectrum splitting process is shown in Figure 5.11. The optical spectrum starts spreading at around 82 mA, and, for a gain value of 88 mA, both the short and long wavelength lobe are well separated (see Figure 5.11 (a) and (b)). In the ACPM case, the splitting in optical spectrum is not accompanied by a kink in *L-I* curve, and the evolution of the optical spectra closely resembles what discussed in chapter 4.

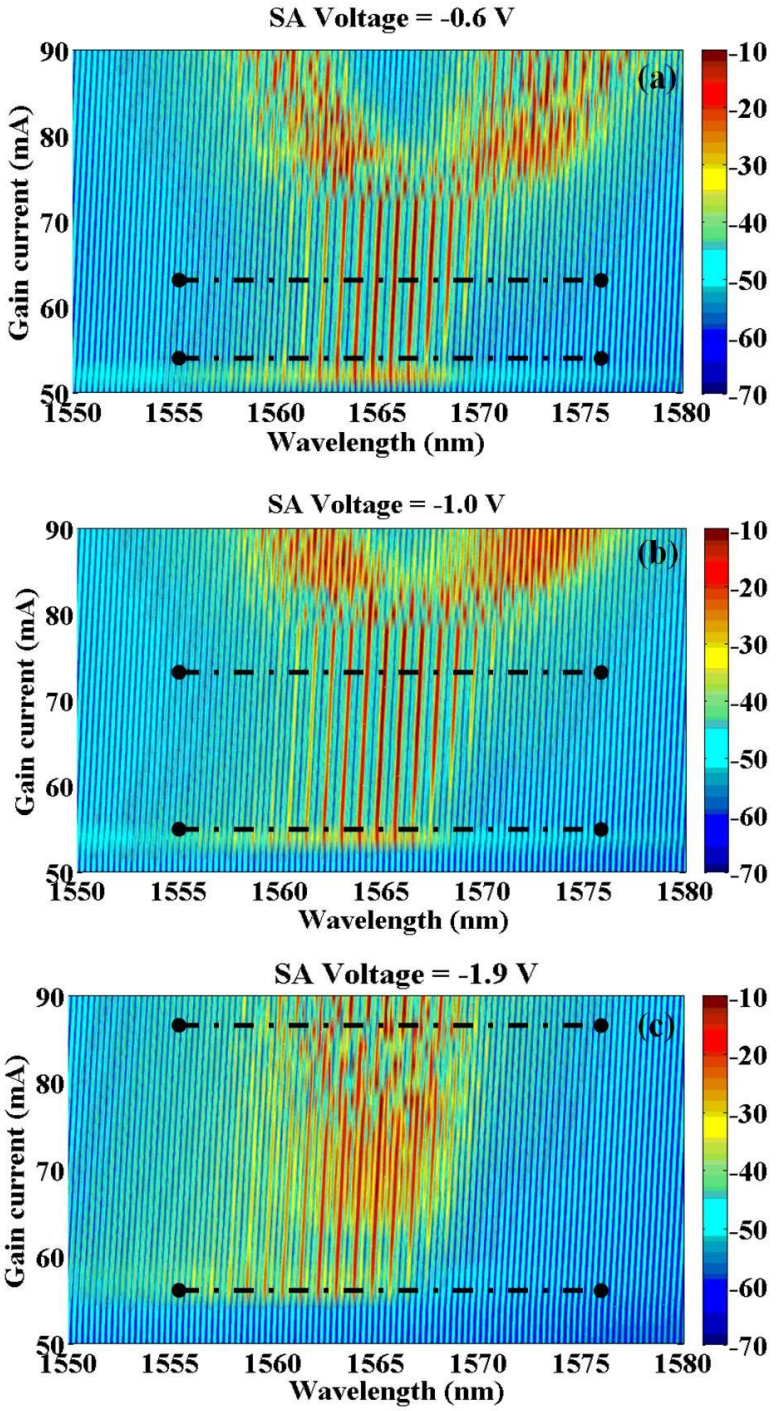

Figure 5.10: Peak wavelength map as a function of gain current at SA reverse voltages of (a) -0.6 V (b) -1.0V (c) -1.9V. Gain current range between the black dotted lines corresponds to mode-locked pulses having extinction ratio of at least 50 %.

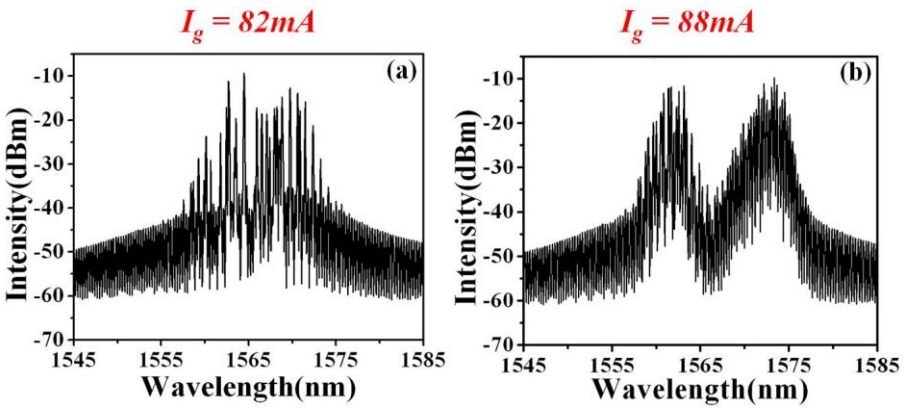

Figure 5.11 : Optical spectra for fixed V_{SA} = -1.0 V (a) in the process of splitting and (b) after splitting.

The recorded autocorrelation traces show that optical pulses with some pedestal start to appear just above threshold, at SA reverse voltages ranging from -0.6 V to -2.8 V. The maximum extinction ratio of the AC traces has been observed for SA reverse voltages ranging from -1.2 to -2.8 V. The optical spectra and corresponding autocorrelation traces for a fixed reverse voltage of -1.9 V are shown in Figure 5.12. Just above threshold, for a gain current value of 56 mA, the optical spectrum consists of a single lobe with every third mode suppressed as shown in Figure 5.12 (I-a). The corresponding autocorrelation trace shown in Figure 5.12 (II-a), indicates that the extinction ratio of the pulses is closer to 50% (i.e. 50% pulse modulation).For an increase in gain current up to 62 mA, the optical spectrum is red shifted and the autocorrelation traces show pulses with a minimum value in the pedestal (i.e. more than 80% pulse modulation). Pulses with maximum extinction ratio of 80% were observed for gain currents in the range 60 to 68 mA. For 76 mA of gain current, the optical spectrum red shifts and the amplitude of the pedestal decreases to around 50 % (see Figure 5.12 (I-c) and (II-c)). A further increase in the gain current up to its maximum value of 90 mA, shows a slight blue shift of the optical spectrum Figure 5.12 (I-d), which suggests the start of the spectrum splitting. This is consistent to what previously observed.

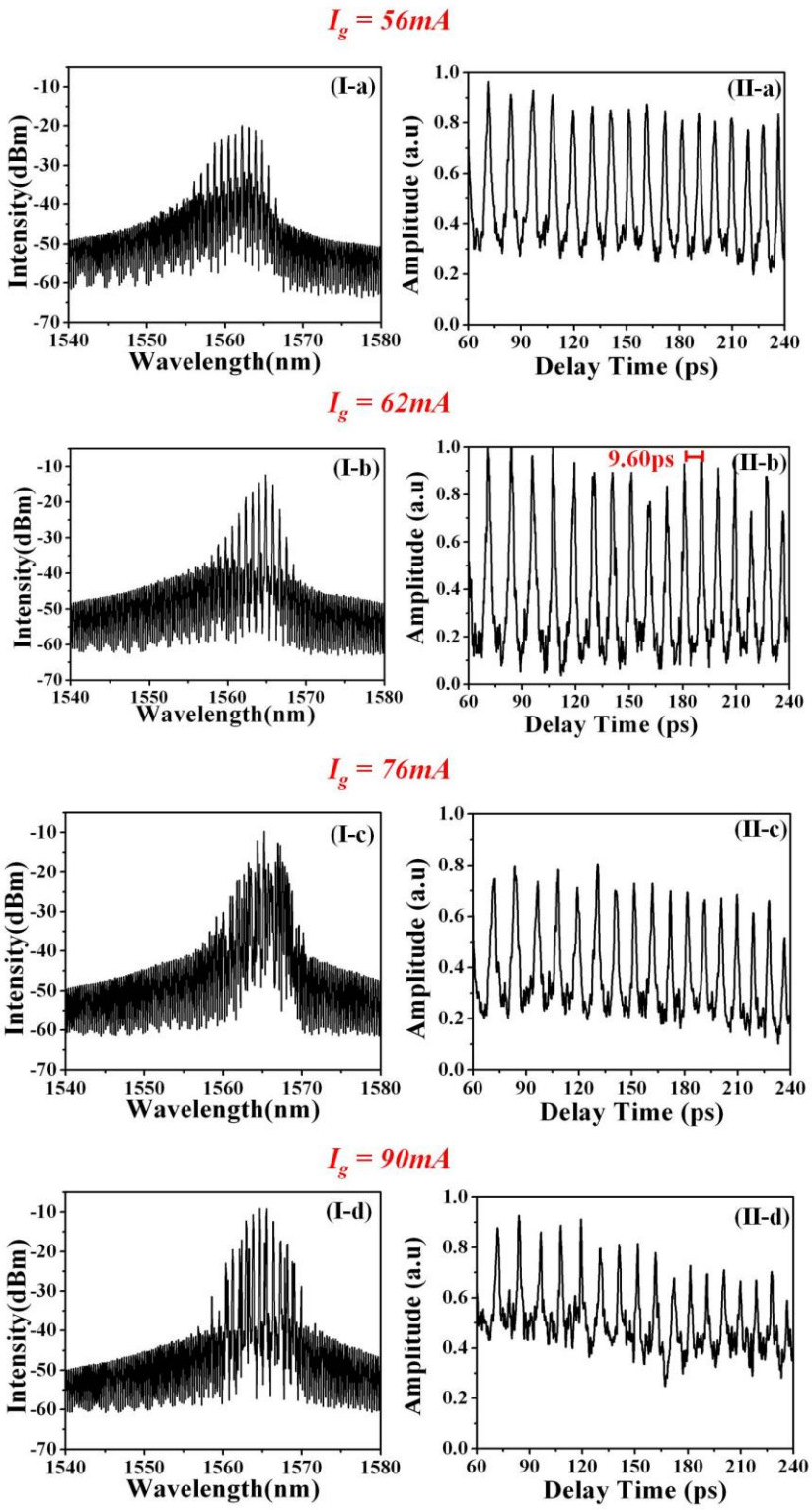

Figure 5.12: For fixed V_{SA} = -1.9 V (I) optical spectra and (II) autocorrelation traces for I_g fixed at (a) 56 mA (b) 62 mA (c) 76 mA (d) 90 mA.

The amplitude of the pedestal for a current value of 90 mA is below 50 %, as shown in, as shown in Figure 5.12 (II-d). The pulse FWHM under optimum mode-locking was around 2.38 ps.

Similar to the CPM laser, the ACPM laser is also a multi-contact laser in which 88.3 %, 6.6 % and 5.0 % of the total cavity length accounts for the gain (forward biased) , gap (unbiased) and absorber (reverse biased) sections. In the two section InAs/InP QD mode-locked lasers that exhibit the best performance, gain, gap and absorber section lengths were in the range of 91.55-93.47 %, 1.22-1.28 % and 5.23- 7.21 %, respectively. This translates into a passive section length that is nearly 5 times larger in multi-section ACPM laser devices. Similarly to what discussed in the CPM laser section, this difference adds to the absorption which is likely to cause an imbalance between the optimum gain and absorption ratio required for stable mode-locking operation.

5.4 Double interval mode-locking laser design

For higher order harmonic mode-locking the single SA is required to be placed closer to the facet, which becomes problematic as the SA section will cover most of the cavity section required to generate the higher order M^{th} harmonic. It appears that there is a trade off between the requirement of placing a short SA close to facet (for high harmonic mode-locking) while at the same time sufficiently long to produce enough absorption for mode-locking operation [19]. To overcome this limitation, higher order harmonic mode-locking was achieved by the double interval mode-locking (DIM) technique, in which two separate SAs are used to generate mode-locking at higher harmonic [12]. A schematic of the DIM configuration with the two SAs is illustrated in Figure 5.13. The position of the two SAs separately defines a low harmonic frequency, while the two jointly reversed biased SAs lead to higher order harmonic mode-locking corresponding to their least common multiple [12]. In the device being investigated, mode locking at the 7^{th} harmonic is obtained by two separate absorbers positioned at $x=L/3.2$, and $y=L/2.3$.

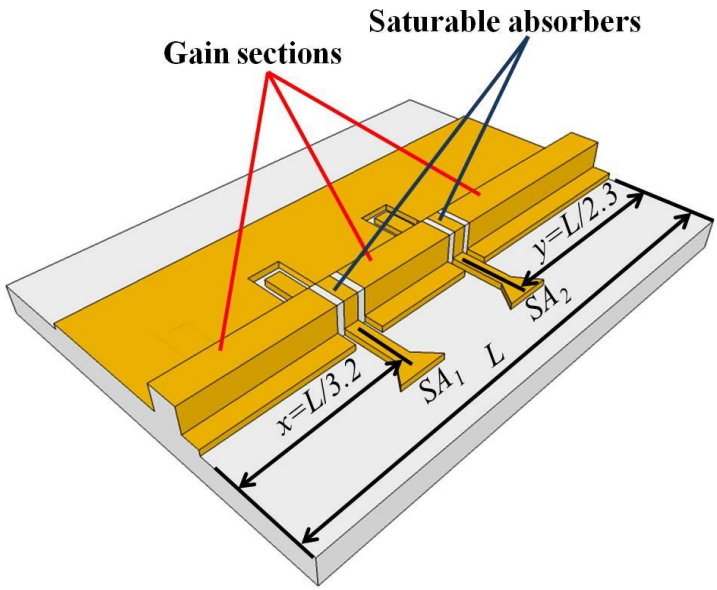

Figure 5.13: Schematic illustrating the DIM technique with three gain an two SA sections positioned at $x=L/3.2$ and $y=L/2.3$ of the cavity length L.

5.4.1 Characterization of DIM lasers

Devices exhibiting harmonic mode-locking using double interval technique were characterised by measuring their output power verses gain current, the optical spectra and the SHG intensity autocorrelation traces.

- ***Light- current characteristics:***

Compared to CPM and ACPM the only difference in the DIM geometry is that two SAs are reversed biased instead of one. Increasing the reverse voltages on both the SAs from 0 V to -2.8 V leads to 66 % increase in threshold current (see Figure 5.14 (a)). A small kink close to threshold in the *L-I* curves appears for reversed voltages exceeding -1.2 V. Unstable and weak mode locking with a substantial pedestal was observed just above the threshold current even when 0 V was applied to both SAs. Figure 5.14 (b) illustrates the out power map for different bias conditions, in which the output powers corresponding to mode-locked pulses having extinction ratio above 50 % are indicated by bold black lines in the power map.

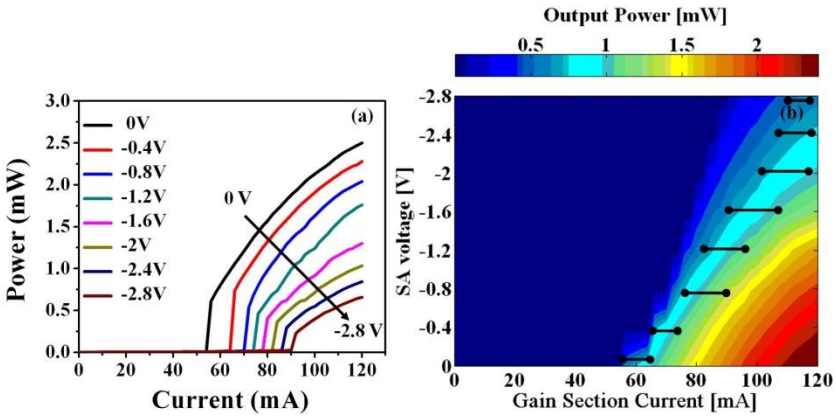

Figure 5.14: (a) *L-I* curves at different SA reverse voltages (b) Output power map as a function of gain current and reverse voltages. Bold black lines correspond to mode-locked pulses having extinction ratio of at least 50 %.

- ***Optical spectra and Autocorrelation measurements:***

The optical spectra clearly show that lasing occurs for every seventh mode of the cavity, while the six modes in between are suppressed. The optical spectrum and mode spacing of optimum mode-locking with minimum pedestal height (V_{SA} = -2.0 V and I_g= 98 mA) are illustrated in Figure 5.15 (a) and (b) respectively. The measured mode-spacing is around 1.98 nm, which corresponds to the seventh harmonic and generate a repetition frequency of around 238 GHz.

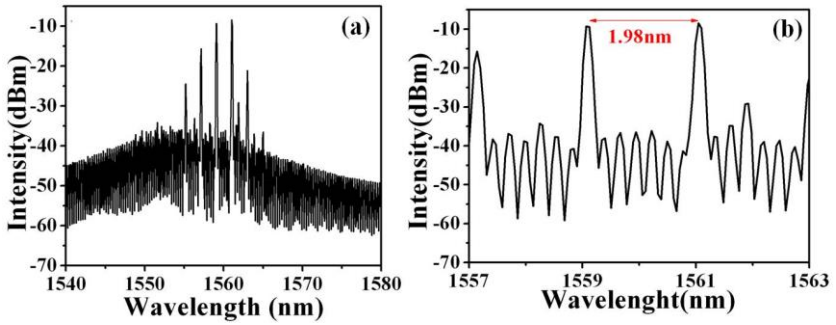

Figure 5.15: (a) Optical spectrum and (b) corresponding mode spacing at

V_{SA} = -2.0 V and I_g = 98 mA.

Peak wavelength maps as a function of the gain current for SA reverse voltages fixed at -0.6 V, -1.0 V and -2.0 V are illustrated in Figure 5.16 (a), (b) and (c), respectively. The red shift in peak wavelength accompanied by optical spectrum splitting was observed with increasing gain current, similarly to what discussed for previous devices. Close to threshold, suppression between the modes is not distinct. As the gain current is increased, a large region with optimum mode-locking appears where a clear suppression takes place every 7^{th} mode. An increase in the reverse bias shifts the optimum mode-locking to higher gain currents. A further increase in the gain current leads to the optical spectrum splitting that occurs at around 90 and 98 mA for fixed reverse voltages of -0.6 and -1.0 V, respectively. The device is measured for gain current up to 120 mA to avoid damage of the contacts, therefore no splitting was observed for the higher reverse voltage value of -2.0 V and it is expected to occur around 122-124 mA of gain current. A comparison of the optical spectra maps for CPM, ACPM and DIM indicates that the optical spectrum splitting and subsequent wavelength shifting for a reverse voltage of -1 V takes place at around 58, 80 and 98 mA, respectively. This is consistent with the different absorption losses incurred in the three geometries that have absorbers of 3.3 %, 5.0 % and 5.3 % of the total cavity length, respectively.

For a fixed reverse voltage of -0.6 V, the optical spectrum splitting process is shown in Figure 5.17. The splitting of the optical spectrum starts at around 90 mA, and spreads at around 92 mA. For gain current values of 120 mA and above, both the short and long wavelength lobes are well separated, as shown in Figure 5.17 (b). Similar to the ACPM case, after the spectral splitting, the intensity of both lobes almost remains same.

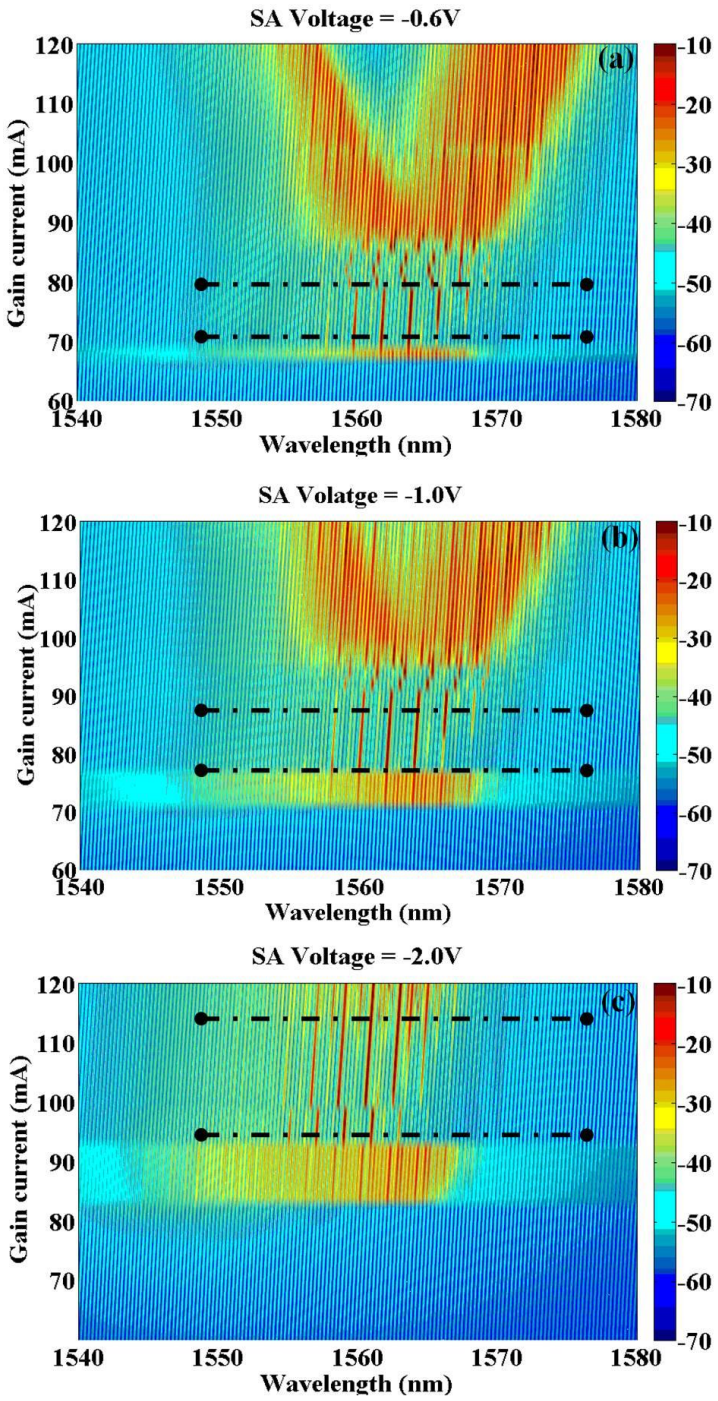

Figure 5.16: Peak wavelength map as a function of gain current at SA reverse voltage of (a) -0.6 V (b) -1.0 V (b) -2.0 V. Gain current range between the black dotted lines correspond to mode-locked pulses having extinction ratio of at least 50 %.

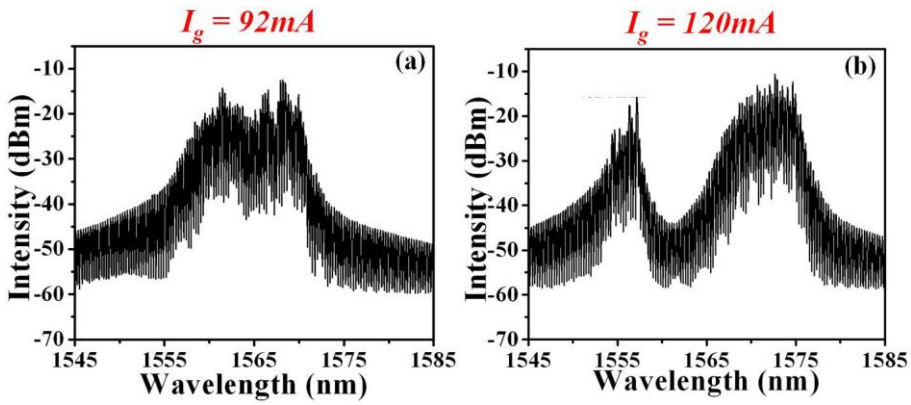

Figure 5.17: Optical spectra for fixed V_{SA} = -0.6 V (a) in the process of splitting and (b) after splitting.

The optical spectra and corresponding autocorrelation traces for a reverse voltage of -2 V are shown in Figure 5.18. The optical spectrum of the device just above threshold is shown in Figure 5.18 (I-a) with its corresponding autocorrelation trace (Figure 5.18 (II-a)). The suppression between the modes is not distinct and mode-locking appears incomplete. For an increase in the gain current up to 92 mA no high harmonic modal suppression occurs and a 2 nm red shift in peak wavelength is observed (Figure 5.18 (I-a)), possibly due to thermal detuning of energy bandgap. At 94 mA, in correspondence to the kink in the *L-I* curve, the peak wavelength suddenly blue-shifts by 5 nm. A similar kink in the *L-I* curve and blue shifting of the peak wavelength was observed for reverse voltage values of -1.2, -1.6 and -2.4 V. Beyond 94 mA, a continuous red shift is observed in peak wavelength and at 98 mA (in the optimum mode-locking region) the peak wavelength is centred at 1561 nm. The mode spacing corresponding to the 7^{th} harmonic and the AC traces for -2.0 V absorber reverse bias and 98 mA gain current are shown in Figure 5.18 (I-c) and (II-c), respectively. As the gain current is further increased up to 114 mA, the optical spectrum is further red shifted and the corresponding pulse train show a degradation of the pulse modulation (Figure 5.18 (I-d) and (II-d)).

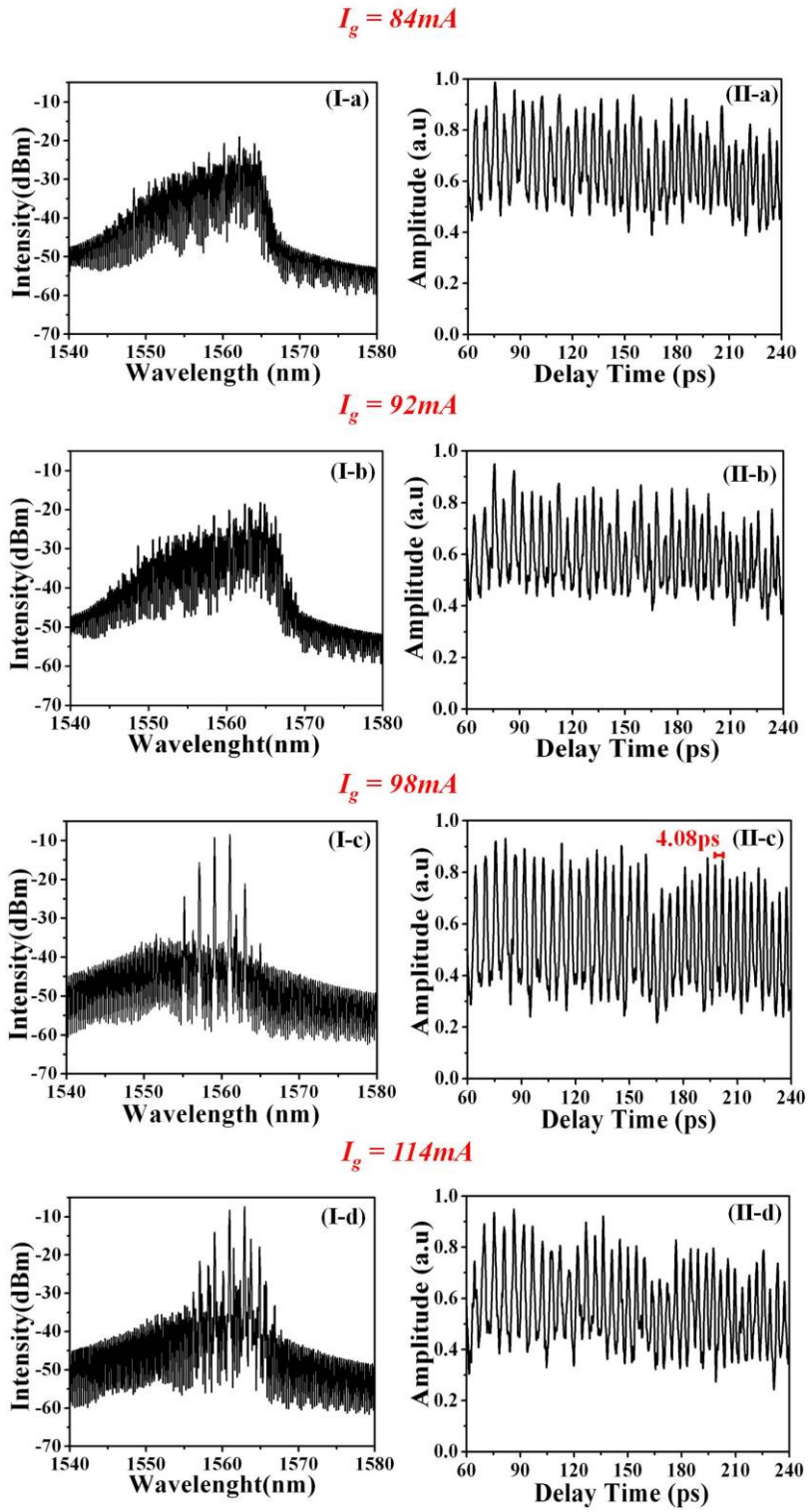

Figure 5.18: For fixed V_{SA} = -2.0 V (I) optical spectra and (II) autocorrelation traces at I_g of (a) 84 mA (b) 92 mA (c) 98 mA (d) 114 mA.

In the current biasing region where pulses have optimum modulation, the pulse FWHM of a pulse is 1.85 ps. The measured pulse spacing corresponds to a repetition frequency of around 238 GHz with a ±3% variation in repetition rate, which is closer to the expected seventh harmonic of the fundamental frequency.

5.5 Conclusions

In this chapter the results obtained by 2^{nd}, 3^{rd} and 7^{th} harmonically mode-locked laser devices were presented. The harmonic mode-locking was obtained by alternating gain and absorbing sections along the cavity so to define precise ratios between the gain sections.. Since the RF spectra of these devices could not be recorded due to bandwidth limitation of the available RF spectrum analyser, the repetition frequency in each case was determined through the assessing the mode-spacing and temporal pulse spacing. Mode-spacing of 0.58 nm, 0.87 nm and 1.98 nm were obtained for 2^{nd}, 3^{rd} and 7^{th} harmonic mode-locking, respectively, in excellent agreement with the expected repetition rates. Although all the geometries presented in this chapter exhibit the expected harmonic mode-locking operation but mode-locking is often incomplete. We identified two main causes that might explain the non-optimal ML performance of the devices:

- The stability of harmonically mode-locked devices critically depends on the ratio between the lengths of the gain sections. A small tilt of the pattern with respect to the crystallographic axes of the sample as well as unavoidable inaccuracies in the cleaving leads to errors in the order 1% to 2% in the definition of the section lengths. As a consequence, the pulses do not simultaneously collide in the SAs and instabilities in the pulse train arise. A solution to this problem is to replace the cleaved cavity mirrors by deeply etched gratings that can be exactly positioned at the lithographic stage.
- The various unbiased gaps that isolate the cavity sections add a substantial contribution to the losses of the devices. In fact, the total length of the unbiased sections in some of the geometries investigated is as much as 5%

of the total cavity, which is comparable to the length of the SA. The consequences of these additional losses were partially overlooked in the design stage and need to be carefully addressed in future devices. One approach would be to make the SA shorter so to decrease the overall losses of the cavity. However, the losses originated by the unbiased gaps are likely to have a very slow recovery time and therefore might not yield the desired performance for optimum mode locking. Defining shorter unbiased gaps could be a better solution provided good electrical insulation is kept between the sections. This can be achieved by etching the cap layer in the gaps [20].

It is worth noting that mode-locking only occurs for low values of the gain current. An improved device design with optimised SA sections and smaller passive gaps will push the mode-locking region to higher current values where a much larger gain spectrum was recorded. Exploring the stability of the mode locking over this wide spectral gain region would be of great interest for generating very high repetition rates and increase the number of modes concurring to mode locking operation.

5.6 References

1. *Shimizu, T., W. Xinglong, and H. Yokoyama. Subterahertz-rate optical pulse generation with asymmetric colliding-pulse mode- locked semiconducto. in Lasers and Electro-Optics, 1995. Technical Digest. CLEO/Pacific Rim'95., Pacific Rim Conference on. 1995.*

2. *Avrutin, E.A., J.H. Marsh, and E.L. Portnoi, Monolithic and multi-gigahertz mode-locked semiconductor lasers: constructions, experiments, models and applications. Optoelectronics, IEE Proceedings -, 2000. 147(4): p. 251-278.*

3. *L W Shi, et al., Status and trends of short pulse generation using mode-locked lasers based on advanced quantum-dot active media Journal of Physics D: Applied Physics, 2007. vol. 40(Issue 18): p. 307-318.*

4. *K A Williams, M.G. Thompson, and a.I.H. White, Long-wavelength monolithic mode-locked diode lasers. New Journal of Physics, 2004. 6(1).*

5. *Arahira, S., Y. Matsui, and Y. Ogawa, Mode-locking at very high repetition rates more than terahertz in passively mode-locked distributed-Bragg-reflector laser diodes. Quantum Electronics, IEEE Journal of, 1996. 32(7): p. 1211-1224.*

6. *Liu, J., et al., Dual-wavelength 92.5 GHz self-mode-locked InP-based quantum dot laser. Opt. Lett., 2008. 33(15): p. 1702-1704.*

7. *Mesaritakis, C., et al., Pulse width narrowing due to dual ground state emission in quantum dot passively mode locked lasers. Applied Physics Letters, 2010. 96(21): p. 211110-3.*

8. *Mesaritakis, C., et al., Dual ground-state pulse generation from a passively mode-locked InAs/InGaAs quantum dot laser. Applied Physics Letters, 2011. 99(14): p. 141109-3.*

9. *Jiang, L. and L.V. Asryan, Multimode emission and optical power in a semiconductor quantum dot laser. Nanotechnology, 2008. 19(41): p. 415204.*

10. *Zhang, L., et al. High-power low-jitter quantum-dot passively mode-locked lasers. in Proc. SPIE 6115, Physics and Simulation of Optoelectronic Devices XIV, 611502 2006.*

11. *Javaloyes, J. and S. Balle, Mode-Locking in Semiconductor Fabry-Perot Lasers. Quantum Electronics, IEEE Journal of, 2010. 46(7): p. 1023-1030.*

12. *Li, Y., et al., Harmonic mode-locking using the double interval technique in quantum dot lasers. Opt. Express, 2010. 18(14): p. 14637-14643.*

13. *Lester, L.F., et al. Reconfigurable, multi-section quantum dot mode-locked lasers. in Lasers and Electro-Optics (CLEO) and Quantum Electronics and Laser Science Conference (QELS), 2010 Conference on.*

14. *Tahvili, M.S., et al., Dual-wavelength passive and hybrid mode-locking of 3, 4.5 and 10 GHz InAs/InP(100) quantum dot lasers. Opt. Express, 2012. 20(7): p. 8117-8135.*

15. *Heck, M.J.R., et al., Observation of Q-switching and mode-locking in two-section InAs/InP (100) quantum dot lasers around 1.55 ?m. Opt. Express, 2007. 15(25): p. 16292-16301.*

16. *Heck, M.J.R., et al., Passively Mode-Locked 4.6 and 10.5 GHz Quantum Dot Laser Diodes Around 1.55 μm With Large Operating Regime. Selected Topics in Quantum Electronics, IEEE Journal of, 2009. 15(3): p. 634-643.*

17. *Thompson, M.G., et al. Absorber length optimisation for sub-picosecond pulse generation and ultra-low jitter performance in passively mode-locked 1.3µm quantum-dot laser diodes. in Optical Fiber Communication Conference, 2006 and the 2006 National Fiber Optic Engineers Conference. OFC 2006.*

18. *Shimizu, T., I. Ogura, and H. Yokoyama, 860 GHz rate asymmetric colliding pulse modelocked diode lasers. Electronics Letters, 1997. 33(22): p. 1868-1869.*

19. *Li, Y., et al., Double-interval harmonic mode-locking technique for diverse waveform generation, in Proc. SPIE 7616, Novel In-Plane Semiconductor Lasers IX, 76160D (February 12, 2010).*

20. *Martins-Filho, J.F., et al., Monolithic multiple colliding pulse mode-locked quantum-well lasers, experiment and theory. Selected Topics in Quantum Electronics, IEEE Journal of, 1995. 1(2): p. 539-551.*

Chapter 6

Monolithic Coupled Cavity Mode-locked Lasers

6.1 Introduction

This chapter describes the design, fabrication and characterisation of monolithic coupled cavity laser devices, realised to achieve ultrahigh repetition frequencies. The most time consuming part of this activity was the fabrication of the deep etched slots for the optical mode coupling between the cavities. The device fabrication part of this chapter explains in details the development of the additional fabrication steps that were required to etch the slots, including the focus ion beam (FIB) milling carried out at the University of Southampton. The last part of the chapter reports on the characterization of the devices and discusses the results.

6.2 Monolithic coupled cavity laser

As discussed in chapter 2, harmonic mode-locking is an effective solution for generating ultra-high repetition frequencies. This can be achieved by either splitting the gain and absorber sections along the laser cavity (see chapter 5) or by

defining intra-cavity reflectors (ICR) through deep etched slots. The etched slot divide the cavity into two coupled FP cavities of lengths L_1 and L_2 that are independently biased as illustrated in Figure 6.1. The coupling between the cavities and the dynamically stability of the laser is critically dependent on the reflectivity provided by the etched ICR, which needs to be carefully optimised [1].

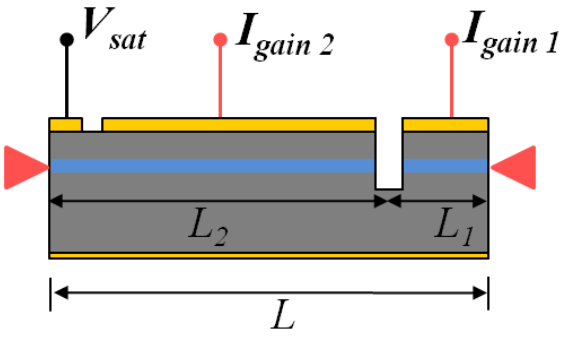

Figure 6.1: Schematic of a monolithic coupled cavity device with the intra-cavity reflector.

The coupled cavity mode-locked (CCM) laser is able to generate pulse trains at the M^{th} harmonic of the fundamental frequency [2], which is related to the ratio between the two sub cavities of length L_1 and L_2. More precisely, in a CCM laser configuration where an ICR is positioned at $1/M$ of the total cavity length, mode-locking at the M^{th} (where $M>2$) harmonic of the fundamental frequency can be achieved if the ratio between the lengths of two coupled sub cavities is given by [2, 3]:

$$\frac{L_1}{L_2} = \frac{1}{M-1}$$

The resultant repetition rate (f) for such coupled cavity configuration is given by the M^{th} harmonic of the fundamental frequency (f_{FP}) [2, 3]:

$$f = Mf_{FP}$$

In such a cavity configuration, the modes which correspond to the harmonic mode-locking are supported, while the others are suppressed [4]. The

mode spacing $\Delta\lambda_{CC}$ in the optical spectrum of a CCM configuration is defined by the shorter sub cavity and experiences an *M*-fold multiplication.

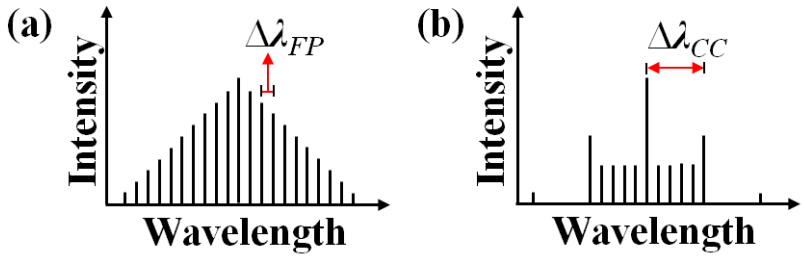

Figure 6.2: Schematic representing mode spacing corresponding to (a) the fundamental mode-locking (FP mode-locked laser) (b) CCM laser with *M=5*.

The mode spacing in a CCM geometry is illustrated by the schematic of Figure 6.2. If the ratio between the cavity lengths, L_1: L_2 is *1:4*, then every 5th mode is supported while the other modes are suppressed.

6.3 Coupled cavity laser design

The cavity of the CCM devices is formed by a standard ridge waveguide, with an etched ICR (consisting of one or two parallel slots), two gain sections (Gain I and II of length of L_1 and L_2 , respectively) and an absorber section that is placed besides the cleaved facet of the longer gain section. The waveguide height and width were optimised for single mode operation prior to the fabrication with a mode solver simulation tool (BEAM PROP). Single mode operation is achieved with a waveguide width of 2.5 μm and a height of 1.535 μm for shallow etched devices.

Both gain sections of the devices were electrically isolated from each other by leaving a 20 μm wide gap in the *p*-contact metal. The saturable absorbers were designed with varying lengths ranging from 4% to 10 % of the total cavity length. In order to compare the device characteristics with different values of the ICR reflectivities, identical devices with 1 and 2 slots etched slots were also fabricated

(see Figure 6.3). The devices are defined on the same cleaved bar to ensure identical length of the optical cavity of ~1200 μm.

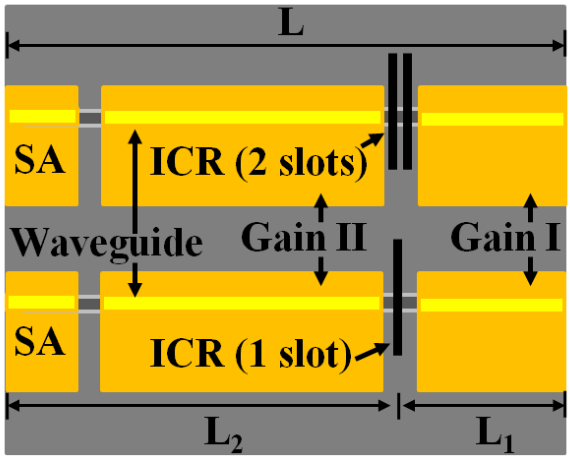

Figure 6.3: Planar view of two parallel devices with 1 and 2 slots ICR.

6.4 Design of sub-cavity ratios

Devices with various cavity ratios up to *M=12* (using one or two deep etched parallel slots as an ICR) were designed and fabricated. Schematics of the various designed coupled cavity devices, using different sub cavity ratios are illustrated in Figure 6.4. Figure 6.4 I (a-d) and II (a-d) illustrate the schematic of a coupled cavity mode-locked laser (MLL) with an ICR (consisting of a single etched slot) used to divide the cavity into two sub-cavities with the desired length ratio. In Figure 6.4 II (a-d), the back facet is a reflector designed to maximise the reflection to values $R > 90\%$. This reflector consists of four deeply etched parallel slots. The additional slot, labelled with *'T'* in Figure 6.4 II (a-d), is a large and deeply etched trench designed to minimise any residual back reflection into the device. An identical set of devices was designed with strongly reflecting ICRs that are formed by two deeply parallel slots. The expected repetition rates and mode-spacing of the devices illustrated in Figure 6.4 are summarised in Table 6.1.

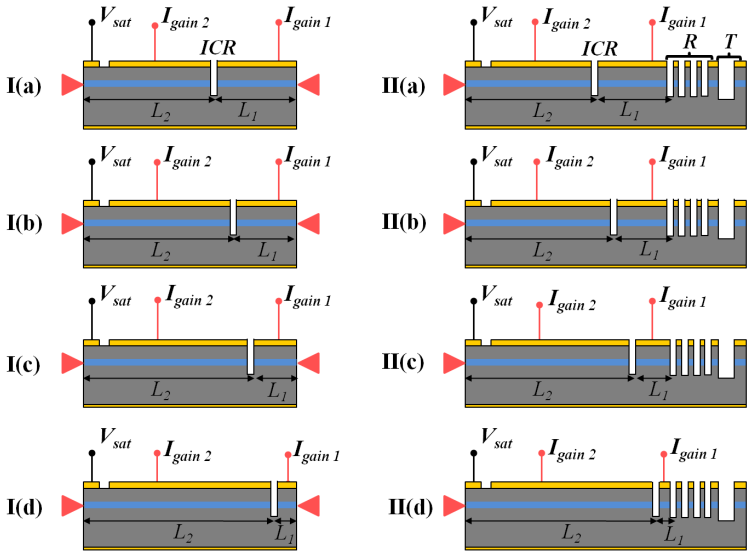

Figure 6.4: Schematics of coupled cavity devices where **I(a-d)** represent cavity ratios 1:2, 1:3, 1:4 and 1:11, respectively, with both facets cleaved. **II(a-d)** represent cavity ratios 1:2, 1:3, 1:4 and 1:11, respectively, with one cleaved facet on the long gain section and one back reflector *R* formed by four etched slots on the short gain section.

Devices description		**Sub-cavity ratios** $L_1:L_2$	**Harmonic Number**	**Expected harmonic frequency (GHz)**	**Expected mode-spacing (nm)**
Gain I (µm)	**Gain II (µm)**				
400	800	1:2	3	$3\ f_{FP} \approx 105$	$3\Delta\lambda_{FP} \approx 0.84$
300	900	1:3	4	$4\ f_{FP} \approx 140$	$4\Delta\lambda_{FP} \approx 1.12$
240	960	1:4	5	$5\ f_{FP} \approx 175$	$5\Delta\lambda_{FP} \approx 1.40$
100	1100	1:11	12	$12\ f_{FP} \approx 420$	$12\Delta\lambda_{FP} \approx 3.36$

Table 6.1: Expected repetition rates and mode spacing for 3rd, 4th, 5th and 12th order harmonic mode-locked coupled cavity lasers.

The values shown in Table 6.1 were calculated by using the mode spacing and repetition rate of the 1220 μm long FP mode-locked laser discussed in chapter 4, where $f_{FP} \approx 35$ GHz and $\Delta\lambda_{FP} \approx 0.28$ nm.

6.5 ICR design and simulations

The design of the ICR is critical to the behaviour of a CCM as its reflectivity defines the coupling between the sub-cavities and strongly influences the dynamics of the devices [1]. The ICR is built on the concept of distributed Bragg reflector (DBR) gratings, where multiple reflections from waveguide corrugations with appropriate periodicity provide constructive interference for the wavelength range of interest. In coupled cavity MLLs, an ICR with broad reflection bandwidth is required to achieve equal reflectivity on all the frequency components existing in the lasing spectrum. In order to maximise the wavelength bandwidth of the reflector the coupling coefficient needs to be as high possible, which demands the fabrication of deeply etched slots that produce a very high modulation of the refractive index (i.e $\Delta n \sim 2.2$) [5]. This ICR geometry has already been successfully applied to demonstrate a repetition rate of 160 GHz with high reflectivity and low mirror losses on AlGaInAs quantum well compound cavity lasers emitting at 1550 nm [6].

The period of the slots can be calculated using the Bragg's diffraction condition [5]:

$$\boldsymbol{2n_{eff}\Lambda = \lambda_o m}$$

where n_{eff} is the effective refractive index of the guided mode, Λ is the period of the grating, m is the order of grating and λ_o is the wavelength in the vacuum. Maximum reflectivity is obtained for $m=1$ but the fabrication of such a narrow gap imposes critical fabrication challenges on both the lithography and dry etching of the grating. The optimum value for the grating order is a compromise between. In this research, 3rd order gratings were chosen as they provide the best compromise between reflectivity and fabrication tolerances. For 3rd order grating

operating at a centre wavelength of 1550 nm, slots with a periodicity of 362 nm (50% duty cycle) are required. Slot period is represented by the schematic of Figure 6.5.

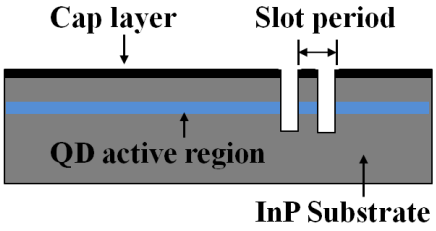

Figure 6.5: Schematic of a deep etched ICR, with two etched slots.

Prior to device fabrication, the deep etched ICR were numerically simulated to determine the peak reflectivity and reflection bandwidth. The simulations were carried out with a two dimensional (2D) simulation software known as cavity modelling framework (CAMFR), which is an open source software developed at Gent University and based on eigenmode expansion (EME) principle [7]. The simulation results for a 2.5 μm deep ICR consisting of one, two and four slots are illustrated in Figure 6.6. At the emission wavelength of 1550 nm, the simulated peak reflectivity obtained for an ICR consisting of one, two and four slots are $R_{1\text{-}slot}$ = 70 %, $R_{2\text{-}slots}$ = 95 % and $R_{4\text{-}slots}$ = 97 %, respectively. The FWHM of the stop-band (or reflection bandwidth) of the slots is around 600 nm wide, which provides a very large fabrication tolerance as the gain bandwidth of the lasers is in the order of 40-60 nm. The main challenge is the fabrication of the ICRs, which requires the development of a lithographic process with a very thick mask and a careful dry etching optimisation to ensure verticality and smoothness of the slot sidewalls. In previous attempts, deep etched ICR were defined by reactive ion etching (RIE) [1, 5] and inductively coupled plasma (ICP) etching processes [6]. In this research, RIE and focused ion beam (FIB) techniques have been used to define the deep etched ICR.

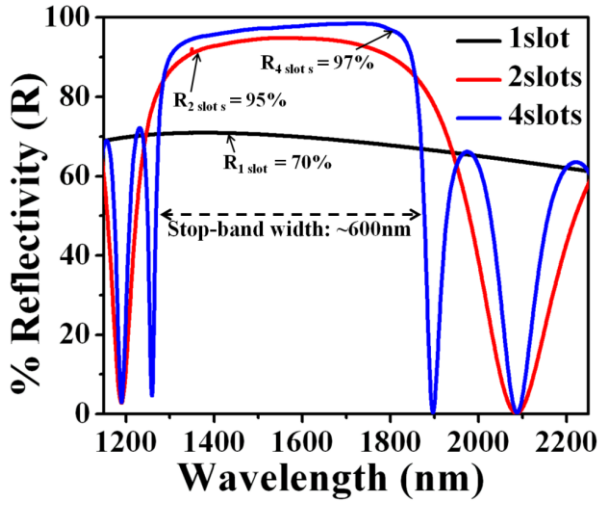

Figure 6.6: Simulated reflectivities for a 2.5 μm deep ICR, consisting of one, two and four slots.

6.6 The RIE lag effect

The RIE lag is phenomenon in which the etch rate decreases as the dimensions of the structure to be etched become narrower [8-10]. Although reactive ion etching (RIE) was previously optimised for achieving vertical and smooth ridge waveguides structures, the analysis of the etched ridge waveguide incorporating narrow slots of sub micron size showed a substantial RIE lag effect in the slots. The SEM images of Figure 6.7 (a) and (b) illustrate the RIE lag effect for two InP samples, etched separately for 40 and 60 minutes, respectively.

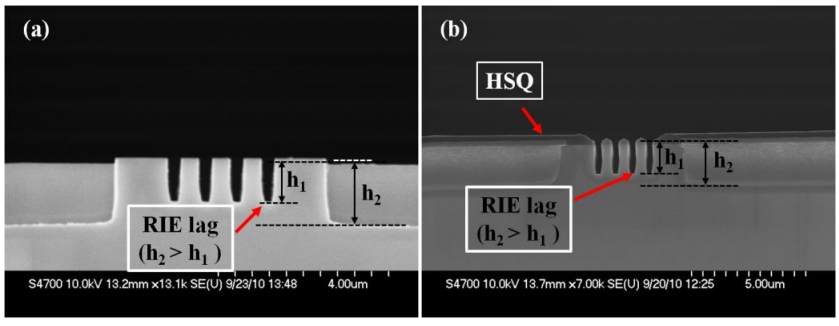

Figure 6.7 : SEM image of the waveguides incorporating slots. The figures show the RIE lag effect for (a) a 40 min etch and (b) a 60 min etch in a $CH_4/H_2/O_2$ chemistry.

In order to minimise the RIE lag effect, a good balance between the physical and chemical components of the etching process is required [9]. The use of a hard mask material such as SiO_2 or SiN, which can provide high resistance to RIE etching is essential in order to achieve the required etch depth [11, 12]. In this research work a ~600 nm, thick layer of HSQ was used as this proved sufficient for etch runs as long as 110 minutes. For very long etch runs up to 205 minutes, a layer of thick PMMA was also used to protect the HSQ hard mask and waveguides.

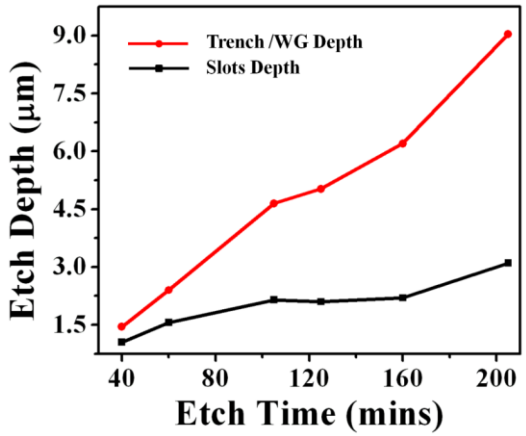

Figure 6.8: Etching depth vs etching time for trench (or waveguide) and 362 nm-wide slots.

Various test runs were carried out in order to optimise the etch time for 362 nm wide slots, the results of which are illustrated in Figure 6.8. The etch depth of the slots (ICR) as a function of the etch time demonstrates that the core layer is etched through (~2.1 μm) with an etching time of around 105 minutes and above.

Three device designs of increasing complexity were considered in this research. This included a single step deep etched waveguide (incorporating the slots), a split waveguide geometry (i.e. with a single gap introduced along the cavity) and a self-aligned process with a bi-level etching design with shallow etched waveguides and deep etched slots. The details of these three designs are given in the next section.

6.6.1 Deep etched waveguide design

A first set of devices was fabricated with a single etch run in which both waveguide and slots were etched simultaneously. The use of single step deep etching simplifies substantially the fabrication processing as it eliminates the lithographic and etching steps that are required to define separately the shallow etched waveguide and deep etched ICRs. A schematic of deep etched waveguide along with the deep etched ICR (considering the RIE lag effect) is illustrated in Figure 6.9 (a) and (b).

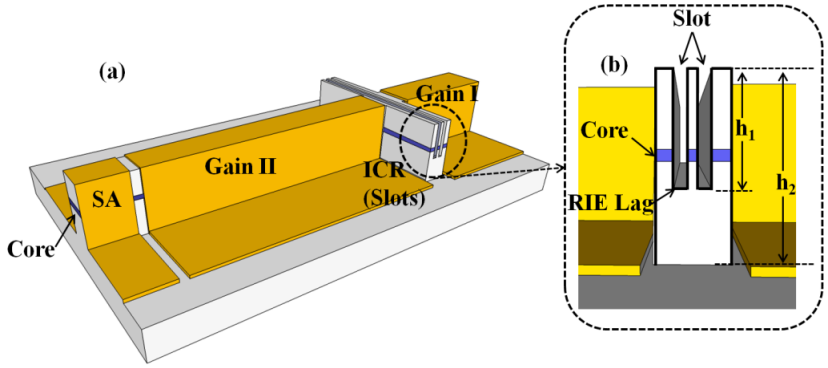

Figure 6.9: (a) Schematic of the deep etched waveguide design (b) Cross-sectional view of the ICR (slots) , which shows the RIE lag effect

where $h_2 > h_1$.

In the ICR region, the lateral dimension is extended to several μm to minimise the chances of filling the slots with silica and HSQ during the planarization process. In fact, a narrow ICR pattern in the lateral dimension shows evidence of silica and HSQ inside the etched slots that affects the reflectivity of the reflectors.

- ***Deep etched waveguide:***

The steps involved in the fabrication of shallow etched ridge waveguide lasers are discussed in chapter 3 (Figure 3.1). Here, a very similar fabrication procedure was followed, with the only difference that the etching time was

increased to 110 minutes. Details of all the processing steps are given in Appendix A. The top and side views of an ICR consisting of two slots and a reflector incorporated at the back end of the waveguide are illustrated in Figure 6.10 (a-b). Two sets of devices were fabricated, the first with a waveguide etch depth close to 4.6 μm (device of Figure 6.11 (b)), the second with an etch depth of 5.2 μm (device of Figure 6.11(d)). Both set of devices did not show any lasing during the characterisation process due to some fabrication faults, as explained below.

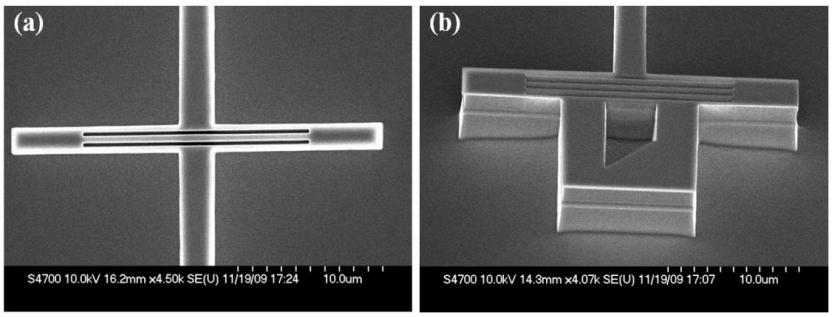

Figure 6.10: (a) Top view of an ICR consisting of two slots in a deeply etched waveguide (b) Deep etched back reflector of the waveguide.

The critical steps in the fabrication process of deeply etched devices are E-beam lithography, etching, metal lift-off and cleaving of individual bars. Parameters such as dose, VRU, beam spot size for E-beam and gas flow, pressure and RF power for dry etch require a careful optimisation to ensure repeatability and accuracy of the process. Similarly, inappropriate handling during thinning or cleaving can easily break or damage the high aspect ratio features. Therefore, proper optimisation of processes was done before carrying out the fabrication of the devices. The two most critical fabrication problems that were encountered were improper metal lift off and device breakage during cleaving. More specifically, in the first set of devices some unnoticeable residual resist was left on the top of the ridge waveguide after the development of the sample. The presence of this resist residual wiped off the metal from the top of the waveguide during the metal lift off process. Missing of *p*-contact metal at the top of ridge waveguide is illustrated in Figure 6.11 (a) and (b). To solve this problem in subsequent samples,

the sample was given a short O_2 clean prior to metallization, in order to remove any residual resist.

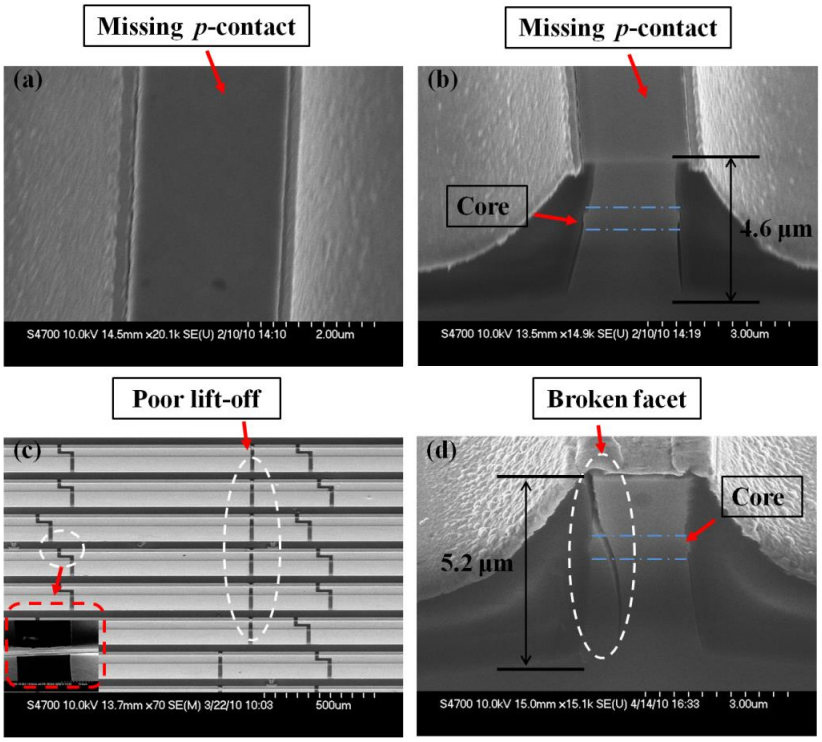

Figure 6.11 : (a) and (b) Missing *p*-contact metal on the top of waveguide (c) Incomplete lift-off between two gain sections as well as between SA and gain section shown by a magnified view on the lower left corner (d) Broken facet of the deep etched waveguide during cleaving.

The processing of the second sample with a very deep etching proved very problematic because of the poor planarity of the surface. In fact, the resist that was spun for the *p*-type metallization lithographic step was much thinner than expected on the top of the ridge waveguides. This caused the collapse of the resist undercut and the subsequent poor lift-off between the two gain sections of the devices as illustrated in Figure 6.11 (c). Furthermore, the narrow and high ridge waveguides resulted in the facets breakage during the cleaving (see Figure 6.11 (d)). These issues lead to the conclusion that deep etched devices would have required a substantial and time consuming optimisation of the processing. It was

decided that the use of a different geometry with shallow etched waveguides was a better option for the fabrication of further devices.

6.6.2 Split waveguide design

This design includes a shallow etched waveguide with a deep etched gap as depicted Figure 6.12. This approach consists of two etching steps. In the first step, shallow etching is used to remove the upper cladding, while the second step penetrates the core and the lower cladding inside the slots. The trench was left open on both sides of the slot in order to provide a better gas flow inside the narrow slots region during the etching process and therefore reduce the RIE lag effect.

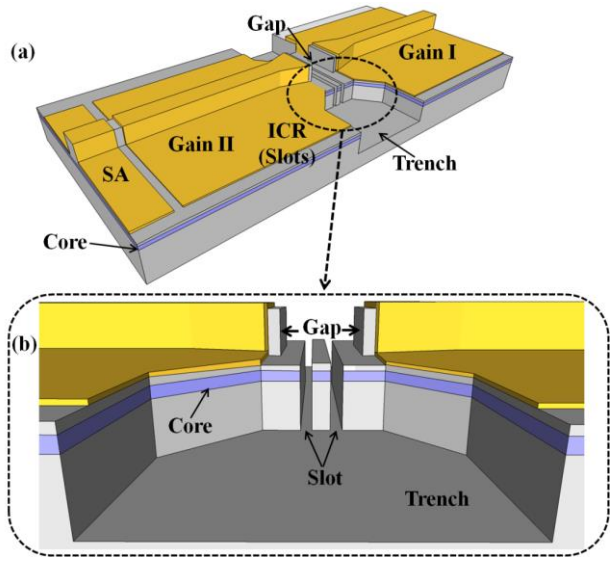

Figure 6.12: (a) Schematic of a split waveguide design with deep etched ICR and (b) magnified view of the deep etched ICR in the gap region.

The fabrication of the split waveguide geometry was first carried out on a test sample to investigate the fabrication tolerance of the design. Details of all the processing steps are given in Appendix B. The main steps followed for the fabrication of the split waveguide design are summarised in Figure 6.13. First, the desired pattern with the ridge waveguide and gap was transferred onto the

semiconductor substrate by using HSQ as a hard mask, followed by a shallow etching (see Figure 6.13 (a)).

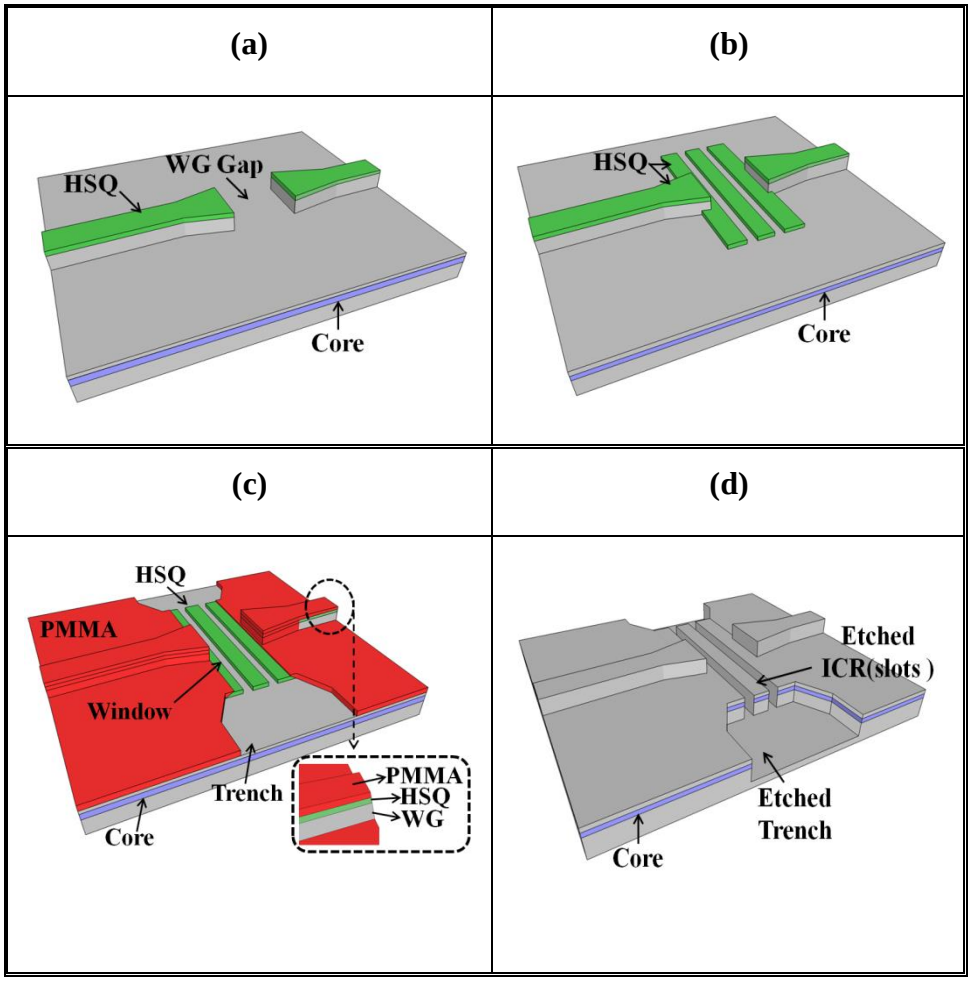

Figure 6.13 : (a) Schematic of the split waveguide geometry after the shallow etch step; (b) second lithographic step with HSQ to define the pattern for the slots; (c) patterning of PMMA resist to protect the waveguide during the deep etching step (d) shallow etched WG with deep etched slots and trench.

As the second step, HSQ was spun and developed for defining a mask for the slots in the gap region of the waveguide (Figure 6.13 (b)). In the third step a thick bi-layer of PMMA was used to protect the entire sample, expect for a window left on the slot region (Figure 6.13 (c)). Finally, after etching, resist

strippers (Acetone and HF acid) were used to remove the PMMA and HSQ resists from the substrate (Figure 6.13 (d)). No further fabrication process was carried out on this sample because of the critical fabrication tolerances that will be discussed below.

Residual HSQ was observed after the development of the slots pattern. A thick layer of HSQ appeared due to accumulation of HSQ between the waveguide gap during resist spinning. The HSQ layer forms a meniscus between the walls of the gap hence adding to the thickness of the resist in the slot area. The SEM images of a thick layer of residual HSQ resist in a single slot illustrating top and cross-sectional views are shown in Figure 6.14 (a) and (b), respectively.

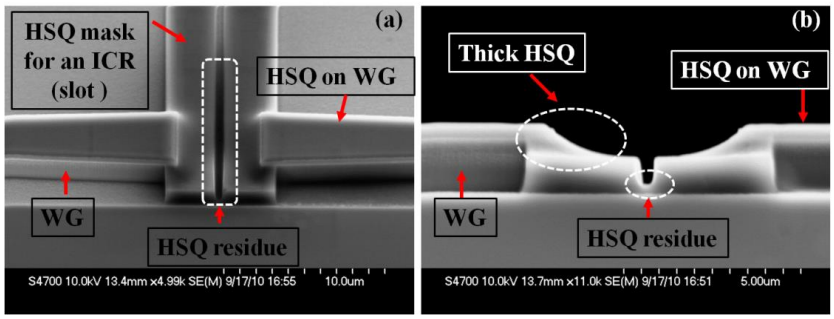

Figure 6.14 : (a) Residual HSQ in the slot area (Top view) and (b) layer of residual HSQ resist in a single slot (cross-sectional view).

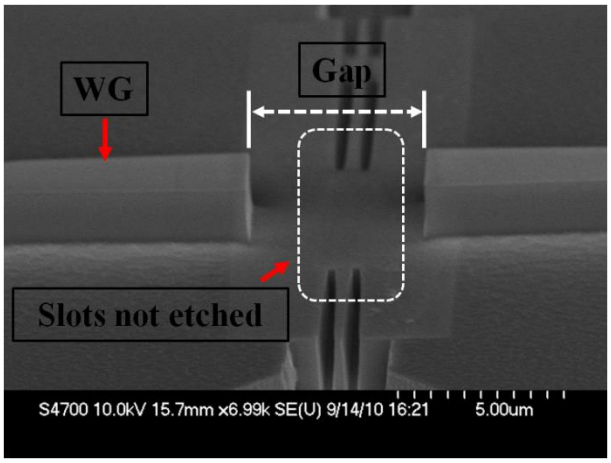

Figure 6.15: Slots are not etched in the gap region, where thick layer of residual resist persisted.

RIE etching was carried out to define the slots as illustrated in Figure 6.15. The SEM image clearly demonstrates that slots were not defined in the gap region of the waveguide, where thick layer of residual resist persisted.

6.6.3 Self aligned bi-level etching design

In order to fabricate the monolithic coupled lasers incorporating the deep etched slots for intra cavity reflector (ICR), a processing similar to the split waveguide approach was finally used. First, both the waveguide and the ICR were patterned and shallow etched in a single step. Then a layer of thick PMMA was patterned to protect the shallow etched waveguides during the deep etching of slots and trench. This approach relaxes substantially the critical alignment tolerances experienced in the previous devices as both slots and waveguide are defined in the same lithographic step. A schematic of the device geometry with the deep etched ICR is illustrated in Figure 6.16.

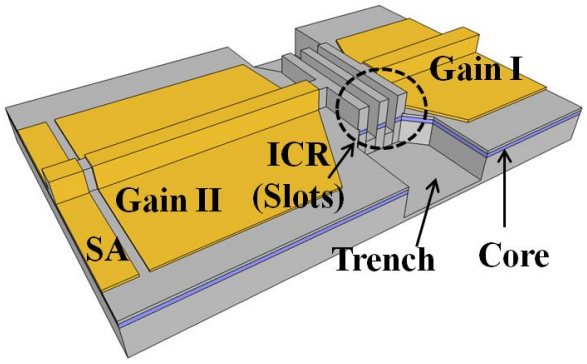

Figure 6.16 : Schematic of shallow etched waveguide design with deep etched ICR(slots) and a trench.

The details of all the steps involved in the fabrication of the self-aligned design are given in Appendix C and the main fabrication steps are summarised in Figure 6.17. First, the desired pattern of the ridge waveguides and slots was transferred onto the semiconductor substrate by using a HSQ hard mask (Figure 6.17 (a)). A shallow etching of the waveguide and ICR was then carried

out, (Figure 6.17 (b)), followed by the patterning of a thick bi-layer of PMMA that protects the entire sample, except for a window on the top of the ICR and trench (Figure 6.17 (c)). The PMMA resist exhibits poor etch resistance, the patterning of the window and the dry etching stage were repeated. Finally, the PMMA and HSQ resists were stripped using Acetone and HF acid (Figure 6.17 (d)). The fabrication process is completed by sample planarisation, contact window opening, metallisation and annealing.

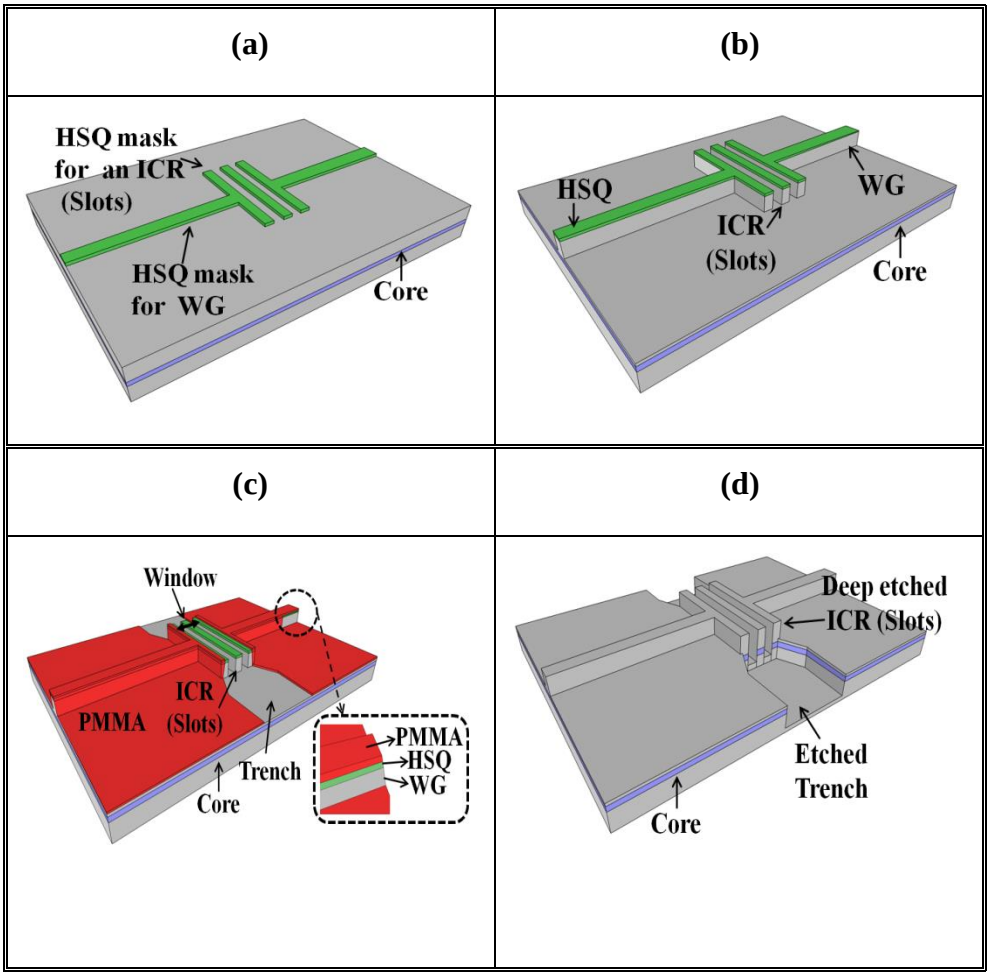

Figure 6.17: (a) Schematic of the HSQ mask for waveguide (WG) and slots; (b) shallow etching of the WG and slots; (c) patterning of PMMA resist to protect the waveguide (the inset on the lower right corner shows a magnified view of the layer of PMMA and HSQ on the top of WG); (d) shallow etched WG with deep etched slots and trench.

A number of test samples were prepared to optimise the various fabrication steps. Figure 6.18 (a) illustrates the shallow etched waveguide with four deep etched slots to form an ICR and the deep etched trench on the side to improve the gas flow during dry etching. Figure 6.18 (b) shows the cross-sectional view of four ~3.1 μm deep etched slots, cleaved along the waveguide.

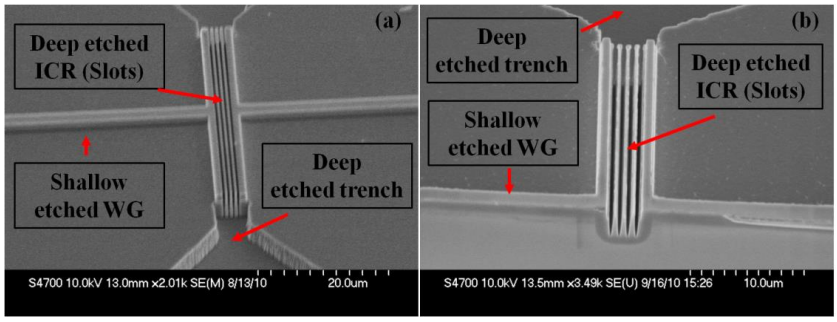

Figure 6.18: (a) Shallow etched waveguide, with four deep etched slots and a deep trench (b) Cross-sectional view of ~3.1 μm deep four slots.

Similarly to the previous set of devices, the development of the HSQ pattern proved more critical than expected. In fact, the central part of the slots was not properly cleared during the HSQ development stage, which resulted in a non-uniform etching of the slots. In the FEI image of Figure 6.19 (a) the white dotted lines illustrate the portion of the slots which is not etched, while the etched portion of the slots is shown by black dotted lines.

Following the deep etching, resist strippers (Acetone and HF acid) were used to remove PMMA and HSQ from the sample. The optical microscope image of a device after resist stripping is illustrated in Figure 6.19 (b). The uniform surface at the waveguide and slot intersection enclosed by white dotted box demonstrates that the slots were not etched. Therefore, after completion of all the fabrication steps it was decided to carry out focus ion beam (FIB) milling in order to define an ICR for the coupled cavity devices. This technique is discussed in the next section.

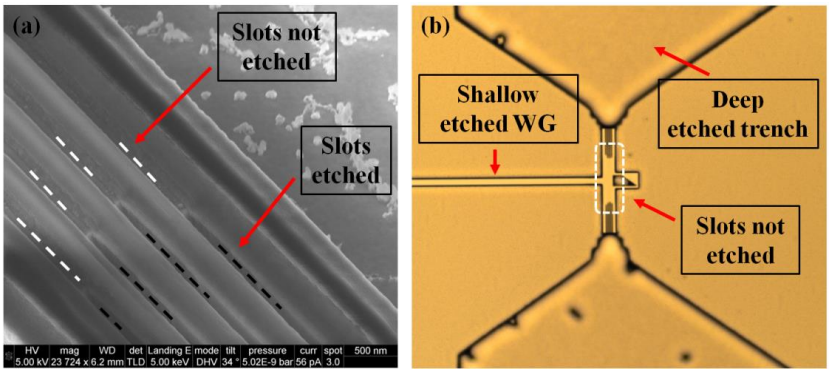

Figure 6.19: (a) White and black dotted lines illustrate the part of the slots which is not etched and etched, respectively. (b) Optical microscope image of the waveguide and slots after resist stripping.

6.7 Focus ion beam milling

Focus ion beam (FIB) milling was used in an attempt to fix the incomplete etching of the slots discussed in the previous section. FIB milling is the ideal technique for post-processing interventions because of its flexibility and its direct writing capability of submicron patterns with high aspect ratio [13]. Moreover, FIB does not require any mask or alignment markers [13-15]. FIB milling of the semiconductor devices mounted on a brass bar was carried out at the University of Southampton by Marek E. Schmidt [16]. The milling was carried out on a bar of devices having cleaved front facets, whereas the back end facet of each device was defined by four parallel slots. The cleaved bar contains 1190 µm long, two sections (SA and gain section) and coupled cavity mode-locked laser (CCM) devices. Schematic of such devices is illustrated in Figure 6.20.

Figure 6.21 illustrates SEM images of top and cross-sectional views of different slots obtained by FIB milling. Several tests were done in order to optimise the process parameters and evaluate the optimal slot width that could provide the desired slot shape and etch depth.

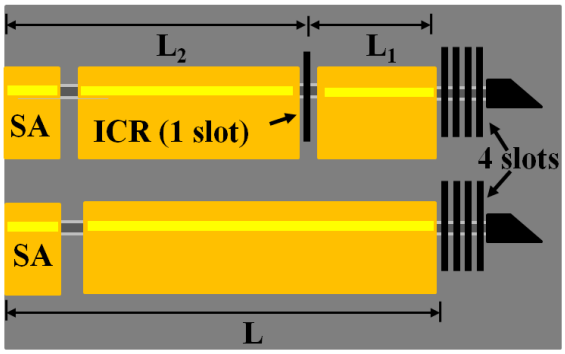

Figure 6.20 : Schematic of devices on which FIB milling was carried out.

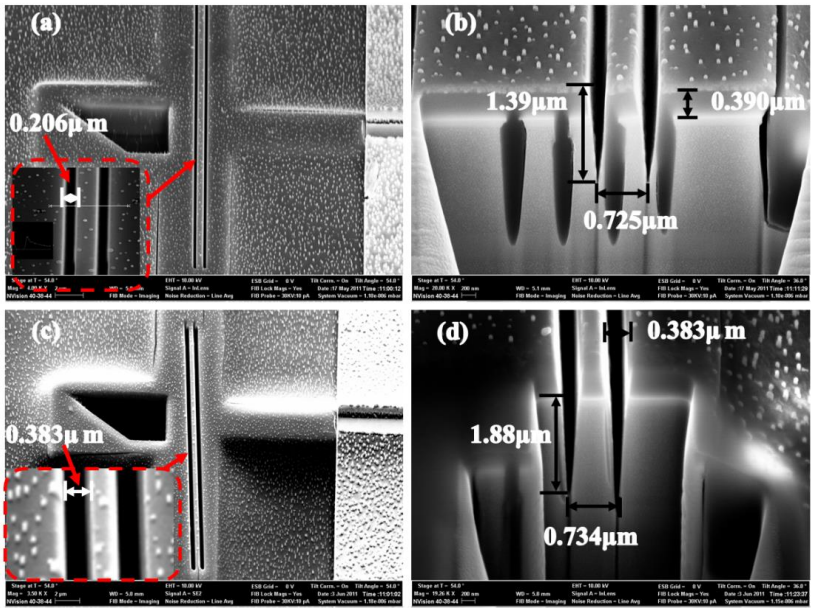

Figure 6.21 : SEM images of 0.206 µm wide and 1.39 µm deep slots: (a) top view and (b) cross-sectional view. SEM images of 0.383 µm wide and 1.88 µm deep slots: (c) top view and (d) cross-sectional view.

The capabilities of the FIB milling technique were initially evaluated using different slot openings of two parallel slots. A magnified top view of nearly 0.206 µm wide slots is illustrated in lower left corner of Figure 6.21 (a), while the cross-sectional view is shown in Figure 6.21 (b). The total depth of the slots is 1.39 µm, which also includes ~0.390 µm planarization and the distance between the centres of the slots satisfies the third order Bragg condition (0.725 µm). In order to

increase the etch depth, a second test milling of two parallel slots was carried out by milling slots with a wider opening, as illustrated in Figure 6.21 (c). The cross-sectional view of the two slots in Figure 6.21(d), shows that the depth of the slots is increased to 1.88 μm (including ~0.390 μm planarisation), which is, however, still insufficient for defining the ICRs. These tests indicate that FIB cannot achieve the required aspect ratio and slot verticality that is required for the ICRs. Therefore, two alternative solutions were explored and will be discussed in the next section.

6.7.1 Deep slot solutions

To achieve deep etched (≥ 2.5μm) slots with narrow width in the core region, two alternative solutions were investigated.

I. Removal of upper cladding:

Milling of deep slots by removing the upper cladding consisted of two steps. In the first step, a large square was FIB etched on the ICR region before the milling of the actual slots (Figure 6.22 (a)). Although a second milling step was able to define slots penetrating through the core of the waveguide, the magnified image in the lower left inset of Figure 6.22 (a) demonstrates the uneven bottom surface of the rectangular pattern. The high variability in the milling rate is a consequence of the poor planarity of the surface. Due to this reason, this technological solution was discarded.

II. Wide single slot:

The tests on the milling of slots with a wider opening indicated that the required depth and slot width in the core region (~0.724 μm) can only be achieved if the opening of the slot on the top of the sample is larger than 1 μm. This is illustrated by the SEM picture of Figure 6.22 (b) where a slot depth of 3.32 μm is achieved with a slot opening of 0.87μm. Therefore, single and wider slots with an opening of 1 μm were milled along the desired location of the waveguide as illustrated in Figure 6.22 (c).Similar slot milling was carried out at the end of each

waveguide to define a back reflector, as illustrated in Figure 6.22 (d). These devices were tested to check the lasing parameters by first measuring their light current *(L-I)* characteristics at room temperature (20°C).

The *L-I* curves of the two section mode-locked lasers were obtained by applying forward bias on both sections. The *L-I* curve of one such device is shown in the Figure 6.23 (a), where the threshold current is around 95 mA. The FIB milling increased the threshold current by nearly 300 % compared to the conventional FP lasers with both cleaved facets.

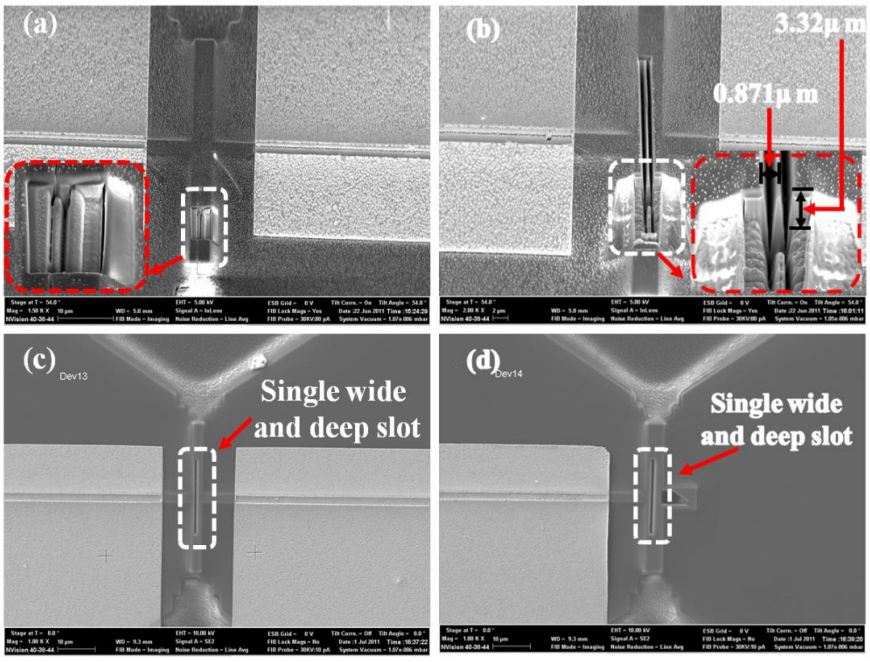

Figure 6.22: SEM image of (a) FIB milled rectangular pattern prior to mill the deep slots; (b) a 0.871 µm wide slot opening with 3.32 µm deep slots; (c) a single slot along the waveguide to define the ICR and (d) at the end of the waveguide to define the back mirror.

Similarly, a significant spread in threshold current from laser to laser was also observed, as the lasing threshold of other devices varied by +/- 10 mA. Such a substantial current threshold increasing is attributed to the severe back scattering of the semiconductor-air interface after the FIB treatment a and possibly to poor

verticality of the slot [17]. The optical spectrum of the two section laser is illustrated in Figure 6.23 (b), while both sections were forward biased at a current of 100 mA. The peak wavelength is around 1530 nm and the mode-spacing corresponds to a repetition frequency of ~36 GHz. This repetition frequency in turns corresponds to a cavity length of around 1190 µm and ascertains that light is reflected by the FIB milled mirror at the back of the cavity.

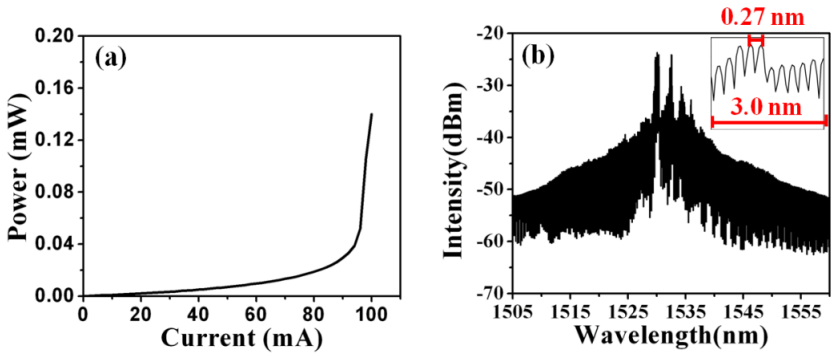

Figure 6.23: Measurement results of a two-section FP laser with a single-slot FIB milled mirror: (a) the *L-I* curve and (b) the optical spectrum (at 100 mA) where both sections are forward biased.

In a second set of measurements, the *L-I* curves and optical spectra of six coupled cavity devices were acquired. Unfortunately, no lasing was observed in any of these devices. The measured *L-I* curve and optical spectrum (at 130 mA current) of one of the coupled cavity devices is illustrated in Figure 6.24 (a) and (b), respectively.

These results indicate that the two section mode-locked laser devices exhibit low output power and higher threshold, while monolithic coupled cavity devices do not lase at all. One reason that could explain this behaviour might be related to the formation of Gallium *(Ga)* residues during the milling, which increase the free carriers on the interfaces resulting in higher optical losses. The easiest solution to remove *Ga* residues is to anneal the devices at high temperature for several hours [18]. Therefore, these devices were annealed at 180° C for four

hours but no improvement in their lasing performance was registered after the annealing.

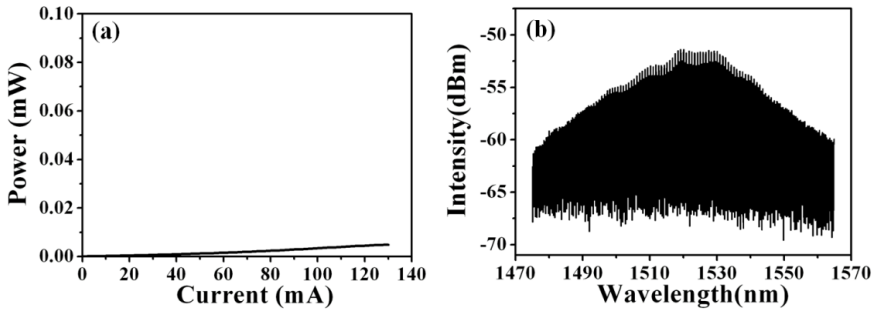

Figure 6.24: Measurements of (a) the *L-I* curve and (b) the optical spectrum (at 130 mA) of a coupled cavity lasers when all the sections are forward biased.

A second reason that could lead to higher optical losses is an insufficient slot depth in the core region. If the slots depth were shallower than the expected, the profile of the slots in the core region might be far from vertical and the interaction with the optical mode would result in scattering most of the light into the lower cladding. To check this, it was decided to FIB mill much wider slots. The wider slots would relax the fabrication tolerance and guarantee vertical sidewalls in the core region with the drawback, however, of increasing the propagation losses due to diffraction.

6.7.2 FIB milling of wide slots

Simulations were performed prior to carrying out any FIB milling to find the optimum slot width. The simulation results shown in the Figure 6.25 illustrate that slot widths of 3.5 and 4.2 μm maximize the reflectivity at a wavelength of 1550 nm. These widths correspond to 29^{th} and 35^{th} order Bragg gratings.

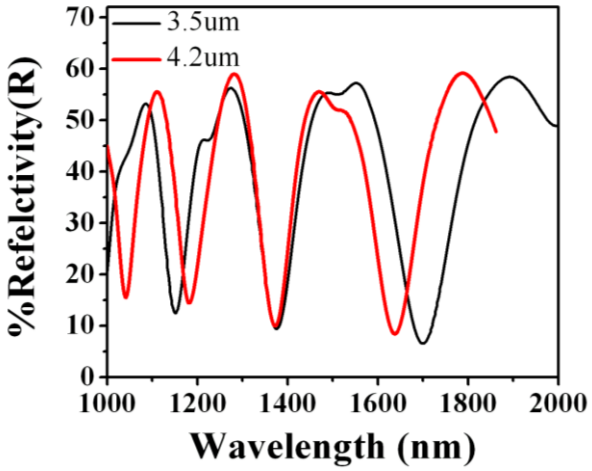

Figure 6.25: Reflectivity from a slot with a width of 3.5 (black curve) and 4.2 µm (red curve) as a function of the wavelength.

Because an effective control over the width in the core region was quite difficult to achieve due to the non-perfect verticality of the milling etching, preliminary tests were carried out on slots with different openings. A wider opening of the slots enabled to achieve slot widths close to the required values in the core region, hence maximizing the reflectivity by taking into account the inclination of the walls. Figure 6.26 (a) and (b), show SEM images of the top and side view of a ~ 8.0 µm deep slot with a ~4.76 µm wide slot opening. As the side walls are not perfectly vertical, milling of a ~4.76 µm wide slot opening enabled to achieve the required ~4.2 µm slot width in core region.

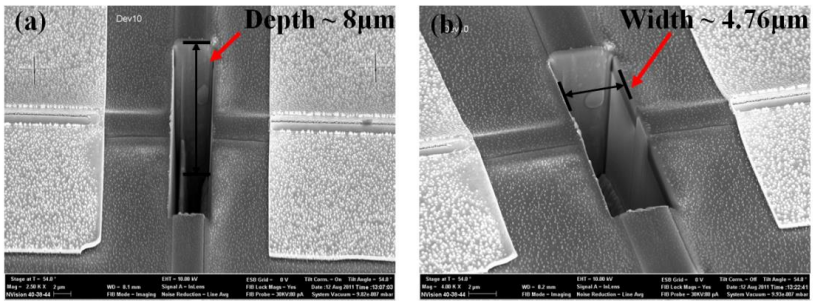

Figure 6.26: SEM images of wider slots: (a) top and (b) side view.

In order to test the lasing characteristics after milling a wider slot into the devices, the *L-I* curves and optical spectra of the devices were measured at room temperature (20°C). The *L-I* curve of a device shown in the Figure 6.27 (a), illustrates that the lasing threshold is 51 mA when both sections of the device are forward biased. Although, an increase in threshold current was observed compared to the lasers with both cleaved facets (i.e. 24 mA), these figures are much lower than the current thresholds measured on the previous milled (~1.0 µm wide slots) devices. This can be attributed to the more vertical profile of the side walls in the core region accompanied by reduced scattering of the optical mode in the lower cladding due to very deep milling (~8.0 µm). The optical spectrum of the two section laser is shown in Figure 6.27 (b), which is measured for a fixed current of 78 mA. The peak wavelength is around 1544 nm and the mode-spacing shown in the inset of Figure 6.27 (b) corresponds to a repetition frequency closer to 37 GHz.

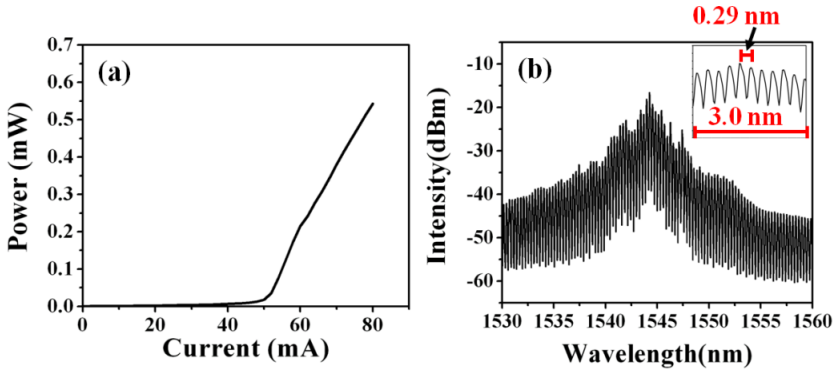

Figure 6.27: Measurements results of a two section laser with one deep single slot when both sections are forward biased: (a) the *L-I* curve and (b) the optical spectrum (at 78 mA).

The *L-I* characteristics and optical spectra of coupled cavity devices consisting of two gain sections *(L_1: L_2 = 1:2* and $L_2 \approx$ 790 µm*)* were also measured. The measurements were first carried out by forward biasing all the sections (i.e SA, Gain I and Gain II) of the device. The measured *L-I* curve and

optical spectrum (at a fixed current of 100 mA) of the coupled cavity device is shown in Figure 6.28 (a) and (b), respectively.

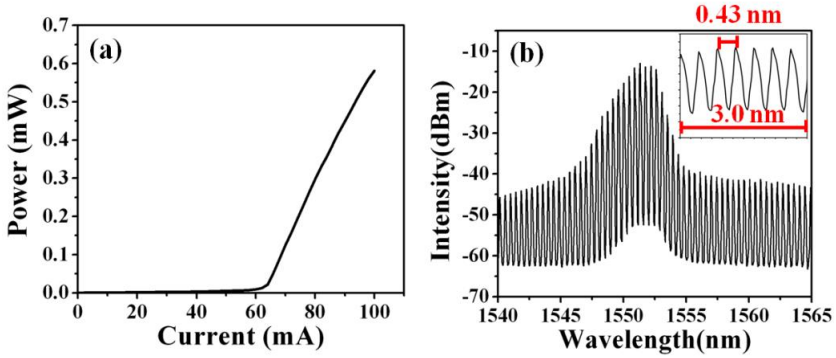

Figure 6.28: Measurements results of a coupled cavity lasers with single-slots when all the sections are forward biased: (a) the *L-I* curve and (b) the optical spectrum (at 100 mA).

The threshold current of the device is around 64 mA and the mode-spacing corresponds to a repetition frequency close to 54 GHz, which is originated by the longer gain section (~790 μm). This result clearly indicates that light is only reflected by the milled mirror of the ICR (slot) between the two gain sections and that no coupling effects between the two cavities occur. No evidence of mode-locking operation was observed when reverse biasing the SA section.

6.7.3 Mode-locking results at low temperature

Semiconductor laser diodes are very sensitive to temperature as discussed in chapter 4 (see characteristic temperature). In QD lasers, at low temperature carriers remain in the QDs where they were first captured [19]. As a consequence the thermal escape of the carriers to the wetting layer is believed to be suppressed, therefore, the nonradiative recombination process is minimised [20]. This indicates that performance of QD laser diodes can substantially be improved at low temperature. The devices were tested at low temperature by using liquid Nitrogen *(LN)* that kept the temperature of the copper heat sink at around -20°C. Only a few modifications were made to the measurement setup as the cooling was

achieved by connecting one end of a copper strip to the copper heat sink and placing the other end in a Pyrex cup filled with *LN*.

The 1190 µm long multi contact device under test is identical to that of Figure 6.28 and consists of two gain sections L_1 and L_2 of lengths 400 µm and 790 µm, respectively. The gain section L_2 also includes an absorber with a length of 86 µm (~7.2 % of the total cavity length). The mode-spacing calculated from the optical spectrum of the FIB milled 1190 µm long FP laser corresponds to an average repetition frequency of ~36 GHz. Therefore, the coupled cavity device consisting of two gain sections *(L_1: L_2 = 1:2),* is expected to operate at third harmonic of the fundamental repetition frequency, which is ~108 GHz. The device at lower temperature was tested under several biasing conditions and exhibited mode-locking when i) All sections were forward biased; (called "FP mode" in the following) ii) SA was left floating ("SA floating mode") and iii) SA was reversed biased ("SA reversed biased mode").

- ***Mode-locking in FP mode:***

In FP mode, mode-locking was achieved when the SA and both gain sections were forward biased. The measured optical spectrum at low gain current (I_g) show a mode spacing of around 54 GHz. Figure 6.29 (a), corresponds to the FSR of the longer gain section indicating that light is mostly reflected by the mirror formed by the milled ICR between the two sub cavities.

Figure 6.29 (b) illustrates the optical spectrum obtained at a higher gain current value of I_g= 140 mA. As a consequence of the higher gain current, the peak wavelength tends to red shift and the optical spectrum clearly demonstrates the suppressed and unsuppressed modes. The modes-spacing (0.87 nm) is illustrated in the inset of Figure 6.29 (b), which corresponds to a repetition frequency of around 108 GHz (third harmonic). This demonstrates that the lower temperature (-20°C) and the higher current (I_g= 140 mA) provide sufficient gain to suppress the additional losses introduced by the FIB milled slots. The inset also illustrates that there exists only one suppressed mode between the two widely

separated modes. The mode corresponding to full FP cavity is not observed in the optical spectrum.

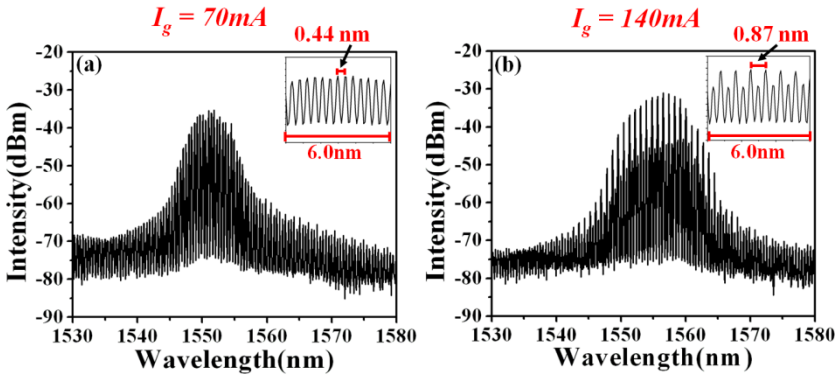

Figure 6.29: Optical spectra of the coupled cavity device measured at a heat sink temperature of -20°C , where all sections are forward biased at (a) 70 mA (b) 140 mA, respectively.

Figure 6.30 (a) illustrates the autocorrelation trace obtained for a fixed gain current, Ig= 70 mA. Although the extinction ratio of the pulses is low, the pulse period (18.49 ps) corresponds to a repetition frequency of ~54 GHz, which in turns can be correlated to the longer sub-cavity length

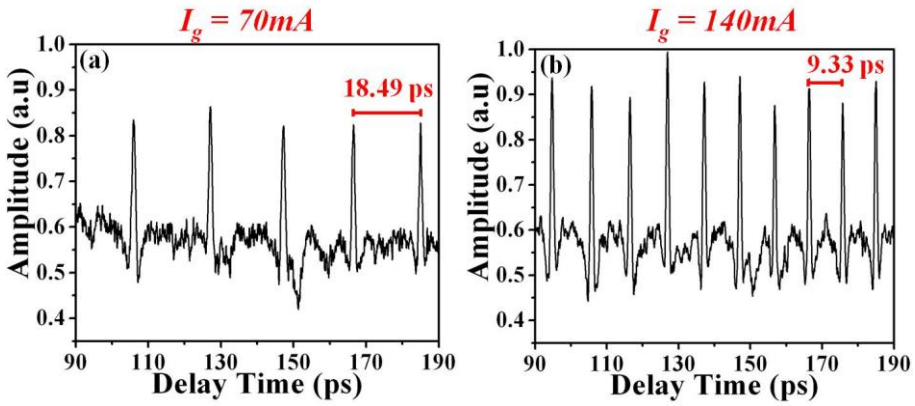

Figure 6.30: The autocorrelation trace of the coupled cavity device measured at heat sink temperature of -20°C , where all the sections are forward biased at (a) 70 mA and (b) 140 mA.

The pulse train at higher gain currents is illustrated in Figure 6.30 (b), and shows an average period of 9.33 ps, confirming the repetition frequency of around 107 GHz. Because the optical pulses had an extinction ratio of less than 50 %, the mode-locking is rather unstable and the extraction of a value for the pulse width is meaningless.

- ***Mode-locking in SA floating mode:***

Evidence of mode locking was also observed when the absorber (SA) was kept floating and both the gain sections were forward biased. Similar to the FP mode, at lower gain current the mode spacing of the measured optical spectrum corresponds to a repetition frequency of ~54 GHz, which corresponds to the longer sub-cavity.

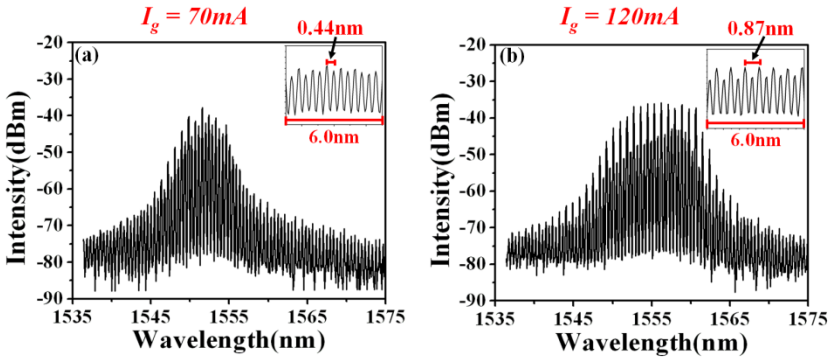

Figure 6.31: Optical spectra of the coupled cavity device measured at a heat sink temperature of -20°C , where SA is floating and the two gain sections are forward biased at (a) 70 mA and (b) 120 mA.

The optical spectrum obtained at I_g= 120 mA (Figure 6.31 (b)) shows the suppressed and unsuppressed modes with a repetition frequency of around 107 GHz.

The autocorrelation trace recorded for I_g= 70 mA is illustrated in Figure 6.32 (a), in which the spacing between two consecutive pulses was 18.70 ps. The autocorrelation trace recorded for I_g= 120 mA is illustrated in Figure 6.32 (b),

where the pulse spacing between two consecutive pulses is 9.32 ps and corresponds to a repetition rate of around 107 GHz.

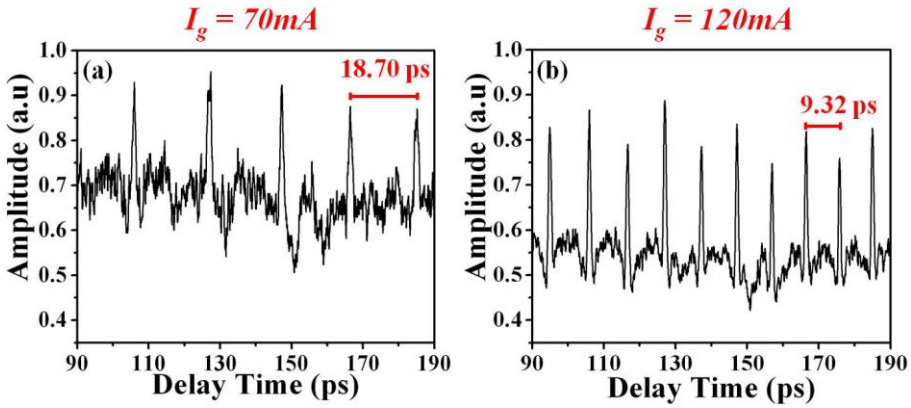

Figure 6.32: Autocorrelation trace of the coupled cavity device measured at a heat sink temperature of -20°C , where SA is floating and the two gain sections are forward biased at (a) 70 mA and (b) 120 mA.

- ***Mode-locking in SA reverse bias mode:***

The optical spectrum and autocorrelation traces were recorded for SA reverse voltages ranging from 0 to -2.8 V and for different gain current values. Similar to the FP and SA floating modes, also the SA reversed bias mode showed a mode spacing corresponding to a repetition frequency of around 54 GHz at V=0 and for low gain current. For SA reverse voltages exceeding -0.2 V and when a low current was applied to the gain sections, the mode spacing corresponding to higher repetition rates was clearly observed. The optical spectrum measured at V_{SA}= -0.2 V and I_g= 80 mA is illustrated in the Figure 6.33 (a), whereas the figure in the inset shows the modes spacing of~0.87 nm that corresponds to the third harmonic repetition rate. As the gain current is increased, both the modal suppression in the optical spectrum and the stability of the pulses in the autocorrelation trace greatly improves. This is illustrated by the optical spectrum and autocorrelation trace measured at V_{SA}= -2.4 V and I_g= 120 mA (Figure 6.33 (b) and Figure 6.34 (b)).

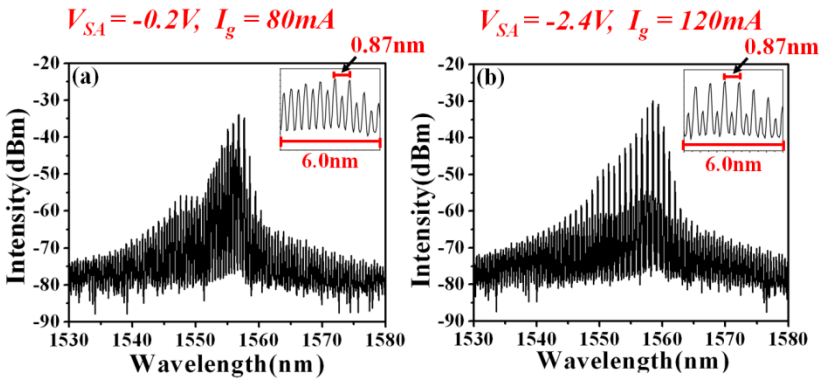

Figure 6.33: Optical spectra of the coupled cavity device measured at a heat sink temperature of -20°C , where SA is reverse biased and two gain sections are forward biased at (a) V_{SA}= -0.2 V, I_g= 80 mA and (b) V_{SA}= -2.4 V, I_g= 120 mA.

The improvement in the mode-locking behaviour at the third harmonic of the fundamental frequency is confirmed by the autocorrelation traces recorded for V_{SA}= -0.2 V, Ig=80 mA and V_{SA}= -2.4 V, Ig= 120 mA as illustrated in the Figure 6.34 (a&b).

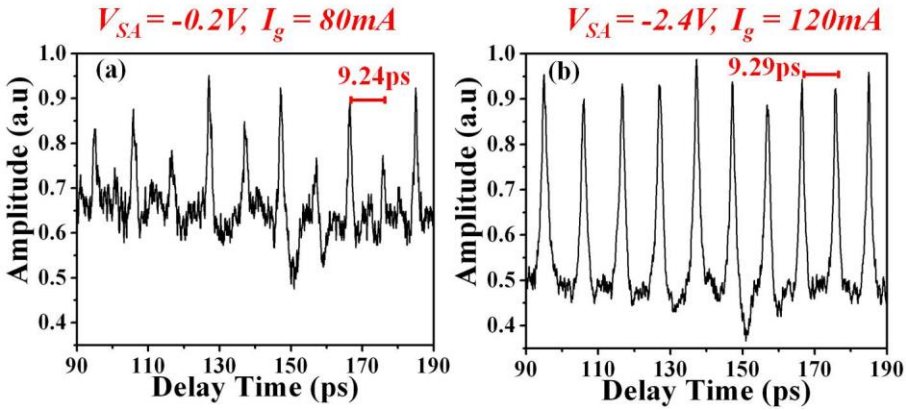

Figure 6.34: Autocorrelation trace of the coupled cavity device when the SA is reverse biased and the two gain sections are forward biased at (a) V_{SA}= -0.2 V, I_g= 80 mA and (b) V_{SA}= -2.4 V, I_g= 120 mA.

- ***Discussion on mode-locking results at low temperature:***

For all the biasing conditions (all sections forward biased and SA floating) the mode spacing of the measured optical spectra at low gain current show a free spectral range (FSR) that corresponds to the longer sub cavity with a repetition rate of around 54 GHz. This indicates that at lower gain current no coupled cavity effect is present probably because the FIB mirrors are very lossy. The observed repetition frequency (~54 GHz) reveals that most of the light is reflected by the mirror formed by the milled air gap (ICR) between two sub cavities and thus the shorter sub-cavity does not take part in the lasing action at low current density.

At higher gain currents, suppressed and unsuppressed modes were clearly observed in the optical spectra. An average mode-spacing of around 0.87 nm was measured, which corresponds to a repetition frequency of around 107 GHz (third harmonic).The absence of the modal structure corresponding to full FP cavity suggests that the two sub-cavities are very weakly coupled due to the high losses of the FIB milled slots that define the cavities. As a consequence, lasing mainly occurs on the longer cavity and some filtering effects from the short cavity only appear for high injection currents.

One surprising result was that mode-locking was observed without any saturable absorber, i.e. when all the device sections were forwarded biased. Passive mode-locking achieved in a single section QD FP-type laser without SA was already reported by a number of groups [21-25]. The InAs/InP QD material is highly nonlinear [26], therefore, passive mode-locking in single section FP devices is either attributed to four-wave mixing (FWM) [22] alone or to a combination of non linear optical effects within the QD gain cavity such as self-phase modulation (SPM), cross phase-modulation (XPM) and FWM [23]. Above lasing threshold, these non linear effects, combined with current fluctuations and temperature variations are responsible for initiating the mode-locking operation [23]. Similarly, mode-locking can occur in a FP cavity with the SA section kept floating.

Similarly to the situations in which the SA is either forward biased or kept unbiased, a low reverse biasing on the SA (i.e. V_{SA}< -0.2 V) exhibits a repetition rate corresponding to the longer sub cavity. When the reverse biasing $V_{SA} \geq$ -0.2 V, the mode spacing and pulse period corresponding to the higher repetition rate is observed even at lower gain current. As expected, the biasing region over which mode-locking is observed largely increase for higher current gain. In fact, for current values nearly twice the threshold, stable mode-locking at the third harmonic occurs for a SA reversed biasing between 0 V to -2.8 V. Also, for higher current values, the extinction ratio of the pulses improves. A similar improvement in the pulse modulation is also observed for higher reverse voltages, which agrees with previous observations that show an improvement in the pulse shaping mechanism for high SA reverse bias, possibly due to the reduction in carrier life time [27]. The CCM laser is a multi- contact 1190 μm long device, consisting of 87.8 %, 5 % and 7.2 % of gain, gap, and SA sections, respectively. In the two section stable mode-locked laser discussed in chapter 4, the length of the gap section was in the range of 1.22-1.28 %, which was 4 times shorter than the gap section in the CCM laser. The longer gap section combined with the additional losses originated by the FIB milled mirrors adds a substantial contribution to the total loss of the cavity. These extra losses, mostly unsaturated, are probably the origin for the non-optimal mode-locking performance observed in the CCM lasers.

6.8 Conclusions

In this chapter, the design of monolithic coupled cavity lasers along with the main fabrication steps and device performance was discussed. Three different device geometries (deep, split and self aligned bi-level etched waveguides) were explored in order to reduce the negative consequences of the RIE lag effect on the deep etched intra-cavity reflectors. Because of a number of problems encountered with the patterning of the mask for the slots, it was decided to define the ICR by FIB milling. The final devices had ICRs made of a single slot with a width of

~4.76 μm and depth of nearly 8.0 μm. These devices exhibit the expected third (~107 GHz) harmonic mode-locking at low temperature (-20°C). Results indicate that mode-locking is incomplete and maximum modulated pulses (i.e. with a 50 % extinction ratio) are achieved for higher gain current and reverse biased conditions. Similarly to what previously discussed in chapter 5, we believe that the main reasons behind the non-optimal mode-locking performance stem from the additional losses originated by the ICR mirrors and the long unbiased section (i.e. 5% of the total cavity length). Moreover, the longer cavity in CCM lasers is defined by cleaving and therefore a slight cavity mismatch might occur which does not allow proper length matching between the sub-cavities. Because of these extra losses, the desired coupled cavity effect is only measured for low temperatures and high cavity gains. Although the final mode-locking performance was not as stable as expected, the development of the CCM devices generated a substantial understanding on both the device design and fabrication processing. In particular, the non-verticality of the sidewalls in the FIB milling cannot produce the low loss ICRs required for CCM mode-locking. The best technological solution for the ICRs appears to be the patterning of a thick HSQ mask followed by dry etching. Both the design and the technological processing for this approach were optimised except for the non-perfect development of the HSQ mask that defines the ICRs. This technological step will require some further development for the fabrication of future CCM devices.

6.9 References

1. *Yanson, D.A., et al., Ultrafast harmonic mode-locking of monolithic compound-cavity laser diodes incorporating photonic-bandgap reflectors. Quantum Electronics, IEEE Journal of, 2002. 38(1): p. 1-11.*

2. *Yanson, D.A., et al. Terahertz-frequency mode-locking of monolithic compound-cavity laser diodes. in Lasers and Electro-Optics Society, 2002. LEOS 2002. The 15th Annual Meeting of the IEEE. 2002.*

3. *Yanson, D.A., et al., Terahertz repetition frequencies from harmonic mode-locked monolithic compound-cavity laser diodes. Applied Physics Letters, 2001. 78(23): p. 3571-3573.*

4. *Avrutin, E.A., et al., Analysis of harmonic (sub) THz passive mode-locking in monolithic compound cavity Fabry-Perot and ring laser diodes. Optoelectronics, IEE Proceedings -, 1999. 146(1): p. 55-61.*

5. *Chong, H.M.H., W.K. Tan, and A.C. Bryce, Reflectivity of deep-etched InGaAs-InP waveguide Bragg reflectors. physica status solidi (c), 2007. 4(5): p. 1646-1648.*

6. *Lianping, H., et al., 160-GHz Passively Mode-Locked AlGaInAs 1.55-μm Strained Quantum-Well Compound Cavity Laser. Photonics Technology Letters, IEEE, 2010. 22(10): p. 727-729.*

7. *[Available online]: http://camfr.sourceforge.net/index.html : 2011.*

8. *Kotlyar, M.V., et al., High-aspect-ratio chemically assisted ion-beam etching for photonic crystals using a high beam voltage-current ratio. Journal of Vacuum Science & Technology B: Microelectronics and Nanometer Structures, 2004. 22(4): p. 1788-1791.*

9. *Karouta, F., et al. Three level masking for improved aspect ratio InP-based photonic crystals. in Indium Phosphide and Related Materials, 2008. IPRM 2008. 20th International Conference on. 2008.*

10. *Gottscho, R.A., C.W. Jurgensen, and D.J. Vitkavage, Microscopic uniformity in plasma etching. Journal of Vacuum Science & Technology B: Microelectronics and Nanometer Structures, 1992. 10(5): p. 2133-2147.*

11. *Happ, T.D., et al., Nanofabrication of two-dimensional photonic crystal mirrors for 1.5 μm short cavity lasers. Journal of Vacuum Science & Technology B: Microelectronics and Nanometer Structures, 2001. 19(6): p. 2775-2778.*

12. *Pommereau, F., et al., Fabrication of low loss two-dimensional InP photonic crystals by inductively coupled plasma etching. Journal of Applied Physics, 2004. 95(5): p. 2242-2245.*

13. *Ren, Q., et al., Etched facet and semiconductor/air DBR facet of a AlGaInP laser diode prepared by focused ion beam milling. Solid State Communications, 2004. 130(6): p. 433-436.*

14. *Sung Won Youn, H.G. Masaharu Takahashi, and and Ryutaro Maeda, A study on focused ion beam milling of glassy carbon molds for the thermal imprinting of quartz and borosilicate glasses. Journal of Micromechanics and Micro Engineering, 2006. 16 p. 2576–2584.*

15. *Sugiyama, M. and a.G. Sigesato, A review of focused ion beam technology and its applications in transmission electron microscopy. Journal of Electron Microscopy, 2004. 53(5): p. 527–536.*

16. *Schmidt, M.E., Plasma enhanced chemical vapor deposition of nanocrystalline graphene and device fabrication development, in Faculty of Physical & Applied Science. 2012, University of Southampton, UK: Sothampton.*

17. *Overwijk, M.H.F. and J.A. de Poorter, High-quality focused-ion-beam-made mirrors for InGaP/InGaAlP visible-laser diodes. Journal of Applied Physics, 1993. 74(12): p. 7048-7053.*

18. *Vallini, F., et al., Effects of Ga^+ milling on InGaAsP quantum well laser with mirrors milled by focused ion beam. Journal of Vacuum Science & Technology B: Microelectronics and Nanometer Structures, 2009. 27(5): p. L25-L27.*

19. *Li, S.G., et al., Temperature dependent lasing characteristics of InAs/InP(100) quantum dot laser. Materials Science in Semiconductor Processing, 2012. 15(1): p. 86-90.*

20. *Rossetti, M., et al., Modeling the temperature characteristics of InAs/GaAs quantum dot lasers. Journal of Applied Physics, 2009. 106(2): p. 023105-023105-8.*

21. *Renaudier, J., et al., 45 GHz self-pulsation with narrow linewidth in quantum dot Fabry-Perot semiconductor lasers at 1.5 Âµm. Electronics Letters, 2005. 41(18): p. 1007-1008.*

22. *Gosset, C., et al., Subpicosecond pulse generation at 134 GHz using a quantum-dash-based Fabry-Perot laser emitting at 1.56 um. Applied Physics Letters, 2006. 88(24): p. 241105-3.*

23. *Lu, Z.G., et al., 312-fs pulse generation from a passive C-band InAs/InP quantum dot mode-locked laser. Opt. Express, 2008. 16(14): p. 10835-10840.*

24. *Merghem, K., et al., Pulse generation at 346 GHz using a passively mode locked quantum-dash-based laser at 1.55 mu m. Applied Physics Letters, 2009. 94(2): p. 021107-3.*

25. *Tahvili, M.S., et al., Dual-wavelength passive and hybrid mode-locking of 3, 4.5 and 10 GHz InAs/InP(100) quantum dot lasers. Opt. Express, 2012. 20(7): p. 8117-8135.*

26. *Lu, Z.G., et al., Highly efficient non-degenerate four-wave mixing process in InAs/InGaAsP quantum dots. Electronics Letters, 2006. 42(19): p. 1112-1114.*

27. Green, R.P., et al., Fast saturable absorption and 10 GHz wavelength conversion in Al-quaternary multiple quantum wells. Opt. Express, 2011. 19(10): p. 9737-9743.

Chapter 7

Conclusions

7.1 Conclusions

This thesis dealt with the development of high repetition rate InAs/InP quantum dot mode-locked lasers operating at wavelength around 1.55 μm. Although a number of fabrication issues hampered the development of the coupled-cavity devices and the dual-lobe spectral characteristic substantially limited the available gain bandwidth for mode-locking, several useful outcomes were generated in the course of this work.

Following a detailed assessment of the QD epilayer structure, shallow etched waveguides were modelled to find the optimum geometry for single mode operation. SMMLs with dual-contact configuration operating at ~35 GHz were then fabricated and characterised as a function of the saturable absorber (SA) length (from 3.2% to 19% of the total cavity length). Optimum mode-locking with pulse widths below 3.5 ps was found for SA lengths in the range of 5.2-7.2 %. A major improvement in the mode-locking performance was found by depositing a HR and AR coating on the two cleaved facets. As a result of the coating deposition, the optimum mode-locking operation shifted to higher injection current and the quantum efficiency increases (by a factor of ~2), which improved the maximum pulse peak power by a of factor of 1.8. Through autocorrelation and sonogram techniques, the behaviour of the mode-locking was evaluated in the

presence of the splitting of the optical spectrum, which is a typical feature of QD already reported by other groups and most likely originating from the splitting of the ground state. The measurements confirmed the presence of two pulse trains under some biasing conditions and the locking of only one lobe at high injection currents with a strong red chirp. In order to obtain higher repetition rates monolithic harmonic mode-locked lasers were designed, fabricated and characterised. Harmonic mode-locking at repetitions rates of ~71 GHz, ~107 GHz and ~238 GHz was demonstrated by placing the absorbers on cavity locations corresponding to the 2^{nd}, 3^{rd} and 7^{th} harmonics, respectively. More precisely, CPM and ACPM configurations, in which a single SA was placed at one-half and one-third of the cavity length, were used to achieve 2^{nd} and 3^{rd} harmonic. Double interval mode-locking (DIM) geometry was employed to generate 7^{th} order harmonic mode-locking. Although the expected harmonic mode-locking rates were obtained in all the tested geometries, mode-locking was often incomplete mainly because of three reasons: i) mismatch in the cavity lengths due to inaccuracies in the cleaving, ii) large unbiased sections increasing the losses in the cavities, and iii) non optimised SA lengths for multi contact devices. Therefore, the non-optimal performance of these devices motivated the development of more sophisticated coupled-cavity geometries that included deep etched intra-cavity reflectors. Such geometries reduce the cavity length mismatch as the position of the mirrors is defined at the lithographic stage. Moreover, because very short cavities can be precisely defined, the simpler single-SA configuration can be used to generate high repetition rates rather than the more complicated multiple SA designs. Reducing the number of SAs improves the robustness of the device and reduces the length of the unbiased sections. Three different design options were investigated which included deep, split and self aligned bi-level etched waveguide. A monolithically integrated coupled cavity device with shallow etched waveguides and an intra cavity reflector exhibited harmonic mode-locking at low temperature (-20°C). The coupled cavity effect was produced by a deep (~8.0 μm) and wide (4.76 μm) FIB milled intra cavity reflector (ICR) and the repetition rate (~107 GHz) corresponded to the expected 3^{rd} harmonic of the

cavity. The design of the ICR was a compromise between the minimum depth of the slot and the aspect ratio that could be achieved with FIB milling. Therefore, the slot had to be made much wider than initially designed with a consequent increase of the cavity losses. Despite the expected increase in the current threshold and the weak coupling between the cavities, the coupled-cavity geometry proved successful in generating harmonic mode-locking.

7.2 Future work

Suggestions for future work as a follow up to this project are outlined below:

- The generation of two distinct trains of pulses is a unique feature of QD gain materials. Although this phenomenon has already been reported by other groups, its origin is still not completely understood and its influence on the mode-locking behaviour is even less clear. The measurements show that the detuning between the two lobes increases with the square root of the optical power up to twice the current threshold thus suggesting a Rabi splitting of the ground state. Also, the sonogram measurements gave a better picture on the chirp of the pulses, but did not provide information on the correlation between the two pulse trains. A measurement of the optical spectrum as a function of the current with a high resolution optical spectrum analyser (i.e. with enough resolution to assess the linewidth of the individual cavity modes) could provide a better understanding on the locking between the two lobes and therefore on the correlation between the pulse trains.
- The most promising geometry for high harmonic mode-locking is that comprising short intra-cavity reflectors that precisely define two sub-cavities. Despite the very high losses introduced by the very large slots etched by FIB, the lasers exhibited harmonic mode-locking at ~107 GHz. Dry etching, which is a better fabrication solution in terms of aspect ratio, verticality and optical losses of the slots, could not be used because the E-beam resist did not completely develop in the slots. A further fabrication run could not be made because of lack of material. Future work should

concentrate on the patterning of the ICR slots, which was the only fabrication step that was not completely optimised.

- The deposition of HR and AR coatings on the two cleaved facets of the lasers proved a very simple technique to substantially increase the performance of the mode-locking. In fact, the maximum pulse peak power, which is highly important in several applications, was improved by a factor of ~1.8. Further measurements should confirm that these devices have a lower phase noise, as predicted by theoretical works. Also, HR/AR coating deposition is a very general approach that could enhance the performance of any type of mode-locked laser.

Appendix 'A'

Deep etched ridge waveguide design fabrication steps

After cleaving the sample, deep etched ridge waveguide laser fabrication process is carried out in the following order.

1. ***Cleaning of the sample:***
   - Clean sample in Opticlear, Acetone, IPA and RO water for 5 minutes each in the ultrasonic bath.
   - Blow dry with gaseous Nitrogen.
2. ***Realisation of e-beam markers:***
   - PMMA (15 % of 2010) at 5000 rpm for 60 seconds. Bake at 180 ºC for 30 minutes.
   - Spin PMMA (4 % of 2041) at 5000 rpm for 60 seconds and bake at 180 ºC for 90 minutes.
   - Clean any resist present on backside of the sample with cotton bud soaked in acetone after each spin.
   - VB6 *e*-beam writing.
   - Development in 1:1 IPA:MIBK solution at 23 ºC for 30 seconds, RO water for 30 seconds, RO water for 30 seconds, IPA for 30 seconds, blow dry with gaseous Nitrogen.
   - Metallisation with 33 nm NiCr: 120 nm Au, using *e*-beam Plassys machine.
   - Lift off deposited metals using acetone in hot water bath at 50 ºC for 2 hour. Clean the sample in acetone, IPA and RO water for 1 minute each. Blow dry with gaseous Nitrogen.
   - O2 ashing using asher for 10 minutes at 100 Watt power.
3. ***Realisation of a ridge waveguide structure:***
   - Pre-bake the sample on hot plate for 2 minutes at 90 ºC.
   - Spin 100 % HSQ at 2000 rpm for 60 seconds.

- Clean backside of the sample and bake at 90 ºC for 10 minutes.
- VB6 *e*-beam writing.
- Development in TMAH at 23 ºC for 30 seconds, RO water for 30 seconds, RO water for 30 seconds, IPA for 15 seconds.
- Blow dry with gaseous Nitrogen.
- Dry etch, using RIE ET340 machine to get ~4.6 μm deep etched waveguides.
- Wet etch the sample with 5:1 ratio of RO water and HF solution for 60 seconds, RO water for 60 seconds. Clean the sample in acetone, IPA and RO water for 2 minute each and blows dry with gaseous nitrogen.

4. Realisation of a current injection window:

- Deposit 200 nm of SiO_2 (PECVD).
- Spin 100 % HSQ at 4000 rpm for 60 seconds. Clean backside of the sample and bake in an oven at 180 ºC for 90 minutes.
- Finally, deposit 100 nm of SiO_2 (PECVD).
- PMMA (15 % of 2010) at 5000 rpm for 60 seconds and bake at 180 ºC for 30 minutes.
- PMMA (15 % of 2010) at 5000 rpm for 60 seconds and bake at 180 ºC for 30 minutes.
- PMMA (15 % of 2010) at 5000 rpm for 60 seconds and bake at 180 ºC for 30 minutes.
- Spin PMMA (4 % of 2041) at 5000 rpm for 60 seconds and bake at 180 ºC for 90 minutes. Clean backside of the sample after each spin.
- VB6 *e*-beam writing.
- Development in 1:1 IPA:MIBK solution at 23 ºC for 35 seconds, RO water for 30 seconds, RO water for 30 seconds, IPA for 30 seconds, blow dry with gaseous Nitrogen.
- Short O_2 clean for 2 minutes at 10 W.
- Dry etch with RIE 80 plus machine.
- O_2 ashing for 15 minutes at 100 Watt power.

- Clean the sample in acetone and then rinse with IPA and RO water for 1 minute each and blow dry with gaseous Nitrogen.

5. Realisation of p-contact:

- PMMA (15 % of 2010) at 5000 rpm for 60 seconds and bake at 180 ºC for 30 minutes.
- PMMA (15 % of 2010) at 5000 rpm for 60 seconds and bake at 180 ºC for 30 minutes.
- PMMA (4 % of 2041) at 5000 rpm for 60 seconds and bake at 180 ºC for 90 minutes. Clean backside of the sample after each spin.
- VB6 *e*-beam writing.
- Development in 1:1 IPA:MIBK solution at 23 ºC for 30 seconds, RO water for 30 seconds, RO water for 30 seconds, IPA for 30 seconds, blow dry with gaseous Nitrogen.
- Short O_2 clean for 2 minutes at 10 W.
- Deoxidise with 1:5 HCl: H_2O mixture for 30 seconds. RO water for 30 seconds and blows dry with gaseous Nitrogen.
- *p*-metal (30 nm Ti, 33 nm Pt and 240 nm Au) deposition using *e*-beam Plassys machine.
- Lift off using acetone in hot water bath at 50 ºC for 2 hours. After left off cleaning with acetone, IPA and RO water for 1 minute each, blow dry with gaseous Nitrogen.
- O_2 ashing for 15 minutes at 100 Watt power.

6. Thinning of the sample:

- Sample mounted *p*-side down on a glass strip, using resist S1818 at 2000 rpm for 5 seconds.
- Sample on glass strip baked at 90 ºC for 60 minutes.
- Mechanical thinning of the sample using aluminium oxide powder (9 µm/ 3 µm granules) with water mix.
- Cleaning in Opticlear for 10 minutes. Un-mount the sample from glass strip by keeping sample in acetone at 50 ºC for 30 minutes.

- Rinse sample with IPA and RO water, blows dry with gaseous nitrogen.

7. Realisation of n-contact:

- Sample mounted *p*-side down on a glass slide, using resist S1818 at 2000 rpm for 5 seconds and baked at at 90 ºC for 60 minutes.
- *n*-metal (14nm Au, 14nm Ge, 14nm Au, 11nm Ni, and 240nm Au) deposition using *e*-beam Plassys machine.
- Un-mount the sample from glass strip by keeping sample in acetone at 50 ºC for 30 minutes.
- Rinse sample with IPA and RO water, blows dry with gaseous Nitrogen.
- RTA annealing at 380 ºC for 60 seconds.

Appendix 'B'

Split waveguide design fabrication steps

The shallow etched split waveguide design fabrication process is carried out in the following order.

1. ***Cleaning of the sample:***
   - Same as in Appendix 'A'.
2. ***Realisation of e-beam markers:***
   - Same as in Appendix 'A'.
3. ***Realisation of a split waveguide structure:***
   - The realisation of split waveguide structure is same as discussed in Appendix 'A'(for deep etched ridge waveguides), with the only difference that time is decreased for dry etching process in order to get shallow etched waveguides.
   - Dry etch, using RIE ET340 machine to get shallow etched waveguides.
   - No wet etch at this stage, in order to keep the HSQ to protect waveguides.
4. ***Realisation of a slots in the split waveguide:***
   - Pre-bake the sample on hot plate for 2 minutes at 90 ºC.
   - Spin 100 % HSQ at 2000 rpm for 60 seconds.
   - Clean backside of the sample and bake at 90 ºC for 10 minutes.
   - VB6 *e*-beam writing.
   - Development in TMAH at 23 ºC for 30 seconds, RO water for 30 seconds, RO water for 30 seconds, IPA for 15 seconds.
   - Blow dry with gaseous Nitrogen.
5. ***Realisation of a window on the slot region***
   - PMMA (15 % of 2010) at 5000 rpm for 60 seconds and bake at 180 ºC for 30 minutes.

- Spin PMMA (4 % of 2041) at 5000 rpm for 60 seconds and bake at 180 ºC for 90 minutes.
- Clean backside of the sample after each spin.
- VB6 *e*-beam writing.
- Development in 1:1 IPA:MIBK solution at 23 ºC for 35 seconds, RO water for 30 seconds, RO water for 30 seconds, IPA for 30 seconds, blow dry with gaseous Nitrogen.
- Dry etch, using RIE ET340 machine to get deep etched slots in the split waveguide region.
- Wet etch the sample with 5:1 ratio of RO water and HF solution for 60 seconds, RO water for 60 seconds. Clean the sample in acetone, IPA and RO water for 2 minute each and blows dry with gaseous nitrogen.

No further fabrication process was carried out on this sample.

Appendix 'C'

Self-aligned bi-level etching design fabrication steps

The shallow etched split waveguide design fabrication process is carried out in the following order.

1. ***Cleaning of the sample:***
   - Same as in Appendix 'A'.
2. ***Realisation of e-beam markers:***
   - Same as in Appendix 'A'.
3. ***Realisation of waveguide and ICR:***
   - The realisation of waveguides and ICR is same as discussed in Annex 'A'(for deep etched ridge waveguides), with the only difference that time is decreased for dry etching process in order to get shallow etched waveguides.
   - Dry etch, using RIE ET340 machine to get shallow etched waveguides (~1.6 μm).
   - No wet etching at this stage, in order to keep the HSQ to protect waveguides.
4. ***Realisation of a window on the slot region***
   - PMMA (15 % of 2010) at 5000 rpm for 60 seconds and bake at 180 ºC for 30 minutes.
   - Spin PMMA (4 % of 2041) at 5000 rpm for 60 seconds and bake at 180 ºC for 90 minutes. Clean backside of the sample after each spin.
   - VB6 e-beam writing.
   - Development in 1:1 IPA:MIBK solution at 23 ºC for 35 seconds, RO water for 30 seconds, RO water for 30 seconds, IPA for 30 seconds, blow dry with gaseous Nitrogen.
   - Dry etch, using RIE ET340 machine to get deep etched slots in the split waveguide region.

- O_2 plasma ash for 15 minutes at 100 W.
- Clean the sample in acetone and then rinse with IPA and RO water for 1 minute each and blow dry with gaseous Nitrogen
- Wet etch the sample with 5:1 ratio of RO water and HF solution for 60 seconds, RO water for 60 seconds. Clean the sample in acetone, IPA and RO water for 2 minute each and blows dry with gaseous nitrogen.

5. Realisation of a current injection window:

- Deposit 200 nm of SiO_2 (PECVD).
- Spin 100 % HSQ at 4000 rpm for 60 seconds. Clean backside of the sample and bake in an oven at 180 ºC for 90 minutes.
- Finally, deposit 100 nm of SiO_2 (PECVD).
- PMMA (15 % of 2010) at 5000 rpm for 60 seconds and bake at 180 ºC for 30 minutes.
- PMMA (15 % of 2010) at 5000 rpm for 60 seconds and bake at 180 ºC for 30 minutes.
- Spin PMMA (4 % of 2041) at 5000 rpm for 60 seconds and bake at 180 ºC for 90 minutes.Clean backside of the sample after each spin.
- VB6 e-beam writing.
- Development in 1:1 IPA:MIBK solution at 23 ºC for 35 seconds, RO water for 30 seconds, RO water for 30 seconds, IPA for 30 seconds, blow dry with gaseous Nitrogen.
- Short O_2 clean for 2 minutes at 10 W.
- Dry etch with RIE 80 plus machine.
- O_2 plasma ash for 15 minutes at 100 W.
- Clean the sample in acetone and then rinse with IPA and RO water for 1 minute each and blow dry with gaseous Nitrogen.

6. Realisation of p-contact:

- PMMA (15 % of 2010) at 5000 rpm for 60 seconds and bake at 180 ºC for 30 minutes.

- PMMA (4 % of 2041) at 5000 rpm for 60 seconds and bake at 180 ºC for 90 minutes. Clean backside of the sample after each spin.
- VB6 e-beam writing.
- Development in 1:1 IPA:MIBK solution at 23 ºC for 30 seconds, RO water for 30 seconds, RO water for 30 seconds, IPA for 30 seconds, blow dry with gaseous Nitrogen.
- Short O_2 clean for 2 minutes at 10 W.
- *p*-metal (30 nm Ti, 33 nm Pt and 240 nm Au) deposition using e-beam Plassys machine.
- Deoxidise with 1:5 HCl: H2O mixture for 30 seconds. RO water for 30 seconds and blows dry with gaseous Nitrogen
- Lift off using acetone in hot water bath at 50 ºC for 2 hours. After left off cleaning with acetone, IPA and RO water for 1 minute each, blow dry with gaseous Nitrogen.
- O_2 ashing for 15 minutes at 100 Watt power.

7. Thinning of the sample:

- Same as in Appendix 'A'.

8. Realisation of n-contact and annealing:

- Same as in Appendix 'A'.